Contemporary Developments in Chemical and Biological Sciences

Edited by

Hari Shankar Biswas
Sandeep Poddar
Dilip Kumar Maiti

Published by :
Lincoln University College
Malaysia

www.lucp.net

Contemporary Developments in Chemical and Biological Sciences

Dr. Hari Shankar Biswas
Department of Chemistry
Surendranath College, India

Dr. Sandeep Poddar
Deputy Vice Chancellor (Research & Innovation)
Lincoln University College, Malaysia

Dr. Dilip Kumar Maiti
Professor, Department of Chemistry University College of Science & Technology, University of Calcuta, Kolkata, India
&
Former Vice-Chancellor, Biswa Bangla Biswabidyalay, West Bengal, India

Published by :
Lincoln University College, Malaysia

www.lucp.net

Copyright © 2026

Lincoln University College, Malaysia

All rights reserved

No part of this book can be reproduced or transmitted by any means, electronic or mechanical, including photocopying recording or by any information storage and retrieval system without prior written permission from the publisher.

Published on: 1th September, 2026

Published by:

Lincoln University College

Wisma Lincoln
No. 12-18, Off Jalan, Perbandaran SS 6/12
47301 Petaling Jaya
Selangor Darul Ehsan
Malaysia
Tel.: +603-7806 3478
Fax: +603-7806 3479
Toll Free: 1-300-880-111
E-mail: lucp@lincoln.edu.my
Web.: www.lucp.net

ISBN: 978-967- 2819-54-7

eISBN: 978-967-2819-55-4

Price: USD 100

Prof. (Dr.) Yogesh Upadhyay, *Ph.D.*
Vice-Chancellor
ITM University Gwalior, India

Foreword

In an era of rapid scientific advancement and increasingly complex global challenges, the chemical and biological sciences continue to play a vital role in expanding knowledge and developing meaningful solutions for society. *Contemporary Developments in Chemical and Biological Sciences"* edited by *Hari Shankar Biswas, Sandeep Poddar, Dilip Kumar Maiti,* published by *Lincoln University College, Malaysia,* is a timely contribution that reflects the diversity, innovation, and interdisciplinary nature of modern scientific research.

This volume brings together studies spanning theoretical and computational chemistry, fluorescence sensing, pharmacokinetic modelling, biological oscillations, advanced polymeric materials, coordination chemistry, catalysis, nanomaterials, and human health. Together, these contributions demonstrate how fundamental scientific understanding can support advances in healthcare, materials science, environmental protection, and emerging technologies.

A particular strength of the book is its emphasis on innovative methodologies, sustainable approaches, and the integration of theoretical knowledge with experimental application. The chapters highlight the growing importance of collaboration across disciplines in addressing contemporary scientific and societal challenges.

The editors and contributors deserve appreciation for compiling this diverse and valuable collection of scholarly work. I am confident that this book will serve as a useful reference for researchers, academicians, students, and professionals, while also encouraging further scientific inquiry and interdisciplinary collaboration.

I commend the authors and editors for their dedication and contribution to the advancement of chemical and biological sciences.

Prof. (Dr.) Yogesh Upadhyay

Contents _____ Pages

Preface

In the present era, chemical and biological sciences are progressing rapidly and contributing significantly to the understanding and solution of various scientific, environmental, and societal challenges. Continuous developments in research methods, technologies, and interdisciplinary approaches have opened new possibilities in areas such as sustainable chemistry, biomedical sciences, nanotechnology, environmental protection, and analytical science. This book, Contemporary Developments in Chemical and Biological Sciences, aims to present recent research trends and innovative scientific approaches while promoting a better understanding of emerging developments and their applications in addressing contemporary challenges.

The chapter “Balancing Static and Dynamic Correlation in Diradicals: A Low-Cost Multireference Perturbative Strategy” explores the theoretical challenges of describing diradicals and open-shell systems, where near-degenerate electronic states demand a balanced treatment of static and dynamic correlation. It highlights state-specific multireference perturbation theory combined with improved virtual orbitals as a computationally efficient strategy for achieving reliable electronic-state descriptions, energy gaps, and chemically meaningful insights with modest cost.

The review "Flourescence sensing mechanism and hydrazide moiety" explores the growing significance of hydrazide-based fluorescent chemosensors in detecting environmentally and biologically important ions. It summarizes recent developments in sensor design, fluorescence sensing mechanisms, selectivity, and practical applications. Particular attention is given to their potential in environmental monitoring, biological imaging, food safety, and future analytical technologies.

This study, authored by Abhradeep Basu and Anamika Basu, presents a physiologically based pharmacokinetic modelling approach to predict the plasma concentration profile of chrysin derived from Mangifera indica. Using PK-Sim® software, the model evaluates chrysin pharmacokinetics in rats, humans, and liver disease populations, providing valuable information about its absorption, metabolism, bioavailability, and potential therapeutic applications.

The chapter "Temperature compensation of Circadian Oscillations" provides a theoretical perspective on temperature compensation in circadian oscillations and chemical oscillatory systems. It examines how activation energy distributions influence reaction kinetics and explains why circadian rhythms remain relatively stable despite temperature variations, offering insight into the relationship between stochastic kinetics, biochemical regulation, and temperature-dependent oscillatory behaviour.

The chapter titled “Towards the Synthesis of Polymeric Ladderphanes from Cyclopropene Monomers: A Model Study” presents Biswajit Panda's exploration of strained cyclopropene monomers as promising precursors for ladderphane synthesis. Emphasizing ROMP polymerization, ring strain, and structural design, the chapter offers valuable insights into advanced polymeric architectures and their potential applications in organic synthesis and materials science.

Chandan Kumar, in his study, explores the preparation, characterization, and antimicrobial potential of heterobinuclear complexes derived from copper and nickel Schiff bases with alkali metal salts. The work highlights their structural features, spectral behavior, bonding characteristics, and promising antibacterial and antifungal activities, contributing to the growing importance of Schiff base metal complexes.

The chapter titled “Oxidation of Hydroxylamine by a Tetranuclear Manganese Complex in Aqueous Acidic Medium–Proton Coupled Electron Transfer” presents Suranjana Chatterjee's study on hydroxylamine oxidation using a stable tetranuclear manganese complex. Emphasizing kinetics, isotope effects, and hydrogen atom transfer, the chapter offers insight into proton-coupled electron transfer processes and manganese-based models relevant to biological oxidation systems.

The chapter by Usha Mandi describes chromium(VI)-immobilized mesoporous polyaniline (Cr-PANI) as a highly efficient heterogeneous catalyst for selective oxidation of alkanes and alkenes under mild reaction conditions. Highlighting catalyst characterization, selectivity, recyclability, and the use of hydrogen peroxide as a green oxidant, the chapter emphasizes sustainable approaches to valuable organic transformations.

The chapter titled “Recent Developments on the Synthesis of Colorless Polyimides” presents Pradip Kumar Tapaswi's review of advanced CPI materials for transparent and flexible electronic applications. It highlights recent monomer design strategies, suppression of charge-transfer interactions, and improvements in optical transparency, thermal stability, and mechanical performance for next-generation optoelectronic devices.

Debarati Dey's chapter provides a comprehensive review of the importance of zinc in human health, highlighting its essential roles in metabolism, immunity, growth, reproduction, enzyme function, and cellular repair. It discusses dietary sources, bioavailability, deficiency-related disorders, and preventive measures, offering valuable insight into zinc's significance as a vital trace element for maintaining human physiological balance.

Prasenjit Mandal and Sk Imran Ali present this work on the experimental characterization of carbon allotropes and nanocomposite materials using advanced analytical techniques. This research demonstrates the necessity of systematic material analysis to understand structural, morphological, chemical, and optical properties, supporting the development of efficient nanomaterials for diverse technological applications.

Together, these chapters showcase the diverse and interdisciplinary progress in chemical and biological sciences. The research contributions highlight innovative methodologies, sustainable technologies, and emerging scientific insights that address challenges in healthcare, materials science, environmental protection, and fundamental biological understanding, paving the way for future advancements.

Hari Shankar Biswas
Sandeep Poddar
Dilip Kumar Maiti

doi: 10.31674/book.2026cdcbs.001

Balancing Static and Dynamic Correlation in Diradicals: A Low-Cost Multireference Perturbative Strategy

Suvonil Sinha Ray

Department of Chemistry, Ramananda College, Bishnupur, Bankura -722122, WB, India

Corresponding Author's Email: suvonil.sinharay@gmail.com

Abstract

Radical systems remain difficult for electronic structure theory arising from their dominant multiconfigurational nature and the presence of near-degenerate electronic states. In such situations, a single reference description is generally insufficient, and even higher single-reference correlation methods can fail to provide a consistent ordering of low-lying states, especially when the single-triplet gap is small. These difficulties generally arise from an inadequate zeroth-order treatment of static correlation. Multireference perturbation theory offers an alternative that is more balanced by incorporating static correlation within a multiconfigurational framework, while dynamic correlation is recovered perturbatively. In a state-specific form, each electronic state is corrected independently, which tends to be more stable in situations where states are near-degenerate. This theory also mitigates some of the compromises that arise in the treatment of state-averaged approaches, although it comes at the cost of treating each state separately. The integration of improved virtual orbitals (IVO) into a specific framework gives additional advantages. By organizing the virtual space according to the desired electric character, the IVO strategy enhances stability and physical consistency in perturbative expansions without any enlargement of the active space. The IVO-enabled SSMRPT (state-specific multireference perturbation theory) method achieves an effective balance between precision and computational expense, making it suitable for the *ab initio* treatment of radiocolloid and open systems prototypes.

Keywords: *Diradicals; Improved Virtual Orbitals; Multireference Perturbation Theories; Open Shell Systems*

Introduction

Diradical and Radicaloids species hold a distinctive position in chemical theory because they contain two weakly interacting electrons that lie in nearly degenerate MOs (Williams *et al*., 2013). These electronic states are either closely or openly spaced, having different spin multiplicities and imparting different levels of chemical reactivity, producing chemical systems that are prominent in different mechanistic pathways in organic, inorganic, and biological chemistry. Starting from pericyclic reactions and bond rearrangement to photochemical reactions, diradical character is the basis of striking chemical phenomena. Many diradicals having low lifetimes restrict them to being detected directly in experimental arrest, thereby elevating the role of theoretical methods in clarifying their structural and electronic properties. The main theoretical difficulty arises from the multiconfigurational electronic character of these systems (Borden *et al*., 1982; Ramos-Cordoba *et al*., 2014). When the FMO (Frontier Molecular Orbitals) become nearly degenerate, the wave function of molecular systems cannot be well captured by a sole Slater-type determinant. In such a context, static (nondynamical) correlations showing the interplay among near-degenerate electrons—becomes dominant. On the same note, dynamical correlation, related to instantaneous electron-electron interactions, persists as essential for total correlation (Liu *et al.*, 2026; Zhao *et al.*, 2026). Single reference strategies, with even high-level correlation treatments, often struggle in the presence of quasi-degenerate cases. This shortcoming typically leads to the incorrect prediction of singlet-triplet energy gaps throughout the reaction coordinates.

These clearly indicate the necessity of applying a multireference (MR) scheme for systems demonstrating profound diradical character. Over the last few decades, a range of MR approaches has been introduced to incorporate dynamical correlation in different levels of theories on addition of a multiconfigurational space. Multireference configuration interaction (MRCI) (Szalay *et al.,* 2012), multireference perturbation theory (MRPT), and multireference coupled cluster (MRCC) methods represent few distinct strategies for achieving the said objective. While MRCC formulations (Čársky *et al.,* 2010) are competent for highly accurate descriptions of electronic states, their computational cost and complexity often restrict the wide usage. Truncated MRCI methods are widely employed, but it is not strictly size-extensive. So, on demand, MRPT approaches have emerged as very attractive and favorable computational methods (Otani *et al.*, 2025; Hubač *et al.*, 2010). But the formulation of wholly reliable MRPT schemes is not a trivial task (Chattopadhyay *et al.*, 2016). Early effective Hamiltonian formulations based on quasi-degenerate perturbation theory are prone to numerical breakdowns forming due to small denominators-termed as intruder-state problems (Sinha Ray, 2020). Several strategies have been proposed, comprising level-shift techniques and intermediate Hamiltonian strategies to isolate physically meaningful roots by limiting fake couplings. The state-specific methods provide a state-by-state basis result and become an important alternative boon. Other second-order MRPT methodologies like PASPT2(Partitioned Active Space Second-Order Perturbation Theory) (Liu *et al.*, 2026), CASPT2 (Complete Active Space Second-Order Perturbation Theory) (Roos *et al.*, 1996), NEVPT2 (N-Electron Valence State Second-Order Perturbation Theory) and MRMP2 (Multi-Reference Møller–Plesset Second-Order Perturbation Theory) have shown their efficacy. These approaches have limitations due to intruder problems and empirical parameter dependence. Multistate (MS) versions increase vivid efficiency in describing the systems, but they are related to effective Hamiltonian formulation. Other complexities may arise. The CAS-based SSMRPT (*aka* Mk-MRPT) (Mahapatra *et al.*, 1999) provides a unique alternative. SSMRPT reduces chance to intruder problems without any dependence on arbitrary level shifts. The method can be designed with different partitioning schemes using Brillouin-Wigner (BW) or Rayleigh-Schrödinger (RS) expansions. Traditional SSMRPT calculations rely on CASSCF i.e. complete active space self-consistent field method. The said method presents a multiconfigurational base with nonlinear optimization of orbitals. It often leads to failures at convergence criteria. Also, multiple unphysical solutions may arise. To ameliorate these concerns, various alternative strategies have been proposed. One such approach involves the use of IVO with complete active space configuration interaction (CASCI). By improving virtual orbitals and also eliminating iterative orbital optimization beyond SCF, the IVO-CASCI framework increases numerical balance and reduces computational cost. The integration of IVO-CASCI reference orbitals with the SSMRPT formalism gives birth to IVO-SSMRPT (Sinha Ray, 2020) methodology. This method attains a favorable balance between accuracy and computational need, making it well suited for the systematic investigation of diradical and other higher-orderradicaloid systems.

In the following section, the efficacy of the developed IVO-SSMRPT approach is compared and analyzed in the context of model quasi-degenerate molecular systems, including singlet m-benzyne and singlet 2,6-pyridyne (Sinha Ray *et al.*, 2016). These species offer strict benchmarks for assessing the robustness and predictive reliability of the method in capturing the characteristics of diradical chemistry.

Results and Discussion

Electronic Structure and Geometry of m-Benzyne:

m-Benzyne (1,3-didehydrobenzene) is one of the most important test scenarios for high-level electronic structure methods. The main issue lies in the essence of its single lowest energy state—whether it is attributed to a monocyclic or a bicyclic closed-shell configuration. The answer to this question depends on a comprehensive analysis of dynamic and non-dynamic electronic correlation. Multiconfigurational self-consistent field (MCSCF) optimizations have indicated that the monocyclic structure is more stable than the bicyclic alternative by the order of 12 to 13 kcal/mol. In contrast, Restricted Hartree-Fock (RHF) calculations

mistakenly favor the bicyclic form by nearly 18 kcal/mol due to the failure of single-reference mean-field approaches (Sinha Ray *et al.*, 2016). High-level correlated treatments provide a more consistent picture. The Monte Carlo approach based on CAS (8,8) references declare the single-ring structure as the lower in energy by about 2 kcal/mol. In a similar manner, coupled-cluster calculations including connected triple excitations like CCSD(T) and CCSDT methods recover the monocyclic structure to be the ground state, whereas lower-level CCSD calculations often predict the bicyclic geometry. This clearly indicates the importance of higher-order correlation inclusion.

Geometry optimizations were executed using the IVO-SSMRPT approach with a compact CAS (2,2) reference. For comparison, CASSCF based on (8,8) space and IVO-CASCI based on (8,8) space calculations were also examined prior to the perturbative approach. It was revealed that this broadening of the active space from (2,2) to (8,8) space did not yield considerable improvements in the structural parameters, indicating that the biradical electronic character is successfully captured within the smaller active space when combined with an appropriate level of dynamical correlation.

At the IVO-SSMRPT/cc-pVTZ level (Sinha Ray *et al.*, 2016) of theory, the optimized monocyclic structure indicates a C1-C3 separation of around 1.89 Å and a C1-C2-C3 bond angle of 90°. SSMRPT calculations, including conventional CAS SCF(2,2) level, predict a similar structural parameter, with a C1 to C3 bond distance close to 1.88 Å and that angle of roughly 87°. These values correspond well compared with Mk-MRPT2 and relaxed Mk-MRPT2 results, which yield the C1 and C3 atomic distances in the range of 1.87 to 2.00 Å according to the treatment of relaxation level. More intensive multireference coupled-cluster calculations (e.g., Mk-MRCCSD/pCVTZ) also tend to the monocyclic structure. Reported C1-C3 separations from CCSD(T) calculations with triple-zeta basis sets generally fall in the range of 2.02 to 2.10 Å, while CASPT2 calculations with high level CAS(12,12) reference space predict values around 2.07 Å and bond angles around 98-99°. Despite the fact that IVO-SSMRPT level predicted C1-C3 bond separation is slightly of smaller extent than some of the larger-active-space CASPT2 alternatives, the overall structural parameters are in close agreement. The small deviations are all within the expected range due to the differences in basis set and active space prototypes.

The comparative data of geometric parameters clearly indicates that the IVO-SSMRPT reproduces the features obtained from the methods which are considerably more costly. It achieves this performance with a compact active space and a state-specific perturbative level. This analysis clearly confirms that the IVO-SSMRPT provides a trustworthy and computationally cost-effective description of the diradicals plagued by static and dynamic correlation effects.

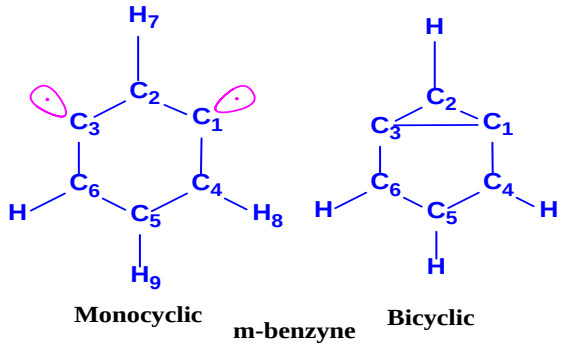

Figure 1**: **Geometrical Arrangement of m-benzyne (Sinha Ray et al., 2016)

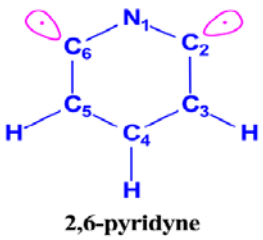

Figure 2: Geometrical Arrangement of 2,6-pyridyne (Sinha Ray et al., 2016)

Electronic Structure and Geometry of 2,6-Pyridyne:

The isomer of di-dehydropyridine molecule i.e. 2,6-pyridyne presents a challenge for high-level electronic structure approaches because of its strong biradical nature and the susceptibility of its ground-state nature to electronic correlation effects. Heterocyclic substitution of a nitrogen atom into the *m*-benzyne framework modifies both the electronic distribution and the geometric parameters of the system, thus influencing the balance between monocyclic and bicyclic structures. Here, the structural assignment may be analyzed either through the C2-C6 internuclear distance or the C2-N1-C6 bond angle.

The energy ordering of the two forms is highly method dependent. At the CCSD level, bicyclic nature is predicted to be energetically lower by approximately 2 kcal/mol. Multireference coupled-cluster treatments, such as Mk-MRCCSD, reverse this energy ordering and stabilize the single-ring form by approximately 4 kcal per mole. Inclusion of triple excitations at the CCSD(T) or CCSDT level further increases the stability of the monocyclic configuration by about 4-6 kcal/mol lower than its bicyclic alternative. These observations clearly indicate that the double excitations alone are insufficient to describe the electronic structure and thus higher-order correlation inclusion is needed. Similarly, Mk-MRCCSD(T) calculations also favor the monocyclic geometry by around 5 kcal/mol. By contrast, Hartree-Fock and other common density functional treatments (e.g., BPW91/cc-pVDZ) lead to a bicyclic minimum level, thereby indicating their inability to capture both types of electronic correlation effects.

Geometry optimization performed at SSMRPT or IVO-SSMRPT/cc-pCVTZ methodology consistently gives a monocyclic ground state. The calculated C2-C6 distances are 2.0434 Å and 2.0421 Å for SSMRPT and IVO-SSMRPT, respectively. These values closely align with those found from the “gold standard” CCSD(T) method and also the Mk-MRCCSD calculations by approximately 2.01 to 2.02 Å. Whereas CCSD predicts a shorter C2 & C6 separation of 1.9140 Å, showing its preference for the bicyclic arrangement.

Table 1: Structural Values of the Lowest-Energy State of m-Benzyne.

Geometrical Parameters	CCSD(T)/ cc-pVTZ	CASPT2/ ANO-L	Mk-MRCCSD/ cc-pCVTZ	SS-MRPT/ cc-pVTZ	IVO-SSMRPT/ cc-pVTZ
R_C1-C2	1.3717	1.367	1.3586 (1.3594)	1.3611	1.3429
R_C1-C4	1.3785	1.368	1.3697 (1.3696)	1.3681	1.3690
R_C4-C5	1.4031	1.397	1.3945 (1.3954)	1.4082	1.4007
R_C1-C3	2.0581	2.074	2.5506 (2.5459)	1.8823	1.8932
R_C2-H7	1.0775		1.0745 (1.0748)	1.0768	1.0745
R_C4-H8	1.0821		1.0789 (1.0788)	1.0817	1.0801
R_C5-H9	1.0862		1.0825 (1.0827)	1.0831	1.0811
∠ C1-C2-C3	97.2	98.7	94.65 (95.60)	87.00	89.60
∠ C2-C3-C6	137.49	136.3	139.66 (138.91)	145.70	144.64
∠ C3-C6-C5	117.00	117.4	116.32 (116.49)	117.07	117.10
∠ C6-C5-C4	113.8	113.9	113.39 (113.61)	113.40	112.82

Source: Sinha Ray et al., 2016
Note: Bond Separations Are in Å and Angles are in Degree (°). Values in Bracket are of Mk-MRCCSD-TCSCF Method

CCSD also yields a relatively shorter angle of 86.15°, whereas SSMRPT and IVO-SSMRPT predict values near 99.8°. These predictions are in well agreement with CCSD(T) (~96.8°) and Mk-MRCCSD (~98°) results. Larger active space-based CASSCF calculations report an even wider angle of ~106°, stating the biradical character of the monocyclic form. In contrast, the BPW91/cc-pVDZ level produces a C2-C6 distance of 1.561 Å and an angle of 69°, indicative of a fully bicyclic structure minimum. Notably, spin-flip EOM-CCSD calculations also provide C2-C6 separations on the order of 2.08 Å, with the same structural finding by the IVO-SSMRPT treatment.

It can be stated safely that the close agreement between SSMRPT/IVO-SSMRPT and high-level triples-inclusive CC or MRCC methods demonstrates that the intrinsic static-dynamic correlation in 2,6-pyridyne is essentially captured within the current framework. At the same time, the IVO-SSMRPT approach avoids

the wrong stabilization of the bicyclic character as suggested in lower-order single-reference wave function-based and DFT treatments. These results clearly predict that an SSMRPT strategy, when combined with an IVO reference space, creates a robust method, namely, IVO-SSMRPT. It can provide a very reliable description of heterocyclic biradical systems at significantly reduced computational cost.

Table 2: Structural Variables of the Global Minimum of 2,6-pyridyne. Bond Distances are in Å and Angles are in Degree (°)

Geometrical Parameters	CCSD(T)	Mk-MRCCSD	B3LYP	CASSCF-SSMRPT	IVO-SSMRPT
N1–C2	1.3470	1.3361	1.337	1.3355	1.3349
C2–C3	1.3801	1.3735	1.380	1.3783	1.3772
C3–C4	1.3964	1.3908	1.411	1.3929	1.4010
C2–C6	2.0146	2.0169		2.0434	2.0421
C3–H	1.0800	1.0777		1.0772	1.0767
C4–H	1.0855	1.0825		1.0808	1.0810
∠C2–N1–C6	96.80	98.01	69	99.82	99.80
∠N1–C2–C3	138.12	137.45		136.99	136.83
∠C2–C3–C4	117.01	116.80		116.07	116.00
∠C3–C4–C5	112.93	113.49	111	113.30	113.22
∠C2–C3–H	119.51	119.78		119.34	119.30

Source: Sinha Ray et al., 2016

By depicting the refined balance between electron pairing during bond formation and biradical delocalization with low computational resources, the IVO-SSMRPT technique offers a realistic alternative to both the CAS-based PT methods and highly iterative MRCC approaches for these representative quasi-degenerate systems.

Conclusion

The present study reflects that an accurate yet computationally efficient multireference framework can be constructed by coupling state-specific perturbation theory with IVO-CASCI reference. Incorporation of a multipartition Møller-Plesset level of Hamiltonian (zeroth level) within the Jeziorski-Monkhorst (JM) ansatz yields the IVO-SSMRPT formulation, which achieves a balanced and theoretically coherent approach of quasi-degenerate electronic systems. It is observed that the IVO-SSMRPT can consider the intricate interplay between static and dynamic correlations of systems with radical characters. The numerical results clearly prove that the IVO-SSMRPT provides geometrical and energy data comparable to those obtained from highly demanding MRCC treatments.

The intrinsic extensive size nature, computational affordability and improved reference space bring the newly developed IVO-SSMRPT method a vital role among other *state of the art* methods related to many-body systems. It highlights its potential for wide usage in chemically and biologically relevant pathways involving radicals of arbitrary levels of electronic correlation effects.

Acknowledgment

The author conveys gratitude to Prof. S. K. Chattopadhyay of IIEST, Shibpur, India, for his encouragement. The author also extends appreciation to Ramananda College, Bishnupur, India, for support and cooperation.

References

Borden, W. T. (1982). Diradicals. In W. T. Borden (Ed.), *Diradicals* (pp. 1–72). New York: Wiley-Interscience.

Čársky, P., Paldus, J., & Pittner, J. (Eds.). (2010). *Recent progress in coupled cluster methods* (Vol. 11). Dordrecht, The Netherlands: Springer. https://doi.org/10.1007/978-90-481-3567-7

Chattopadhyay, S., Chaudhuri, R. K., Sinha Mahapatra, U., Ghosh, A., & Sinha Ray, S. (2016). State-specific multireference perturbation theory: Development and present status. *WIREs Computational Molecular Science, 6*, 266–291. https://doi.org/10.1002/wcms.1258

Hubač, I., & Wilson, S. (2010). Brillouin–Wigner methods for many-body systems. In *Progress in Theoretical Chemistry and Physics* (Vol. 21). New York: Springer. https://doi.org/10.1007/978-90-481-3698-8

Liu, C., Zhang, N., & Liu, W. (2026). PASPT2: A Size-Extensive and Size-Consistent Partial-Active-Space Multistate Multireference Second-Order Perturbation Theory for Strongly Correlated Electrons. *Precision Chemistry,* https://doi.org/10.1021/prechem.5c00408.

Mahapatra, U. S., Datta, B., & Mukherjee, D. (1999). A size-consistent state-specific multireference coupled cluster theory: Formal developments and molecular applications. *Journal of Chemical Physics, 110*, 6171–6188. https://doi.org/10.1063/1.478523

Otani, Y., Nakatani, K., & Nakatani, N. (2025). Multi-reference perturbation theories based on the DOCI wavefunction. *Journal of Chemical Physics, 163*, 214113. https://doi.org/10.1063/5.0293297

Ramos-Cordoba, E., & Salvador, P. (2014). Characterization and quantification of polyradical character. *Journal of Chemical Theory and Computation, 10*, 634–641. https://doi.org/10.1021/ct400987h

Roos, B. O., Andersson, K., Fülscher, M. P., Malmqvist, P.-Å., Serrano-Andrés, L., Pierloot, K., & Merchán, M. (1996). Multiconfigurational perturbation theory: Applications in electronic spectroscopy. In I. Prigogine & S. A. Rice (Eds.), *Advances in Chemical Physics* (Vol. 93, pp. 219–331). https://doi.org/10.1002/9780470141458.ch4

Sinha Ray, S. (2020). Ab initio diagnosis of isomerization pathway of diphosphene and diphosphinylidene. *Chemical Physics, 529*, 110555. https://doi.org/10.1016/j.chemphys.2019.110555

Sinha Ray, S., Ghosh, A., Chattopadhyay, S., & Chaudhuri, R. K. (2016). Taming the electronic structure of diradicals through the window of computationally cost effective multireference perturbation theory. *The Journal of Physical Chemistry A*, *120*(29), 5897-5916. https://doi.org/10.1021/acs.jpca.6b03211

Szalay, P. G., Müller, T., Gidofalvi, G., Lischka, H., & Shepard, R. (2012). Multiconfiguration self-consistent field and multireference configuration interaction methods and applications. *Chemical Reviews, 112*, 108–181. https://doi.org/10.1021/cr200137a

Williams, W. P. E., Jankiewicz, B. J., Yang, L., & Kenttämaa, H. I. (2013). Properties and reactivity of gaseous distonic radical ions with aryl radical sites. *Chemical Reviews, 113*, 6949–6985. https://doi.org/10.1021/cr300463n

Zhao, T., & Krylov, A. I. (2026). Analytic gradients for EOM-DEA-CCSD and EOM-DIP-CCSD: Theory, implementation, and application to diradicals. *Journal of Chemical Physics, 164*, 014116. https://doi.org/10.1063/5.0308620

doi: 10.31674/book.2026cdcbs.002

Flourescence Sensing Mechanism and Hydrazide Moiety

Chandana Sen

Department of Chemistry, Behala College, Behala, Parnasree 700060, West Bengal, India

Corresponding Author's Email: chandanasen2016@gmail.com

Abstract

Hydrazide-based fluorescent chemosensors have emerged as a versatile and highly efficient class of molecular probes for the selective and sensitive detection of biologically and environmentally important cations and anions. The growing concern over the toxicity of toxic metal ions, such as Hg^{2+}, Pb^{2+}, Cd^{2+}, and Cu^{2+}, as well as hazardous anions including F^-, CN^-, and $H_2PO_4^-$, has intensified the need for rapid, cost-effective, and reliable sensing strategies. Hydrazide moieties possess unique structural features, including nitrogen and oxygen donor atoms, facile hydrogen-bonding capability, and tunable electronic properties, making them excellent recognition units for ion sensing. Upon interaction with target ions, hydrazide-based sensors exhibit significant fluorescence responses through mechanisms such as photoinduced electron transfer (PET), intramolecular charge transfer (ICT), chelation-enhanced fluorescence (CHEF), and excited-state intramolecular proton transfer (ESIPT). This review highlights recent advances in hydrazide-based fluorescent chemosensors, emphasizing their design strategies, sensing mechanisms, selectivity toward cations and anions, and practical applications in environmental monitoring, biological imaging, and food safety. Furthermore, the review discusses current challenges and future perspectives in developing highly selective, sensitive, and multifunctional hydrazide-derived fluorescent sensors for real-world analytical applications.

Keywords: *Biological; Environmental; Fluorescent Chemosensor; Hydrazide; Toxicity*

Introduction

With expanded population and degradation of Mother Nature are very closely associated with each other. The modern habitat is now in major demanding situation due to uncontrolled urbanization and industrialization and different agricultural impurifications. Large amount of artificial and man-made chemical compounds is ejected every moment to the environment and increases day to day; about 700 new synthetic materials are inaugurated into the market every year in the US only (U.S. Environmental Protection Agency, 2014; Pye & Patrick, 1983). Synthetic components are of particular worry is that those may collectively developing severe damage to individual wellness. Some components are directly associated with endocrine disrupting effects, some artificial components are suspected of being promote cancer or directly stored and biomagnified through the food chain (Kantiani *et al.*, 2010). Not only individual deed but also natural calamities like Earthquakes, Volcanoes, Floods, changes of the river pathways, uncontrolled development of different fungi and microbes etc. are responsible of ecological catastrophe and thread to human being.

Around 2 million tonnes of refuse products manufactured by different subjects are being deposited daily into the ocean, sea, river, lakes etc. (Fan *et al.*, 2012; Rijith *et al.*, 2012) in whole world. Around 70% of crude hazards are ejected into the running water bodies in different up growing nations. Every living entity suffered from wastewater contamination from running water body (Li *et al.*, 2013). Developing countries are more liable to those dangerous effects of different contaminants concerning wellbeing and environmental suffering. Villagers are more affected by different diseases because difficulty in establishment, functing and up-keep of trash matter treatment plants and the restricted alternative sources of water supply (Kansal & Kumari, 2014; Shafiquzzaman *et al.*, 2009).

High toxic consequences of chemical contaminants to individuals and the surroundings, communal concerns over chemical wastes in the environment and in diet have been up growing immoderately

(Govindhan *et al.*, 2014). Acute contamination in both abiotic and biotic communities has been distressing from different contaminants like various metal ions, toxic anions and pesticides; has become a subject of great trouble (Dhillon *et al.*, 2015).

Chemical Elements and the Human Health

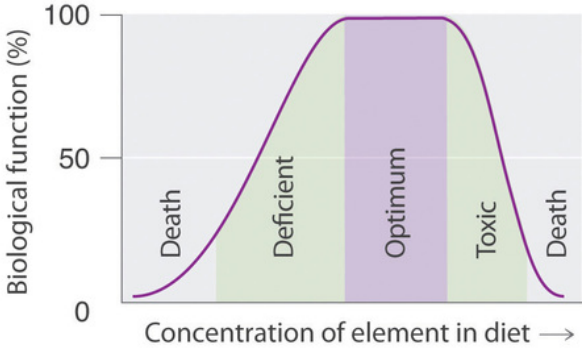

Figure 1: Effect of Different Concentrations of an Essential Element in Human Health

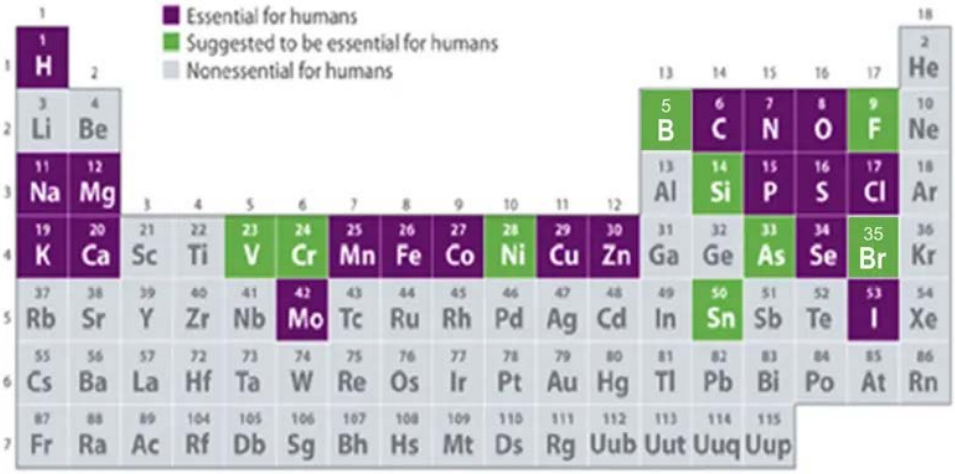

Figure 2: The Essential Elements for Human Health in the Periodic Table.

Among 92 naturally occurring elements bulk elements are 11 (C, H, N, O, Ca, Na, K, Mg, P, S, Cl) and 16 appear in trace/ultratrace concentration (Mn, Fe, Co, Cu, Zn, P, S, I, V, Cr, Ni, Se, Mo, I, B, Br) constitute our biology (Figure 1 and 2). Essential ions both at higher and lower concentration become toxic. Both excessive and deficient quantities of ions are poisonous to human health. Majority of ions are nonbiodegradable.

Toxicity of Anions

CO_3^{2-}, OH^-, NO^{3-}, NO^{2-}, Phosphates (PO_4^{3-}, HPO_4^{2-} , $H_2PO_4^-$, $P_2O_7^{4-}$), Cl^-, Br^-, I^-, CN^-, SCN^-, OCl^-, SO_3^{2-}, SO_4^{2-}, $S_2O_3^{2-}$ anions are essential in different stages of metabolic process in various functions. Arsenic (AsO_2^- or AsO_3^{3-}/AsO_4^-) is most toxic among all those panic creating ions. The United States Agency for Toxic Substances and Disease Registry (ATSDR) has decelerated arsenic is utmost dangerous element for a lot of decades because of its ecological existence and burial wellness issues (Shen *et al.*, 2013).

Different natural weathering, natural chemical changes materialize within aerosphere, earth's crust and water bodies (geochemical reactions), various anthropogenic activities, biological activity, volcanic degradations influence mobility of arsenic (Moriarty *et al.*, 2013; Sullivan *et al.*, 2010).

Excessive consumption of fluoride (>1.5 mg L^{-1}) may cause fluorosis (Ayoob & Gupta, 2006) and urolithiasis (Upadhyay *et al.*, 2010), has been reported in various countries, including India, China. Increasing bone density and cancer may cause by fluoride toxicity (Kleerekoper, 1998).

Hypophosphatemia, musculoskeletal and cardiovascular systems, tissue damage highly affected by phosphate toxicity (Razzaque, 2011). Eutrophication has become a global issue in immobile water bodies such as reservoirs, lakes and estuaries (Mak *et al.*, 2003). Excessive soluble phosphates usually conduct to unusual algal growth along with depletion in dissolved oxygen, decomposition, eutrophication and finally reduction in water standard (Warwick *et al.*, 2013).

Chloride and nitrate levels have been executed to trace pollution from different agriculture field, fish farms from waste accumulation. Highly toxic cyanide can lead to severe problems to animals (Dale & Rebek, 2006). Gold mining, electroplating, and the production of various organic chemicals and polymers, including nitriles, nylon and acrylic plastics, increase the likelihood of unintended cyanide release (Westley *et al.*, 1981).

Cations and their Toxicity

Most of the enzyme contains different transition metals at their active site. Free forms of transition metal ions are highly toxic in nature. Histidines, cysteines, aspertates and glutamates (small) are attracted by free Zn^{2+} ions, allows Zn^{2+} to bind to various proteins even at Nano molar concentrations. As a result, induction of protein–protein interactions and enzyme inhibition are common issues. Redox active iron and copper are influential catalysts to generate free radical species (Hessels & Merkx, 2015).

Abnormal deposition of aluminium in body tissues in humans and animals can cause Alzheimer's disease, Parkinson's disease, colic and gastrointestinal problems, rickets, lung cancer etc., it can also damage the brain, liver and kidneys (Becaria *et al.*, 2002).

Inadequate amount of chromium can increase the threats associated with diabetes, cardiovascular diseases and central nervous system disorders (Arakawa *et al.*, 2000) and also higher levels Cr^{3+} may even lead to cancer (Vincent, 2000).

Above discussion clearly shows that ions are essential for healthy life, but they are toxic after a limit. For the healthy living, different internationally accreditation organizations like American Public Health Association (APHA), United States Environmental Protection Agency (USEPA), World Health Organization (WHO), Indian Standard Institution (ISI), Indian Council of Medical Research (ICMR) and Central Pollution Control Board (CPCB) directed the safe limits of various ions in drinking water (Kumar & Puri, 2012).

From the above discussion it is recognized that ions are vital for environmental safety and healthy life. The measurement of ions' concentration is necessary for Growing public interest and increasingly stringent legal requirements for environmental, food, and water monitoring. One of the important aspects is to couple various methodologies, physical process to develop analytical techniques those are highly sensitive, specific, cheap, environmentally benign, easy to handle and versatile. Thus, market demanding research in chemistry is adopting its space.

Instrumental Techniques of Detection

Different techniques have been used for elemental analysis like flame or graphite furnace atomic absorption spectroscopy (AAS) (Cerchiaro *et al.*, 2013), inductively coupled plasma-atomic emission spectrometry (ICP-AES) (Pomazal *et al.*, 1999), voltammetry (van den Berg, 2006), inductively coupled plasma mass spectrometry (ICPMS) (Pröfrock & Prange, 2012), CE (capillary electrophoresis) (Timerbaev *et al.*, 1999), FAAS (flame atomic absorption spectroscopy) (Shamspur *et al.*, 2005), thin chitosan films (McIlwee *et al.*, 2008), functionalized metal nanoparticles (Mehta *et al.*, 2014), flow injection (Ussher *et al.*, 2009), carbon dots (Zhao *et al.*, 2014), graphene quantum dots (Ananthanarayanan *et al.*, 2014), fiber-optic redox

methods (Chudyk *et al.*, 2014) and cyclodextrin supramolecular complex (Xu *et al.*, 2010). However, these techniques are costly, sophisticated; quite inconvenient for its complexity. Furthermore, UV-visible and fluorescence spectroscopy are the most regularly used modes as well as the most favourable methods for the detection of physiologically and environmentally important analyte, due to their low detection limit and imaging of analyte in biological system. Among various sensing techniques UV-visible and fluorescence spectroscopy grabs the most attention of sensor laboratories due to its low cost, simple in operation method, highly selective and sensitive in nature.

Chemical Sensor

Optical absorption, redox potential, luminescence etc. are mostly used techniques. However, sensors based on other spectroscopic techniques, as well as those utilizing optical parameters such as reflectivity and refractive index, have also been extensively developed (McDonagh *et al.*, 2008). Fluorescence spectroscopic technique can provide excellent sensitivity and fluorescent sensors are 105 times more sensitive than any other absorption spectroscopic technique (Valeur, 2002). Excitation and emission spectra, fluorescence intensity, anisotropy, Stokes shift and fluorescence lifetime can provide qualitative recognition and quantitative measurement of various cat ions, anions and particles (Parker, 2000) in case of fluorescence technique.

Basis of Designing Fluorescent Probe

A fluorescent chemosensor is a molecular system that exhibits a change in its fluorescence spectra when an interconnection take place with a chemical species. Two different chemical specieses produced a new species called a fluorescent chemosensor. Where fluorophore is a signalling unit and guest receptor has identification power, spacer is the connecting unit of them (Figure 3), the newly formed species is so-called fluorophore–spacer–receptor scaffold (Lodeiro *et al.*, 2010). When the receptor unit bind with the guest molecule, automatically different fluorophoric property changes, for instances emission wavelength, fluorescence intensity and fluorescence lifetime. They follow different mechanism too. It is a mandatory task to develop and improve various sophisticated fluorescence chemosensor. It uses in different disciplines such as process control, environmental monitoring, food product etc (Bell & Hext, 2004).

The signaling moiety is a signal transducer, i.e. it transfers the information into an optical signal presented as changes in the various photophysical characteristics of the fluorophore. The sensing mechanism basically controlled by different concepts, such as soft-hard acid base principle is the fundamental concept of selection, the principle of coordination theory, size of chelate ring, size of space in chelate cavity etc.

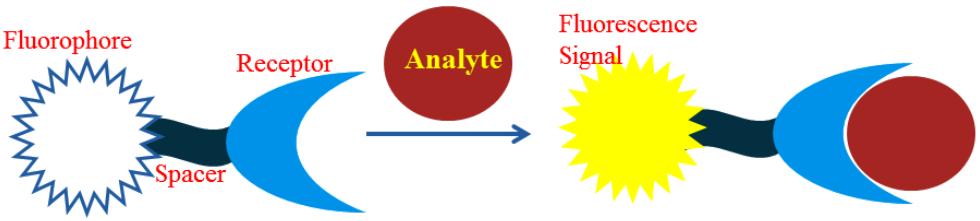

Figure 3: Schematic Diagram Depicting the Binding of an Analyte (Guest) to a Chemosensor (Host), Resulting in the Formation of a Host–Guest Complex with Altered Optical Properties

Most conventional sensing mechanisms are photoinduced electron transfer (PET) (Martinez-Manez *et al.*, 2003), intramolecular charge transfer (ICT) (Kim & Quang, 2007), metal–ligand charge transfer (MLCT) (Zhao & Huang, 2010), twisted intramolecular charge transfer (TICT), electronic energy transfer (EET) (De Silva *et al.*, 1997; Martinez-Manez *et al.*, 2003), and fluorescence resonance energy transfer (FRET) (Carlson & Campbell, 2009) and excimer/exciplex formation (Martinez-Manez *et al.*, 2003), . Based on

conformational restriction, two mechanisms are also available, that are Aggregation-induced emission (AIE) (Hong *et al.*, 2009), and CQN isomerisation. ESIPT is another sensing mechanism (Berezin & Achilefu, 2010) but not been well reviewed. Non radiative decay and radiative decay generally encourage by a flexible structure and a rigid fluorophoric structure; Isomerization of the double bond requires energy and promotes nonradiative decay (Toyota, 2010); the rate of electron transfer in the excited state is significantly slower than that of proton transfer (Hsieh *et al.*, 2008). Molecular rotation reduces fluorescence intensity.

Different Functional Motifs to Chemosensor

Hydrazides contain a nitrogen-to-nitrogen covalent bond and at least one acyl group, again 3 substituents also; the derivatives belong to the organic compounds (McNaught *et al.*, 1997). Hydrazides generally have the structure E (=O)-NR-NR_2, with the R substituents most commonly being hydrogen atoms. There is another classification depending on atom attached to the oxygen in hydrazide moiety: sulfonohydrazides (R-S (=O)$_2$-NH-NH_2), carbohydrazides (R-C(=O)-NH-NH_2) and phosphonic dihydrazides (R-P(=O) (-NH-NH_2)$_2$. Various bioactive heterocyclic compounds contain hydrazides and hydrazones moiety; they have wide clinical and biological applications (Narang *et al.*, 2012). Hydrazide derivatives have various biological applications i.e. anthelmintic, anti-inflammatory, anticancer, antimicrobial, anti-HIV, antimycobacterial, antidiabetic, trypanocidal as well antimalarial activities.

Hydrazide derivatives have strong binding ability with different metal ions through stable chelate formation (Das *et al.*, 2015) and due to presence of hydrazides-NH, it may bind with anions via H-bond formation (Samanta *et al.*, 2015). Presence of free -NH_2 creates a wide range of simple condensation probability with carbonyl to generate new and new Schiff bases.

Hydrazide Appended Fluorescence Probes as Analyte Sensors

Here are some pioneering works related to hydrazide moieties sensitive for selective fluorescence sensors are discussing below.

(a) ((2-hydroxy-5-methyl-1,3-phenylene)bis(methanylylidene))bis(quinoline-2-carbohydrazide)

Quinaldic hydrazide (2 mmol) was added to an ethanolic solution of 2,6-diformyl-4-methylphenol (1 mmol), resulting in the formation of a yellow precipitate of the probe (Figure 4). The probe shows multi-analyte sensitivity by displaying distinct emission spectra characteristic of Al^{3+}, Zn^{2+}, and F^- ions. On excitation at 450 nm, the probe showed a remarkable enhancement in emission spectra exclusively in the presence of Al^{3+} and Zn^{2+}, with two distinct emission maxima observed at 500 nm and 550 nm, respectively.

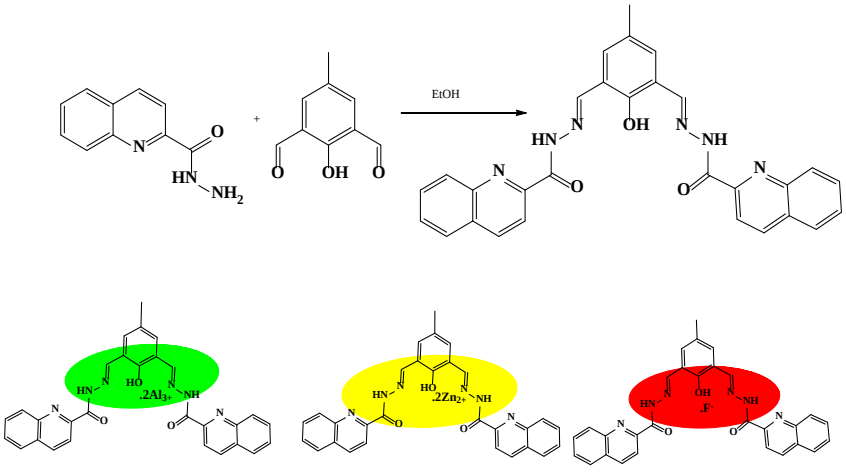

Figure 4: Synthesis of Probe and Schematic Representation of Sensing of Al^{3+}, Zn^{2+} and F^- by Probe

This response was evaluated in a buffered solution containing various competing metal ions, including Na^+, K^+, Mg^{2+}, Ca^{2+}, Cr^{3+}, Fe^{3+}, Co^{2+}, Ni^{2+}, Cu^{2+}, Zn^{2+}, Cd^{2+}, Hg^{2+}, Ag^+, Pb^{2+}, and Al^{3+}. Also, fluorescence sensitivity of the probe was checked with various anions (F^-, Cl^-, Br^-, I^-, OH^-, NO^{3-}, S^{2-}, SO_4^{2-}, HSO_3^-, ClO_4^-, ClO_3^-, CN^-, $H_2PO_4^-$, and PO_4^{3-}), only F conveyed an alteration in the emission spectra of the probe by enhancing emission intensity at 575 nm in in an acetonitrile solvent medium with 0.33% DMSO as a co-solvent. The detection limit of probe for Zn^{2+}, Al^{3+} and F^- is 35 ppb, 32 ppb and 40 ppb respectively. Interaction between probe and analyses follow the chelation enhanced fluorescence (CHEF) mechanism. In general, deprotonation initiates the ICT process, resulting in the activation ("turn-on") of the receptor's fluorescence (Datta *et al.*, 2015).

(b) (E)-N'-((E)-3-(4-(dimethylamino)phenyl)allylidene)quinoline-2-carbohydrazide

To a methanolic solution of quinaldic hydrazide, 4-(dimethylamino)cinnamaldehyde was added, followed by the addition of approximately two drops of acetic acid. The reaction mixture was then stirred at room temperature for 12 hours, resulting in the formation of an orange solid probe. The probe can identify Zn^{2+}, Cd^{2+} and Pb^{2+} are environmentally and biologically significant metal ions, in the presence of various metal ions (Na^+, K^+, Ca^{2+}, Mg^{2+}, Al^{3+}, Cr^{3+}, Fe^{3+}, Ni^{2+}, Co^{2+}, Cu^{2+}, Zn^{2+}, Hg^{2+}, Pb^{2+}, Cd^{2+}, and Ag^+) via selective turn-on fluorescence responses under physiological pH conditions. In the presence of excess (20 equivalents) Pb^{2+}, probe showed a ~ 20 fold increase in its fluorescence intensity with a well-defined emission maximum at 582 nm. Similarly, addition of excess (20 equivalents) Zn^{2+} and Cd^{2+} to probe led to approximately a 10-fold and 9-fold increase in fluorescence intensity of the probe, along with the appearance of new emission maxima at 573 nm and 608 nm, respectively (Figure 5). The detection limits for Zn^{2+}, Cd^{2+}, and Pb^{2+} were determined to be 21.27 ppb, 72.81 ppb and 0.68 ppm, respectively. The selective turn-on emission of the probe in the presence of Pb^{2+}, Zn^{2+}, and Cd^{2+} can be attributed to the chelation-enhanced fluorescence (CHEF) mechanism (Samanta *et al.*, 2016).

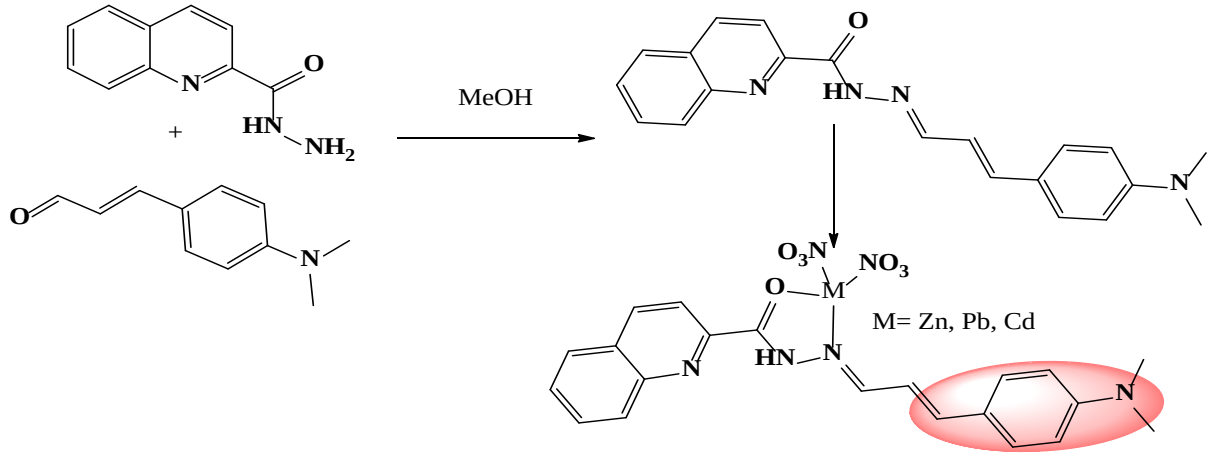

Figure 5: Synthesis of Probe and Schematic Representation of Sensing of Zn^{2+} , Pb^{2+} and Cd^{2+} by Probe

(c) (3,5-dichloro-2- hydroxybenzylidene) quinoline-2-carbohydrazide

A methanolic solution of quinoline-4-carboxylic hydrazide was added to a methanolic solution of 3,5-dichlorosalicylaldehyde, and the resulting reaction mixture was refluxed for 5 hours under a nitrogen (N_2) atmosphere. The mixture was separated by removing solvent under reduced pressure and kept into refrigerator 24 hours. By filtration probe was collected as yellow mass. The probe selectively identifies Al^{3+} in EtOH-H_2O and Complexed with Al^{3+} in a 1:1 molar ratio. The detection limit was very low as 0.012 μM (Fig 6). But probe-Al^{3+} was destroyed by F^- in the solution, the complex could be used to identify F^- in solution phase future. The enhancement fluorescence of the probe was explained by CHEF mechanism

induced by Al^{3+}. The probe was successfully employed for the sensitive detection of trace Al^{3+} in human blood serum and tap water samples. Furthermore, it was utilized for fluorescence imaging of Al^{3+} in HeLa cells, demonstrating its potential for both environmental and biological applications (Zhou *et al.*, 2018).

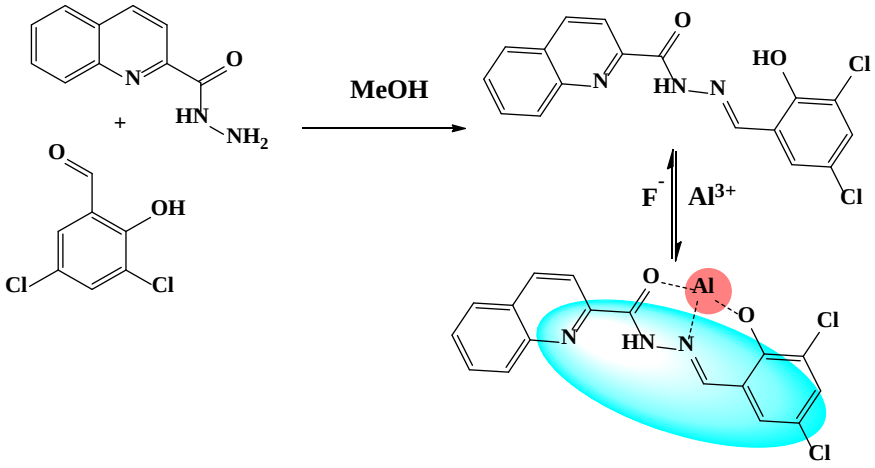

Figure 6: Synthesis of Probe and Schematic Representation of Sensing of Al^{3+} and F^- by Probe

(d) 2-((2-Hydroxynaphthalen-1-yl)methylene)hydrazine carbothioamide

Condensation of simple hydrazide, Thiosemicarbazide and 2-hydroxy-1-naphthaldehyde synthesised 2-((2-hydroxynaphthalen-1-yl)methylene)hydrazine carbothioamide (Fig 7), which recognize AsO_2^- and CN^- ions. At an excitation wavelength of 363 nm, arsenite and cyanide ions are selectively exhibited a 'turn-on' fluorescence emission at 495 nm in the presence of the target analyte, while showing negligible response toward the other anions investigated (F^-, Cl^-, Br^-, I^-, SO_4^{2-}, SCN^-, SO_3^{2-}, $H_2PO_4^-$, HPO_4^{2-}, CH_3COO^-, NO_3^-, N_3^- , PO_4^{3-} and IO_3^-) in DMF: H_2O medium. The limits of detection (LODs) for cyanide and arsenite ions were 77 nM and 66 nM, respectively. Extensive hydrogen bonding accompanied by deprotonation between the probe and two anions was the driving force for enhancement in the intensity of emission spectra (Yadav *et al.*, 2016).

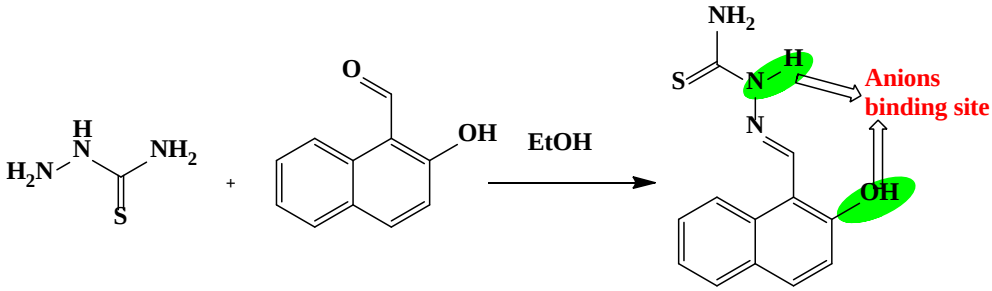

Figure 7: The Synthesis of Dual AsO_2^-, CN^- Sensor Probe with Assignment of Anions Binding Unit

(e) 2,2'-((2-hydroxy-5-methyl-1,3-phenylene)bis(methanylylidene))bis(hydrazinecarbo thioamide)

The probe was synthesized by condensation of thiosemicarbazide with 2-hydroxy-5-methylbenzene-1,3-dialdehyde in 2:1 moler ratio in ethanolic solution and a yellow mass was obtained with good yield (Fig 8). The probe was selectively identifying acetate ion in DMSO medium by reflecting tricolour emission (Lohar *et al.*, 2016). At the initial stage, the emission peak at 562 nm (orange) gradually decreases in intensity while exhibiting a blue shift to 548 nm (yellow) over the first 1 h. Between 1 and 1.5 h, the emission intensity increases at the same wavelength (548 nm) without any further shift. From 1.5 to 2 h, the emission intensity decreases again, accompanied by an additional blue shift. The emission intensity at 515 nm (green)

increased continuously over the time interval from 30 s to 2 h. The association constant (Ka) of the probe toward AcO^-, determined using the Benesi–Hildebrand method, was $6.6 \times 10^4\ M^{-1}$, while the detection limit for AcO^- was calculated to be 1.06×10^{-7} M.

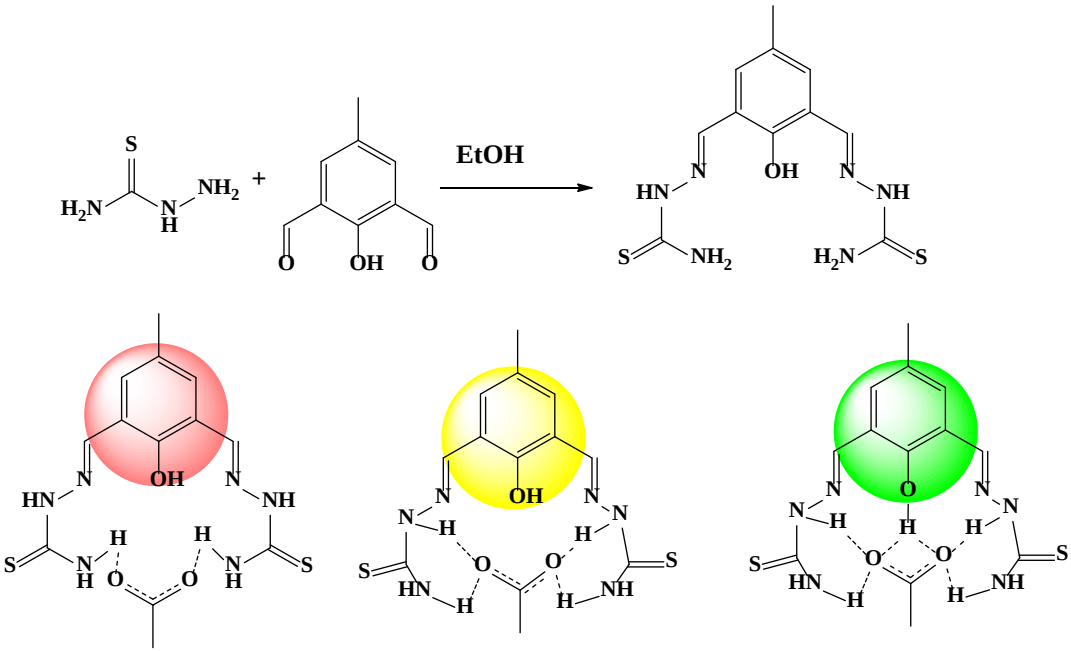

Figure 8: Synthesis of Probe and Schematic Representation of Sensing of AcO- by Probe

Tang *et al.* (2017a) reported the same fluorescence probe selectively identifies Zn^{2+} and Hg^{2+} in the aqueous HEPES buffer through turn-on fluorescence pathway. On excitation at 390 nm wavelength the probe shows Strong fluorescent emission was observed at 478 nm and 580 nm in the presence of Zn^{2+} and Hg^{2+}, respectively. The limit of detection (LOD) was determined to be 1.46×10^{-7} M for Zn^{2+} and 2.50×10^{-7} M for Hg^{2+}. Furthermore, the probe was successfully employed for the fluorescence imaging and detection of Zn^{2+} and Hg^{2+} in living cells, demonstrating its potential for biological applications.

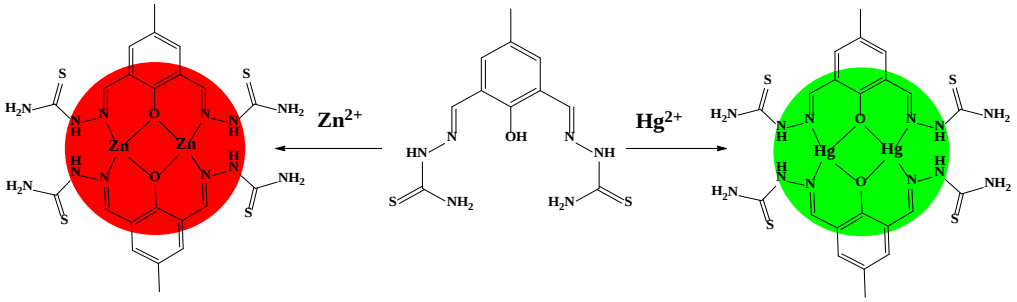

Figure 9: Schematic Representation of Sensing of Zn^{2+} and Hg^{2+} by Probe

(f) (E)-N'-(2-hydroxy-5-methyl-3-(4-oxo-3,4-dihydroquinazolin-2-yl)benzylidene)

picolinohydrazide

Picolinohydrazide was mixture with 2-Hydroxy-5-methyl-3-(4-oxo-3,4-dihydro-quinazolin-2-yl)-benzaldehyde in DMSO medium and refluxed for 3 hours at 70°C. The reaction mixture was slowly poured into ice-cold water under continuous stirring. The resulting precipitate was collected by filtration and thoroughly washed with distilled water. A orange yellow solid was obtained (Fig 10). In Tris- HCl buffer solution, probe selectively identify Al^{3+} ion over other metal ions, exhibiting a significant blue shift and

enhanced emission at 473 nm. The probe binds with Al^{3+} in a 1:2 stoichiometric ratio and exhibits a detection limit of 4.79×10^{-8} M. For real-world application, its performance was evaluated through proof-of-concept studies using tap water and lake water samples (Tang *et al.*, 2017b).

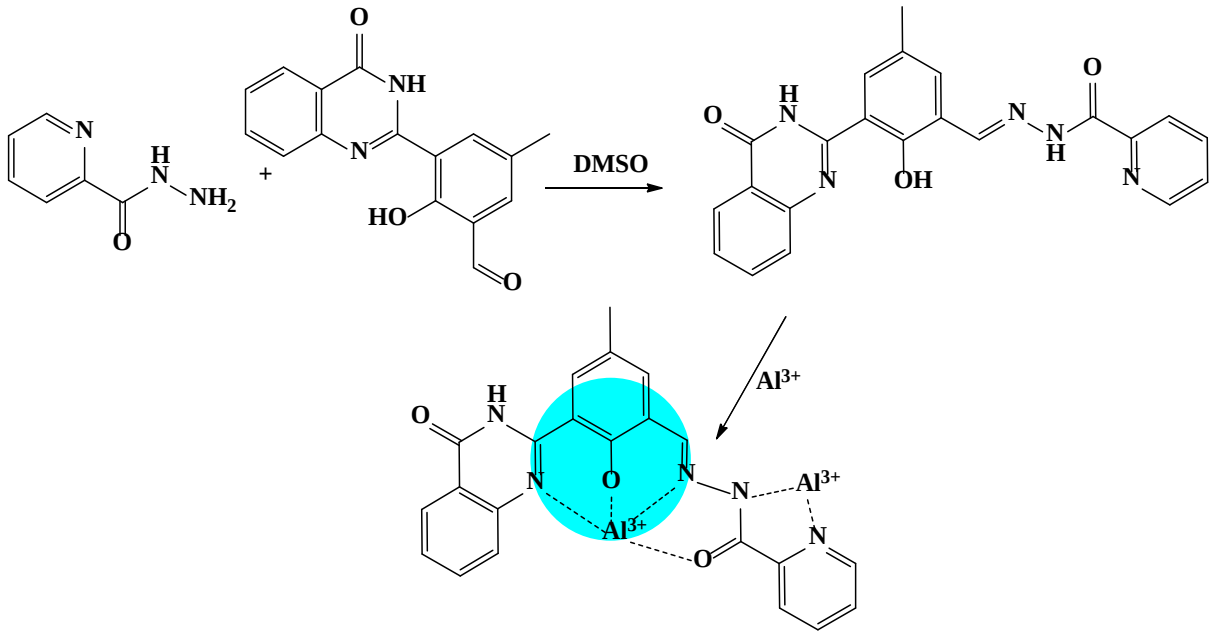

Figure 10: Synthesis of Probe and Schematic Representation of Sensing of Al^{3+} by Probe

(g) (E)-N'-((7-(diethylamino)-2-oxo-2H-chromen-3-yl)methylene)picolinohydrazide

2-picolinyl hydrazide and 7-diethylaminocoumarin-3-aldehyde was mixed in ethanolic solution and by condensation the peobe was synthesized. The Probe exhibits a strong green fluorescence at 509 nm. Fluorescence intensity of the probe was enhanced by adding 1.4 equiv. of Cu^{2+} (Fig 11). The probe acts as a “turn off” fluorescence chemosensors for Cu^{2+}. Intramolecular photoinduced electron transfer (PET) from the excited fluorophore to Cu^{2+} upon complex formation can lead to fluorescence quenching. Again, research indicates that copper-probe complexe is a “turn-on” Fluorescent chemosensors for cyanide ions (CN^{-}). The detection limits for CN^{-} is 0.019 µM in acetonitrile medium (Wang *et al.*, 2016).

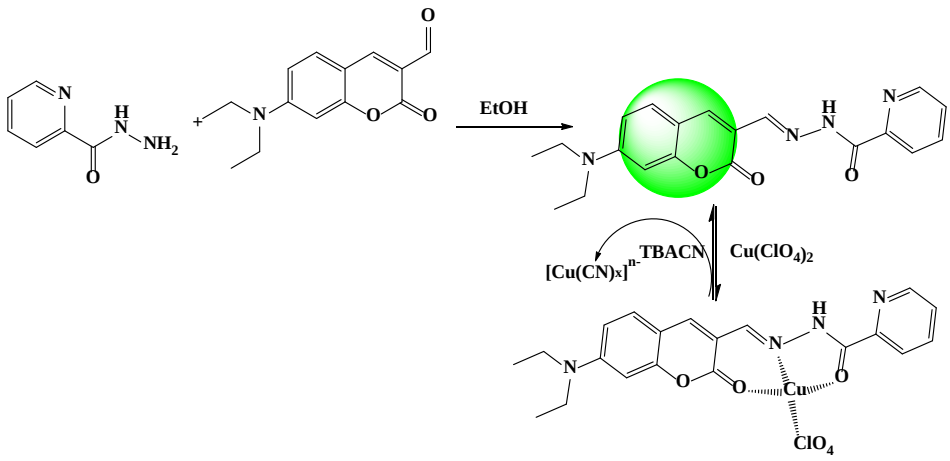

Figure 11: Synthesis of Probe and Schematic Representation of Sensing of Cu^{2+} by Probe

(h) (N',N'''E,N',N'''E)-N',N'''-((2-hydroxy-5-methyl-1,3-phenylene)bis (methanylylidene))di(picolinohydrazide)

Picolinic hydrazide (2 mmol) was added to an ethanolic solution of 2,6-diformyl-4-methylphenol (1 mmol), and the mixture was refluxed for 4 hours. A yellow crystalline crude product was obtained, which was used as the probe (Fig 12). The probe selectively identifies Zn^{2+} is preferentially utilized over other metal ions under physiological conditions. The fluorescence emission intensity was significantly enhanced upon addition of Zn^{2+}, accompanied by a red shift of approximately 25 nm. The experiment was performed under fully physiological conditions (99.7% HEPES buffer) and exhibited visible-light excitation capability. The association constant between probe and Zn^{2+} was found to be 5.58 × 105 M-1. The probe could detect as low as (LOD) 69 ppb Zn^{2+}. The sensing mechanism was explained by chelation enhanced fluorescence (CHEF) processes and intramolecular charge transfer (ICT). The probe was completely non-toxic and enabled intracellular Zn^{2+} detection in HeLa cells, as demonstrated by fluorescence imaging studies (Datta *et al.*, 2014).

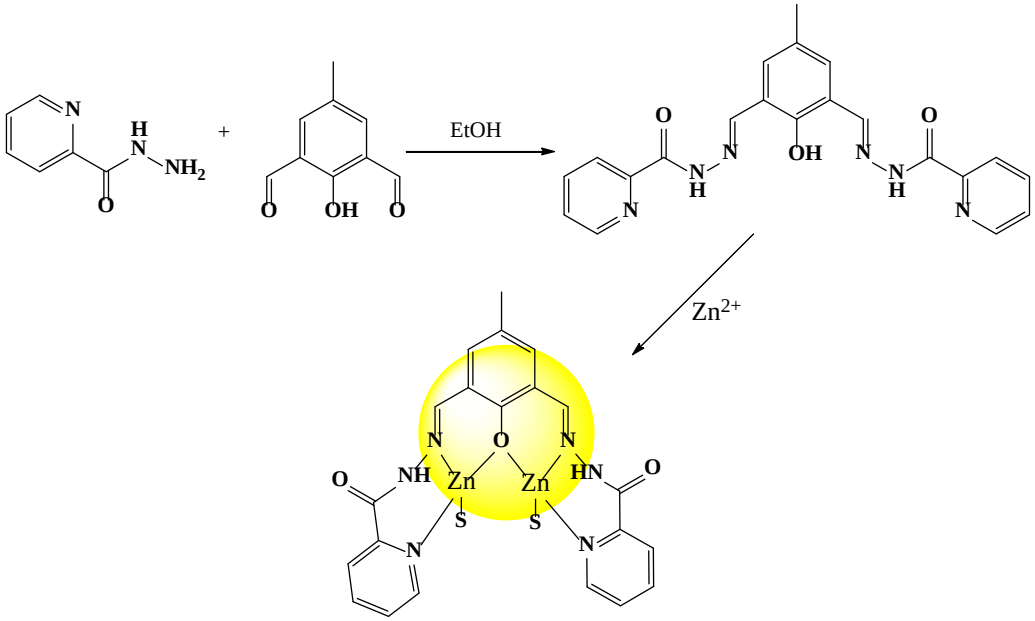

Figure 12: Synthesis of Probe and Schematic Representation of Sensing of Zn^{2+} by Probe

Conclusion

The multitude references reported in the articles emphasize the synthesis of different hydrazide appended fluorometric chemosensors which are able to detect different metal ions in solution phase and in physiological conditions. This research field is prosperous and still flourishing with great dedication.

Acknowledgement

The author gratefully acknowledges Dr. Rakesh Purkait, Jadavpur University, India, for his valuable support, guidance, and insightful contributions throughout the course of this work.

References

Ananthanarayanan, A., Wang, X., Routh, P., Sana, B., Lim, S., Kim, D. H., & Chen, P. (2014). Facile synthesis of graphene quantum dots from 3D graphene and their application for Fe3+ sensing. *Advanced Functional Materials, 24*(20), 3021-3026. https://doi.org/10.1002/adfm.201303441

Arakawa, H., Ahmad, R., Naoui, M., & Tajmir-Riahi, H. A. (2000). A Comparative Study of Calf Thymus DNA Binding to Cr (III) and Cr (VI) Ions: evidence for the guanine N-7-chromium-phosphate chelate formation. *Journal of Biological Chemistry, 275*(14), 10150-10153. https://doi.org/10.1074/jbc.275.14.10150

Ayoob, S., & Gupta, A. K. (2006). Fluoride in drinking water: a review on the status and stress effects. *Critical Reviews in Environmental Science and Technology, 36*(6), 433-487. https://doi.org/10.1080/10643380600678112

Becaria, A., Campbell, A., & Bondy, S. C. (2002). Aluminum as a toxicant. *Toxicology and Industrial Health, 18*(7), 309-320. https://doi.org/10.1191/0748233702th157oa

Bell, T. W., & Hext, N. M. (2004). Supramolecular optical chemosensors for organic analytes. *Chemical Society Reviews, 33*(9), 589-598. https://doi.org/10.1039/B207182G

Berezin, M. Y., & Achilefu, S. (2010). Fluorescence lifetime measurements and biological imaging. *Chemical Reviews, 110*(5), 2641-2684. https://doi.org/10.1021/cr900343z

Carlson, H. J., & Campbell, R. E. (2009). Genetically encoded FRET-based biosensors for multiparameter fluorescence imaging. *Current Opinion in Biotechnology, 20*(1), 19-27. https://doi.org/10.1016/j.copbio.2009.01.003

Cerchiaro, G., Manieri, T. M., & Bertuchi, F. R. (2013). Analytical methods for copper, zinc and iron quantification in mammalian cells. *Metallomics, 5*(10), 1336-1345. https://doi.org/10.1039/c3mt00136a

Chudyk, W., Sotolongo, C., & Mueller, E. (2014). A fiber-optic redox sensor for the iron (III)–iron (II) transition. *Environmental Monitoring and Assessment, 186*(1), 415-420. https://doi.org/10.1007/s10661-013-3386-x

Dale, T. J., & Rebek, J. (2006). Fluorescent sensors for organophosphorus nerve agent mimics. *Journal of the American Chemical Society, 128*(14), 4500-4501. https://doi.org/10.1021/ja057449i

Das, K., Panda, U., Datta, A., Roy, S., Mondal, S., Massera, C., ... & Kobayashi, K. (2015). An enolato-bridged dinuclear Cu (II) complex with a coumarin-assisted precursor: a spectral, magnetic and biological study. *New Journal of Chemistry, 39*(9), 7309-7321. https://doi.org/10.1039/c5nj00789e

Datta, B. K., Thiyagarajan, D., Ramesh, A., & Das, G. (2015). A sole multi-analyte receptor responds with three distinct fluorescence signals: traffic signal like sensing of Al3+, Zn2+ and F−. *Dalton Transactions, 44*(29), 13093-13099. https://doi.org/10.1039/C5DT01468A.

Datta, B. K., Thiyagarajan, D., Samanta, S., Ramesh, A., & Das, G. (2014). A novel chemosensor with visible light excitability for sensing Zn2+ in physiological medium and in HeLa cells. *Organic & Biomolecular Chemistry, 12*(27), 4975-4982. https://doi.org/10.1039/C4OB00653D

De Silva, A. P., Gunaratne, H. N., Gunnlaugsson, T., Huxley, A. J., McCoy, C. P., Rademacher, J. T., & Rice, T. E. (1997). Signaling recognition events with fluorescent sensors and switches. *Chemical reviews, 97*(5), 1515-1566. https://doi.org/10.1021/cr960386p

Dhillon, A., Nair, M., & Kumar, D. (2015). Analytical methods for sensing of health-hazardous arsenic from biotic and abiotic natural resources. *Analytical Methods, 7*(24), 10088-10108. https://doi.org/10.1039/C5AY02430G

Fan, H. T., Fan, X., Li, J., Guo, M., Zhang, D., Yan, F., & Sun, T. (2012). Selective removal of arsenic (V) from aqueous solution using a surface-ion-imprinted amine-functionalized silica gel sorbent. *Industrial & Engineering Chemistry Research, 51*(14), 5216-5223. https://doi.org/10.1021/ie202655x

Govindhan, M., Adhikari, B. R., & Chen, A. (2014). Nanomaterials-based electrochemical detection of chemical contaminants. *RSC Advances, 4*(109), 63741-63760. https://doi.org/10.1039/C4RA10399H

Hessels, A. M., & Merkx, M. (2015). Genetically-encoded FRET-based sensors for monitoring Zn2+ in living cells. *Metallomics, 7*(2), 258-266. https://doi.org/10.1039/c4mt00179f

Hong, Y., Lam, J. W., & Tang, B. Z. (2009). Aggregation-induced emission: phenomenon, mechanism and applications. *Chemical Communications, 45*(29), 4332-4353. https://doi.org/10.1039/b904665h

Hsieh, C. C., Cheng, Y. M., Hsu, C. J., Chen, K. Y., & Chou, P. T. (2008). Spectroscopy and femtosecond dynamics of excited-state proton transfer induced charge transfer reaction. *The Journal of Physical Chemistry A, 112*(36), 8323-8332. https://doi.org/10.1021/jp804216u

Kansal, S. K., & Kumari, A. (2014). Potential of M. oleifera for the treatment of water and wastewater. *Chemical Reviews, 114*(9), 4993-5010. https://doi.org/10.1021/cr400093w

Kantiani, L., Llorca, M., Sanchís, J., Farré, M., & Barceló, D. (2010). Emerging food contaminants: a review. *Analytical and Bioanalytical Chemistry, 398*(6), 2413-2427. https://doi.org/10.1007/s00216-010-3944-9

Kim, J. S., & Quang, D. T. (2007). Calixarene-derived fluorescent probes. *Chemical Reviews, 107*(9), 3780-3799. https://doi.org/10.1021/cr068046j

Kleerekoper, M. (1998). The role of fluoride in the prevention of osteoporosis. *Endocrinology and Metabolism Clinics, 27*(2), 441-452. https://doi.org/10.1016/S0889-8529(05)70015-3

Kumar, M., & Puri, A. (2012). A review of permissible limits of drinking water. *Indian Journal of Occupational and Environmental Medicine, 16*(1), 40-44. https://doi.org/10.4103/0019-5278.99696

Li, C., Xu, W., Jia, D., & Liu, X. (2013). Removal of arsenic from drinking water by using the Zr-loaded resin. *Journal of Chemical & Engineering Data, 58*(2), 427-435. https://doi.org/10.1021/je301148t

Lodeiro, C., Capelo, J. L., Mejuto, J. C., Oliveira, E., Santos, H. M., Pedras, B., & Nunez, C. (2010). Light and colour as analytical detection tools: a journey into the periodic table using polyamines to bio-inspired systems as chemosensors. *Chemical Society Reviews, 39*(8), 2948-2976. https://doi.org/10.1039/b819787n

Lohar, S., Sinha, S., Ghosh, S., & Das, D. (2016). Tri-color emission and colorimetric recognition of acetate using semicarbazide and thio-semicarbazide derivatives: Experimental and computational studies. *Spectrochimica Acta Part A: Molecular and Biomolecular Spectroscopy, 155*, 75-80. https://doi.org/10.1016/j.saa.2015.10.018

Mak, W. C., Chan, C., Barford, J., & Renneberg, R. (2003). Biosensor for rapid phosphate monitoring in a sequencing batch reactor (SBR) system. *Biosensors and bioelectronics, 19*(3), 233-237. https://doi.org/10.1016/S0956-5663(03)00209-4

Martinez-Manez, R., & Sancenón, F. (2003). Fluorogenic and chromogenic chemosensors and reagents for anions. *Chemical Reviews, 103*(11), 4419-4476. https://doi.org/10.1021/cr010421e

McDonagh, C., Burke, C. S., & MacCraith, B. D. (2008). Optical chemical sensors. *Chemical Reviews, 108*(2), 400-422. https://doi.org/10.1021/cr068102g

McIlwee, H. A., Schauer, C. L., Praig, V. G., Boukherroub, R., & Szunerits, S. (2008). Thin chitosan films as a platform for SPR sensing of ferric ions. *Analyst, 133*(5), 673-677. https://doi.org/10.1039/b717736d

McNaught, A. D., Wilkinson, A., & Jenkins, A. D. (1997). International union of pure and applied chemistry. Compendium of chemical terminology: IUPAC recommendations, 2.

Mehta, V. N., Kailasa, S. K., & Wu, H. F. (2014). Sensitive and selective colorimetric sensing of Fe3+ ion by using p-amino salicylic acid dithiocarbamate functionalized gold nanoparticles. *New Journal of Chemistry, 38*(4), 1503-1511. https://doi.org/10.1039/c3nj01468a

Moriarty, M. M., Koch, I., & Reimer, K. J. (2013). Arsenic species and uptake in amphibians (Rana clamitans and Bufo americanus). *Environmental Science: Processes & Impacts, 15*(8), 1520-1528. https://doi.org/10.1039/c3em00223c

Narang, R., Narasimhan, B., & Sharma, S. (2012). A review on biological activities and chemical synthesis of hydrazide derivatives. *Current Medicinal Chemistry, 19*(4), 569-612.

Parker, D. (2000). Luminescent lanthanide sensors for pH, pO2 and selected anions. *Coordination Chemistry Reviews, 205*(1), 109-130. https://doi.org/10.1016/S0010-8545(00)00241-1

Pomazal, K., Prohaska, C., Steffan, I., Reich, G., & FK Huber, J. (1999). Determination of Cu, Fe, Mn, and Zn in blood fractions by SEC-HPLC-ICP-AES coupling. *Analyst, 124*(5), 657-663. https://doi.org/10.1039/a809688k

Pröfrock, D., & Prange, A. (2012). Inductively coupled plasma-mass spectrometry (ICP-MS) for quantitative analysis in environmental and life sciences: a review of challenges, solutions, and trends. *Applied spectroscopy, 66*(8), 843-868. https://doi.org/10.1366/12-06681

Pye, V. I., & Patrick, R. (1983). Ground water contamination in the United States. *Science, 221*(4612), 713-718. https://doi.org/10.1126/science.6879171

Razzaque, M. S. (2011). Phosphate toxicity: new insights into an old problem. *Clinical science, 120*(3), 91-97. https://doi.org/10.1042/CS20100377

Rijith, S., Anirudhan, T. S., & Shripathi, T. (2012). Evaluation of iron (III) chelated polymer grafted lignocellulosics for arsenic (V) adsorption in a batch reactor system. *Industrial & Engineering Chemistry Research, 51*(32), 10682-10694. https://doi.org/10.1021/ie300732t

Samanta, S., Datta, B. K., Boral, M., Nandan, A., & Das, G. (2016). A multi-responsive turn-on flurogenic probe to sense Zn2+, Cd2+ and Pb2+: left-right-center emission signal swing. *Analyst, 141*(14), 4388-4393. https://doi.org/10.1039/C6AN00657D

Samanta, S., Manna, U., Ray, T., & Das, G. (2015). Aggregation-induced emission (AIE) active probe for multiple targets: Fluorescent sensor for Zn^{2+} and Al^{3+} and colorimetric sensor for Cu^{2+} and F^{-}. *Dalton Transactions, 44*, 18902–18910. https://doi.org/10.1039/c5dt03186a

Shafiquzzaman, M., Azam, M. S., Mishima, I., & Nakajima, J. (2009). Technical and social evaluation of arsenic mitigation in rural Bangladesh. *Journal of Health, Population, and Nutrition, 27*(5), 674–683. https://doi.org/10.3329/jhpn.v27i5.3779

Shamspur, T., Sheikhshoaie, I., & Mashhadizadeh, M. H. (2005). Flame atomic absorption spectroscopy (FAAS) determination of iron (III) after preconcentration on to modified analcime zeolite with 5-((4-nitrophenylazo)-N-(2′, 4′-dimethoxyphenyl)) salicylaldimine by column method. *Journal of Analytical Atomic Spectrometry, 20*(5), 476-478. https://doi.org/10.1039/b416097e

Shen, S., Li, X. F., Cullen, W. R., Weinfeld, M., & Le, X. C. (2013). Arsenic binding to proteins. *Chemical Reviews, 113*(10), 7769-7792. https://doi.org/10.1021/cr300015c

Sullivan, C., Tyrer, M., Cheeseman, C. R., & Graham, N. J. (2010). Disposal of water treatment wastes containing arsenic—a review. *Science of the Total Environment, 408*(8), 1770-1778. https://doi.org/10.1016/j.scitotenv.2010.01.010

Tang, X., Han, J., Wang, Y., Bao, X., Ni, L., Wang, L., & Li, L. (2017a). A highly sensitive turn-on fluorescent chemosensor for recognition of Zn^{2+} and Hg^{2+} and applications. *Spectrochimica Acta Part A: Molecular and Biomolecular Spectroscopy, 184,* 177–183. https://doi.org/10.1016/j.saa.2017.05.011

Tang, L., Ding, S., Zhong, K., Hou, S., Bian, Y., & Yan, X. (2017b). A new 2-(2′-hydroxyphenyl) quinazolin-4 (3H)-one derived acylhydrazone for fluorescence recognition of Al3+. *Spectrochimica Acta Part A: Molecular and Biomolecular Spectroscopy, 174*, 70-74. https://doi.org/10.1016/j.saa.2016.11.026

Timerbaev, A. R., Dabek-Zlotorzynska, E., & Hoop, M. A. V. D. (1999). Inorganic environmental analysis by capillary electrophoresis. *The Analyst, 124*(6), 811-826. http://lib3.dss.go.th/fulltext/Journal/analyst/Analyst1999/no.6/1999v124n6p811-826.pdf

Toyota, S. (2010). Rotational isomerism involving acetylene carbon. *Chemical Reviews, 110*(9), 5398-5424. https://doi.org/10.1021/cr1000628

U.S. Environmental Protection Agency. (2014). TSCA Chemical Substance Inventory. https://www.epa.gov/tsca-inventory

Upadhyay, K. K., Mishra, R. K., Kumar, V., & Chowdhury, P. R. (2010). A coumarin based ICT probe for fluoride in aqueous medium with its real application. *Talanta, 82*(1), 312-318. https://doi.org/10.1016/j.talanta.2010.04.041

Ussher, S. J., Milne, A., Landing, W. M., Attiq-ur-Rehman, K., Séguret, M. J., Holland, T., ... & Worsfold, P. J. (2009). Investigation of iron (III) reduction and trace metal interferences in the determination of dissolved iron in seawater using flow injection with luminol chemiluminescence detection. *Analytica Chimica Acta, 652*(1-2), 259-265. https://doi.org/10.1016/j.aca.2009.06.011

Valeur, B. (2002). Molecular fluorescence: Principles and applications. Wiley-VCH Verlag GmbH.

van den Berg, C. M. (2006). Chemical speciation of iron in seawater by cathodic stripping voltammetry with dihydroxynaphthalene. *Analytical Chemistry, 78*(1), 156-163. https://doi.org/10.1021/ac051441+

Vincent, J. B. (2000). Quest for the molecular mechanism of chromium action and its relationship to diabetes. *Nutrition Reviews, 58*(3), 67-72. https://doi.org/10.1111/j.1753-4887.2000.tb01841.x

Wang, K., Ma, L., Liu, G., Cao, D., Guan, R., & Liu, Z. (2016). Two fluorescence turn-on coumarin Schiff's base chemosensors for cyanide anions. *Dyes and Pigments, 126*, 104-109. https://doi.org/10.1016/j.dyepig.2015.11.019

Warwick, C., Guerreiro, A., & Soares, A. (2013). Sensing and analysis of soluble phosphates in environmental samples: a review. *Biosensors and Bioelectronics, 41*, 1-11. https://doi.org/10.1016/j.bios.2012.07.012

Westley, J., Vannesland, B., Conn, E. E., Knowles, C. J., & Wissing, F. (1981). Cyanide in biology. Academic Press, New York, 61.

Xu, M., Wu, S., Zeng, F., & Yu, C. (2010). Cyclodextrin supramolecular complex as a water-soluble ratiometric sensor for ferric ion sensing. *Langmuir, 26*(6), 4529-4534. https://doi.org/10.1021/la9033244

Yadav, N., & Singh, A. K. (2016). Dual anion colorimetric and fluorometric sensing of arsenite and cyanide ions. *RSC Advances, 6*(102), 100136-100144. https://doi.org/10.1039/c6ra19781g

Zhao, A., Zhao, C., Li, M., Ren, J., & Qu, X. (2014). Ionic liquids as precursors for highly luminescent, surface-different nitrogen-doped carbon dots used for label-free detection of Cu2+/Fe3+ and cell imaging. *Analytica Chimica Acta, 809,* 128-133. https://doi.org/10.1016/j.aca.2013.10.046

Zhao, Q., Li, F., & Huang, C. (2010). Phosphorescent chemosensors based on heavy-metal complexes. *Chemical Society Reviews, 39*(8), 3007-3030. https://doi.org/10.1039/b915340c

Zhou, F., Wang, H., Liu, P., Hu, Q., Wang, Y., Liu, C., & Hu, J. (2018). A highly selective and sensitive turn-on probe for aluminum (III) based on quinoline Schiff's base and its cell imaging. *Spectrochimica Acta Part A: Molecular and Biomolecular Spectroscopy, 190*, 104-110. https://doi.org/10.1016/j.saa.2017.09.007

doi: 10.31674/book.2026cdcbs.003

Physiologically Based Pharmacokinetic Modelling and Simulation Study to Predict the Plasma *Concentration Profile* of Chrysin Obtained from the Extract of Mangifera Indica

Abhradeep Basu[1], Anamika Basu[2]*

[1]Department of Software Systems, School of Computer Science and Engineering, Vellore Institute of Technology, Vellore, Tamilnadu- 632014, India

[2]Department of Biochemistry, Gurudas College, Kolkata 700054, India

**Corresponding Author's Email: anamika.biochem@gurudas.education*

Abstract

Chrysin is the identified flavonoid compound present in the mango pulp extract, having antioxidant properties. The aim of this study is to develop a physiologically based pharmacokinetic (PBPK) model of chrysin to simulate its plasma concentration profile in rats and humans after oral administration of the extract of Mangifera indica. The physiologically based pharmacokinetic model of chrysin is developed and verified by the pharmacokinetic data in rats. Then the PBPK model has been extrapolated to humans with PK-Sim® software. In order to assess the accuracy of the extrapolation, the extrapolated model is compared with the multiple-dose clinical study of chrysin. The predictive performance of the PBPK model is mainly evaluated by visual predictive checks and fold error of Cmax and AUC0-t of chrysin (the ratio of predicted to observed). Finally, the adult PBPK model is extended to several subpopulations, including liver disease patients. Chrysin undergoes rapid metabolism in rat and human liver microsomes by phase II metabolic enzymes like UGT and SULT. By utilizing literature data, the PBPK model of chrysin is well established in rats and humans. The predicted plasma concentration profiles of chrysin are consistent with the corresponding observed data from previous studies, and the fold error values are within the 2-fold acceptance criterion. No significant pharmacokinetic differences are observed after extrapolation for liver disease patients in PK-Sim software. The established PBPK model of chrysin gives valuable insight into the use of the flavonoid extract of Mangifera indica in liver disease patients, in spite of its poor bioavailability.

Keywords*: Chrysin; Physiologically Based Pharmacokinetic (PBPK) Model; PK-Sim® Software*

Introduction

Chrysin is a key flavonoid compound identified in Mangifera indica (mango) pulp extract, known for its significant antioxidant properties. This study utilizes Physiologically Based Pharmacokinetic (PBPK) modeling to predict its plasma concentration profile in both rats and humans (Boonpawa, 2017). In the human body system, the flavonoid chrysin undergoes extensive phase II metabolism in the liver, catalyzed by UGT and SULT enzymes to form chrysin-7-O-sulfate and chrysin 7-O-glucuronide conjugates (Panchal *et al.*, 2026). The pharmacokinetic model of chrysin incorporates enterohepatic recycling (Tu *et al.,* 2021; Chou *et al*., 2025), where conjugates are transported into the intestine, hydrolyzed by microbial β-glucuronidases in the colon, and reabsorbed as free chrysin. This chrysin, when circulated through blood plasma, plasma protein albumin, can act as a carrier molecule. These adsorption, digestion, metabolism, and excretion (ADME) kinetics result in high accumulation of chrysin in the liver periportal tissue, which indicates the important role of chrysin for treating liver disease. The pharmacokinetics of chrysin in the gastrointestinal system is schematically represented in Figure 1.

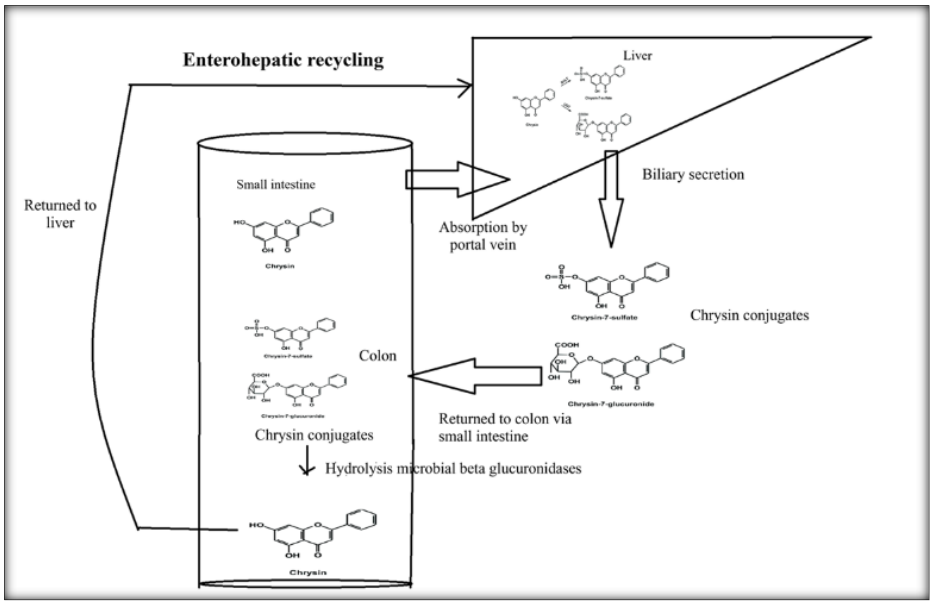

Figure 1: Schematic Representation for Pharmacokinetics of Chrysin

Methodology

Pharmacokinetic parameters of chrysin are calculated by PK-Sim v9.0, which is part of the Open Systems Pharmacology suite (www.open-systems-pharmacology.org) (Lippert *et al.*, 2019; Bharadwaj, 2024). The optimization and sensitivity analysis of model input parameters are carried out by PK-Sim. The steps for a physiologically based pharmacokinetic modeling and simulation study for the nutraceutical chrysin have been depicted in figure 2.

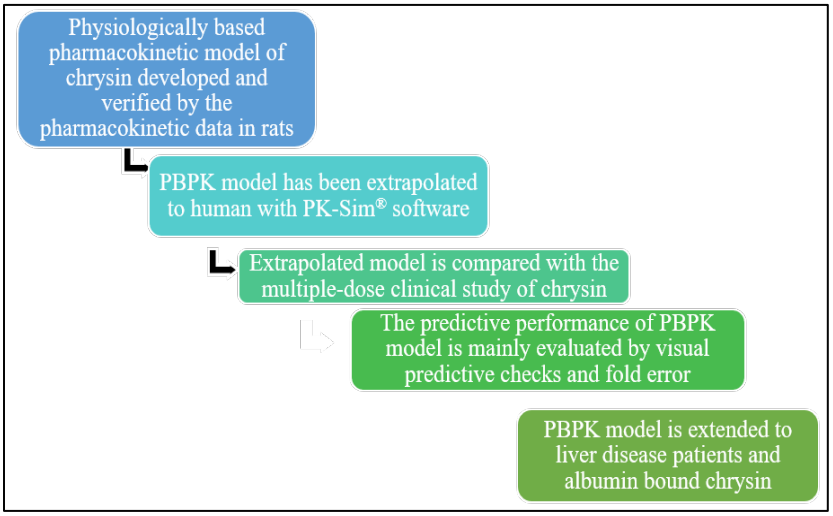

Figure 2: Flowchart for Physiologically Based Pharmacokinetic Modelling and Simulation Study

The most common tool in the area, the Open Systems Pharmacology (OSP) Suite, is an open-source platform for PBPK modeling. PK-Sim (Willmann *et al*., 2003) functions as a whole-body modeling program within this package, enabling the development, optimization, and simulation of PBPK models. MoBi (Hack *et al.*, 2020; Balhara *et al.,* 2022) serves as a Quantitative Systems Pharmacology (QSP) modeling platform in the OSP Suite when used with PK-Sim. By enabling the use of bespoke models for organs, MoBi expands the suite's PBPK modeling capabilities. A thorough investigation of chrysin molecular behavior at both the

systemic and organ-specific levels is made possible by the ability to simulate these organ-specific models separately or incorporate them into whole-body PBPK models created using PK-Sim.

Results

PKML models encompass chemical species, reactions, and transport processes, which exist in various compartments of the body and serve as containers. Model parameters are depicted with descriptors considering compartments, chemicals, reactions, transports, etc. Every parameter in the model has a value, a dimension, and a distinct route. This route typically connects physical and chemical descriptors to chemicals, reaction rates to specific reactions, transport rates to mechanisms, and dosages to events; it may also link anatomical or physiological data to model compartments. The chrysin molecule in its free form and bound form with serum albumin protein is pharmacokinetically modelled in the gastrointestinal system in Figure 3.

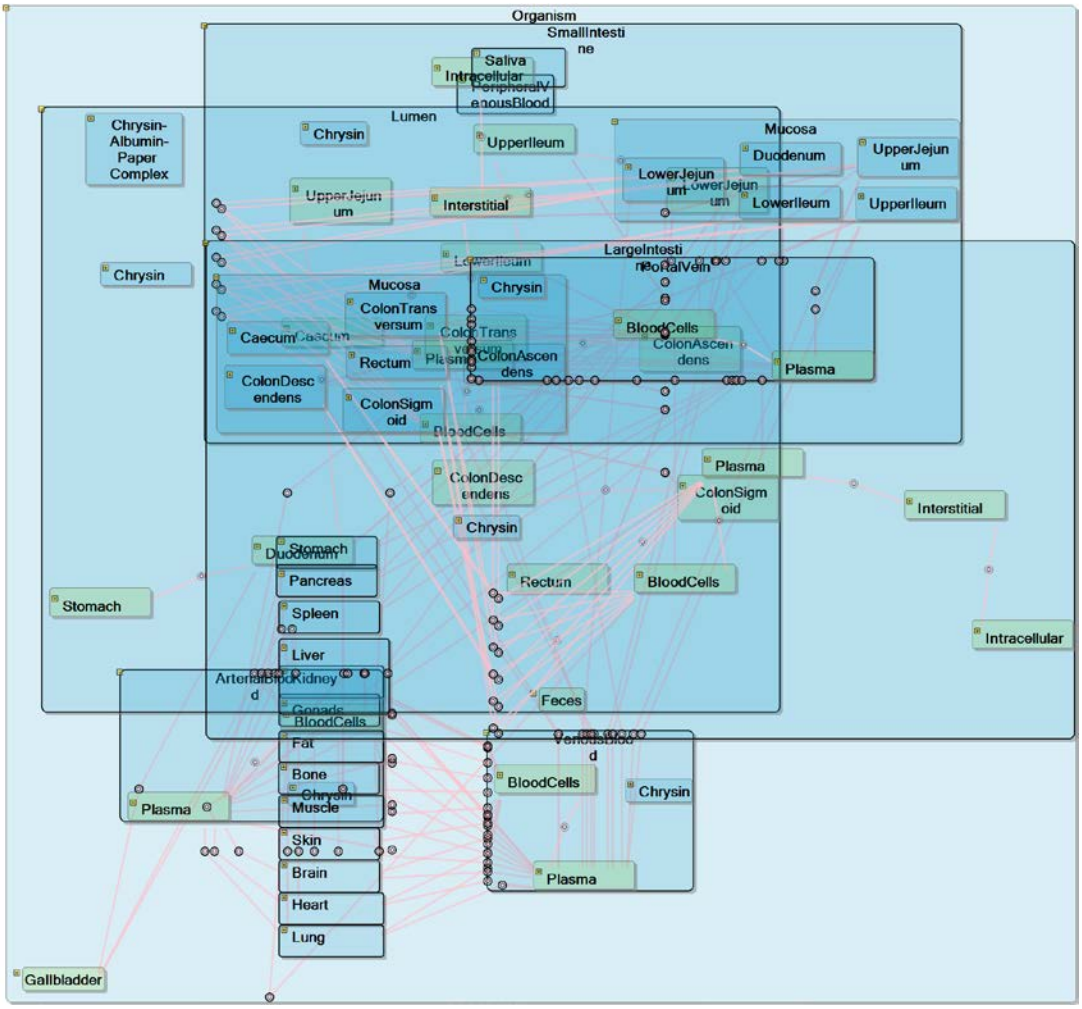

Figure 3: Diagram for Chrysin and Chrysin Bound Albumin in Different Compartments

A PBPK model has been developed in rats, and the plasma concentration profile of chrysin over time in different organs or compartments, such as the liver, kidney, duodenum, ileum, jejunum, large intestine, and arterial and venous blood, is shown in Figure 4a. The similar plasma concentration profile curve for the human body system is also exhibited in Figure 4b.

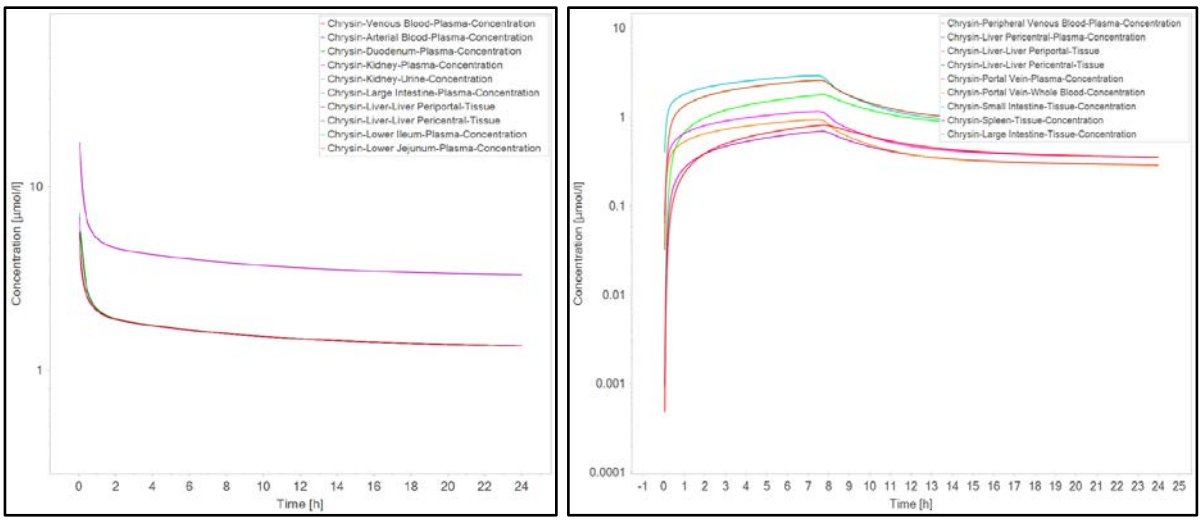

Figure 4: a) Plasma Concentration Profile of Chrysin with Time in Rat, b) Plasma Concentration Profile of Chrysin with Time in Human

A pharmacokinetic sensitivity analysis plot for the rat model is created using a tornado plot and shown in Figure 5.

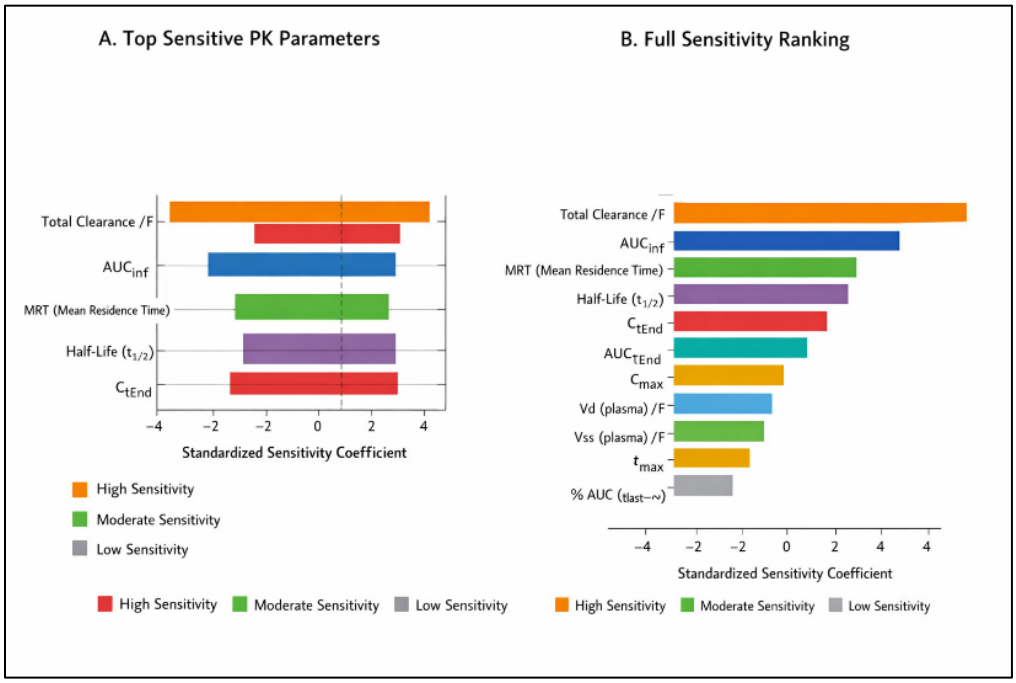

Figure 5: Pharmacokinetic Sensitivity Analysis Using Tornado Plot for Rat Model

The sensitivity analysis shows that the pharmacokinetic variability of chrysin in the rat model is mostly controlled by processes related to clearance. Metrics such as AUC_inf are highly sensitive to the elimination kinetics, whereas the distribution parameters have a secondary effect on this metric. The parameters associated with terminal phase extrapolation have virtually no effect on the total uncertainty of the exposure metric, indicating adequate representation of the elimination phase through modeling.

All of the above demonstrate how critical the role of elimination and clearance processes are in modulating the pharmacokinetics of chrysin, as visualized in Figure 6.

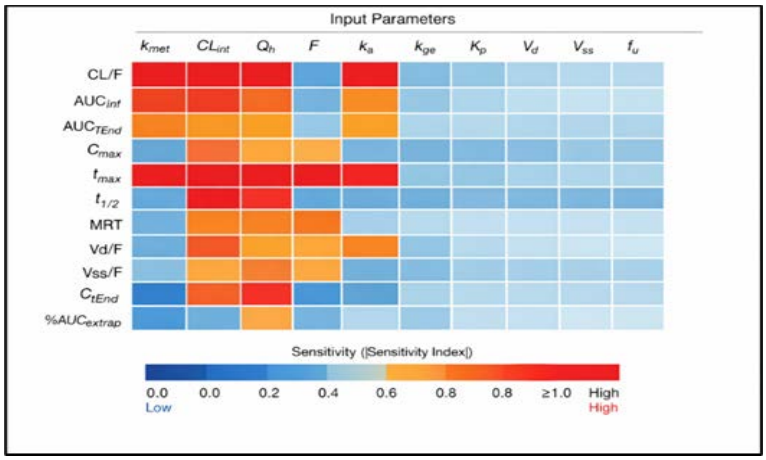

Figure 6: Visualization of Pharmacokinetics Sensitivity Analysis by Heat Map method

The visualization of the parameter-output relationship demonstrates that metabolic clearance is the most important process impacting the overall pharmacokinetics. Additionally, drug absorption influences both peak exposure and the timing of peak levels, whereas distribution parameters only modulate pharmacokinetics without controlling them. All of the above results provide a mechanistic basis for optimization of chrysin pharmacokinetic experiments, based on metabolism.

The chrysin PBPK model is verified by comparison with the available human pharmacokinetic data of chrysin after both intravenous and oral dosing methods (Gao *et al*., 2021). The simulated profiles of pharmacokinetics are highly comparable with those described in scientific literature, showing fold errors within an acceptable 2-fold error range. The simulations revealed the presence of a large amount of chrysin molecules in the liver periportal tissue.

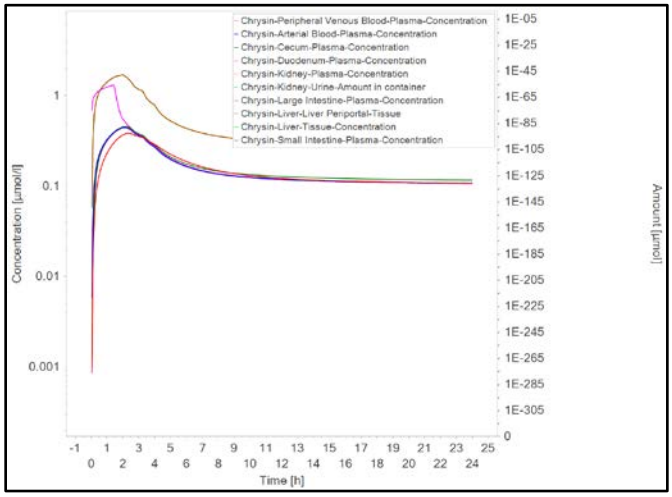

Figure 7: Chrysin Concentration in Blood Plasma with Liver Diseased Condition in Different Organs in Human

Utilizing PK-Sim® software, the PBPK model is used for extrapolation of the distribution of chrysin into humans having liver disease. The time-concentration curve indicates the maximal concentration of chrysin in the periportal tissue of the liver relative to plasma and other organs. These results show that despite physiological changes associated with the development of liver disease, the pharmacokinetic parameters do not change significantly, supporting the potential therapeutic use of *Mangifera indica* extract for the treatment of diseases of the liver.

Both Table 1 and Figure 8 show a global pharmacokinetic analysis for all rats, healthy humans, and humans with liver disease.

Table 1: The Comparison of Global Pharmacokinetic Parameters for Rats, Healthy Humans, And Humans with Liver Disease

Parameter	Rat	Healthy Human	Diseased Human
Vss (plasma) (mg/kg)	2604.37	3966.43	9141.99
Vd (plasma) (mg/kg)	2628.14	4106.73	9446.55
Total plasma clearance (mg/min/kg)	0.15288	0.51224	0.57291
Bioavailability		0.13504	0.08472
Fraction absorbed		0.17131	0.05497

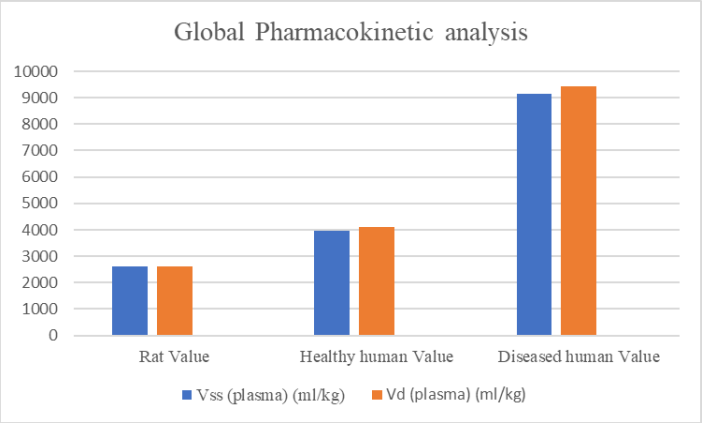

Figure 8: Two Types of Volume of Distributions of Chrysin in Rat and Human Models

The comparative data clearly indicate the presence of distinct pharmacokinetic differences caused by liver diseases. The first parameter, which should be emphasized, is the volume of distribution (Vss), being 9141.99 ml/kg in comparison with healthy individuals at 3966.43 ml/kg. Thus, the accumulation in the tissues takes place much more efficiently in diseased patients. It can also be seen from Figure 8 that both bioavailability and fraction absorbed decrease (0.085 and 0.135, respectively) with the presence of liver disease. This means that despite increased uptake, systemic exposure is affected negatively because of altered absorption.

Table 2: Pharmacokinetic Parameters for Different Tissues in Rat and Human Beings for Both Normal and Diseased Ones

Parameter	Rat Liver Periportal	Human Healthy Small Intestine	Diseased Human Liver
AUC_inf [µmol*min/l]	62251.47656	9217.473633	5811.99
AUC_inf_norm [µg*min/l]	1.58268E+13	6.84289E+11	4.3E+11
AUC_tEnd [µmol*min/l]	5634.948242	2142.894043	693.268
AUC_tEnd_norm [µg*min/l]	1.43263E+12	1.59085E+11	5.1E+10
C_max [µmol/l]	17.56756401	2.942610741	1.69445
C_max_norm [mg/l]	4466377.258	218454.3014	125793
C_tEnd [µmol/l]	3.32366538	0.800254107	0.27841
Total body clearance/F[ml/min/kg]	0.063183907	1.461370382	2.31765
% AUC (tlast-∞)	0.90948087	0.767518282	0.88072
MRT [h]	281.0208984	133.651766	291.995
t_max [h]	0.05	7.5	2
Half-Life [h]	196.7887044	102.1284912	212.395
Vd (plasma)/F [ml/kg]	1076.297641	12919.1227	42610.6
Vss (plasma)/F [ml/kg]	1065.359831	11718.88447	40604.4

Table 2 Illustrates the Pharmacokinetic Analysis of the Tissues with the Maximum Level of Chrysin in Rats, Healthy People, and Diseased People.

In this analysis, the primary concern will be the tissues that show maximum chrysin uptake by the subject groups, which include rats, healthy people, and humans with liver diseases. As indicated, the half-life of chrysin in diseased people is much higher than that of healthy individuals, that is, 212.4 hours vs. 102.1 hours. Furthermore, the volume of chrysin distribution (Vss/F) in diseased people is higher than in healthy subjects, implying that chrysin is mainly sequestered in liver tissues when the patient suffers from a hepatic disorder. This means that chrysin stays longer at the target site, despite low levels of it in the plasma.

The effect of albumin binding as a chrysin transporter in the pharmacokinetic modeling of chrysin: Albumin constitutes the main protein present in plasma. Numerous chemicals and drugs can interact with albumin and eventually become released into the plasma. Therefore, chrysin is dynamically equilibrated in between its unbound form (free chrysin) and its bound form (albumin-bound chrysin). Albumin-bound chrysin plays an important role as a chrysin reservoir, and once free chrysin gets depleted, the bound chrysin is released to maintain equilibrium. This interaction between chrysin and albumin produces various impacts on the pharmacodynamics of chrysin, including long circulation time, steady plasma concentration, and minimal toxicity. Figure 9 illustrates the dynamic behavior of both forms of chrysin in the human body system.

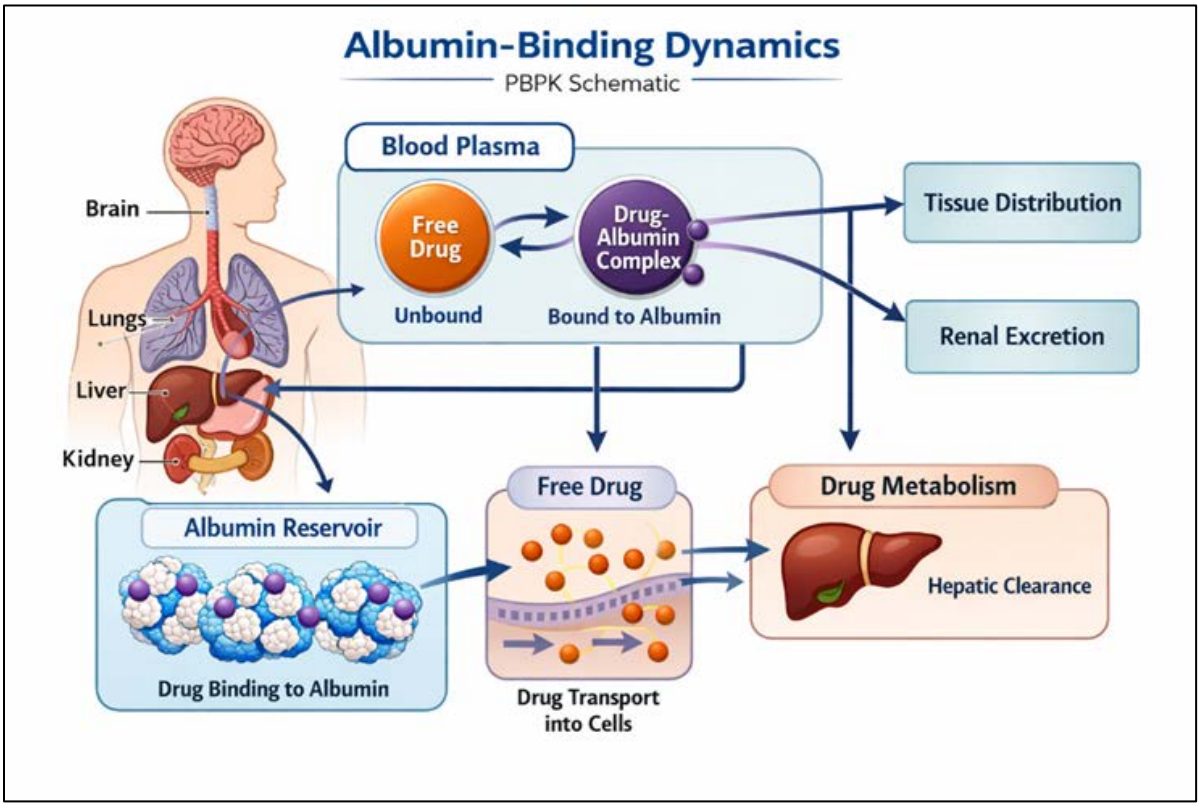

Figure 9: Schematic Diagram for Dynamic Behavior of Both Free form and Bound Form of Chrysin with Albumin

The plasma concentration graph against time for both the bound form with human serum albumin and the unbound form of chrysin is illustrated in Figure 10.

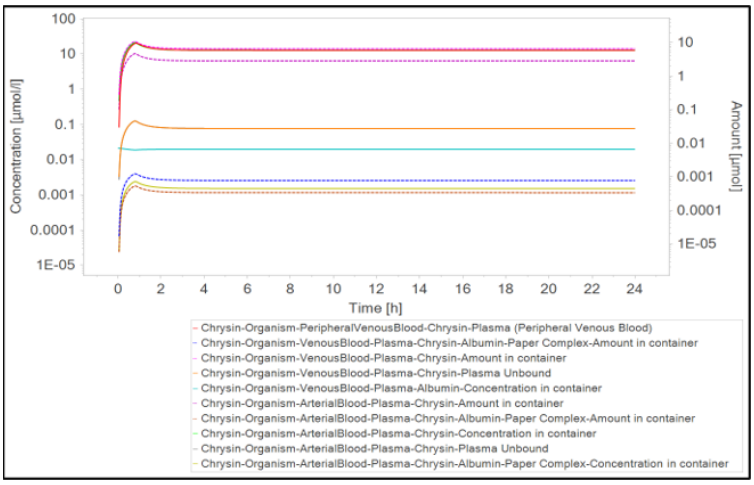

Figure 10: Plasma Concentration Profile of Bound and Unbound Chrysin

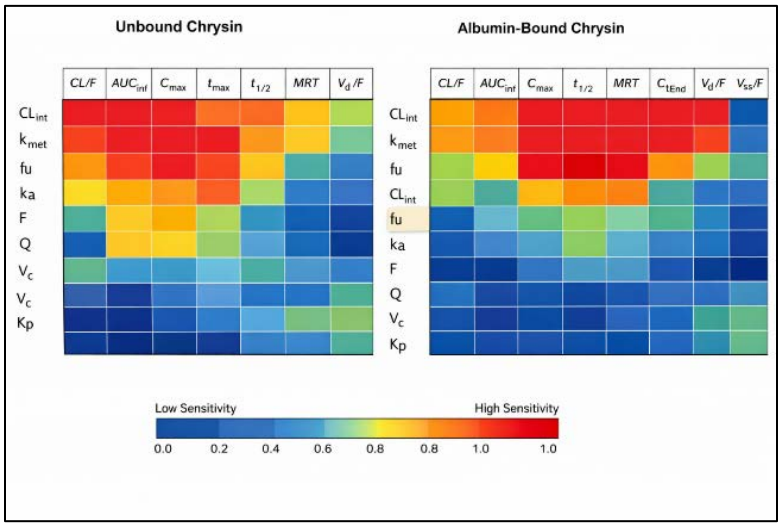

Figure 11: Comparison of Unbound Chrysin with Its Albumin Bound Form Considering Different Pharmacokinetic Parameters

Binding to albumin significantly modulated both the magnitude and variability of pharmacokinetic outputs of the chrysin molecule. Albumin binding with chrysin regulates chrysin clearance, reducing the fraction of chrysin available for hepatic metabolism. This results in lower apparent clearance variability as well as increased systemic stability of the chrysin molecule. Since only free chrysin is cleared from the system, albumin binding increases systemic exposure and ultimately stabilizes parameter AUC (area under plasma concentration time curve) by limiting rapid elimination. Plasma protein albumin binding reduces the free peak concentration of chrysin, which is acting as a reservoir that releases chrysin gradually in the human body system. Albumin-bound chrysin shows prolonged half-life and MRT (mean residence time) values and also shows reduced sensitivity to clearance fluctuations. Moreover, that albumin protein binding maintains prolonged terminal-phase concentrations, which is consistent with the depot-like behavior of the chrysin molecule.

Discussion

The development and validation of the physiologically based pharmacokinetic (PBPK) model according to the 2-fold criterion proves the accuracy of simulating the in vivo processes that reflect the highly complex

disposition pattern of chrysin in rats and humans (Yamazaki & Shimizu, 2025). The global sensitivity analysis reveals that the overall pharmacokinetics of chrysin depends on its metabolic clearance kinetics; it is consistent with conventional sensitivity analyses performed using the platform of the Open Systems Pharmacology Suite (Najjar *et al*., 2024). Nevertheless, the dynamic equilibrium provided by the binding of the compound to plasma serum albumins plays the role of an essential "distribution-buffering" effect. This process decreases the fraction of the compound available for fast phase II metabolism in the liver (Panchal *et al.,* 2026), and therefore it results in decreased clearance variance, decreased rate of compound elimination, and increased exposure, which is shown by a stable AUC profile along with increased half-life and MRT values. In addition, this continuous exposure is due to a specific recycling process of chrysin within the body, including its enteric recycling (Tu *et al.,* 2021). Notably, upon projection into a human population with a liver condition using PK-Sim® (Lippert *et al.,* 2019; Willmann *et al*., 2003; Niederalt *et al*., 2018), the significant physiological changes resulted in an increase in the volume of distribution (Vss/F) and the elimination half-life of chrysin within the liver and peripherally targeted tissue, despite relatively minimal drops in the overall systemic bioavailability and the absorption fraction. The pronounced accumulation of chrysin suggests that there is pooling of chrysin in the relevant target site. Overall, these results establish a sound and strong physiological basis for addressing bioavailability challenges in formulations and maximize its potential (Gao *et al.,* 2021; Kurkiewicz *et al.,* 2025; Stompor-Gorący *et al.*, 2021). These results, therefore, clearly highlight the clinical potential for applying extracts from *Mangifera indica* in the treatment of liver conditions.

Conclusion

By utilizing literature data, the PBPK model of chrysin is successfully established and verified in both rat and human systems. The predicted plasma concentration profiles are consistent with observed clinical data, with fold error values falling strictly within the 2-fold acceptance criterion. Time profile analysis reveals that the very high concentrations of chrysin are specifically in the liver periportal tissue of diseased human individuals. Finally, it results in the effective localization of chrysin at the disease site.

The PBPK model of chrysin is well established in rats and humans. Time profile analysis shows very high concentrations of chrysin in plasma, in the liver periportal tissue of rats, in the small intestine of healthy humans, and in the liver periportal tissue of diseased humans. The established PBPK model of chrysin provides valuable insight into the use of the flavonoid extract of Mangifera indica in liver disease patients, in spite of its rapid metabolism and poor water solubility.

Albumin binding with chrysin during the transport of the chrysin molecule through blood plasma can stabilize pharmacokinetic parameters in the human body system. In rat models' metabolic clearance processes are the primary determinants of overall pharmacokinetics performances. In the human model, this clearance sensitivity is attenuated in the bound form of chrysin with albumin. Moreover, that exposure (AUC) increases significantly upon albumin binding. Lastly, half-life and MRT are prolonged due to reduced free fraction. Finally, it can be concluded that albumin protein binding to chrysin fundamentally shifts chrysin's pharmacokinetics from a clearance-dominated to a distribution-buffered system.

Acknowledgment

The authors would like to acknowledge Vellore Institute of Technology, Vellore, India and Gurudas College, India for providing support.

Reference

Balhara, A., Kale, S., & Singh, S. (2022). Physiologically based pharmacokinetic (PBPK) modelling. In *Computer aided pharmaceutics and drug delivery: an application guide for students and researchers of pharmaceutical sciences* (pp. 255-284). Singapore: Springer Nature Singapore. https://doi.org/10.1007/978-981-16-5180-9_9

Bharadwaj, K. K., Rabha, B., Ahmad, I., Mathew, S. P., Bhattacharjee, C. K., Jaganathan, B. G., ... & Ghosh, A. (2024). Rhamnetin, a nutraceutical flavonoid arrests cell cycle progression of human ovarian cancer (SKOV3) cells by inhibiting the histone deacetylase 2 protein. *Journal of Biomolecular Structure and Dynamics*, *42*(24), 13421-13436. https://doi.org/10.1080/07391102.2023.2275187

Boonpawa, R. (2017). *Physiologically based kinetic modelling-based prediction of oral systemic bioavailability of flavonoids, their metabolites, and their biological effects* (Doctoral dissertation, Wageningen University and Research).

Chou, P., Shannar, A., Pan, Y., Dave, P. D., Xu, J., & Kong, A. N. T. (2025). Application of physiologically-based pharmacokinetic (PBPK) model in drug development and in dietary phytochemicals. *Current Pharmacology Reports*, *11*(1), 45. https://doi.org/10.1007/s40495-025-00427-w

Gao, S., Siddiqui, N., Etim, I., Du, T., Zhang, Y., & Liang, D. (2021). Developing nutritional component chrysin as a therapeutic agent: Bioavailability and pharmacokinetics consideration, and ADME mechanisms. *Biomedicine & Pharmacotherapy*, *142*, 112080. https://doi.org/10.1016/j.biopha.2021.112080

Hack, C. E., Efremenko, A. Y., Pendse, S. N., Ellison, C. A., Najjar, A., Hewitt, N., ... & Clewell III, H. J. (2020). Physiologically based pharmacokinetic modeling software. In *Physiologically Based Pharmacokinetic (PBPK) Modeling* (pp. 81-126). Academic Press. https://doi.org/10.1016/B978-0-12-818596-4.00004-7

Kurkiewicz, M., Moździerz, A., Rzepecka-Stojko, A., & Stojko, J. (2025). Chrysin: A comprehensive review of its pharmacological properties and therapeutic potential. *Pharmaceuticals*, *18*(8), 1162. https://doi.org/10.3390/ph18081162

Lippert, J., Burghaus, R., Edginton, A., Frechen, S., Karlsson, M., Kovar, A., ... & Teutonico, D. (2019). Open systems pharmacology community—an open access, open source, open science approach to modeling and simulation in pharmaceutical sciences. *CPT: Pharmacometrics & Systems Pharmacology*, *8*(12), 878. https://doi.org/10.1002/psp4.12473

Najjar, A., Hamadeh, A., Krause, S., Schepky, A., & Edginton, A. (2024). Global sensitivity analysis of Open Systems Pharmacology Suite physiologically based pharmacokinetic models. *CPT: Pharmacometrics & Systems Pharmacology*, *13*(12), 2052-2067. https://doi.org/10.1002/psp4.13256

Niederalt, C., Kuepfer, L., Solodenko, J., Eissing, T., Siegmund, H. U., Block, M., ... & Lippert, J. (2018). A generic whole body physiologically based pharmacokinetic model for therapeutic proteins in PK-Sim. *Journal of Pharmacokinetics and Pharmacodynamics*, *45*(2), 235-257. https://doi.org/10.1007/s10928-017-9559-4

Panchal, N. S., Lodha, S. R., Sen, D., Khanra, S., Shah, N. R., Sindhi, F. A., ... & Harde, M. T. (2026). Unlocking the potential of natural products: A comprehensive review of chrysin derivatives and their biological activities. *Arabian Journal of Chemistry*, *19*. https://doi.org/10.25259/AJC_429_2025

Stompor-Gorący, M., Bajek-Bil, A., & Machaczka, M. (2021). Chrysin: Perspectives on contemporary status and future possibilities as pro-health agent. *Nutrients*, *13*(6), 2038. https://doi.org/10.3390/nu13062038

Tu, Y., Wang, L., Rong, Y., Tam, V., Yin, T., Gao, S., ... & Hu, M. (2021). Hepatoenteric recycling is a new disposition mechanism for orally administered phenolic drugs and phytochemicals in rats. *Elife*, *10*, e58820. https://doi.org/10.7554/eLife.58820

Willmann, S., Lippert, J., Sevestre, M., Solodenko, J., Fois, F., & Schmitt, W. (2003). PK-Sim®: a physiologically based pharmacokinetic 'whole-body'model. *Biosilico*, *1*(4), 121-124. http://dx.doi.org/10.1016/S1478-5382%2803%2902342-4

Yamazaki, H., & Shimizu, M. (2025). Prediction of internal exposures after virtual oral doses of disparate chemicals in rats and humans using simplified physiologically based pharmacokinetic models within silico-generated input parameters. *Chemical Research in Toxicology*, *38*(7), 1157-1166. https://pubs.acs.org/doi/abs/10.1021/acs.chemrestox.5c00157

doi: 10.31674/book.2026cdcbs.004

Temperature Compensation for Circadian Oscillations: A Brief Theoretical Explanation

Shrabani Sen

Department of Chemistry, Rammohan College, Kolkata- 700009, West Bengal, India

Corresponding Author's Email: sen.shrabani@gmail.com

Abstract

This chapter discusses temperature dependence of homogeneous chemical oscillations in two different systems: the Belousov–Zhabotinsky reaction in a continuously stirred tank reactor (CSTR) and a circadian oscillatory system. A theoretical framework is proposed to investigate the temperature dependence of chemical oscillations and the mechanisms responsible for temperature compensation. The theory is based on distribution of activation energies around the experimental mean and averaging of rate constants. It can conclude both cases. The finite width of the activation energy distribution associated with the corresponding rates characterizes the compensatory kinetics of circadian oscillations, whereas a vanishing width corresponds to Arrhenius-type temperature-dependent kinetics. Both scenarios are supported by experimental findings reported in the existing literature. The theoretical findings are in good agreement with the experimental observations.

Keywords: *Circadian Rhythm; Oscillatory Reactions; Stochasticity; Temperature Dependence*

Introduction

The speed of a chemical or biochemical reaction depends on temperature. When the temperature increases, the reaction speed also increases. This is a well-known principle explained by the Arrhenius rate equation, which states that the rate constant has an exponential dependence on temperature. This relationship has remained central to chemistry, biology, and physics for more than a century. However, the temperature of a reaction does not remain steady throughout the reaction time. There are different examples, such as the application of homogeneous temperature oscillatory fields, which can be achieved by varying temperature gradients spatially, as well as temperature compensation in chemical and biological systems. Temperature compensation refers to the ability of a biological clock or system to maintain a nearly constant rhythm or rate despite changes in environmental temperature (Kidd *et al*., 2015; Xiao *et al*., 2025).

In circadian rhythms, temperature compensation ensures that the internal biological clock continues to function with an approximately 24-hour cycle even when the surrounding temperature changes (Dunlap, 1999; Maeda & Nakamichi, 2025). Normally, most chemical and biochemical reactions speed up with increasing temperature and slow down with decreasing temperature. However, circadian oscillations remain relatively stable because of temperature compensation.

This property is important because it helps organisms maintain regular physiological and behavioral activities under varying environmental conditions (François *et al*., 2012). Without temperature compensation, circadian rhythms would become faster in warm conditions and slower in cold conditions, disrupting normal biological functions.

All these applications have attracted wide attention. Studies have revealed extensive information regarding the temperature dependence of physiological regulatory functions and the adaptation of bio-organisms to their surrounding thermal environments (Field & Noyes, 1974). The frequencies and amplitudes of complex oscillations in the Belousov–Zhabotinskii (BZ) reaction within a stirred tank reactor are influenced by temperature variations (Zaikin & Zhabotinsky, 1970; Dutt & Müller, 1993). Furthermore, it has been reported

that introducing a temperature gradient can initiate the propagation of traveling waves in oscillatory glycolysis within yeast extracts (Foerster *et al*., 1990). Numerous studies demonstrate that temperature serves as an important factor in regulating feedback mechanisms in biochemical systems.

A closely related phenomenon is the temperature compensation observed in circadian oscillations of cells and living organisms (Hastings & Swinny, 1957). These oscillations help organisms synchronize physiological processes with the natural 24-hour light–dark cycle on Earth. When a particular biochemical process or reaction rate becomes insensitive to temperature changes, the effect is commonly termed "immediate temperature compensation." Various mechanisms responsible for enzymatic temperature adaptation have been discussed in the referenced studies.

Circadian Oscillations

Circadian oscillations are natural rhythms that repeat approximately every 24 hours, influencing various biological processes in living systems. They are regulated by a circadian clock, primarily locates in the suprachiasmatic nucleus (SCN) of the brain, which coordinates these rhythms with external cues like light and darkness (Mieda, 2020). These rhythms are crucial for regulating sleep wake cycles, hormone secretion and other physiological functions. Light is the primary environmental factor that influences circadian oscillations, helping the body maintain synchronization with external day and night conditions. Circadian oscillations regulate many important body functions such as the sleep–wake cycle, hormone secretion, body temperature, metabolism, and feeding behavior. For example, melatonin secretion increases during the night to promote sleep (Jia *et al*., 2025), while alertness and body activity are generally higher during the daytime.

Circadian oscillation is fundamentally a biochemical oscillation and an essential feature while understanding chemical oscillations in the concept of a limit cycle formed by the interacting components involved in the rate-determining steps. Most characteristic properties of such oscillatory behavior can be effectively described within the framework of a limit cycle. However, because kinetic rate constants are generally temperature dependent, the dynamics of limit-cycle oscillations, including their associated periods, would ordinarily be expected to exhibit significant variations in response to changes in temperature. In contrast, circadian systems exhibit remarkable insensitivity of oscillatory periods to temperature variation. The time period of the BZ oscillation is temperature-dependent, whereas circadian oscillations are temperature-insensitive. The search for an explanation of this type of insensitivity began several years ago. The explanation proposed by Rouf *et al.* (2003), which suggests that temperature compensation results from a delicate balance between opposing positive and negative contributions involving control coefficients and activation energies, has gained broad acceptance in the scientific community (Hong *et al.,* 2007).

This theoretical framework is applied to circadian systems, and it is observed that one of the fundamental requirements of such a mechanism is the presence of a specific set of activation energies. In many cases, these activation energies need to be considerably high, thereby reducing the likelihood of the associated reaction pathways (Ruoff *et al*., 1999; Ruoff *et al*., 2003). Furthermore, the combination of control coefficients responsible for maintaining the required balance is not necessarily unique.

This finding for the stringent delicate balance conditions leads to find another theoretical logic for the temperature compensation for the circadian oscillations.

Average Rate Constant, Temperature Dependence

In complex biological organisms, the number of reacting species involved in the rate-determining steps may vary significantly as they traverse potential barriers containing multiple local minima. Furthermore, during the transition from the reactant well to the product well, a species may follow multiple pathways characterized by different activation energies, depending on the nature of enzymatic complexation and the local heterogeneity of the reaction medium. This suggests that the kinetics may be more appropriately

described by an average rate constant rather than a single rate constant. To address this issue, a framework is proposed in which the averaging of rate constants is performed over a distribution of activation energies centered around the experimental mean value. The width of this distribution can be estimated based on the requirement of temperature-compensated kinetics within a cell, indicating that the distribution width reflects the self-regulating nature of the biological system.

Since BZ-type and other oscillating chemical reactions are not self-regulatory, their oscillation periods depend on temperature and follow Arrhenius kinetics. It is shown that, in such cases, the width of the activation energy distribution tends to vanish, thereby reducing the system to the conventional Arrhenius temperature dependence of the rate constant.

To obtain an overall average rate constant from a distribution of energies around an mean value of experimental data, a distribution function $P(E;\langle\Delta E^2\rangle,\langle E\rangle)$ is introduced where (E) represents energy of activation. The normalisation property of the distribution function is maintained such that

$$\int_0^\infty dE\, P(E\,;\,\langle\triangle E^2\rangle,\,\langle E\rangle) = 1$$

Let us further assume that the spread in activation energies is temperature dependent and is given by $\langle\Delta E^2\rangle = \frac{B}{RT}$ where R is the Universal gas constant and B is the numerically derivable constant from the proposed theoretical framework. Averaging over over Arrhenius rate constant ($k = Ae^{\frac{-E}{RT}}$) for a reaction step is then given by

$$\langle k\rangle = \int_0^\infty dE\, Ae^{(-E/RT)}\, P(E;\langle\triangle E^2\rangle,\langle E\rangle)$$

Where frequency factor is designated by A. Temperature compensation means the first derivative with respect to the temperature is null. Which means

$$\frac{\partial\langle k\rangle}{\partial T} = 0$$

This yields the relation

$$\frac{1}{RT^2}\langle E.k\rangle + \int_0^\infty dE\, k\,\frac{\partial P}{\partial T} = 0$$

Now to make use of some partial derivative and specialize the case for normal Gaussian distribution function, one can easily obtain the following transcendental equation

$$B = \frac{\langle k.E\rangle}{\frac{1}{2}\left[\frac{(RT)^2\langle k(E-\langle E\rangle)^2\rangle}{B^2} - \frac{RT\langle k\rangle}{B}\right]}$$

Now two different scenarios can easily be concluded

(i) Temperature-compensating kinetics—For a given experimental average activation energy value and temperature (T), the above algebraic equation can be solved numerically in a self-consistent manner to determine the parameter (B). The obtained value of (B), and consequently the corresponding distribution width, produces an average rate constant that exhibits clear temperature compensation. As a result, the oscillation period remains nearly unaffected by changes in temperature.

In contrast, for chemical reactions occurring in homogeneous systems such as a petri dish or continuously stirred tank reactor (CSTR), the spread in activation energies approaches zero because only a single

discrete activation energy is available (→ 0). Under these conditions, the Gaussian distribution (P(E)) becomes a delta function, a δ-function δ(E −). Consequently, the expression for the average k becomes Arrhenius.

$$\langle k \rangle = Ae^{(-\langle E \rangle / RT)}$$

These expressions form the basis for describing the kinetics of biochemical systems. Therefore, in biological systems, the distribution of activation energies—whether arising through mutation or other processes—must possess a self-regulating nature such that the width of the distribution adjusts automatically to satisfy the condition of temperature compensation. Since this adjustment is statistical in origin, it is inherently more robust than the condition proposed by Rouff *et al*. (1999), which requires a much stricter balance.

Belousov-Zhabotinskii Reaction and Oregonator Model

Field and Noyes originally proposed Oregonator model as a highly idealized minimal representation of the Belousov–Zhabotinskii (BZ) reaction, was developed to describe the cerium-ion-catalyzed oscillatory malonic acid. The model consists of some reacting species, namely Y1, Y2, Y3 and X1, X2, X3 and is characterized by the following reaction steps.

$$X_1 + Y_2 \xrightarrow{k_1} Y_1$$
$$Y_1 + Y_2 \xrightarrow{k_2} Z_1$$
$$X_2 + Y_1 \xrightarrow{k_3} 2Y_1 + Y_3$$
$$2Y_1 \xrightarrow{k_4} Z_2$$
$$X_3 + Y_3 \xrightarrow{k_5} Y_2$$

Here the X's are the large numbers and treated as constants. The Gillespie algorithm is applied for stochastic simulation of the abovementioned reaction steps. The resultant temperature dependence is just that of the Arrhenius rate law (Figure 1).

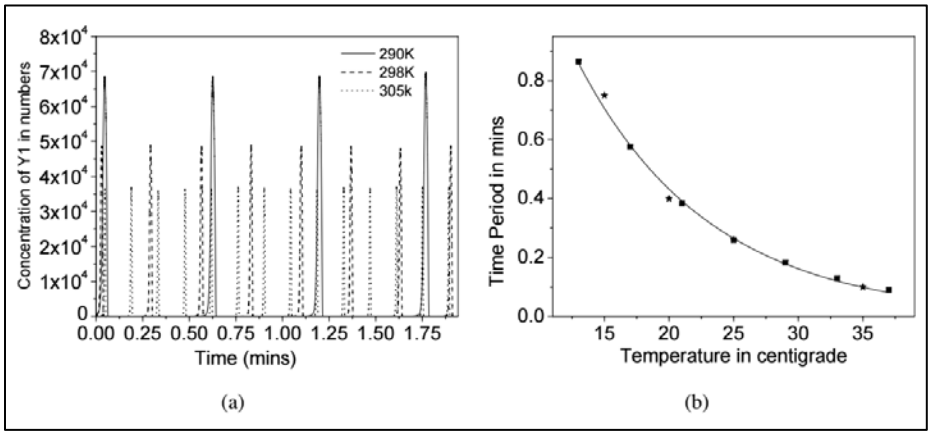

Figure 1: (a) Numerical Simulations Showing the Oscillatory Behavior in the Oregonator Model at Different Temperatures (b) Dependence of the Time Period of Oscillation on Temperature (Sen et al., 2008)

To study temperature compensation within the framework, the model of Gonze and Goldbeter (2006) is considered. The oscillatory dynamics of both models were investigated using stochastic simulation techniques based on the approach developed by Gillespie (1977). The objective is to incorporate stochastic

effects directly into dynamic reactions. Following the Gillespie algorithm, a stochastically determined reaction probability density is introduced.

Let us first clarify the concept of stochasticity. Stochasticity refers to the property of being adequately described by a probability distribution and is therefore associated with a probabilistic modeling framework. Although the terms stochasticity and randomness are often used interchangeably, they are technically distinct. Stochasticity pertains to the mathematical description of a system, whereas randomness refers to the inherent unpredictability of the underlying phenomenon. One of the simplest continuous-time stochastic processes is Brownian motion, which was first observed by the botanist Robert Brown while examining pollen grains suspended in water under a microscope. There should always be some otherways by which the reaction may take place. Among them the minimum energy path is the experimental one. The averaging method is discussed above. For the circadian oscillation model the the rate constants are investigated by averaging the Gaussian distribution width around the mean experimental activation energy. It is observed that the time periods are not sensitive towards temperature here. As it is self-regulatory it can adjust its width to get it compensated. In contrast, chemical oscillations such as those observed in a BZ reaction within a CSTR or in glycolysis in a cell-free yeast extract are non-endogenous, with their dynamics being determined primarily by external reaction conditions, such as the stirring rate and other experimental parameters. In such cases, the width of the activation energy distribution is expected to approach zero.

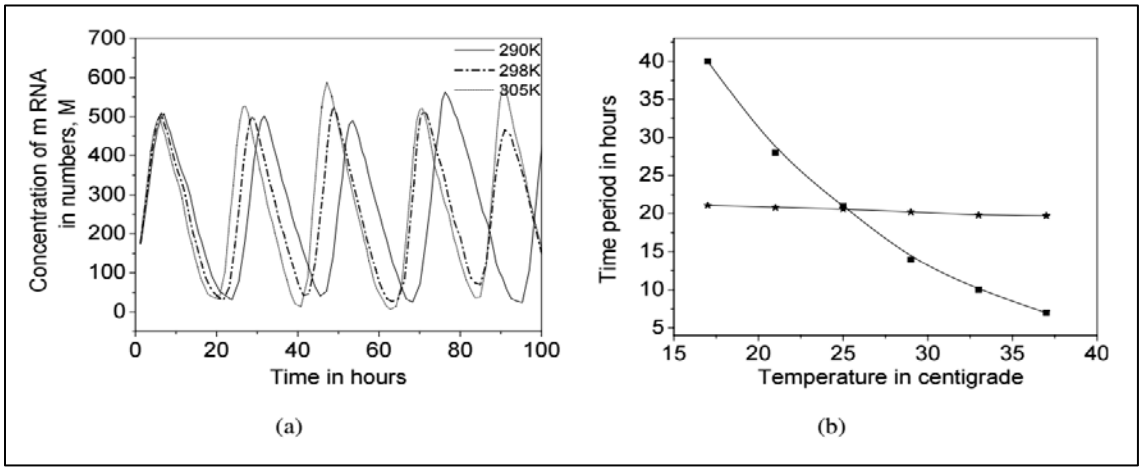

Figure 2: (a): Oscillations of m-RNA Obtained by Stochastic Simulation of the Model for Circadian Rhythm by Gonze-Goldbeter with Temperature Compensated Rate Constants (b): Temperature Dependence (Dark square) and Temperature Compensation (Dark stars) of the Time Period (Sen et al., 2008)

Conclusion

A simple theory is developed to explain the temperature compensation of circadian oscillation. The BZ reaction model and Gonze Goldbetter model for mRNA oscillation in Drosophila are used. The Gillespie algorithm is used for numerical simulation. The analysis demonstrates temperature dependence by the Arrhenius theory, and the same compensated behavior exhibits two far-away cases of the activation energies. Additional experimental studies on the temperature dependence of chemical oscillations may reveal intermediate regimes of the distribution width where partially compensated behavior and deviations from Arrhenius-type oscillatory kinetics can arise.

Acknowledgement

The author gratefully acknowledges Prof. Debshankar Ray for his valuable support and encouragement throughout the course of this work.

References

Dunlap, J. C. (1999). Molecular bases for circadian clocks. *Cell, 96*(2), 271-290. https://doi.org/10.1016/S0092-8674(00)80566-8

Dutt, A. K., & Müller, S. C. (1993). Effect of stirring and temperature on the Belousov-Zhabotinskii reaction in a CSTR. *The Journal of Physical Chemistry, 97*(39), 10059-10063. https://doi.org/10.1021/j100141a027

Field, R. J., & Noyes, R. M. (1974). Oscillations in chemical systems. IV. Limit cycle behavior in a model of a real chemical reaction. *The Journal of Chemical Physics, 60*(5), 1877-1884. https://doi.org/10.1063/1.1681288

Foerster, P., Müller, S. C., & Hess, B. (1990). Temperature dependence of curvature-velocity relationship in an excitable Belousov-Zhabotinskii reaction. *Journal of Physical Chemistry, 94*(26), 8859-8861. https://doi.org/10.1021/j100389a001

François, P., Despierre, N., & Siggia, E. D. (2012). Adaptive temperature compensation in circadian oscillations. *PLOS Computational Biology, 8*(7), e1002585. https://doi.org/10.1371/journal.pcbi.1002585

Gillespie, D. T. (1977). Exact stochastic simulation of coupled chemical reactions. *The Journal of Physical Chemistry, 81*(25), 2340-2361. https://doi.org/10.1021/j100540a008

Gonze, D., & Goldbeter, A. (2006). Circadian rhythms and molecular noise. *Chaos: An Interdisciplinary Journal of Nonlinear Science, 16*(2). https://doi.org/10.1063/1.2211767

Hastings, J. W., & Sweeney, B. M. (1957). On the mechanism of temperature independence in a biological clock. *Proceedings of the National Academy of Sciences, 43*(9), 804-811. https://doi.org/10.1073/pnas.43.9.804

Hong, C. I., Conrad, E. D., & Tyson, J. J. (2007). A proposal for robust temperature compensation of circadian rhythms. *Proceedings of the National Academy of Sciences, 104*(4), 1195-1200. https://doi.org/10.1073/pnas.0601378104

Jia, M., Luo, A., Wei, M., Zhang, Y., Wu, T., & Chen, N. (2025). Melatonin: beyond circadian regulation-exploring its diverse physiological roles and therapeutic potential. *Sleep Medicine Reviews, 82,* 102123. https://doi.org/10.1016/j.smrv.2025.102123

Kidd, P. B., Young, M. W., & Siggia, E. D. (2015). Temperature compensation and temperature sensation in the circadian clock. *Proceedings of the National Academy of Sciences, 112*(46), E6284-E6292. https://doi.org/10.1073/pnas.1511215112

Maeda, A. E., & Nakamichi, N. (2025). Temperature compensation of the Arabidopsis circadian clock. npj *Biological Timing and Sleep, 2*(1), 40. https://doi.org/10.1038/s44323-025-00058-w

Mieda, M. (2020). The central circadian clock of the suprachiasmatic nucleus as an ensemble of multiple oscillatory neurons. *Neuroscience Research, 156*, 24-31. https://doi.org/10.1016/j.neures.2019.08.003

Ruoff, P., Christensen, M. K., Wolf, J., & Heinrich, R. (2003). Temperature dependency and temperature compensation in a model of yeast glycolytic oscillations. *Biophysical chemistry, 106*(2), 179-192. https://doi.org/10.1016/S0301-4622(03)00191-1

Ruoff, P., Vinsjevik, M., Mohsenzadeh, S., & Rensing, L. (1999). The Goodwin Model: Simulating the Effect of Cycloheximide and Heat Shock on the Sporulation Rhythm ofNeurospora crassa. *Journal of theoretical biology, 196*(4), 483-494. https://doi.org/10.1006/jtbi.1998.0846

Sen, S., Riaz, S. S., & Ray, D. S. (2008). Temperature dependence and temperature compensation of kinetics of chemical oscillations; Belousov–Zhabotinskii reaction, glycolysis and circadian rhythms. *Journal of Theoretical Biology, 250*(1), 103-112. https://doi.org/10.1016/j.jtbi.2007.08.029

Xiao, Y., Sainoo, Y., Nishimura, T., & Ito, H. (2025). Low temperature abolishes human cellular circadian rhythm through Hopf bifurcation. *npj Systems Biology and Applications, 12*(1), 5. https://doi.org/10.1038/s41540-025-00628-5

Zaikin, A. N., & Zhabotinsky, A. M. (1970). Concentration wave propagation in two-dimensional liquid-phase self-oscillating system. *Nature, 225*(5232), 535-537. https://doi.org/10.1038/225535b0

doi: 10.31674/book.2026cdcbs.005

Towards the Synthesis of Polymeric Ladderphanes from Cyclopropene Monomers: A Model Study

Biswajit Panda

Department of Chemistry, Ramnagar College, Purba Medinipur- 721453, India

Corresponding Author's Email: biswajitchem@gmail.com

Abstract

Ladderphanes are special types of polymers characterized by parallel, covalently connected backbones that show exceptional rigidity, anisotropy, and potential utility in advanced materials. The work described here is a model strategy for the synthesis of a strain cyclopropene monomer, followed by Ring-Opening Metathesis Polymerization (ROMP) polymerization. The synthesis of strain cyclopropene is challenging and faces various difficulties, which are successfully overcome using different modification techniques. Due to their characteristic ring strain and high reactivity, cyclopropenes serve as attractive precursors for controlled polymerization. This study will help to design the synthesis of different cyclopropane derivatives, which may be highly useful for many organic transformations.

Keywords: *Cyclopropene; Ladderphanes; Metathesis; Organic Synthesis; ROMP; Strained Hydrocarbons*

Introduction

Ladderphane is defined as a double-stranded polymer composed of multiple layers of cyclophanes, in which the tethers are part of the polymeric backbone (Figure 1) (Luh *et al.*, 2023). Interestingly, if one considers the DNA molecule as an illustrative example of a ladder-like architecture, it can be viewed as a specialized form in which complementary base pairs are held together through hydrogen bonding interactions and connected perpendicularly to the deoxyribose phosphate backbones. In this structure, the sugar-phosphate backbones are stereochemically isotactic in nature. The spacing of adjacent base pair layers is about 3.4 Å, and this distance indicates that there should be strong interactions between adjacent layers of base pairs. These features could be advantageous in the plan and preparation of double-stranded DNA-like polymeric ladderphanes.

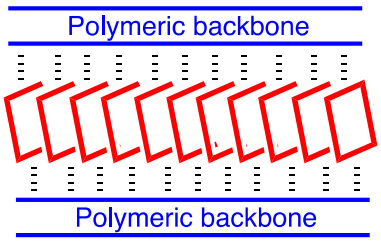

Figure 1: Polymeric Backbone of Ladderphane

Generally, three different methods have been used for the synthesis of polymeric ladderphanes (Figure 2). The initial strategy involves the simultaneous polymerization of a monomer bearing two reactive polymerizable units bridged by a rigid spacer. In this strategy, symmetric ladderphanes are obtained. The second and third protocols involve the synthesis of unsymmetrical ladderphanes where the two polymeric backbones are not identical but complementary. The latter method has been employed for replication to synthesize a range of condensation polymers with precisely controlled chain lengths and low dispersity.

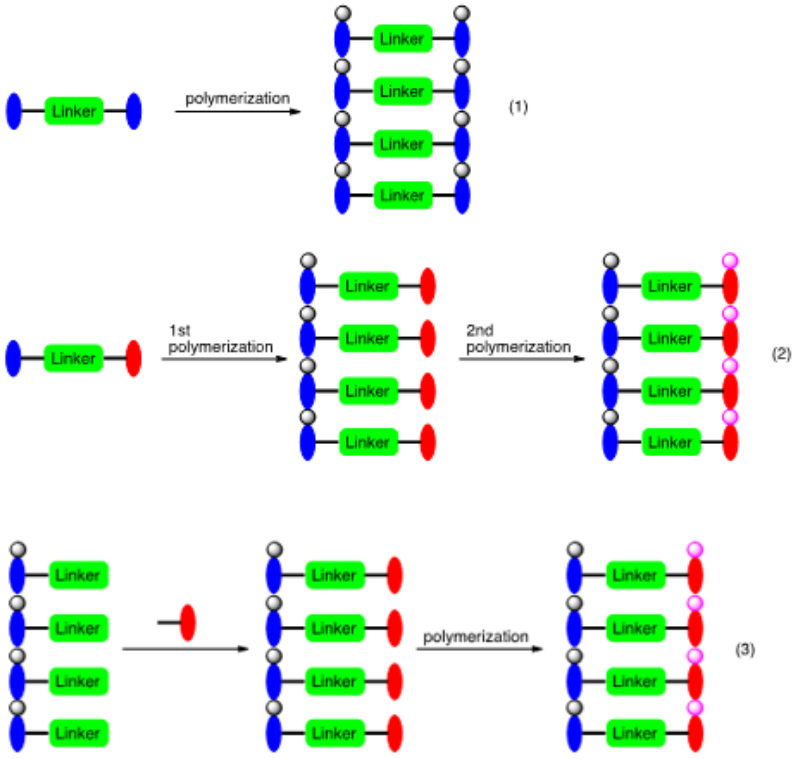

Figure 2: Different Strategies for the Synthesis of Polymeric Ladderphanes

Ring-opening metathesis polymerization, commonly abbreviated as ROMP, holds a leading position in polymer chemistry and enables the synthesis of structurally diverse polymers with tailored architectures and functional properties (Nomura & Jaiyen, 2026). In ROMP, the driving force for polymer formation arises from the relief of ring strain in the cyclic olefin monomer (negative ΔH), although a reduction in entropy accompanies this process (Lessard *et al.*, 2024). It has been found that living ROMP is an effective method to produce a large number of different polymers and block copolymers having a particular molecular weight range and lower polydispersity, as well as unique properties. Structures of different catalysts commonly used in the ROMP process are shown in Figure 3. Five-membered cyclic olefins, e.g., norbornene and its derivatives, are widely employed as monomers because of their high reactivity in ROMP and the ease with which functional groups can be introduced onto the ring framework (Alentiev & Bermeshev, 2022). Polynorbornenes generated through metal-catalyzed ROMP of functionalized norbornene derivatives have shown broad utility in areas such as catalysis (García-Loma & Albéniz, 2019), light-harvesting systems (Boyd & Schrock, 1999), photoinduced electron transfer, ion transport (Liu *et al.*, 2026), and optoelectronic materials (Sutthasupa *et al.*, 2025). Polynorbornene is also used for the target gas separation (Wang *et al.*, 2021). Luh and co-workers (2008) demonstrated that when norbornene derivatives bearing a 5,6-endofused N-arylpyrrolidine unit undergo ROMP in the presence of the first-generation Grubbs catalyst, the resulting polymers exhibit a high degree of stereochemical order. Specifically, the process yields isotactic, single-stranded polynorbornenes characterized by uniformly trans-configured double bonds and a consistent alignment of pendant groups along one direction, reflecting a remarkable level of structural control during polymer growth. It is plausible that π–π stacking interactions among the pendant aryl substituents occur during the polymerization process, thereby influencing and directing the observed stereoselective outcome. The same group also revealed that in a contrasting scenario, substituting the *N*-aryl group with an *N*-cyclohexyl moiety leads to a loss of stereocontrol, producing polynorbornenes with a mixed cis/trans double-bond distribution (21:79) and only weakly defined tacticity (Wang *et al.*, 2009).

Interestingly, this strategy has also been effectively applied to construct relatively rigid, polynorbornene-derived double-stranded ladderphane architectures (Luh, 2013) and has further enabled the templated replication of a single-stranded polynorbornene into its complementary counterpart. In polynorbornenes, the distance between adjacent repeating units is roughly 5.5 Å, a spacing that allows significant interactions to arise between neighboring pendant groups or between linkers in ladderphane structures.

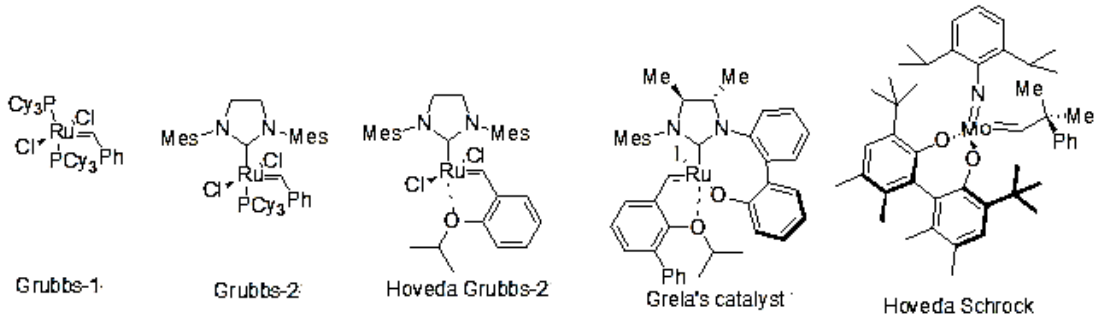

Figure 3: Commonly Used Catalysts in Metathesis Reactions

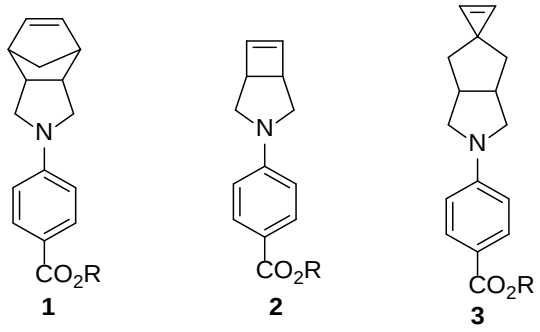

Figure 4: Different Cyclo-Ene Monomers

Comparatively, ROMPs of cyclobutene derivatives have gained less interest, and the reactions generally are nonselective, forming polymers formed as a mixture of both Z- and E-double bonds, unless specifically designed substrates are used (Lin *et al.*, 2013). It is expected that the separation of each of the monomeric units in polycyclobutenes would be somewhat shorter than polynorbornenes due to the absence of bridging methylene groups. Moving from cyclobutene to cyclopropene will bring joy and challenges in the ROMP process. Cyclopropene possesses a substantial ring strain of approximately 228 kJ mol^{-1}. Owing to its distinctive status as the smallest unsaturated cyclic framework, cyclopropene derivatives have long captured the interest of both theoretical and experimental chemists. In an early investigation, Allen and co-workers demonstrated that the vinylic carbon atoms in cyclopropene employ $sp^{1.19}$ hybrid orbitals for bonding with substituents, whereas $sp^{2.68}$ hybrid orbitals are utilized for bonding within the ring σ framework (Allen, 1982). The increased s-character (ca. 43%) of the cyclopropene C–H bonds enable cyclopropene to occasionally exhibit reactivity similar to that of a terminal alkyne, thereby serving as a versatile three-carbon building block.

Notably, no reports describing the ROMP of cyclopropene appeared in the literature until Singh and co-workers disclosed the successful ROMP of 3,3-disubstituted cyclopropenes in 2006. Two years later, the same group reported that the highly tactic trans-polycyclopropene was prepared through enantiomorphic site control using initiators closely related to those previously employed in asymmetric metathesis reactions (Singh & Schrock, 2008). The reason behind its living nature likely arises because the alkylidene unit in the propagating species resembles a neopentylidene or neophylidene moiety, both of which are recognized as

the most stable terminal alkylidenes in the Mo(NR)(CHR')(OR'')$_2$ family with respect to bimolecular decomposition. The small ring metathesis is really an interesting and growing topic in organic chemistry (Panda, 2018). It was proposed that trans linkages between adjacent repeat units in poly(**4**) arise from steric congestion within the molybdabicyclopentane intermediate (Scheme 1). When the substituents at C(3) of the cyclopropene are different, as in compound **4**, the resulting polymer can display tacticity. Shown below are the two regular structural arrangements possible for trans-poly(**4**). The spacing between adjacent pendants in polycyclopropenes would therefore be shorter compared to polynorbornenes and even shorter than polycylobutenes. Accordingly, the interactions among pendant groups in polycyclopropenes are expected to differ from those observed in polynorbornenes or polycyclobutenes. Therefore, the introduction of a congener of norbornene and cyclobutene, cyclopropene fused with N-arylpyrrolidine, will open a new arena in template-assisted duplex polymer synthesis. The close proximity of aryl pendants may show the strong π-π interactions, which will contribute to the well alignment for the formation of ladderphanes. In 2019, Peng and co-workers reported a stereospecific synthesis of polymers from cyclopropene monomers by ROMP method.

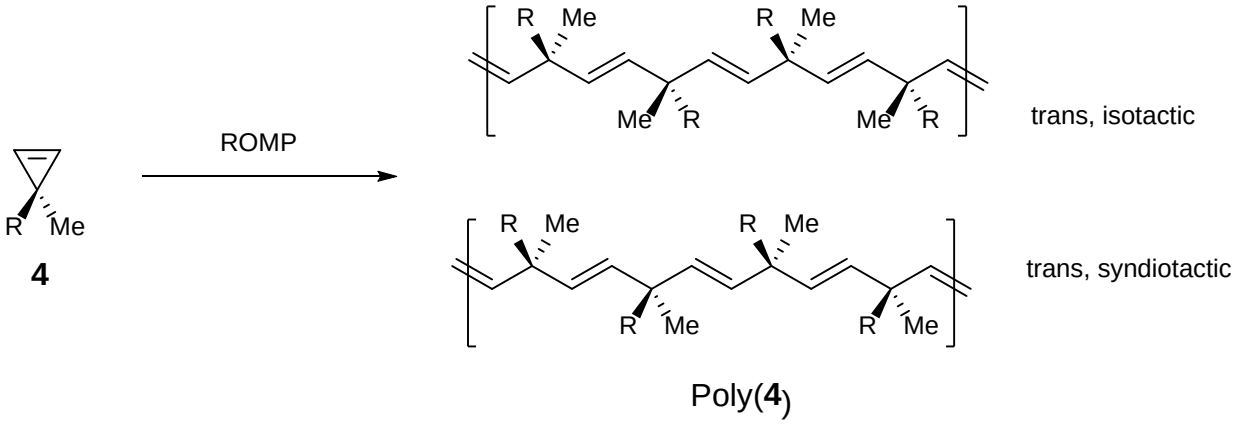

Scheme 1: ROMP of Cyclopropane Monomer

As with polynorbornenes, in polycyclopropenes, face-to-face long-range π-stacking that promotes a well-organized layered arrangement of aromatic rings may give rise to strong electronic coupling between these π-conjugated systems. (Scheme 2). Charge-carrier mobility would be strongly influenced by these intermolecular interactions, as efficient orbital overlap and enhanced electronic communication between adjacent π-conjugated units can facilitate the transportation of charge through the material. It has been anticipated that the self-organization of multichromophoric building blocks designed for light-harvesting and photophysical studies will lead to intriguing outcomes. In this context, supramolecular frameworks such as double-stranded ladderphanes could provide an alternative strategy for arranging these planar π-systems in a face-to-face manner. The polymeric backbone can also function as a barrier, effectively preventing interactions between neighboring arene arrays. Beyond covalently linked ladder-type polymers, double-stranded oligomeric or polymeric architectures can be constructed by associating two single strands through various noncovalent interactions, including metal coordination, hydrogen bonding, π–π stacking, ionic interactions, or host–guest inclusion (Elling & Neary, 2026). From another perspective, replication may be viewed as a templated process in which a single-stranded polymer directs the formation of a complementary strand, ultimately yielding an unsymmetrical double-stranded ladderphane. If the polymerization degree and polydispersity of the template are precisely regulated, this strategy could enable the synthesis of daughter polymers exhibiting controlled chain lengths and narrow polydispersity.

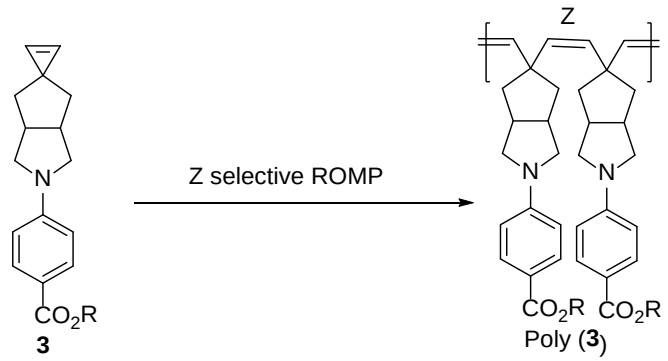

Scheme 2: Z-Selective ROMP of Pyrrolidine Containing Cyclopropene 3

Results and Discussion

For the preliminary study towards the synthesis of polymeric ladderphanes from cyclopropene monomer, 3-*p*-bromophenyl, 3-methyl cyclopropene (9) was selected as a model compound for the investigation of ROMP of cyclopropene moiety using different ruthenium and molybdenum-based catalytic systems.

Similar to its application in total synthesis, retrosynthetic analysis serves as a highly effective strategy for determining the synthetic route of any target molecule (Panda, 2019). Thus, with a view to synthesizing 3-*p*-bromophenyl, 3-methyl cyclopropane **5**, the retro-synthetic analysis is presented in Scheme 3. It has been envisaged that the conversion of 4-bromo acetophenone **5** into α-methyl styrene **6** can easily be achieved in a single step using Wittig olefination. An alternate approach is also possible from 4-bromo acetophenones **5** through a two-step process with the addition of methyl magnesium bromide, after that the acid-catalyzed dehydration of the generated tertiary alcohols, but the preparation of olefins from this method is highly prone to acid-catalyzed polymerization. It will then involve a three-step sequence, namely, the conversion of α-methyl styrene **6** to the dibromocyclopropane **7**, partial reduction of dibromocyclopropanes will provide monobromocyclopropane **8,** which is then dehydrohalogenated to furnish the required cyclopropene derivative **9**.

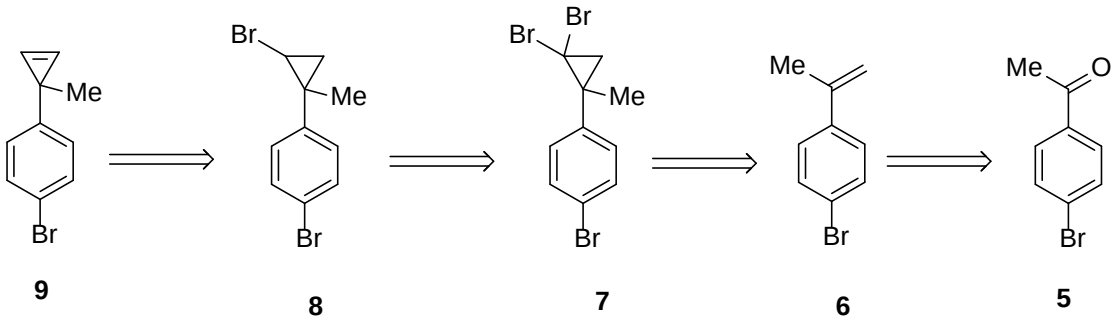

Scheme 3: Retrosynthesis of Cyclopropene Derivative 9

The forward synthesis was commenced using commercially available 4-bromoacetophenone **5** (Scheme 4). The bromo substituent was incorporated into the aromatic ring because it can be readily functionalized through various cross-coupling reactions, enabling the introduction of diverse functional groups (Panda & Sarkar, 2010). Wittig olefination provides styrene derivative **6** in 92% yield. Dibromocyclopropanes **7** were synthesized through the cyclopropanation process of crude olefins **6** using dibromocarbene, produced under modified Makosza's phase transfer catalysis (PTC) conditions. Notably, employing a different addition method than the one originally described by Makosza, where an aqueous base solution was added dropwise into a rapidly stirred mixture containing the organic components, proved to be advantageous for enhancing the reaction yields. This revised method significantly suppressed resin formation, thereby enabling cleaner and more efficient isolation of the target compound.

To manage the exothermic nature of the reaction, especially during the initial stages, the reaction was performed in a 1:1 (v/v) mixture of bromoform and dichloromethane. Refluxing this mixture was crucial for preventing overheating of the reaction mixtures and ensuring temperatures did not exceed 40–45°C. During the later stages of the process, once the intense exothermic reactions subsided, the residual dichloromethane was removed at 50°C. It is well established that the kinetics of cyclopropanation reactions under phase-transfer conditions depend significantly on the structure of the phase-transfer catalyst. Typically, the highest reaction rates and optimal conversions are achieved when employing benzyltriethylammonium (TEBA) salts. However, it was observed that the use of tetrabutylammonium (TBA) and TEBA salts introduced additional challenges, including pronounced foaming and the formation of persistent emulsions during the aqueous workup, particularly in large-scale reactions.

In contrast, when hexadecyl- or tetradecyltrimethylammonium salts were used in catalytic amounts, the biphasic solution was separated more efficiently. This led to quicker and more effective extraction, ultimately resulting in higher overall yields. The final product was isolated by straightforward filtration through a short column of silica gel. Cyclopropanation of α-methyl styrene **6** with dibromocarbene produces dibromocyclopropane **7** in 82% isolated yield. The reduction of dibromocyclopropanes **7** was followed by the established procedure with some practical adjustments necessary for scale-up (Sheshenev *et al.*, 2009). To ensure safety and efficiency, several modifications were made.

Firstly, due to the evolution of flammable gases such as ethylene and ethane, the reaction was conducted in a fume hood where ventilation is good. The reaction vessel was filled to less than one-third of its capacity and was fitted with a proficient reflux condenser. The extra space acted as a safeguard against irregular boiling and unexpected splashing, crucial especially during the quench step when a significant amount of heat and gas was generated. Secondly, the reaction exhibited an initiation phase where the initial 20 mol % of the Grignard reagent was utilized for the reduction of the Ti(IV) complex into the Ti(II) species. The generation of the catalytically active complex was indicated by a change in colour from pale yellow to dark brown. However, this colour change did not always signify the end of the activation period. The process might take more time when the addition of the Grignard reagent was too rapid, exceeding the rate of Ti(IV)/Ti(II) reduction. Therefore, there is a significant risk of the reaction mixture violently boiling and splashing. Therefore, during the early stages of the reaction, it is essential to add the Grignard reagent dropwise at a reasonably slow rate. This allows for the solvent to boil and the gaseous byproducts to evolve gradually. Additionally, close monitoring of the reaction through GC analysis is imperative to prevent the overreduction of the target monobromide **8** to the corresponding cyclopropane compound **10**.

It is crucial to use the Grignard reagent having exact strength; otherwise, if the Grignard reagent is not titrated before use, there is a possibility of forming the undesired byproducts in a considerable amount. To address this, approximately 1.1 equivalents of EtMgBr were added dropwise. The reaction mixture was then allowed to stir for 15 minutes and studied using GC. The requirement of any additional amount of Grignard reagent was accurately determined based on the GC conversion.

Under typical conditions, the crude reaction mixture was found to contain 98–99% bromocyclopropane **8**, with residual starting material **7** accounting for no more than 1%. Considering the subsequent step, it is preferable to retain some dibromide **7** instead of risking overreduction into compound **10**. This preference arises because dibromide **7** will ultimately be eliminated by the treatment of strong base t-BuOK through the β-elimination process. In contrast, the separation of compounds **9** and **10** is exceedingly challenging due to their similar polarity. Hence, if a significant amount of the over-reduced product **10** is generated, it becomes necessary to purify monobromide **8** through column chromatography.

In the synthesis of cyclopropenes, diastereoselectivity does not play a significant role because both diastereomeric forms of compound **8** are capable of undergoing dehydrohalogenation under the reaction conditions. Cyclopropenes **9** were synthesized from monobromocyclopropanes **8** by carrying out the

reaction in anhydrous DMSO in the presence of a slight excess of t-BuOK. Under these conditions, the base-promoted dehydrohalogenation of the bromocyclopropane intermediates proceeded efficiently to afford the corresponding cyclopropenes. Because this reaction is highly sensitive to moisture and oxygen, it requires careful handling and precautions to prevent degradation or failure. For this reason, potassium tert-butoxide was kept and used in a nitrogen-filled glovebox.

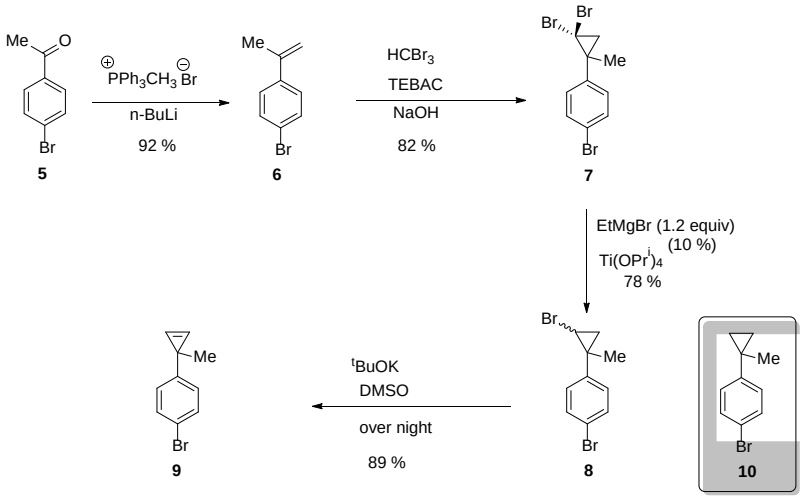

Scheme 4: Synthesis of Cyclopropane 9

After successful synthesis of cyclopropane **9**, the ROMP reaction was investigated under different ruthenium-based catalytic conditions (Scheme 5). Both Grubb's 1st generation catalyst and Grubb's-Hoveda 1st generation catalysts were proven to be less effective in ROMP polymerization of cyclopropane **9.** It has been found that using 10 mol % of catalysts and stirring at room temperature for up to 36 hours shows very little conversion of starting material. However, other ruthenium-based catalysts, such as Grubb's 2nd generation catalyst, proved to be efficient on ROMP reactions, as using 12 mol % of catalyst, full conversion of the starting material was observed within 24 hours of stirring at ambient temperature. The polymer's NMR spectrum displays a broadened proton signal in the 5–6 ppm region. The gel permeation chromatography (GPC) analysis shows the low polydispersity of the formed polymer (Figure 5). Gel permeation chromatography (GPC) analysis of the polymer exhibited a single, well-defined peak with a narrow polydispersity (PDI = 1.06), consistent with characteristics of a living polymerization process.

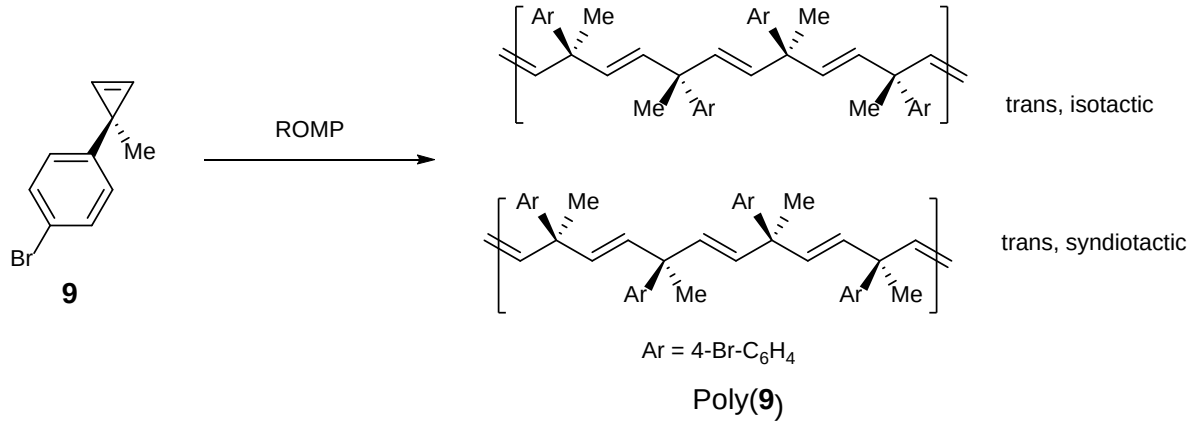

Scheme 5: ROMP of Cyclopropane 9

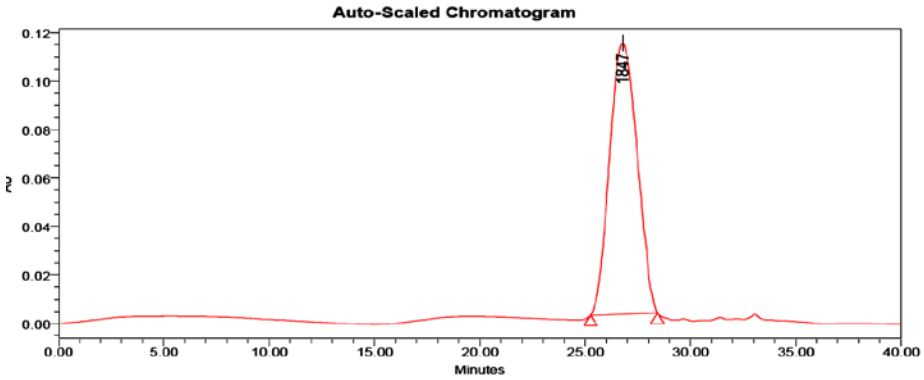

GPC Results

	Dist Name	Mn	Mw	MP	Mz	Mz+1	Mv	Polydispersity	MW Marker 1	MW Marker 2
1		1741	1856	1847	1975	2092		1.066423		

Figure 5: Gel Permeation Chromatogram

Following the successful synthesis of the cyclopropene polymer poly (**9**), the next goal was to prepare polymeric ladderphanes from monomer **3**, a project that is currently underway in the laboratory. The synthetic methods discussed above provide an understanding of how to plan a synthesis using a retrosynthetic pathway. In forward synthesis, various problems may arise that must be solved sequentially to achieve the target molecule. Thus, target-oriented and total synthesis have expanded the knowledge and built the expertise necessary to successfully execute various chemical reactions (Panda & Sarkar, 2013). Additionally, modern techniques such as cross-coupling reactions or C-H activations, as well as the development of various catalytic transformations, make this target-oriented synthesis more efficient compared to classical methods in organic synthesis.

Conclusion

The strain cyclopropene monomer was successfully synthesized, and then it was used for a ring-opening metathesis polymerization reaction. It gives the desired polymer in good yield and low polydispersity. This study will help to build the strategy for the synthesis of polymeric ladderphanes from cyclopropene monomers with low polydiversity. Since the span of each monomeric unit of the polymer derived from cyclopropene is less, it may show strong and better activity and will be helpful in different photophysical studies. This model system creates a conceptual framework for future efforts intended for synthesizing fully conjugated and structurally precise ladderphanes from cyclopropene monomers.

Acknowledgement

The author is thankful to his post-doc supervisor, Prof. T. Y. Luh. He is grateful to Ramnagar College, India for encouraging him. He must express his sincere thanks to Dr. Moumita Gangopadhyay for her continuous support.

References

Alentiev, D. A., & Bermeshev, M. V. (2022). Design and synthesis of porous organic polymeric materials from norbornene derivatives. *Polymer Reviews*, *62*(2), 400-437. https://doi.org/10.1080/15583724.2021.1933026

Allen, F. H. (1982). The geometry of small rings—IV: Molecular geometry of cyclopropene and its derivatives. *Tetrahedron*, *38*(5), 645-655. https://doi.org/10.1016/0040-4020(82)80206-8

Boyd, T. J., & Schrock, R. R. (1999). Sulfonation and epoxidation of substituted polynorbornenes and construction of light-emitting devices. *Macromolecules*, *32*(20), 6608-6618. https://doi.org/10.1021/ma990489k

Elling, B. R., & Neary, W. J. (2026). Strain-Driven Ring-Opening Metathesis Polymerization. *Chemical Reviews*, *126*(7), 4318-4374. https://doi.org/10.1021/acs.chemrev.5c00974

García-Loma, R., & Albéniz, A. C. (2019). Vinylic addition polynorbornene in catalysis. *Asian Journal of Organic Chemistry*, *8*(3), 304-315. https://doi.org/10.1002/ajoc.201800646

Lessard, J. J., Mejia, E. B., Kim, A. J., Zhang, Z., Berkey, M. G., Medina-Barreto, Z. S., ... & Moore, J. S. (2024). Unraveling reactivity differences: room-temperature ring-opening metathesis polymerization (ROMP) versus frontal ROMP. *Journal of the American Chemical Society*, *146*(11), 7216-7221. https://doi.org/10.1021/jacs.4c01578

Lin, N. T., Ke, Y. Z., Satyanarayana, K., Huang, S. L., Lan, Y. K., Yang, H. C., & Luh, T. Y. (2013). On the Stereoselectivity of Ring-Opening Metathesis Polymerization (ROMP) of N-Arylpyrrolidine-Fused Cyclobutenes with Molybdenum–and Ruthenium–Alkylidene Catalyst. *Macromolecules*, *46*(18), 7173-7179. https://doi.org/10.1021/ma401007b

Liu, W., Tai, X., Wang, N., Pang, B., Wu, X., Chen, W., & He, G. (2026). Polynorbornene-Based Anion Exchange Ionomers with Percolated Dual-Domain Ion-Transport Channels. *Industrial & Engineering Chemistry Research*, *65*(22). https://doi.org/10.1021/acs.iecr.6c01233

Luh, T. Y. (2013). Ladderphanes: a new type of duplex polymers. *Accounts of Chemical Research*, *46*(2), 378-389. https://doi.org/10.1021/ar300170b

Luh, T. Y., Xie, M., Ding, L., & Chen, C. H. (2023). Ladderphanes and related ladder polymers. *Ladder Polymers: Synthesis, Properties, Applications, and Perspectives*, 247-284. https://doi.org/10.1002/9783527833306.ch9

Luh, T. Y., Yang, H. C., Lin, N. T., Lin, S. Y., Lee, S. L., & Chen, C. H. (2008). OMCOS for functional polymers-double-stranded DNA-like polymers. *Pure and Applied Chemistry*, *80*(5), 819-829. https://doi.org/10.1351/pac200880050819

Nomura, K., & Jaiyen, K. (2026). Ring-Opening Metathesis Polymerization (ROMP) of cyclic olefins: stereospecific ROMP and precision synthesis of bottlebrush polymers. *Polymer Journal*, 58, 485–509. https://doi.org/10.1038/s41428-025-01129-2

Panda, B. (2018). Small-Ring Metathesis: Delights and Difficulties. *Asian Journal of Organic Chemistry*, *7*(12), 2386-2396. https://doi.org/10.1002/ajoc.201800515

Panda, B. (2019). Total synthesis of xyloketals and related natural product alboatrin: strategies and tactics. *ChemistrySelect*, *4*(31), 9143-9164. https://doi.org/10.1002/slct.201900779

Panda, B., & Sarkar, T. K. (2010). On the catalytic duo PdCl2 (PPh3) 2/AuCl (PPh3) that cannot effect a Sonogashira-type reaction: a correction. *Tetrahedron Letters*, *51*(2), 301-305. https://doi.org/10.1016/j.tetlet.2009.11.003

Panda, B., & Sarkar, T. K. (2013). Gold catalysis: regio-and stereoselective total synthesis of xyloketals D and G and the related natural product alboatrin. *The Journal of Organic Chemistry*, *78*(6), 2413-2421. https://doi.org/10.1021/jo302545n

Peng, J. J., Panda, B., Satyanarayana, K., Yang, H. R., Huang, S. L., Huang, M. J., ... & Luh, T. Y. (2019). Stereospecific Synthesis of Poly (methylene-E-vinylene) by Ring Opening Metathesis Polymerization of Substituted Cyclopropene Using Grubbs Catalysts. *Macromolecules*, *52*(20), 7749-7755. https://doi.org/10.1021/acs.macromol.9b01956

Sheshenev, A. E., Baird, M. S., Croft, A. K., & Bolesov, I. G. (2009). Generation and stereoselective transformations of 3-phenylcyclopropene. *Tetrahedron*, *65*(48), 10036-10046. https://doi.org/10.1016/j.tet.2009.09.098

Singh, R., & Schrock, R. R. (2008). Stereospecific ring-opening metathesis polymerization of 3-methyl-3-phenylcylopropene by molybdenum alkylidene initiators. *Macromolecules*, *41*(9), 2990-2993. https://doi.org/10.1021/ma800280q

Singh, R., Czekelius, C., & Schrock, R. R. (2006). Living ring-opening metathesis polymerization of cyclopropenes. *Macromolecules*, *39*(4), 1316-1317. https://doi.org/10.1021/ma052560u

Sutthasupa, S., Wangngae, S., Khunpiluek, T., Thisan, S., Jarisarapurin, W., Kumphune, S., ... & Chaiwat, W. (2025). Tryptophan-Derived Polynorbornene–Multiwalled Carbon Nanotube Fluorescent Chemosensors for Cu2+ Detection

and Thiol Discrimination. *ACS Applied Polymer Materials*, *7*(16), 10465-10481. https://doi.org/10.1021/acsapm.5c01243

Wang, H. W., Liu, Z. C., Chen, C. H., Lim, T. S., Fann, W., Chao, C. G., ... & Luh, T. Y. (2009). Coherently aligned porphyrin-appended polynorbornenes. *Chemistry–A European Journal*, *15*(23), 5719-5728. https://doi.org/10.1002/chem.200900195

Wang, X., Wilson, T. J., Alentiev, D., Gringolts, M., Finkelshtein, E., Bermeshev, M., & Long, B. K. (2021). Substituted polynorbornene membranes: A modular template for targeted gas separations. *Polymer Chemistry*, *12*(20), 2947-2977.https://doi.org/10.1039/d1py00278c

doi: 10.31674/book.2026cdcbs.006

Complexes Derived from Copper and Nickel Schiff Base and Alkali Metal Salts: Preparation and Antimicrobial Study

Chandan Kumar

Department of Chemistry, Deoghar College, Deoghar, Jharkhand- 814113, India

Corresponding Author's Email: chandankumar78@yahoo.com

Abstract

Complexes derived from Schiff bases received prominent attention because of their specific structure and antimicrobial properties. The preparation and characterization of heterobinuclear alkali metal complexes of copper(II) and nickel(II) Schiff bases are investigated in this study. The Schiff's base has been obtained by condensation of 2-hydroxyacetophenone with ethylenediamine, which is used to prepare binuclear complexes with transition and alkali metals. These complexes are characterized by analytical, spectral and magnetic measurement results. The bondings in the complexes are explained on the basis of spectral studies. The lower conductivity measurement values suggested the non-electrolytic property of the compounds. It is found that the uC-O(phenolic) in infrared spectra shifted to the higher side on complexation, which revealed the dative bond of C-O(phenolic). Ultraviolet spectra specify the d-d transition as well as charge transfer of ligand to metal. The square planar geometry of the complex is explained with the magnetic measurement results. These complexes show considerable positive antimicrobial properties with fungi *S. aureus* and also with bacteria *E. coli* and *C. albicans.*

Keywords: *2-hydroxyacetopheone; Alkali Metal; Antimicrobial Studies; Binuclear Complexes; Ethylenediamine; Schiff Base; Spectra*

Introduction

Schiff bases have a strong ability to generate a large number of metal complexes (Meena *et al.,* 2023) and it deserve commendable attention because of their biological activity (Zoubi, 2013 & Thakur *et al.,* 2024). Several Schiff base complexes have been synthesized, characterized, and studied for antimicrobial activities; they have been found to have antibacterial and antifungal activities (More *et al.,* 2001). The heterobinuclear complexes show antimicrobial properties and they exhibit appreciably more activities in comparison to their parent ligands. In continuation of our earlier works (Prakash *et al.,* 2009; Kumar, 2024), the study of heterobinuclear complexes prepared with copper and nickel Schiff bases is reported here. The Schiff's base was obtained by refluxing ethylenediamine and *o*-hydroxyacetophenone, which form the binuclear complex with transition and alkali metals. The spectral study supported that there is a dative bond between the transition metal and alkali metal complex through the oxygen atom of the phenolic group. These antimicrobial compounds show significant antibacterial and antifungal properties.

Methodology

The chemicals and reagents were of AR grade. Infrared spectra were recorded through the Shimadzu-FTIR spectrophotometer and Perkin Elmer Lambda-UV-visible spectra (Refat *et al.* 2013). Molar conductance was measured through a Systronics conductivity meter. The results of elemental analysis were recorded with the Thermo Fisher Scientific Flash instrument. An electrical melting point apparatus was used to measure the melting point of the compounds.

Methods of Preparation

Schiff base and metal complex as ligand: The Schiff base N,N'-bis(2-hydroxyacetophenone) ethylenediamine (HAPEN) was prepared from 2-hydroxyacetophenone and ethylenediamine through

refluxing them in alcohol in 2:1 molar ratio for 30-60 min. The obtained Schiff base was yellow in color, which was filtered and dried. The Cu(II) complex (CuHAPEN) was prepared by adding copper(II) acetate (2.0g) gradually in a hot alcoholic solution of Schiff base. A deep red copper complex was deposited after cooling, which was filtered and dried. Similarly, brownish orange Ni(II) complex (NiHAPEN) was obtained by mixing nickel(II) acetate tetrahydrate (2.5g) and Schiff base.

Heterobinuclear complexes containing Cu(II) metal and alkali metal: The alcoholic solution of (CuHAPEN]) and alkali metal salts of *o*-nitrophenol was added in 1:1 molar proportion. This mixture was refluxed and stirred for 30-60 min at 75-80^{0}C. The adducts of characteristic colour were precipitated, which was cooled, filtered and dried.

Heterobinuclear complexes containing Ni(II) metal and alkali metal: The alcoholic solution of [NiHAPEN] and alkali metal salts of o-nitrophenol were added in 1:1 molar proportion. This mixture was refluxed and stirred for 30-60 min at 75-80^{0}C. The adducts of characteristic colour were precipitated, which was cooled, filtered and dried.

Results and Discussion

The heterobinuclear alkali metal complexes with formula M_aHAPEN.M_bL, where M_a = Cu(II) or Ni(II), HAPEN = Schiff base of o-hydroxyacetophenone and ethylenediamine, M_bL= Li, Na or K salts of 2-nitrophenol, were synthesized. The Schiff base metal chelates of Cu(II) and Ni(II) and their alkali metal binuclear complexes are powder and stable compounds. All the compounds are generally soluble in acetone, benzene, methanol and DMF, while in water they are insoluble. The elemental analysis results indicated well with the planned formula for the binuclear complexes. Molar conductivities ($\Omega^{-1}cm^2mol^{-1}$) are measured at 30($\pm$0.5)^{0}C at the concentration of 10^{-3}M in DMF. The compounds show lower value of molar conductivity, suggesting their covalent nature (Geary, 1971) (Table 1).

Table 1: Analytical Results of the Complexes

Compounds [M_aEDHAP. M_bL]	Colour	M.P ((^{0}C)	Molar cond.	Elemental analysis (%) Found(cal)					Yield (%)
				C	H	N	M_a	M_b	
CuHAPEN	Deep rose	280	2.7	60.13 (60.42)	4.92 (5.03)	**7**.61 (7.83)	17.59 (17.76)	- -	71.00
CuHAPEN.LiL	Pale rose	282	2.1	57.25 (57.31)	4.31 (4.38)	8.32 (8.36)	12.55 (12.64)	1.37 (1.39)	77.11
CuHAPEN.NaL	Pale rose	285	3.1	55.45 (55.54)	4.21 (4.24)	8.01 (8.10)	12.15 (12.25)	4.41 (4.44)	71.36
CuHAPEN.KL	Pale rose	292	2.6	53.75 53.88)	4.10 (4.12)	7.83 (7.86)	11.80 (11.88)	7.23 (7.30)	79.51
NiHAPEN	Brownish orange	280	4.8	61.05 (61.24)	5.02 (5.10)	7.76 (7.94)	16.56 (16.64)	- -	75.50
NiHAPEN.LiL	Yellowish orange	265	2.4	57.78 57.87)	4.38 (4.42)	8.36 (8.44)	11.76 (11.79)	1.38 (1.41)	74.34
NiHAPEN.NaL	Yellowish orange	>300	2.0	56.00 (56.06)	4.21 (4.28)	8.11 (8.18)	11.39 (11.43)	4.41 (4.48)	74.95
NiHAPEN.KL	Yellowish orange	>300	1.8	54.32 (54.37)	4.11 (4.15)	7.88 (7.93)	11.01 (11.08)	7.33 (7.36)	73.15

Spectra and Magnetic Results:

The IR spectra of heterobinuclear complexes display certain deviations from that of the transition metal complex, as the ligand furnishes information about the nature of bond and structure. The disappearance of sharp absorption peak (3500 cm^{-1}, υ_{OH}) in the complexes indicates the loss of phenolic proton.

Table 2: Spectral and Magnetic Results of Complexes

Compound	Infrared spectra (cm^{-1})			UV-Vis spectra *λ(nm)*	μ_{eff}
	υ(C-O)	υ(M-N)	υ(M-O)		
CuHAPEN	1531	521	490	227, 270, 400, 653	1.50
CuHAPEN.LiL	1537	560	470	228, 266, 347, 653	1.70
CuHAPEN.NaL	1532	562	440	230, 232, 350, 652	1.74
CuHAPEN.KL	1535	550	465	227, 260, 345, 653	1.73
NiHAPEN	1530	518	495	212, 246, 390, 653	Dia.
NiHAPEN.LiL	1590	565	460	207, 261, 384, 653	Dia.
NiHAPEN.NaL	1568	562	465	207, 261, 384, 653	Dia.
NiHAPEN.KL	1565	555	462	214, 280, 389, 653	Dia.

The metal complexes' ligand of transition metal and their binuclear alkali metal complexes show bands in region 1530-1590 cm^{-1} (Table 2). This may be due to stretching frequency of phenolic C-O in complexes rather than that of C=N (El-Sonbati *et al.,* 2012).

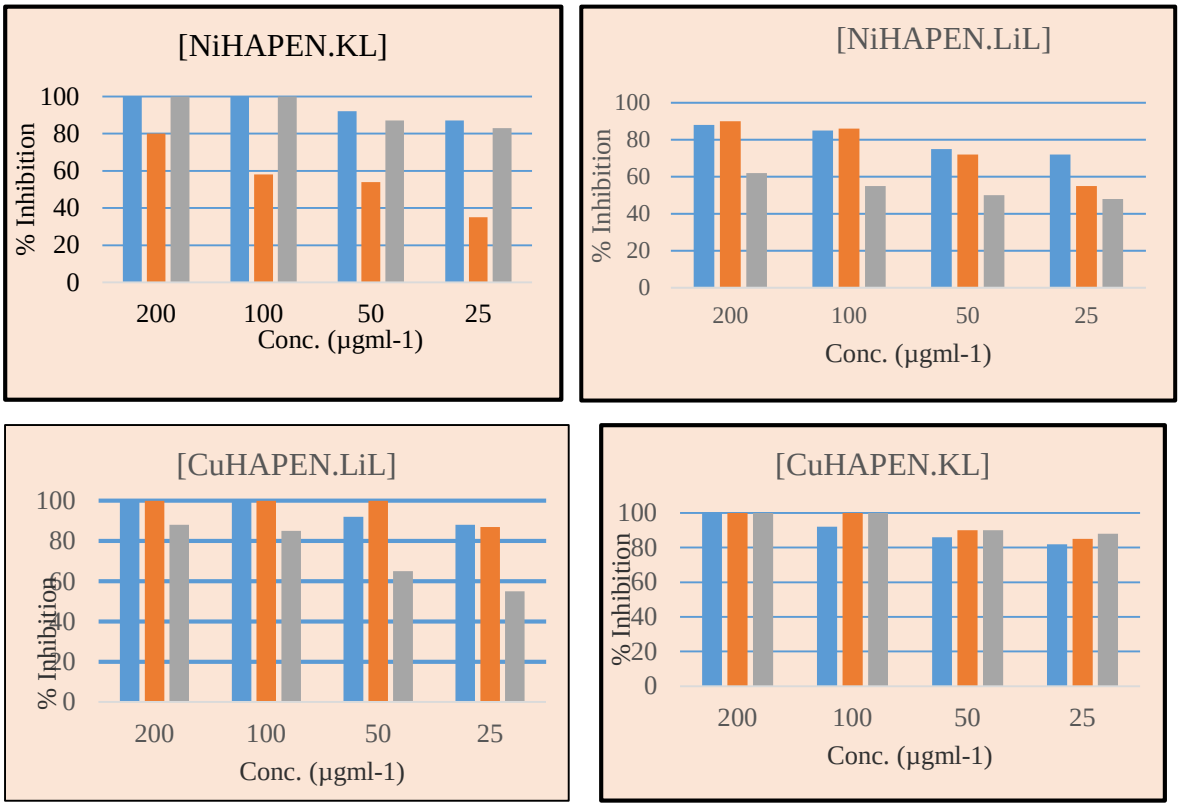

Figure 1: Antimicrobial Activity of Complexes

Comparing the C-O infrared bands of binuclear alkali metal complexes with the metal complex as a ligand, it is found they remain almost near to each other. However, the considerable shifting of C-O frequency of binuclear complex to higher side as compared to the metal complex as a ligand is observed. This is because the ring current arises from delocalized electrons. The shift of around 69 cm^{-1} is found, revealing

the presence of a phenoxy bridge in the compound. The IR bands in the range 440-470 cm^{-1} and 550-565 cm^{-1} of medium intensity in binuclear complexes may be expected due to υ_{M-O} and υ_{M-N} respectively (Nakamoto, 2009 & Kumar *et al.,* 2025). These bands are not found in the transition of metal chelates, while these show at regions 490-495 cm^{-1} and 518-521 cm^{-1}. This result indicated the coordination of phenolic oxygen and nitrogen atoms of $–NO_2$ with alkali metals (Barreras-Contreras *et al.,* 2025).

The electronic spectra absorption at 207-280 nm of compounds indicates a π-π^* transition in aromatic ring as well as due to C=N chromophore. The band of medium intensity at 350-400 nm is due to transfer transition from ligand to metal (Table 2). The bands appearing between ~653 nm in all the complexes indicated a d-d transition (Thirumavalavan *et al.,* 2006; Popov *et al.,* 2023). These results propose that the complexes have square planar geometry with four coordination numbers. The copper complexes show the magnetic moment value (μ_{eff}) 1.5 BM, indicating the presence of one unpaired electron. However, the magnetic moment values of its adducts lie in the range of 1.70 to 1.74 BM. These results revealed the compound has square planar geometry with four coordination numbers The magnetic moment values of NiHAPEN and its binuclear complex show much less value, suggesting the diamagnetic nature and square planar geometry. On the basis of results, the proposed structure of prepared compounds having general formula (M_aHAPEN.M_bL) [where M_a = Cu(II) or Ni(II); M_bL= Li, Na or K salt of 2-nitrophenol] is shown with Fig.1. The complexes have shown significant antimicrobial activity.

Antimicrobial Activity

Antimicrobial activity of some binuclear complexes was examined against bacteria viz. E*. coli*, S*. aureus* and fungi viz. *C. albicans.* The serial dilution method was used at the concentration from 25 to 200 µg ml^{-1} for this test. The results are demonstrated with Table 3 and Fig.2, which indicate that complexes show great degree of activity. It is observed that with concentration the antimicrobial activity of the adduct increases simultaneously. The activities of some of the complexes explained by chelation theory (Panchal & Patel, 2006).

Table 3: Antimicrobial Results of Complexes

Compound	**Conc. (μgml^{-1})**	**Percentage Inhibition**		
		E.coli	*S.aureus*	*C. albicans*
NiHAPEN.KL	200	100	80	100
	100	100	58	100
	50	92	54	87
	25	87	35	83
NiHAPEN.LiL	200	88	90	62
	100	85	86	55
	50	75	72	50
	25	72	55	48
CuHAPEN.LiL	200	100	100	88
	100	100	100	85
	50	92	100	65
	25	88	87	55
CuHAPEN.KL	200	100	100	100
	100	92	100	100
	50	86	90	90
	25	82	85	88

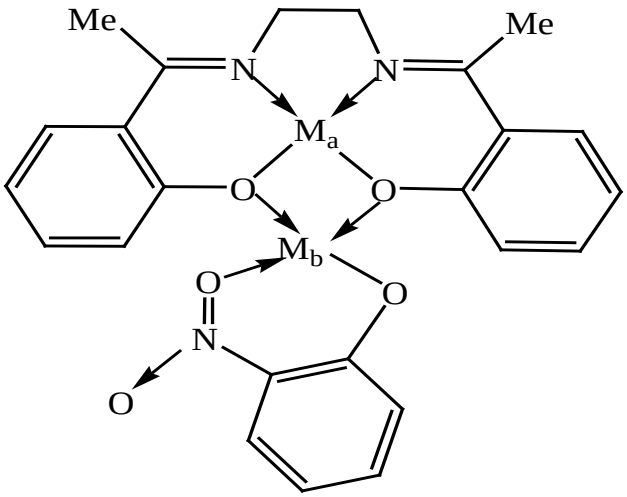

Figure 2: Proposed Structure of Complex

Conclusion

The copper and nickel metal complexes as ligands and their alkali metals were prepared. The characteristics and structure of the compounds are supported by analytical, spectral and magnetic results. They are bonded through a dative bond through two oxygen atoms of the phenolic group. The results are discussed, which indicate that the metal complex as a ligand and its adducts have square planar geometry.

Acknowledgement

The author is thankful to the director, Central Drug Research Institute, Lucknow, India and the head, Department of Chemistry, Banaras Hindu University, Varanasi, India for conducting spectral measurement and magnetic measurement.

References

Al Zoubi, W. (2013). Biological activities of Schiff bases and their complexes: a review of recent works. *International Journal of Organic Chemistry*, *3*(3A), 73-95. https://doi.org/10.4236/ijoc.2013.33A008

Barreras-Contreras, L. A., Moreno-Urbalejo, J., Chávez-Urías, I. F., Plascencia-Martínez, D. F., Hernández-Martínez, D., Velázquez-Contreras, E. F., ... & Rocha-Alonzo, F. (2025). Schiff Bases and Metal Complexes as Multifunctional Platforms: Bridging Bioinorganic Chemistry, Catalysis, Sensing, and Energy Applications. *Bioinorganic Chemistry and Applications*, *2025*(1), 8829417. https://doi.org/10.1155/bca/8829417

El-Sonbati, A. Z., Al-Shihri, A. S., & El-Bindary, A. A. (2004). Stereochemistry of new nitrogen containing heterocyclic aldehyde: Part XI. Novel ligational behaviour of quinoline as chelate ligand toward transition metal ions. *Spectrochimica Acta Part A: Molecular and Biomolecular Spectroscopy*, *60*(8-9), 1763-1768. https://doi.org/10.1016/j.saa.2003.08.026.

Geary, W. J. (1971). The use of conductivity measurements in organic solvents for the characterisation of coordination compounds. *Coordination Chemistry Reviews*, *7*(1), 81-122. https://doi.org/10.1016/S0010-8545(00)80009-0

Kumar, C. (2024). Synthesis, Characterization and Biological activity of Schiff Base Metal (II) Binuclear Complexes with Alkali metal salt of o-Nitrophenol. *Sustainable Chemical Insight in Biological Exploration.* 50-57. https://doi.org/10.31674/book.2024scibe.006

Kumar, M., Singh, A. K., Singh, S., Singh, A. K., Rao, P. K., Yadav, R. K., ... & Tripathi, U. N. (2025). Exploration of iron (III) complexes with bidentate N, O-donor Schiff base ligands through synthesis, characterization, DFT, and antibacterial studies. *Journal of Molecular Structure*, *1319*(2), 139496. https://doi.org/10.1016/j.molstruc.2024.139496

Meena, R., Meena, P., Kumari, A., Sharma, N., & Fahmi, N. (2023). Schiff Bases and Their Metal Complexes: Synthesis, Structural Characteristics and Applications. In *Schiff Base in Organic, Inorganic and Physical Chemistry.* 47-70. https://doi.org/10.5772/intechopen.108396

More, P. G., Bhalvankar, R. B., & Pattar, S. C. (2001). Synthesis and biological activity of Schiff bases of aminothiazoles. *Journal of the Indian Chemical Society*, *78*(9), 474-475. Nakamoto, K. (2009). *Infrared and Raman spectra of inorganic and coordination compounds, part B: applications in coordination, organometallic, and bioinorganic chemistry*. John Wiley & Sons.

Panchal, P. K., & Patel, M. N. (2006). Synthesis, spectroscopy, and antibacterial activity of some transition metal complexes with tridentate (ONS) and bidentate (NN) donor Schiff bases. *Pharmaceutical Chemistry Journal*, *40*(10), 544-548. https://doi.org/10.1007/s11094-006-0189-1

Popov, I., Raenko, D., Tchougréeff, A., & Besley, E. (2023). Electronic structure and d–d spectrum of metal–organic frameworks with transition-metal ions. *The Journal of Physical Chemistry C*, *127*(44), 21749-21757. https://doi.org/10.1021/acs.jpcc.3c05025

Prakash, D., Kumar, C., Prakash, S., Gupta, A. K., & Singh, K. R. R. P. (2009). Synthesis, spectral characterization and antimicrobial studies of some new binuclear complexes of CuII and NiII Schiff base. *Journal of the Indian Chemical Society*, *86*(12), 1257-1261. https://doi.org/10.5281/zenodo.5823781

Refat, M. S., El-Deen, I. M., Zein, M. A., Adam, A. M. A., & Kobeasy, M. I. (2013). Spectroscopic, structural and electrical conductivity studies of Co (II), Ni (II) and Cu (II) complexes derived from 4-acetylpyridine with thiosemicarbazide. *International Journal of Electrochemical Science*, *8*(7), 9894-9917. https://doi.org/10.1016/S1452-3981(23)13021-5

Thakur, S., Jaryal, A., & Bhalla, A. (2024). Recent advances in biological and medicinal profile of schiff bases and their metal complexes: An updated version (2018–2023). *Results in Chemistry*, *7*, 101350. https://doi.org/10.1016/j.rechem.2024.101350

Thirumavalavan, M., Akilan, P., & Kandaswamy, M. (2006). Synthesis of heterobinuclear Cu (II) Zn (II) complexes derived from lateral macrobicyclic tricompartmental ligands: Spectral, electrochemical and kinetic studies. *Polyhedron*, *25*(13), 2623-2628. https://doi.org/10.1016/j.poly.2006.03.018

doi: 10.31674/book.2026cdcbs.007

Oxidation of Hydroxylamine by a Tetranuclear Manganese Complex in Aqueous Acidic Medium– Proton Coupled Electron Transfer

Suranjana Chatterjee

Department of Chemistry, Ananda Mohan College, Kolkata-700009, India

Corresponding Author's Email: ranjanasur@yahoo.com

Abstract

Hydroxylamine and its mono protonated conjugate acid form are both quantitatively oxidized to nitrous oxide by a quadrinuclear tetravalent manganese complex $[Mn_4(\mu\text{-}O)_6(bipy)_6]^{4+}$ (1, bipy = 2,2′-bipyridine) and its conjugate acid form $[Mn_4(\mu\text{-}O)_5(\mu\text{-}OH)(bipy)_6]^{5+}$ ($1H^+$) in water in the pH range of 2.0-6.0. NH_2OH and its conjugate acid NH_3OH^+ are the active reducing agents, which are oxidized into N(+I) state. As usual, the oxo-bridge protonated metallic oxidant **1H⁺** reacts at a faster rate than **1**. An aqueous solution of complex **1** shows extreme stability over a wide pH range and no ligand dissociation equilibria are monitored in its solution, irrespective of different conditions like varying ligand or reducing agent concentrations. The reaction exhibits noticable kinetic isotope effect by decreasing the reaction rate in D_2O media. A Hydrogen Atom Transfer (HAT), i.e., one electron and one proton (1e, $1H^+$; electroprotic) transaction, is suitable to elaborate the isotope effect.

Keywords: *Hydroxylamine; Isotope Effect; Kinetics; Manganese*

Introduction

Dioxygen evolved in green biosystems by the process of photosynthesis in presence of a higher valent multinuclear manganese complex termed as oxygen evolving complex (OEC) which is usually structured by a set of three or four manganese atoms coordinated to each other (Kirby *et al.*, 1981; McEvoy & Brudvig, 2004). During the process of oxygen evolution, this Mn tetramer smoothly transitions between five separate oxidation levels, demarked as $S_0 – S_4$ as we came to know in the groundbreaking work of Kok *et al.* (1970) involving di to tetra valency of metal (Dekker *et al.*, 1984). The metal ions in the reactive core are formed by di-μ-oxo units, which may be either oxo or carboxylate linkage. The targeted oxidant $[Mn_4(\mu\text{-}O)_6(bipy)_6]^{4+}$ (**1**, Figure 1, bipy = 2,2′-bipyridine) of title kinetic investigation is structurally identical to the model proposed by OEC (Yachandra *et al.*, 1993). Generated one-electron reduced complex, which is a mixture of two Mn atoms at different oxidation states, ($Mn^{IV}{}_3Mn^{III}$) structurally parallel to EPR-spectral model for the S_2 state of the OEC (Philouze *et al.*, 1994).

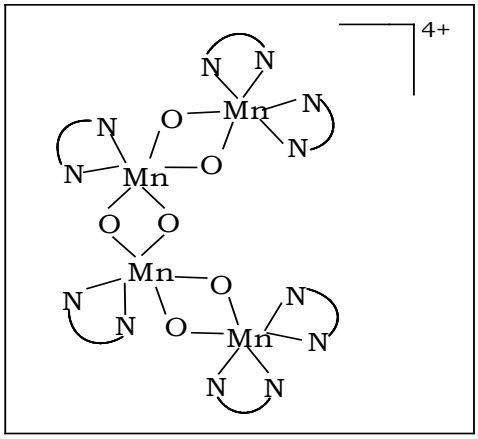

Figure 1: Structural Framework $[Mn_4(\mu\text{-}O)_6(bipy)_6]^{4+}$ is 2,2'-bipyridine

It is previously reported in the study that the chosen reducing agent, hydroxylamine (NH_2OH), acts as a reducing agent of the Manganese ions of OEC in PS II (Beck & Brudvig, 1987). The bond dissociation energy values of N–H bond in NH_2OH (92 kcal $mole^{-1}$) and O–H bond in tyrosine attached to the OEC are very close to each other (Blomberg *et al.*, 1997). Therefore, it is interesting to study the NH_2OH reduction where it can be compared with tyrosine for the mechanism of proton coupled electron transfer, like tyrosine activity in PS II. With reference to the activity of tyrosine in PS II, the oxidation-reduction study of this title work will be worthy enough for creating a clear perception of electron transfer mechanism in PS II.

Experimental

Materials

Target oxidant is prepared in pure crystalline form with molecular formula $[Mn_4(\mu\text{-}O)_6(bipy)_6](ClO_4)_4.2H_2O$ (**1**) according to the reported method (Philouze *et al.*, 1994). The complex makes a clear transparent solution in water, and the spectral patterns of these solutions remain unchanged for a long period of time over a wide pH range up to pH 6.0. Pure Hydroxylamine nitrate was prepared in situ by double decomposition of hydroxylamine sulphate (G. R., E. Merck) with barium nitrate (G. R., E. Merck) and purity of the reductant is checked by oxidation with $KBrO_3$ in dilute H_2SO_4 medium (Jeffery, 1989). The strength of the stock solutions remains unaltered for long period of time when kept at ~10 °C.

$NaNO_3$ solution was standardized by a common acid-based titration and for this purpose, it was passed through a Dowex cation-exchange resin (in acid form) and the acidic eluate was estimated by an acid base titration reaction using standard sodium hydroxide solution and phenolphthalein as indicator. Solid 2,2′-bipyridine of G. R., E. Merck, was purchased and used in the process. D_2O (99.9 atom % D) and DNO_3 (99+ atom % D) were used in the experiment and purchased from Sigma. Used other chemicals and reagents were of reagent grade quality. Doubly distilled deionized water was useful for the depicted reaction setup.

Equilibrium Measurements

Acid dissociation constants (K_a) of the reductant NH_3OH^+ cation in 95% D_2O media were determined by pH-metric titration using a Metrohm 736-GP-Titrino autotitrator at I = 1.0 M ($NaNO_3$) at 25°C. The reported pK_a value (Lumme *et al.*, 1965) in H_2O media for NH_3OH^+ cation was used. Same type of pH metric titration was executed several times in the working pH range of the reaction to evaluate any pK_a value for the protonation of oxo-bridges of Mn tetramer.

Stoichiometric Measurements

Stoichiometry of the title reaction was resolute in both kinetic (when reagent concentration is more than the complex concentration) and non-kinetic situations (when complex is more than the reagent in same volume). Solutions for kinetic study used 8 – 15 times more hydroxylamine than the colored Manganese tetramer for a complete reaction and ended up without any visible color (absorbance at 420 nm was less than 0.01). In this reaction setup, unused N(-I) was determined by a titration procedure with standard $KBrO_3$, where Mn^{II}, bipy and ClO_4^- had no interference. Existence of nitrite or nitrate anions as the oxidation product was nullified after testing the coupling reaction of sulfanilic acid and α-naphthylamine where no characteristic red azo dye was reported.

Complexometric EDTA-EBT (at pH 10) titration method was deployed to measure the exact amount of Mn^{2+} ions formed after the complete reduction of the tetravalent complex.

It was also tested that no interferences were noted by any other reaction components existing in the solution. In non-kinetic situation, less than stoichiometric amount of measured hydroxylamine was allowed to react with the complex at similar reaction condition and after a finite time gap, the absorbance value of

unreacted complex from the equilibrated reaction mixtures was monitored at 420 nm (ε=7.5×10^3 M^{-1} cm^{-1}) to calculate the unreacted quantity of tetramer that remains.

Physical Measurements and Kinetics

All physical parameters, like absorbances and spectra of the described reaction, were recorded with a Shimadzu (1601 PC) spectrophotometer using 1.00 cm quartz cells. The kinetics were monitored *in situ* with the instrument in "kinetic mode" at 420 nm in an electrically controlled thermostated 25.0 (±0.1) °C cell housing (CPS –240 A).

A Shimadzu (1601 PC) spectrophotometer with 1.00 cm quartz cells was utilized to follow the described kinetics spectrophotometrically. The machine worked in thermostated mode at 25.0 (±0.1) °C. Apart from the Mn(IV) tetramer no other substance absorbs any radiation in the 420 nm range. The medium ionic strength was usually fixed at 1.0 M with Sodium nitrate. Excess (range 1 – 80 mM) bipy concentration, (C_{bipy} = [(Hbipy)$^+$] + [bipy]) maintained in all the kinetics serves the roll of a good buffer in the reactions medium. It was possible that the hydroxylamine cation could act as an additional buffering agent with the excess ligand bipy. NH_3OH^+ (pK_a = 6.00) would impart its buffering action at higher pH extremes. The pH of the reacting solutions was watched at both initiation and ending of every set by using an Orion – Ross combined-electrode system -model 81-02. Calibration of the pH meter was performed with standard HNO_3 solutions, also maintaining a medium unit molar ionic strength with sodium nitrate. Accurate comparison of kinetic studies in similar pH in D_2O media and in H_2O media was done by selecting solutions with a 0.4-unit higher value of pH in dauterated environment than that in aqueous medium (Covington *et al.*, 1966). To maintain first-order kinetics, concentration of the reducing agent keeps high throughout, and the rate constants (k_0) were calculated by using the techniques of least square slopes of $\log_{10}$(abs) *vers*us time plots. Rate measurements were usually done at 25.0 ^{o}C and at I = 1.0 M ($NaNO_3$) unless stated specifically.

Results and Discussion

Equilibrium Measurements

The pK_a values of the title acid N(-I) in a 95% deuterated media and in aqueous media are found to be 6.40 ± 0.10 and 6.00 ± 0.20 respectively, at 25.0 ^{o}C and at I = 1.0 M ($NaNO_3$). Numerous projects were carried out to discover any sort of value of protonation constant for the oxo bridges of the title compound during the reaction conditions. Title oxidant does not exhibit any proper numerical value of protonation or ionization in the reaction condition.

Stoichiometric Measurements

The described kinetics resulted in the following stoichiometry, i.e., $\triangle[Mn^{IV}_4]/\triangle[T_R]$ = 0.25 ± 0.03 and T_R = [N(-I)] = [NH_2OH] + [NH_3OH^+]. Tetramer quantitatively reduced into Mn^{II} state as revealed from EDTA titration and exists as a stable Mn^{II}- bipy complex. Formation of Mn^{II}- bipy complex is supported by the study of optical spectra. In similar conditions, a mixture of manganese nitrate and 2,2'-bipyridine generates similar spectral patterns, like reaction product solutions. All the above findings guided to equation (1).

$$[Mn_4O_6(bipy)_6]^{4+} + 4NH_2OH + 4H^+ \longrightarrow 4Mn^{2+} + 2N_2O + 6bipy + 8H_2O \quad (1)$$

Kinetics

The above-described reaction process in kinetic situation obeys a good first order reaction mechanism for up to a minimum of four half-lives. Kinetic pathways of reduction of colored compounds are tracked spectrophotometrically in the range of 380 nm to 500 nm wavelengths. Facts and findings revealed that the first order reaction kinetics are independent of the selected wavelength. Each k_0 value reported is an

average value of three self-reliant resolutions when the individuals rate constant having maximum of 3% the coefficients of variation (CV). The first order rate constants are determined from the slope of straight-line fitting graph of $\log_{10}$(absorbance) *versus* time plots. For title redox k_0 increase with an increase in pH but this trend is just reversed at high acidic region. The reaction rates remain unaltered with the variation of concentration of additional free bipyridine ligand (3 – 80 mM) which clearly precluded the prospect of any sort of equilibrium of the complex which set free bipy ligand from compound to the solution. The described kinetics highly displays first-order relation with the total concentration of the reducing species throughout the pH range it studied. The experimentally derived rate constants are unaltered by the switching of compound concentration in varied concentration, like 0.05 – 0.2 mM or presence or absence of ambient light in the reaction medium. The effect of increasing ionic strength of the medium increases the oxidation rate significantly at lower pH regions, *ca*. at pH 2.1 or 3.6, indicating the reaction between similarly charged species. Whereas the first-order rates remain unchanged during ionic strength variation when the oxidation reaction is carried out in higher pH (~ 5 - 6) region.

Table 1: Some Illustrative Data Representing First-Order Rate Constants of the Described Kinetics

pH	T_R, M	C_{bipy}, mM	$10^4 k_0$, s^{-1}
2.04	0.01	5.0	3.60 (3.58)
2.37	0.01	5.0	1.95 (1.92)
3.02	0.01	5.0	0.79 (0.84)
3.20	0.01	5.0	0.73 (0.76)
3.42	0.01	5.0	0.74 (0.74)
4.00	0.01	5.0	1.19 (1.12)
4.41	0.01	5.0	1.98 (2.10)
4.84	0.01	5.0	4.52 (4.69)
5.35	0.01	5.0	12.2 (12.4)
6.00	0.01	5.0	32.0 (32.2)
3.61	0.02	5.0	1.51 (1.58)
3.62	0.04	5.0	3.23 (3.18)
3.61	0.10	5.0	7.79 (7.90)
4.11	0.01	1.0	1.21 (1.30)
4.10	0.01	10	1.23 (1.28)
4.13	0.01	20	1.29 (1.34)
4.12	0.01	40	1.37 (1.32)
4.12	0.01	60	1.42 (1.32)
5.95	0.01	5.0	30.1[a]
5.93	0.01	5.0	30.5[b]
2.11	0.01	5.0	2.61[a]
2.12	0.01	5.0	2.08[b]
3.60	0.01	5.0	1.22[a]
3.62	0.01	5.0	1.05[b]

[a] I = 0.5 M ($NaNO_3$). [b] I = 0.1 M ($NaNO_3$).

[Mn^4] = (0.10 mM) at Temp = 25.0 °C, I = 1.0 M ($NaNO_3$). Values within the parenthesis are back calculated k_0 values using published rate constants of Table 2 in equation (9).

The observed k_0 vs. pH graph of the aforesaid reaction may be best illustrated and rationalized by strategy described below. Described proton dependent equilibrium in equation (2) and in equation (3) plays a major role for observed kinetics. Here RH signifies protonated form of reducing agent (NH_3OH^+) and R^- represents NH_2OH.

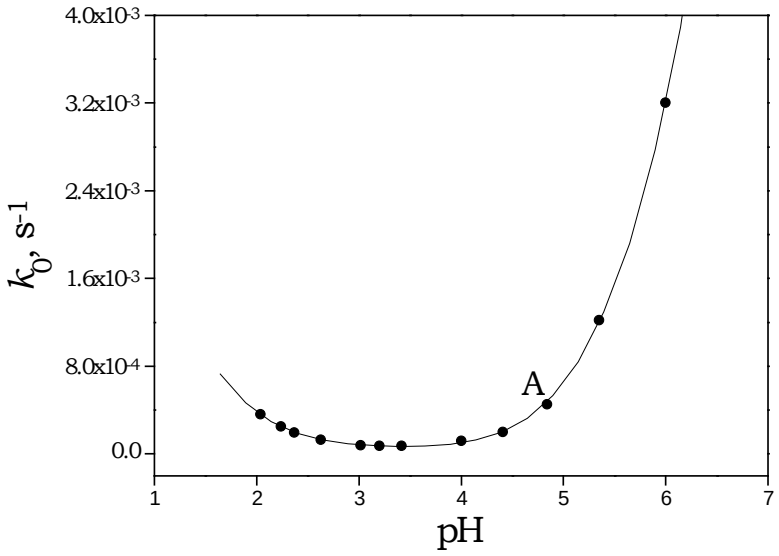

Figure 2: Plotting of k_0 versus $[H^+]$. $[Mn_4]$ = 0.10 mM, Temp = 25.0 ℃ , I = 1.0 M ($NaNO_3$), [bipy] = 3.0 mM

$$RH \rightleftharpoons[K_a] R^- + H^+ \quad (2)$$

$$\mathbf{1} + H^+ \rightleftharpoons[K_1] \mathbf{1}H^+ \quad (3)$$

$$\mathbf{1}H^+ + RH \xrightarrow{k_1} \text{Products} \quad (4)$$

$$\mathbf{1}H^+ + R^- \xrightarrow{k_2} \text{Products} \quad (5)$$

$$\mathbf{1} + RH \xrightarrow{k_3} \text{Products} \quad (6)$$

$$\mathbf{1} + R^- \xrightarrow{k_4} \text{Products} \quad (7)$$

Scheme 1

Scheme 1 Leads to the Rate Law Equation (8)

$$k_0(1 + K_1[H^+])(K_a + [H^+])/T_R = k_1K_1[H^+]^2 + (k_2K_1K_a + k_3)[H^+] + k_4K_a \quad (8)$$

K_1 is the protonation constant of complex **1**, the protonation occurs at the oxo-bridge of the oxidant. Several attempts have been made to evaluate the protonation constant of the title oxidant in our working pH range. Also, no pK_a value was obtained from the pH-meric titration of the complex solution, indicating very weak basic nature of the oxo-bridges in water solution. Available literature reports on study over a numerous multicore higher valent Mn complex (Thorp, 1989) suggest very weak basic nature of the oxo-bridges in aqueous medium. Hence, from all the above information we may assume that in our system $K_1[H^+] << 1$. The maximum concentration of H^+ used in our study is of order of 10^{-2}. Therefore, $(K_1)_{max}10^{-2} << 1$, i.e., $(K_1)_{max} << 10^2$, so $(K_1)_{max} \leq 10$, i.e., upper limit of K_1 is nearly at 10. Now, applying the assumption $K_1[H^+] << 1$, the equation (8) is simplified and takes the form described in equation (9).

$$k_0(K_a + [H^+])/T_R = k_1K_1[H^+]^2 + (k_2K_1K_a + k_3)[H^+] + k_4K_a \quad (9)$$

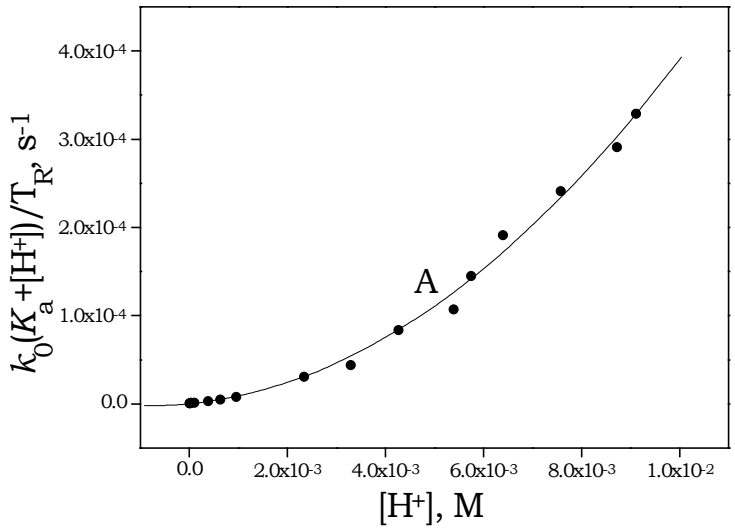

Figure 3: LHS of eqn. (9) vs. [H⁺]. [Mn₄] = 0.10 mM, Temp=25.0 ℃, I=1.0 M(NaNO₃), [bipy]=3.0 mM

LHS of eqn. 9 is drawn on y-axis of a graph w.r.t. Hydrogen ion concentration on x-axis ended up with a nicely fitted polynomial curve representing the title kinetics (Figure 3, $r > 0.98$). Solving the fit composite or single rate constants is reported (Table 2). Recalculation of first order rate constants is executed with the data exhibited in Table 2. Recalculated values have very small deviations (within 7%) from the values noted experimentally. Similar treatments are pursued with the first order rate constants acquired when the kinetics are carried in D_2O medium and enlisted in Table 2.

Table 2: Representation of Rate Parameters for the Title Reaction

Reaction Path	k_1K_1 ($M^{-2}\,s^{-1}$)	($k_2K_1K_a + k_3$) ($M^{-1}\,s^{-1}$)	k_4 ($M^{-1}\,s^{-1}$)
H_2O medium	3.43 ± 0.20	$(4.4 \pm 0.3) \times 10^{-3}$	$(6.6 \pm 0.4) \times 10^{-1}$
95% D_2O medium	0.65 ± 0.04	$(1.9 \pm 0.1) \times 10^{-4}$	$(5.5 \pm 0.3) \times 10^{-2}$

Note: Conditions are similar like Table 1

For hydroxylamine reaction, k_4 pathway was found to be significant above a pH about 4. k_4 path effectively contributes to the observed first-order rate constants as judged by the relative contributions of the $k_1K_1[H^+]^2$ and $(k_2K_1K_a + k_3)[H^+]$ and k_4K_a values towards the noticed rate and at pH greater than or equal to 5.3, only k_4 path is enough to describe the overall kinetics. So, at higher pH ($pH \geq 5.3$) the right-hand side of the equation (9) contains only k_4K_a term and rearranges accordingly to give equation (10).

$$k_0(K_a + [H^+])/T_R = k_4K_a$$
$$T_R/k_0 = 1/k_4 + [H^+]/k_4K_a \qquad (10)$$

A plot of T_R/k_0 *versus* $[H^+]$ was found to be a good straight line (Figure 4) whence the value of k_4 was evaluated from the slope [k_4 = 1/(K_a.slope)] and the intercept (k_4 = 1/intercept) of the graphical plotting depicted in Figure 4 and are listed in Table 3, which match well with the values reported in Table 2.

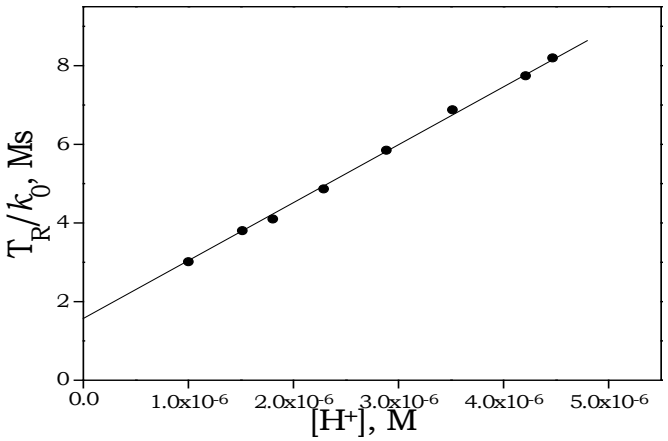

Figure 4: Plot of T_R/k_0 versus $[H^+]$. [1] = 0.10 mM, Temp = 25.0 °C, I = 1.0 M ($NaNO_3$)

Table 3: Comparison of the Value of the Second-Order Rate Constant (k_4).

k_4 from Slope ($M^{-1} s^{-1}$) pH ≥ 5.3	k_4 from Intercept ($M^{-1} s^{-1}$) pH ≥ 5.3	k_4 from Table 2 ($M^{-1} s^{-1}$) pH = 2.0 – 6.0
$(6.7 \pm 0.4) \times 10^{-1}$	$(6.6 \pm 0.4) \times 10^{-1}$	$(6.6 \pm 0.4) \times 10^{-1}$

Value obtained from non-identical situation for the reduction of **1** by N(-I) at [bipy]=5.0 mM, Temp=25.0°C, I = 1.0 M ($NaNO_3$).

Therefore, from Table 3, it can be concluded that the k_4 path alone is enough to guide effectively the overall reaction at pH ≥ 5.3, as concluded from the relative contributions of the $k_1K_1[H^+]^2$, $(k_2K_1K_a + k_3)[H^+]$ and k_4K_a values towards the observed rate.

NH_3OH^+ cation is the main prevalent form of NH_2OH at high acidic zones, like pH less than 3, whose oxidation by $\mathbf{1}H^+$ is electrostatically more unfavorable than the oxidation of NH_2OH. Oxidation of cationic NH_3OH^+ requires higher concentrations of $\mathbf{1}H^+$, which are produced at much lower pH.

In title redox reactions, the rate of the redox process drops down noticeably with decrease of ionic strength of the reactive solution towards lower pH range, *ca*. at pH 2.1 or 3.6 where $[NH_3OH^+] >> [NH_2OH]$ i.e., the reaction between similarly charged species. But the first-order rates are unchanged during ionic strength variation when the N(-I) oxidation reaction is carried out in higher pH (~ 5 - 6) region (where $[NH_2OH] > [NH_3OH^+]$).

From Table 2, it is concluded that highest limit for k_3 pathway (where form **1** reacts with acidic reductant) will be 4.4×10^{-3} $M^{-1} s^{-1}$ for N(-I) redox. For NH_2OH oxidation $(k_3)_{max} << k_4$ indicating superior reactivity of NH_2OH as the reactivity goes up with increasing pH, only at very low pH (~ 2 – 3) the rate increases with increasing acidity due to high activity of the additional cationic oxidizing agent-$\mathbf{1}H^+$ over the **1**. To draw out the whole redox process, the formidable supremacy of $\mathbf{1}H^+$ is established. Initially it is assumed that $K_1[H^+]$ is lower in value than 1, and this puts up a higher value for the K_1 almost to 10. As it is considered that rate of diffusion-controlled reaction is 10^{11} $M^{-1} s^{-1}$, then the minimum value of K_1 estimated from the k_1K_1 value tabulated in Table 2 is of the order of 10^{-9}.

Mechanism

Tittle reaction process deals with altogether eight electronic transfers, but not through an individual process, rather through multistep electron transfer.

In spectral investigation no immediate changes in the pattern of reactants were observed in the reaction condition. Also, throughout the reaction, the rate constant, k_0 varies linearly with the total concentration of hydroxylamine, proposing the generation of a weak adduct between both the reagents. The electrochemistry of $[Mn_4(\mu\text{-}O)_6(bipy)_6]^{4+}$ has been comprehensively observed by Dunand-Sauthier *et al.* (1997, 1998, 1999). Complex **1** is electrochemically converted into a mixed valent binuclear $[Mn^{III,IV}_2(\mu\text{-}O_2)(bipy)_4]^{3+}$ and uninuclear $[Mn^{II}(bipy)_3]^{2+}$ systems and *vice versa*. A study in HNO_3 media at pH around 2 converted the compound electrochemically into divalent Manganese ion.

Isolation of the mono reduced form $[Mn^{IV}_3Mn^{III}(\mu\text{-}O)_6(bipy)_6]^{3+}$ by general inorganic reducing method is quite impossible. From the work of Blondin *et al.* (1997), the one electron reduced complex was accumulated with very high chemical reactivity by the method of cryogenic radiolytic reduction of mother complex. This single reduced form is even very much unstable at lower temperatures, like 190K. From the above discussion it can be concluded that the tetrameric complex is not a powerful oxidant. The overall process of reducing tetramer Mn^{IV} to Mn^{II} is a smooth transition, but initially mono electronic transfer to generate the mixed valent tetramer is not an energy-smooth active process. In the whole redox process (equations 4 – 7), assuming initial one electron donation process is the rate limiting step that generate the active internal form $[Mn^{IV}_3Mn^{III}(\mu\text{-}O)_6(bipy)_6]^{3+}$, it is again converted to ultimate format in a very fast process with help of extra reductant components or with the generated radicals at the RDS. No evidence of polymerization was noted during the studied reaction of tetramer and reductant when it was carried out in a 6% v/v acrylonitrile solution; still, it can't rule out the situation of radical production.

It may happen that generated radical reacts with the mono reduced Mn tetramer at a much faster rate compared to the polymerization reaction. The mono reduced components of oxidant or protonated oxidant will have oxo-bridges of highly basic nature, as a result, it immediately abstracts a proton from the reaction solution, and this removes thermodynamic or kinetic barricades for subsequent reduction to final state (Baldwin & Pecoraro, 1996; Vrettos *et al.*, 2001). It is one of the main characteristics involved in the reduction process of the Kok cycle in PS II (Renger, 2004).

Radicals generated after mono electronic oxidation of hydroxylamine, i.e., NH_2OH^+ are listed and its mechanistic approach leading to the production of nitrous oxide is well documented in nitrogen chemistry. Reaction of hydroxylamine is carried out in D_2O media (95%) and treated further in exactly the similar way to that in aqueous medium for further verification of the electron transfer procedure. Described redox is an outstanding example of kinetic isotope effect. The overall reaction rate for N(-I) oxidation decreases when it is executed in 95% D_2O medium compared to the rate observed in aqueous media. Electroprotic mechanism is established by diminishing of reaction rates in medium concentrated with D_2O. It was found that diminishing rates in H_2O/D_2O mix medium are directly proportional ($r > 0.98$) with the amount of D_2O present, indicating the one electron movement of a proton at the slow RDS.

In practice it was observed that acidic power decreases in D_2O media (Wiberg, 1955; Ghosh *et al.*, 2002) and it is observed that pK_a's of many reducing weak acids noticeably increased in D_2O medium, like glyoxylic, pyruvic (Das *et al.*, 2006), nitrous (Das & Mukhopadhyay, 2007) and hydroxylammonium cation. It can be concluded that for the oxidant the protonation constant (K_1) also increases in D_2O medium; it implies that concentration of $\mathbf{1}H^+$ is more in D_2O medium compared to H_2O medium in similar conditions. These redox reactions may be an example of a secondary isotope effect, as in the moment of isotope replacement, no oxygen bonded to H/D is formed or ruptured during RDS., suggesting a strong bonding association of isotopes via H-bond in the intermediate structure. This experimental fact again supports the existence of postulated hydrogen-bonding network in the OEC. In the observed oxidation, all the second order rate constants decrease in D_2O media. Decreased k_1 outweighs the increment of K_1, hence slowing down the N(-I) redox. Numerical value of K_a in deuterated medium is reduced compared to its valuation in

H_2O and this again drops the value of combined rate constants ($k_2K_1K_a + k_3$) value in deuterated media. Both NH_2OH and NH_3OH^+ are reacting with the title oxidizing agent.

The molecular mechanics generated organization of the oxygen-evolving complex points out well systematic array of hydrogen bonding frameworks in the vicinity of the OEC moiety (Jeans *et al.*, 2002); these title redox tries to provide a clear look on the transfer of proton and water in the active position.

Conclusion

Existence of a hydrogen cation in chosen reductant may be one of the reasons for the described redox activity. Also, HAT mechanism operated from the hydroxylamine to generate radical $NHOH^{\cdot}$ and mono-reduced multivalent $Mn^{IV}{}_3Mn^{III}$ tetramer attached with a proton on its oxo bridges. In general, protonated oxidant **1**H^+ is expected to be more kinetically reactive in oxidizing the hydroxylamine than **1**. This higher oxidizing nature of **1**H^+ is predicted due to the very swift transaction of hydrogen or hydrogen ions throughout the structured H-bonding network created by combination of oxo-bridges in the center of the protonated metal core with the oxygen and hydrogen atoms of the reductant.

Acknowledgment

The author is thankful to the higher authorities of Ananda Mohan College, Kolkata, India, for their continuous support.

Reference

Baldwin, M. J., & Pecoraro, V. L. (1996). Energetics of proton-coupled electron transfer in high-valent Mn2 (μ-O) 2 systems: Models for water oxidation by the oxygen-evolving complex of photosystem II. *Journal of the American Chemical Society*, *118*(45), 11325-11326. https://doi.org/10.1021/ja9626906

Beck, W. F., & Brudvig, G. W. (1987). Reactions of hydroxylamine with the electron-donor side of photosystem II. *Biochemistry*, *26*(25), 8285-8295. https://doi.org/10.1021/bi00399a040

Blomberg, M. R., Siegbahn, P. E., Styring, S., Babcock, G. T., Åkermark, B., & Korall, P. (1997). A quantum chemical study of hydrogen abstraction from manganese-coordinated water by a tyrosyl radical: a model for water oxidation in Photosystem II. *Journal of the American Chemical Society*, *119*(35), 8285-8292. https://doi.org/10.1021/ja9642323

Blondin, G., Davydov, R., Philouze, C., Charlot, M. F., Åkermark, B., Girerd, J. J., & Boussac, A. (1997). Electron paramagnetic resonance study of the S= ½ ground state of a radiolysis-generated manganese (III)–trimanganese (IV) form of [Mn IV 4 O 6 (bipy) 6] 4+(bipy= 2, 2′-bipyridine). Comparison with the photosynthetic Oxygen Evolving Complex. *Journal of the Chemical Society, Dalton Transactions*, (21), 4069-4074. https://doi.org/10.1039/A703381H

Covington, A. K., Robinson, R. A., & Bates, R. G. (1966). The ionization constant of deuterium oxide from 5 to 50. *The Journal of Physical Chemistry*, *70*(12), 3820-3824. https://doi.org/10.1021/j100884a011

Das, S., & Mukhopadhyay, S. (2007). Mechanistic studies on oxidation of nitrite by a {Mn 3 O 4} 4+ core in aqueous acidic media. *Dalton Transactions*, (22), 2321-2327. https://doi.org/10.1039/B702740K

Das, S., Bhattacharyya, J., & Mukhopadhyay, S. (2006). Mechanistic Studies on the Oxidation of Glyoxylic and Pyruvic Acid by a [Mn4O6] 4+ Core in Aqueous Media: Kinetics of Oxo-Bridge Protonation. *Helvetica Chimica Acta*, *89*(9), 1947-1958. https://doi.org/10.1002/hlca.200690186

Dekker, J. P., Van Gorkom, H. J., Wensink, J., & Ouwehand, L. (1984). Absorbance difference spectra of the successive redox states of the oxygen-evolving apparatus of photosynthesis. *Biochimica et Biophysica Acta (BBA)-Bioenergetics*, *767*(1), 1-9. https://doi.org/10.1016/0005-2728(84)90073-2

Dunand-Sauthier, M. N. C., Deronzier, A., & Piron, A. (1999). Electrochemical behaviour of [Mn2III, IVO2 (phen) 4] 3+ complex in aqueous phen+ phenH+ buffer; phen= 1, 10-phenanthroline. *Journal of Electroanalytical Chemistry*, *463*(1), 119-122. https://doi.org/10.1016/S0022-0728(98)00429-X

Dunand-Sauthier, M. N. C., Deronzier, A., Piron, A., Pradon, X., & Ménage, S. (1998). New Chemical and Electrochemical Synthesis of the [Mn 4 IV O 6 (bpy) 6] 4+ Cluster. Electrochemical Interconversion with Corresponding

Bi-and Mononuclear Complexes. *Journal of the American Chemical Society*, *120*(22), 5373-5380. https://doi.org/10.1021/ja974246o

Dunand-Sauthier, M. N. C., Deronzier, A., Pradon, X., Ménage, S., & Philouze, C. (1997). Electrochemical interconversion of mono-, bi-, and tetranuclear (bipyridyl) manganese complexes in buffered aqueous solution. *Journal of the American Chemical Society*, *119*(13), 3173-3174. https://doi.org/10.1021/ja964102u

Ghosh, D., Shukla, A. D., Banerjee, R., & Das, A. (2002). Kinetics of oxidation of ascorbic acid and 1, 4-dihydroxybenzene by semiquinone radical bound to ruthenium (ii). *Journal of the Chemical Society, Dalton Transactions*, (6), 1220-1225. https://doi.org/10.1039/B104585G

Jeans, C., Schilstra, M. J., Ray, N., Husain, S., Minagawa, J., Nugent, J. H. A., & Klug, D. R. (2002). Replacement of tyrosine D with phenylalanine affects the normal proton transfer pathways for the reduction of P680+ in oxygen-evolving photosystem II particles from Chlamydomonas. *Biochemistry*, *41*(52), 15754-15761. https://doi.org/10.1021/bi020558e

Jeffery, G. H. (1989). *Textbook of quantitative chemical analysis*. Longman.

Kirby, J. A., Robertson, A. S., Smith, J. P., Thompson, A. C., Cooper, S. R., & Klein, M. P. (1981). State of manganese in the photosynthetic apparatus. 1. Extended x-ray absorption fine structure studies on chloroplasts and di-. mu.-oxo-bridged dimanganese model compounds. *Journal of the American Chemical Society*, *103*(18), 5529-5537. https://doi.org/10.1021/ja00408a042

Kok, B., Forbush, B., & McGloin, M. (1970). Cooperation of charges in photosynthetic O2 evolution–I. A linear four step mechanism. *Photochemistry and Photobiology*, *11*(6), 457-475. https://doi.org/10.1111/j.1751-1097.1970.tb06017.x

Lumme, P., Lahermo, P., & Tummavuori, J. (1965). Thermodynamics of the ionization of hydroxylamine and nitrous acid in water. *Acta Chem. Scand*, *19*(9).

McEvoy, J. P., & Brudvig, G. W. (2004). Structure-based mechanism of photosynthetic water oxidation. *Physical Chemistry Chemical Physics*, *6*(20), 4754-4763. https://doi.org/10.1039/B407500E

Philouze, C., Blondin, G., Girerd, J. J., Guilhem, J., Pascard, C., & Lexa, D. (1994). Aqueous chemistry of high-valent manganese. Structure, magnetic, and redox properties of a new type of Mn-Oxo cluster,[Mn4IVO4 (bpy) 6] 4+: relevance to the oxygen evolving center in plants. *Journal of the American Chemical Society*, *116*(19), 8557-8565. https://doi.org/10.1021/ja00098a016

Renger, G. (2004). Coupling of electron and proton transfer in oxidative water cleavage in photosynthesis. *Biochimica et Biophysica Acta (BBA)-Bioenergetics*, *1655*, 195-204. https://doi.org/10.1016/j.bbabio.2003.07.007

Thorp, H. H., Sarneski, J. E., Brudvig, G. W., & Crabtree, R. H. (1989). Proton-coupled electron transfer in manganese complex [(bpy) 2Mn (O) 2Mn (bpy) 2] 3+. *Journal of the American Chemical Society*, *111*(26), 9249-9250. https://doi.org/10.1021/ja00208a029

Vrettos, J. S., Limburg, J., & Brudvig, G. W. (2001). Mechanism of photosynthetic water oxidation: combining biophysical studies of photosystem II with inorganic model chemistry. *Biochimica et Biophysica Acta (BBA)-Bioenergetics*, *1503*(1-2), 229-245. https://doi.org/10.1016/S0005-2728(00)00214-0

Wiberg, K. B. (1955). The deuterium isotope effect. *Chemical Reviews*, *55*(4), 713-743. https://doi.org/10.1021/cr50004a004

Yachandra, V. K., DeRose, V. J., Latimer, M. J., Mukerji, I., Sauer, K., & Klein, M. P. (1993). Where plants make oxygen: a structural model for the photosynthetic oxygen-evolving manganese cluster. *Science*, *260*(5108), 675-679. https://doi.org/10.1126/science.8480177

doi: 10.31674/book.2026cdcbs.008

Chromium (VI) Immobilized on Mesoporous Polyaniline (Cr-PANI) as a Catalyst for the Oxidation of Alkanes and Alkenes Under Mild Conditions

Usha Mandi

Department of Chemistry, Jogamaya Devi College, Kolkata- 700026, West Bengal, India

Corresponding Author's E-mail: uusha.chem@gmail.com

Abstract

A mesoporous polyaniline-supported chromium (VI) composite (Cr-PANI) was synthesized via a straightforward in-situ radical polymerization of aniline, subsequently modified with potassium dichromate. To evaluate its structural, morphological, and thermal properties, the resulting material was characterized using X-ray diffraction (XRD), transmission electron microscopy (TEM), Fourier transform infrared spectroscopy (FR-IR), UV-vis diffuse reflectance spectroscopy, and thermogravimetric analysis (TGA). Structural and morphological analysis via XRD and TEM suggested that the material possesses a mesostructured framework characterized by disordered, worm-like mesopores. When evaluated as a catalyst, Cr-PANI demonstrated excellent efficiency in liquid-phase oxidation of alkanes and alkenes, utilizing aqueous 30% hydrogen peroxide (H_2O_2) as the oxidant. Operating under mild conditions, the catalytic system provided high product selectivity and satisfactory yields. Moreover, the catalyst demonstrated strong reusability, maintaining its performance over five consecutive cycles without significant loss of activity.

Keywords*: Alkenes and Alkanes; H_2O_2; Mesoporous Polyaniline; Oxidation; Water*

Introduction

Catalytic oxidation represents one of the most important transformations in organic synthesis, providing efficient routes to a wide range of value-added oxygenated products such as alcohols, aldehydes, ketones, carboxylic acids and epoxides. In particular, hydrogen peroxide-based oxidation processes are highly attractive owing to the benign nature of water as the only by-product, together with their environmental and economic advantages (Mukherjee *et al*., 2006; Mandi *et al*., 2014; Salam *et al.,* 2012). While alkanes and alcohols are readily oxidized, the selective activation of C–H bonds in alkanes remains challenging because of their inherent stability, often leading to overoxidation. The selective oxidation of primary alcohols to aldehydes, in particular, has significant applications in pharmaceuticals, dyes and agrochemicals.

Polymer-bound metal complexes have been widely explored as heterogeneous catalysts for oxidation reactions due to their ability to merge the high catalytic performance and selectivity of homogeneous systems with the practical advantages of heterogeneous catalysts, such as simple separation, catalyst recovery and recyclability (Mondal *et al*., 2013). Conducting polymer metal composites, especially those based on polyaniline (PANI), have attracted considerable attention due to their synergistic properties, facile synthesis, environmental stability, insolubility in most solvents and wide conductivity range (Banjar *et al*., 2023; Haral *et al*., 2024; Nazerian *et al*., 2025). Polyaniline-supported catalysts show various catalytic activities for organic transformations (Behera, 2024), electrochemical energy conversion (Wu *&* Li, 2025), enhanced oxygen reduction reactions (Yang *et al*., 2024), and oxygen evolution activities for rechargeable Zn-air batteries (Zou *et al*., 2025). PANI-supported metal catalysts, including vanadium, Fe (II), cobalt, Mn (II) porphyrins, $FeCl_2$, and $CuCl_2$, have demonstrated high efficiency in the selective oxidation of alcohols and alkenes (Reddy *et al*., 2004; Pielichowski *&* Kowalski, 2010), oxidation of propanol (Watanabe *et al*., 2025), oxidation of methanol (Teng *et al*., 2023), and oxidation of nitrophenols (Khani *et al*., 2023).

Encouraged by these findings, we prepared mesoporous PANI-supported Cr (VI) catalysts to capitalize on the synergistic benefits of homogeneous and heterogeneous catalytic approaches. The catalysts were characterized by TEM, XRD, FTIR, TGA and UV-visible spectroscopy, confirming their nanostructured nature. The Cr-PANI system showed excellent catalytic activity for the oxidation of alkenes and alkanes using 30% H_2O_2 in an aqueous medium and retained its activity over multiple cycles, demonstrating high stability and recyclability.

This work highlights the potential of PANI-supported Cr(VI) as a sustainable and efficient heterogeneous catalyst for selective oxidation reactions, combining high catalytic performance with environmental and economic benefits.

Synthetic Procedure

Materials

Aniline, potassium dichromate ($K_2Cr_2O_7$), ammonium persulphate ($(NH_4)_2S_2O_8$), and concentrated hydrochloric acid (HCl) were sourced from Merck. Ammonium persulphate served as the oxidizing initiator during the aqueous-phase polymerization of aniline. Sodium dodecyl sulphate (SDS), obtained from Loba Chemie, was utilized as a structure-directing agent (SDA) to facilitate the formation of the desired polymer morphology. Alkenes, alkanes, and alcohols were supplied by Merck or Fluka.

Synthesis of Mesoporous Polyaniline (PANI)

The meso-PANI (Scheme 1) was prepared through template-assisted polymerization of aniline. For the synthesis, 0.02 mol of aniline was first dissolved in 5 mL of aqueous HCl containing 0.02 mol acid. This solution was then added to 20 mL of an aqueous SDS solution (0.01 mol) with continuous stirring. The reaction mixture was cooled in an ice-salt bath and maintained at 4-5°C. Subsequently, 20 mL of an ice-cold ammonium persulphate solution (0.04 mol) was introduced gradually into the mixture. Once a homogeneous solution was obtained, stirring was halted, and the mixture was left undisturbed at 4-5°C for 48 hours to allow aging. The solid product formed was separated by filtration, rinsed several times with deionized water, and finally dried under vacuum at room temperature. The mesoporous PANI was finally extracted using an aqueous ammonium acetate solution.

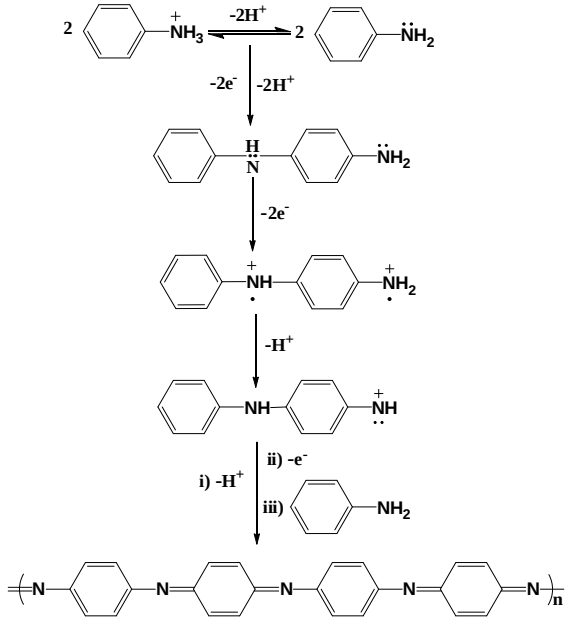

Scheme 1: Schematic Diagram Showing the Polymerization of Aniline

Synthesis of Cr-PANI

In a typical procedure, 500 mg of mesoporous polyaniline and 100 mg of potassium dichromate were placed in a 50 mL round-bottom flask. Subsequently, 10 mL of double-distilled water was added to obtain a homogeneous suspension. The mixture was stirred vigorously at room temperature for 24 hours. After completion of the reaction, the resulting precipitate was collected by filtration, thoroughly washed with double-distilled water, and dried under vacuum.

Results and Discussion

Characterization of Synthesized Cr-PANI

X-ray Diffraction (XRD) Studies

Figure 1 presents the small-angle XRD pattern of the dichromate-loaded polyaniline material (Cr-PANI). A distinct diffraction peak appears at $2\theta = 2.41^{o}$, indicating the presence of a mesophase structure in the material. This observation suggests that the incorporation of Cr (VI) species does not significantly alter the structural integrity of the mesophase.

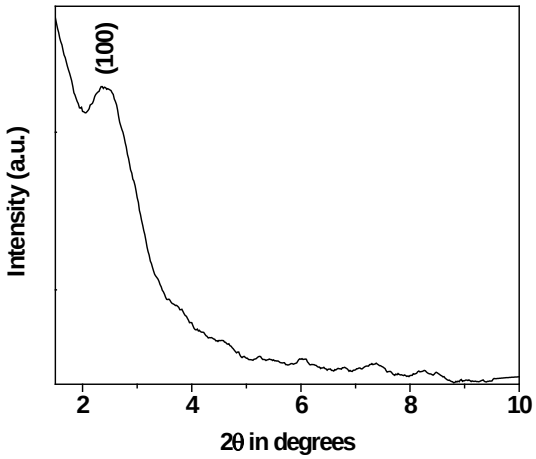

Figure 1: Small Angle X-ray Diffraction (XRD) Pattern of Cr-PANI

Transmission electron microscopy (TEM) Analysis

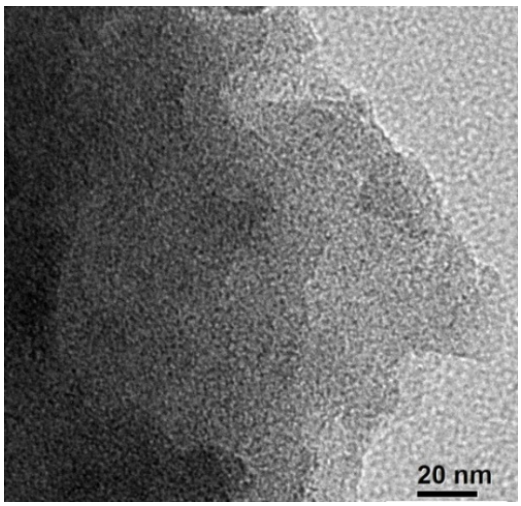

Figure 2: Transmission Electron Microscopy (TEM) Image of Cr-PANI

The representative transmission electron microscopy (TEM) image of the material is shown in Figure 2. The image shows low electron-density regions, attributed to pores, that are uniformly distributed throughout the sample. The average pore size is approximately 2.3 nm. Compared to the parent PANI sample, a slight reduction in pore size is evident after $Cr_2O_7^{2-}$ loading, likely resulting from the deposition of dichromate species onto the pore surfaces.

UV-Visible Spectra

The UV-Visible spectra of mesoporous PANI and Cr-PANI (Figure 3) reveal broad absorption bands centered within the regions of 310-460 nm and 660-720 nm for mesoporous PANI. Such absorption behavior is characteristic of nanostructured polyaniline, which commonly exhibits two distinct electronic transitions at around 320-340 nm and 600-660 nm (Laska *&* Widlarz, 2005). The higher-energy band is attributed to the π→π* transition of the benzenoid rings, while the lower-energy band corresponds to the transition from benzenoid to quinoid structures. In the case of Cr–PANI, the absorption band associated with the quinoid transition shifts from around 700 nm to a higher wavelength region (red shift) upon incorporation of Cr (VI). This shift can be explained by the formation of a more compact coil structure in the Cr–PANI chains, which reduces the energy gap associated with the quinoid transition, thereby facilitating electronic transitions. In contrast, the π→π* transition band shows a negligible shift, indicating that Cr (VI) species preferentially interact with the nitrogen atoms of the quinoid segments.

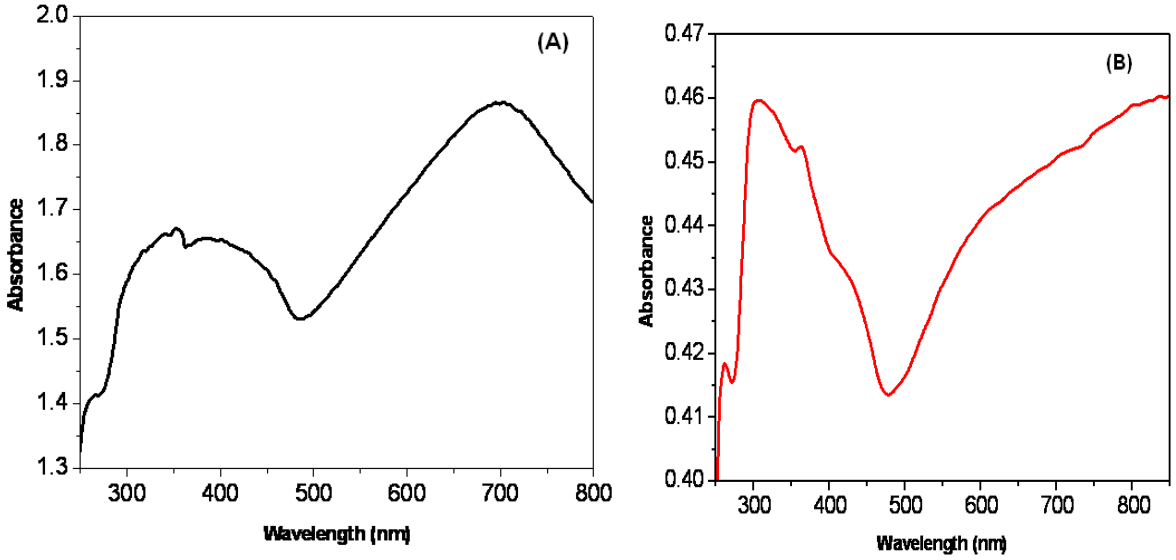

Figure 3: UV-Visible Spectra of (A) PANI and (B) Cr-PANI

Fourier Transform Infrared (FTIR) Spectra

FTIR spectroscopy (Figure 4) further confirmed the interaction between Cr (VI) species and the PANI framework. The FTIR spectrum of PANI exhibits distinct bands at 1578 and 1493 cm^{-1}, attributed to the C=C stretching vibrations of quinoid and benzenoid rings, respectively (Chen *et al.*, 2010). The absorption peak located at 1306 cm^{-1} is associated with the stretching vibration of C-N bonds (Ahn *et al.*, 2011), whereas the band appearing at 1148 cm^{-1} is attributed to the in-plane bending vibration of C-H bonds (Dexmer *et al.*, 2008). In the Cr-PANI composite, the C=C stretching bands exhibit a noticeable blue shift, indicating strong interaction between Cr (VI) and the polymer backbone (Han *et al.*, 2013). Additionally, the C–N stretching band shifts to a lower wavenumber upon Cr (VI) incorporation, suggesting coordination between chromium species and nitrogen atoms in the polymer chain.

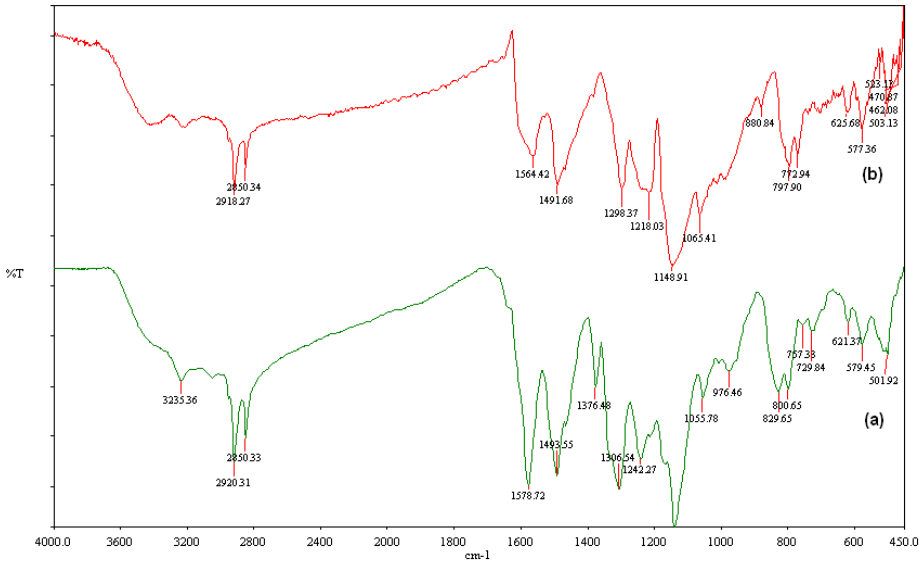

Figure 4: FT-IR Spectra (a) PANI and (b) Cr-PANI

Thermogravimetric (TG) Analysis

Thermal stability of the mesoporous polyaniline materials was evaluated using thermogravimetric analysis (TGA), as shown in Figure 5. The measurements were carried out under a nitrogen atmosphere at a heating rate of 10 °C min^{-1} over the temperature range of 50-600°C. Mesoporous PANI exhibits significant weight loss in the temperature range of 190-475°C, corresponding to the thermal degradation of the polymer backbone.

In comparison, the Cr-PANI nanocomposite displays a similar degradation profile; however, the onset of mass loss shifts to a higher temperature (~230°C), indicating enhanced thermal stability. Notably, the thermal stability of Cr–PANI improves by approximately 40-50°C relative to pristine PANI. This increased stability is attributed to strong interactions between Cr(VI) species (originating from $K_2Cr_2O_7$) and the PANI chains, which restrict the segmental motion of the polymer and delay its thermal decomposition.

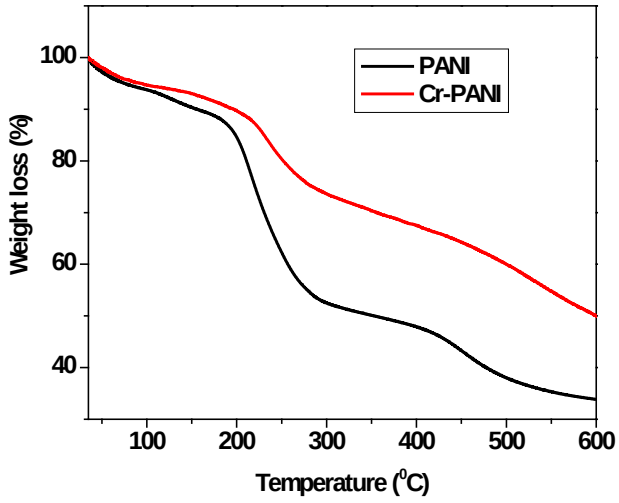

Figure 5: TGA Plots of Mesoporous PANI and Cr-PANI

Overall, the combined XRD, TEM, UV-Vis, FTIR, and TG analyses reveal that while the mesoporous structure and backbone of PANI remain largely intact after Cr(VI) loading, significant electronic and chemical interactions occur between Cr(VI) species and the mesostructure polymer.

Catalytic Activity

Oxidation of Alkenes Catalyzed by Cr-PANI

The epoxidation activity of Cr-PANI toward various alkenes in the liquid phase was investigated, and the results are presented in Table 1. Alkenes possessing terminal C=C bonds showed high levels of conversion and selectivity (Table 1, entries 1 and 2), yielding only the corresponding epoxide products. In contrast, the oxidation yield decreased progressively with increasing aliphatic chain length in alkenes containing a single terminal double bond, which may be attributed to steric constraints and reduced diffusion efficiency. In contrast, cyclic unsaturated hydrocarbons containing one or more double bonds demonstrated significantly higher reactivity. These substrates were efficiently converted to their corresponding epoxides within 4-6 hours, depending on the nature of the substrate (Table 1, entries 3-5). The enhanced reactivity of cyclic alkenes may be attributed to their higher electron density and favorable interaction with the active sites of the Cr-PANI catalyst. In the Cr-PANI-catalyzed oxidation of cyclohexene, cyclohexene oxide was produced with 97% selectivity after a reaction time of 4 h (Table 1, Entry 3).

In contrast, aromatic alkenes generally require longer reaction durations than carbocyclic alkenes to achieve comparable conversions. Styrene was efficiently transformed into styrene oxide in high yield (Table 1, Entry 6), while substituted styrene also selectively formed the corresponding epoxide products (Table 1, Entries 7 and 8). Similarly, *α*-methyl styrene predominantly afforded its epoxide as the dominant product (Table 1, Entry 9). However, substrates bearing a double bond at the benzylic position show high reactivity, leading to the formation of a considerable number of by-products during oxidation. Depending on the nature of the substrate, aldehydes and/or ketones are generated as the major side products. Cr-PANI also demonstrates notable catalytic performance in the oxidation of terpenes, where the corresponding epoxides are predominantly formed under similar reaction conditions (Table 1, Entries 10 and 11). In contrast, the oxidation of indene mainly produces the corresponding ketone in high yield (Table 1, Entry 12).

Table 1: Epoxidation of Alkenes with Cr-PANI Catalyst Using 30% H_2O_2

Entry	Substrate	Time (h)	Conversion (%) [a]	Product	Selectivity (%) [a]
1	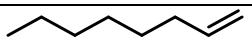	12	76	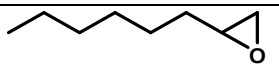	100
2		12	69	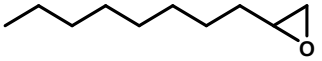	100
3		4	92	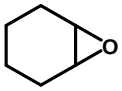	97
4	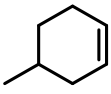	4	94	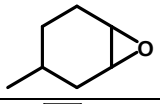	95
5	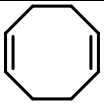	5	82	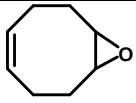	93
6	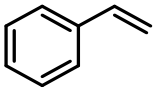	8	89	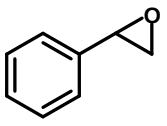	95

7	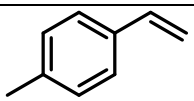	8	90	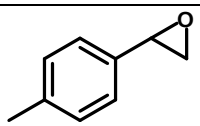	94
8	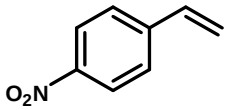	8	78	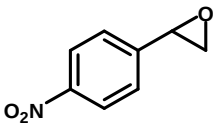	90
9	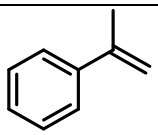	8	82	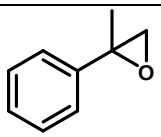	89
10	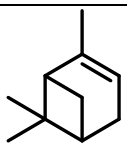	4	48		67
11	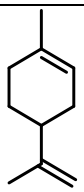	3	56	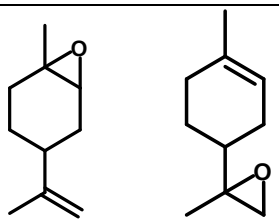	72
12	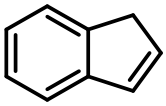	3	86	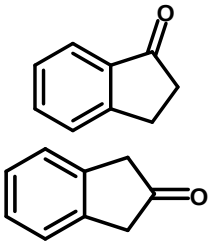	86

Reaction conditions: catalyst (0.02 g), alkene (5 mmol), water (10 mL), 30% aqueous H_2O_2 (10 mmol), reaction temperature 60°C. [a] Conversion and selectivity were determined by GC analysis.

Oxidation of Alkanes Catalyzed by Cr-PANI

The Cr-PANI catalyst was also investigated for the oxidation of alkyl benzenes using H_2O_2 at 70°C. As shown in Table 2, it effectively promotes the oxidation of various alkyl benzenes bearing electron-donating groups, producing the corresponding aldehydes with good yields and high selectivity. For toluene derivatives bearing electron-donating groups, the reaction proceeded at a significantly faster rate than that observed for unsubstituted toluene.

With reactions reaching near completion within 4 hours (Table 2, entries 2–4). Similarly, *p*-methoxy toluene, which contains a strongly electron-donating methoxy group, exhibited a high reaction rate and conversion. However, it showed relatively lower selectivity (75%) toward 4-methoxybenzaldehyde (Table 2, entry 5), possibly due to competing side reactions under the reaction conditions. The high reactivity of *p*-methoxy toluene can be attributed to the electron-donating effect of the methoxy group, which activates the benzylic position toward oxidation. As a result, besides the formation of 4-methoxybenzaldehyde, some over-oxidized products, such as carboxylic acids, were also observed. In the case of ethylbenzene, oxidation occurred exclusively at the benzylic C–H bond, leaving the methyl group intact, yielding acetophenone in high yield (94%) and selectivity (96%) (Table 2, Entry 8).

In contrast, toluene derivatives bearing electron-withdrawing groups exhibited lower reactivity compared to those with electron-donating substituents (Table 2, entries 6 and 7). This diminished reactivity can be ascribed to the reduced electron density on the aromatic ring, which makes it less susceptible to oxidation. As an example, *p*-chlorotoluene was oxidized to 4-chlorobenzaldehyde with 85% selectivity (Table 2, Entry 6). The strongly electron-withdrawing nitro group in *o*-nitrotoluene further decreased reactivity, giving only 34% yield of 2-nitrobenzaldehyde with 91% selectivity after 6 hours (Table 2, Entry 7).

Table 2: Oxidation of Various Alkanes with Cr-PANI Catalyst Using 30% H_2O_2

Entry	Substrate	Time (h)	Conversion (%) [a]	Product	Selectivity (%) [a]
1	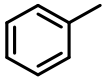	6	79	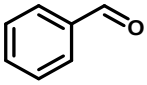	84
2	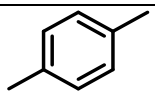	4	87	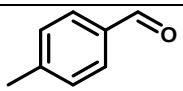	90
3	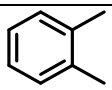	4	92	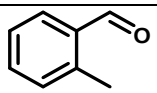	86
4	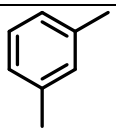	4	81	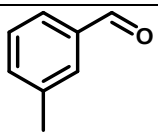	92
5	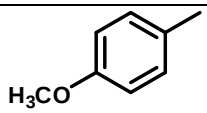	4	86	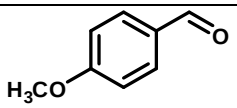	75
6	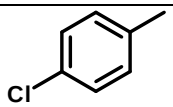	6	46	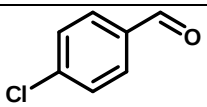	85
7	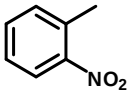	6	37	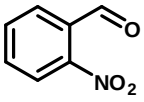	91
8	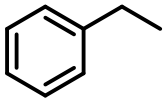	4	94	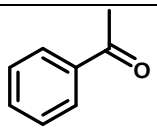	96

Reaction condition: catalyst (0.02 g), substrate (5 mmol), H_2O_2 (10 mmol), water 10 mL, temperature (70 °C). [a] *Conversion and selectivity were determined by GC analysis*.

Heterogeneity Test

To examine possible chromium leaching during the process, styrene oxidation was selected as a model reaction under optimized conditions. After 3 hours, the reaction was stopped, and the filtrate was collected and further treated under the same conditions for an additional 3 hours. The lack of any further increase in conversion indicated the absence of active catalyst species in the solution phase. The stability of the Cr-PANI catalyst was further evaluated using UV-visible spectroscopy. Following the first reaction run, the spectrum of the reaction mixture showed no distinct absorption features attributable to chromium species, indicating that metal leaching during oxidation was minimal. These findings confirm that chromium species are strongly immobilized on the polyaniline surface, supporting the heterogeneous character of the catalyst. They further show that Cr-PANI remains stable and can be recycled through several oxidation cycles with no significant decrease in activity.

Reusability of the Catalyst

A major benefit of heterogeneous catalysis is the ease with which the catalyst can be recovered and reused. Because the catalyst is insoluble under the reaction conditions, it can be readily separated by simple filtration and then washed. The reusability of the heterogeneous Cr-PANI catalyst was investigated in the oxidation of styrene and ethyl benzene (Figure 6). After each run, the catalyst was collected by filtration, rinsed successively with ethyl acetate and acetone, and finally dried under reduced pressure at 60°C. The recovered catalyst was then used in subsequent runs with the addition of fresh substrates under the optimum reaction conditions. As shown in Figure 6, the recycled catalyst exhibited no significant loss of activity, indicating that it is stable and can be regenerated for repeated use over an extended period.

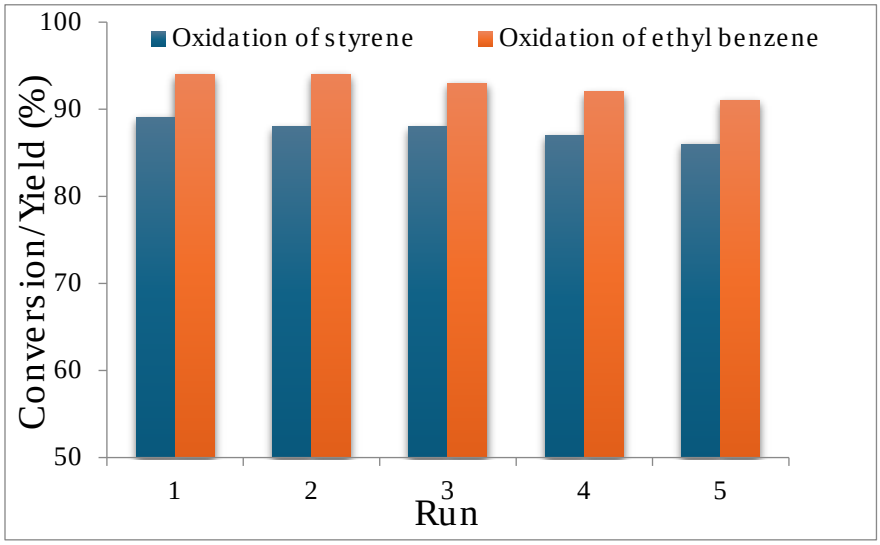

Figure 6: Reusability Test for the Oxidation of Styrene and Ethyl Benzene Using Cr- PANI

Conclusion

Mesoporous Cr-PANI was prepared via immobilization of chromate anions on the polyaniline surface. The resulting heterogeneous catalyst shows high catalytic performance in the oxidation of alkenes and alkanes, selectively giving epoxides from alkenes, while alkanes are converted into the corresponding aldehydes or ketones. A key advantage of this catalyst is its stability and recyclability under the reaction conditions. Recycling experiments show no significant loss of activity, and leaching tests confirm that the active sites remain bound to the support, indicating the reaction proceeds primarily via a heterogeneous mechanism. The catalyst can be reused multiple times without appreciable decrease in performance. The high catalytic efficiency of this chromium-grafted mesoporous polymer suggests promising potential for future applications of related mesoporous organic polymers.

Acknowledgement

The author expresses her gratitude to Professor Sk. Manirul Islam and Professor Asim Bhaumik for their constant help and support. UM acknowledges the Department of Chemistry, Jogamaya Devi College, Kolkata, India.

References

Ahn, D., Yoo, I., Koo, Y. M., Shin, N., Kim, J., & Shin, T. J. (2011). Effects of cobalt-intercalation and polyaniline coating on electrochemical performance of layered manganese oxides. *Journal of Materials Chemistry*, *21*(14), 5282-5289. https://doi.org/10.1039/C0JM03548C

Banjar, M. F., Abedin, F. N. J., Fizal, A. N. S., Sarih, N. M., Hossain, M. S., Osman, H., Khalil, N. A., Yahaya, A. N. A., & Zulkifli, M. (2023). Synthesis and Characterization of a Novel Nanosized Polyaniline. *Polymers, 15*(23), 4565. https://doi.org/10.3390/polym15234565

Behera, S. (2024). A Review on polyaniline-supported catalyst for organic transformations. *ACS Omega*, *9*(51), 50097-50117. https://doi.org/10.1021/acsomega.4c04352

Chen, Y., Yang, G., Zhang, Z., Yang, X., Hou, W., & Zhu, J. J. (2010). Polyaniline-intercalated layered vanadium oxide nanocomposites—One-pot hydrothermal synthesis and application in lithium battery. *Nanoscale*, *2*(10), 2131-2138. https://doi.org/10.1039/c0nr00246a

Dexmer, J., Leroy, C. M., Binet, L., Heresanu, V., Launois, P., Steunou, N., ... & Backov, R. (2008). Vanadium Oxide− PANI nanocomposite-based macroscopic fibers: 1d alcohol sensors bearing enhanced toughness. *Chemistry of Materials*, *20*(17), 5541-5549. https://doi.org/10.1021/cm800886v

Han, J., Dai, J., Zhou, C., & Guo, R. (2013). Dilute cationic surfactant-assisted synthesis of polyaniline nanotubes and application as reactive support for various noble metal nanocatalysts. *Polymer Chemistry*, *4*(2), 313-321. https://doi.org/10.1039/C2PY20536J

Haral, S.S., Tupe, U. J., & Kale, V.S. (2024). Synthesis and applications of Polyaniline: A Brief Review. *International Journal of Scientific Development and Research*, *9*(2), 358-362. https://ijsdr.org/papers/IJSDR2402052.pdf

Khani, M., Sammynaiken, R., & Wilson, L. D. (2023). Electrocatalytic Oxidation of Nitrophenols via Ag Nanoparticles Supported on Citric-Acid-Modified Polyaniline. *Catalysts*, *13*(3), 465. https://doi.org/10.3390/catal13030465

Laska, J., & Widlarz, J. (2005). Spectroscopic and structural characterization of low molecular weight fractions of polyaniline. *Polymer*, *46*(5), 1485-1495. https://doi.org/10.1016/j.polymer.2004.12.008

Mandi, U., Pramanik, M., Roy, A. S., Salam, N., Bhaumik, A., & Islam, S. M. (2014). Chromium (VI) grafted mesoporous polyaniline as a reusable heterogeneous catalyst for oxidation reactions in aqueous medium. *RSC Advances*, *4*(30), 15431-15440. https://doi.org/10.1039/C3RA47884J

Mondal, P., Sinha, A., Salam, N., Roy, A. S., Jana, N. R., & Islam, S. M. (2013). Enhanced catalytic performance by copper nanoparticle–graphene based composite. *RSC advances*, *3*(16), 5615-5623. https://doi.org/10.1039/C3RA23280H

Mukherjee, S., Samanta, S., Roy, B. C., & Bhaumik, A. (2006). Efficient allylic oxidation of cyclohexene catalyzed by immobilized Schiff base complex using peroxides as oxidants. *Applied Catalysis A: General*, *301*(1), 79-88. https://doi.org/10.1016/j.apcata.2005.11.015

Nazerian, V., Dizaj, M. H., & Sutikno, T. (2025). Polyaniline as a conductive polymer and its role in improving the efficiency and conductivity of perovskite solar cells. Int J Pow Elec & Dri Syst, 16(4), 2731-2743. https://doi.org/10.11591/ijpeds.v16.i4.pp2731-2743

Pielichowski, J., & Kowalski, G. (2010). Novel polyaniline supported Cobalt catalyzed aerobic oxidation of unsaturated organic compounds. *Molecular Crystals and Liquid Crystals*, *522*(1), 105-405. https://doi.org/10.1080/15421401003719829

Reddy, S. R., Das, S., & Punniyamurthy, T. (2004). Polyaniline supported vanadium catalyzed aerobic oxidation of alcohols to aldehydes and ketones. *Tetrahedron letters*, *45*(18), 3561-3564. https://doi.org/10.1016/j.tetlet.2004.03.056

Salam, N., Mondal, P., Mondal, J., Roy, A. S., Bhaumik, A., & Islam, S. M. (2012). Highly efficient base catalysis and sulfide oxidation reactions over new functionalized mesoporous polymers. *RSC Advances*, *2*(16), 6464-6477. https://doi.org/10.1039/C2RA20630G

Teng, Z., Zhang, Z., & Li, X. (2023). Preparation of Pt catalysts supported on polyaniline modified carbon black and electrocatalytic methanol oxidation. *Synthetic Metals*, *293*, 117256. https://doi.org/10.1016/j.synthmet.2022.117256

Watanabe, K., Okamoto, K., Kawakami, H., Yoshida, S., Kurioka, T., Chen, C. Y., ... & Chang, T. F. M. (2025). Polyaniline-Supported Atomic-Level Pt and Pt-Au Clusters as Catalytic Electrodes in Propanol Oxidation. *Materials*, *18*(11), 2594. https://doi.org/10.3390/ma18112594

Wu, S. X., & Li, G. R. (2025). Recent progress in polyaniline-based catalysts for electrochemical energy conversion. *Nanoscale*, *17*(27), 16114-16152. https://doi.org/10.1039/D5NR00966A

Yang, X., Song, R., Tian, F., Ding, C., Du, H., Liu, Q., ... & Fu, X. (2024). Polyaniline nanofiber supported Pt catalyst with optimized Pt nanoparticle size for enhanced oxygen reduction reaction. *International Journal of Hydrogen Energy*, *82*, 225-232. https://doi.org/10.1016/j.ijhydene.2024.07.442

Zou, X., Lu, Q., Tang, M., Wu, J., Zhang, K., Li, W., ... & An, L. (2025). Catalyst–Support Interaction in Polyaniline-Supported Ni3Fe Oxide to Boost Oxygen Evolution Activities for Rechargeable Zn-Air Batteries. *Nano-micro letters*, *17*(1), 6. https://doi.org/10.1007/s40820-024-01511-4

doi: 10.31674/book.2026cdcbs.009

Recent Developments on the Synthesis of Colorless Polyimides

Pradip Kumar Tapaswi

Department of Chemistry, Narasinha Dutt College, Howrah- 711101, West Bengal, India

Corresponding Author's Email: pradipkumartapaswi@gmail.com

Abstract

Driven by the rapid advancement of transparent and flexible electronic technologies, colorless polyimides (CPIs) have emerged as an important class of high-performance polymeric materials. In recent years, the increasing demand for lightweight, flexible, and optically transparent substrates for advanced optoelectronic devices has stimulated extensive research on CPI materials. Compared with conventional aromatic polyimides, which generally exhibit deep coloration due to strong intermolecular charge-transfer interactions, CPIs are specifically designed to achieve high optical transparency while retaining the outstanding thermal, mechanical, and chemical resistance characteristics intrinsic to polyimides. Owing to these unique properties, CPI films have found potential applications in flexible displays, foldable smartphones, organic light-emitting diode (OLED) devices, solar cells, touch panels, flexible printed circuit boards, and other next-generation electronic systems. Recent developments in CPI research have primarily focused on molecular design strategies aimed at suppressing charge-transfer complex formation without significantly compromising thermal stability and dimensional integrity. Various structural modifications, including the incorporation of fluorinated groups, bulky substituents, asymmetric moieties, alicyclic units, and non-coplanar rigid structures, have been widely explored to improve optical transparency and solubility. At the same time, considerable attention has been devoted to maintaining high glass transition temperatures, low coefficients of thermal expansion, and excellent thermo-mechanical properties required for advanced device fabrication processes. This chapter reviews the recent synthesis of CPIs and outlines future prospects, focusing on recent developments in novel monomer design and their influence on the thermal and optical properties of the resulting polyimides.

Keywords: *Charge-Transfer Interactions; Colorless Polyimides (CPIs); Flexible Optoelectronic Devices; Optical Properties; Thermal Properties*

Introduction

Over the past two decades, colorless and optically transparent polymers have found significant applications in touch panels, flexible displays, organic photovoltaics, optical films, flexible printed circuit boards, and other advanced flexible optonic devices, where glass substrates were traditionally used. In recent years, the demand for flexible and transparent materials coated with conductive oxides (Indium Tin Oxide) has further increased, particularly in display technologies and microelectronics.

However, ITO-based systems suffer from several limitations. Indium is a rare and costly element and achieving high-quality ITO (Indium Tin Oxide) coatings typically requires high-temperature processing, especially when deposited on glass substrates. In addition, glass itself is inherently brittle and lacks flexibility, making it unsuitable for next-generation flexible devices (Choi *et al.,* 2010). Replacing conventional fragile inorganic glass substrates (typically 400–700 µm thick) with much thinner plastic substrates (less than 50 µm) can make display devices lighter, more durable, and highly flexible.

Many polymer optical films are recently applied in the fabrication of different flexible smart optonic devices. For this purpose, optical polymer films must meet several critical requirements such as glass transition temperature above 300 °C, high transparency in UV-Vis region, high processability, sufficient film flexibility, excellent mechanical properties, roll-to-roll (R2R) compatible, compatibility with film-forming processes,

resistance to solvents, and a low coefficient of thermal expansion (CTE). Among these, maintaining high optical transparency at very high processing temperatures is most important. For example, in the fabrication of next-generation flexible thin-film transistor (TFT)-driven active-matrix liquid crystal display (TFT-LCD) devices and flexible active-matrix organic light-emitting diode (AMOLED) displays, polymer film substrates are often exposed to demanding thermal conditions, with processing temperatures exceeding 300°C. In addition, key photoelectric fabrication techniques, such as physical vapor deposition (PVD) and plasma-enhanced chemical vapor deposition (PECVD), typically involve even higher temperatures, which can surpass 400°C (Liu *et al.,* 2017). Such elevated processing temperatures impose stringent requirements on substrate materials. However, most conventional optically transparent plastic substrates are not designed to withstand these harsh conditions. As a result, they tend to suffer from thermal deformation, loss of optical transparency, and degradation of mechanical strength, making it difficult to maintain their desired performance during device fabrication.

Based on their glass transition temperature (T_g), polymer-based optical films can be broadly categorized into three groups: conventional optical films ($T_g < 100°C$), intermediate or common high-temperature optical films ($100°C \leq T_g \leq 200°C$), and high-temperature optical films ($T_g > 200°C$), as illustrated in Figure 1. This classification highlights the thermal limitations of different polymer systems in relation to their suitability for advanced optoelectronic applications.

Although several commercially available colorless super-engineering plastics exhibit excellent optical transparency, their glass transition temperatures are generally inadequate for high-temperature processing environments. For instance, poly(ethylene terephthalate) (PET) possesses a T_g of approximately 78°C, poly(ethylene naphthalate) (PEN) around 120°C, polycarbonate (PC) about 145°C, and poly (ether sulfone) (PES) near 225°C (Figure 2). These T_g values remain significantly below the thermal demands of modern device fabrication processes. In particular, processes such as lead-free solder reflowing, which typically occur at temperatures around 270°C, and silicon-based thin-film transistor (TFT) fabrication, which can involve short-term exposure to temperatures approaching 400°C, exceed the thermal tolerance of these materials. Consequently, such polymers are unable to maintain their structural integrity and functional performance under these harsh processing conditions, thereby limiting their applicability in next-generation flexible electronic and optoelectronic devices (Yang & Yuan, 2018).

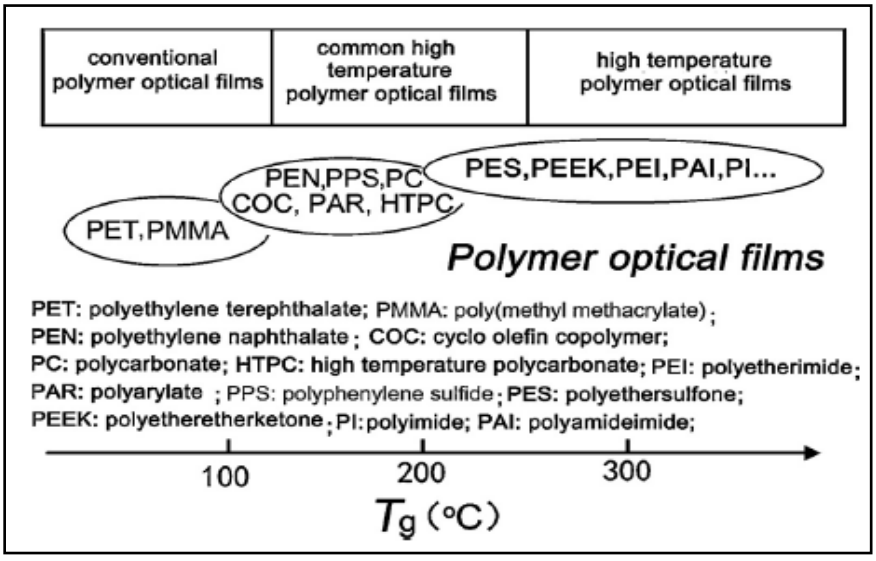

Figure 1: Glass Transition Temperature (T_g) of Polymer Films Used in Optical Devices (Yang & Yuan, 2018)

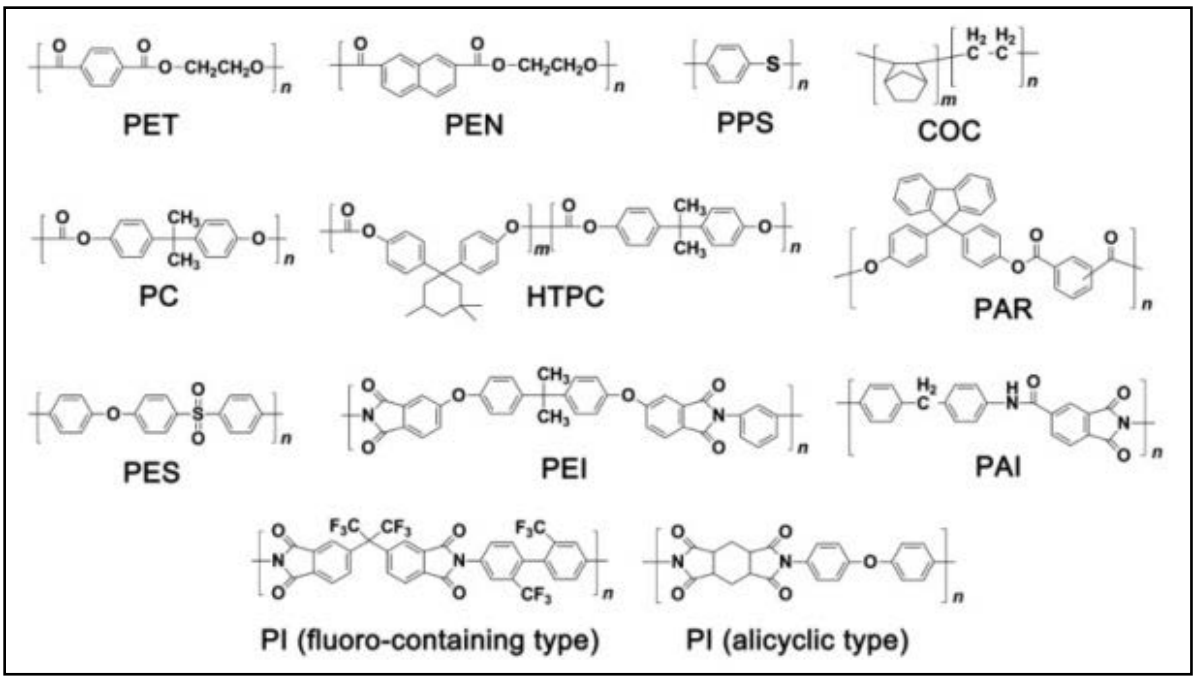

Figure 2: Chemical Structures of Various Polymer Optical Films (Liu et al., 2015)

The rapid advancement of optoelectronic technologies has driven the demand for polymeric materials that combine high optical transparency with excellent thermal, mechanical, and processing properties. Among high-performance polymers, polyimides (PIs) and probenazole's exhibit sufficiently high glass transition temperatures (T_g); however, the practical application of colorless probenazole's is limited by issues such as poor processability, availability of very few monomers, complex synthetic methodologies and manufacturing requirements (Tapaswi & Ha, 2019).

In contrast, colorless polyimides (CPIs) dominate the field; accounting for the majority of optically transparent polymer films (Yi *et al.,* 2020). Colorless polyimides (CPIs) are widely utilized across advanced flexible electronic applications. They serve as (i) base substrates for foldable and flexible display panels, including OLEDs, enabling high-definition, transparent, and mechanically robust bendable devices; (ii) substrates in flexible perovskite solar cells and organic photovoltaics (OPVs), where high optical transmittance and excellent flexural durability are essential; and (iii) materials for flexible printed circuit boards (PCBs) and sensor platforms that demand exceptional thermal stability (typically T_g > 300°C), particularly in automotive and aerospace applications. Their widespread use is attributed to their balanced optical, thermal, dielectric, and mechanical performance, along with their structural tunability through molecular design. Consequently, CPIs are extensively utilized in advanced optoelectronic applications, including flexible electronic substrates.

Polyimide (PI) is basically a condensation polymer of carboxylic dianhydrides and diamines. All polyimides possess highly stable heterocyclic imide ring system. It has become the most popular high-performance polymer in last two decades because of its outstanding thermal and chemical stability, excellent mechanical properties. PI offers outstanding promise for the high technology applications in the future. Polyimides (PIs) are widely used in aerospace, electronics, energy devices, membranes, sensors, and composite materials (Zhuang *et al.,* 2019).

Polyimide (PI) chemistry dates back to 1908 with its initial synthesis from 4-aminophthalic acid, but major progress occurred in 1955 when high–molecular weight aromatic PIs were prepared via a two-step polycondensation of pyromellitic dianhydride (PMDA) with aromatic diamines (Mittal, 2007). This

breakthrough enabled large-scale development, leading to the commercialization of PMDA-ODA–based PI films in the early 1960s, with a trade name of Kapton® known for their exceptional thermal stability (T_g up to 385°C) and widespread use in flexible electronics and aerospace systems. Two other commercially successful thermally stable PI films are Novax™ and Upilex-S™. Further advancements followed with the introduction of other thermally robust PI films and the development of aliphatic and alicyclic PIs in the early 1970s (Lee *et al.,* 1971). Since then, a wide range of polyimides has been developed to take advantage of their excellent overall performance and versatility.

The outstanding thermo-mechanical stability of polyimides primarily arises from the presence of heterocyclic imide rings in their backbone. Incorporation of aromatic rings, either in the main chain or side chain significantly enhances the thermo-mechanical stability of aromatic polyimides. It has been well established that charge transfer complexes (CTCs) form between electron-donating diamine moieties and electron-withdrawing dianhydride units along the polyimide chain. These interactions tightly bind the polymer chains, restricting segmental motion, leading to a high glass transition temperature (T_g). Consequently, CTC formation largely accounts for the superior thermal, mechanical, and dielectric properties, as well as the excellent chemical resistance of polyimides, albeit at the cost of reduced solubility and increased processing difficulty.

Unfortunately, most of the aromatic PI films are deep in colors (brown, yellowish brown or amber) with poor optical transmittance (Tan *et al.,* 2020). Hence, these aromatic PIs cannot be used as optical transparent polymer in microelectronic and optoelectronic devices, as they fail to provide the required colorless transparency (Crawford, 2005).The deep color of conventional aromatic PIs is mainly, due to the intra- and inter-molecular charge-transfer (CT) interactions (Figure 3).The charge transfer complexes (CTCs) in PIs are formed due to the electronic transition between the highest occupied molecular orbital (HOMO) of the diamines and the lowest unoccupied molecular orbital (LUMO) of the dianhydrides. A larger HOMO-LUMO energy gap corresponds to absorption at shorter wavelengths, resulting in lighter-colored polyimide (PI) films. Suppression of CT interactions can be effectively achieved by reducing the electron-withdrawing strength of dianhydride moieties and the electron-releasing ability of diamine components (increasing the HOMO-LUMO energy gap), thereby improving the colorlessness of the PI films. Therefore, an effective strategy to obtain colorless polyimides (CPIs) is to employ weakly electron-withdrawing dianhydrides and/or weakly electron-donating diamines, thereby minimizing charge-transfer interactions (Guan *et al.*, 2014).

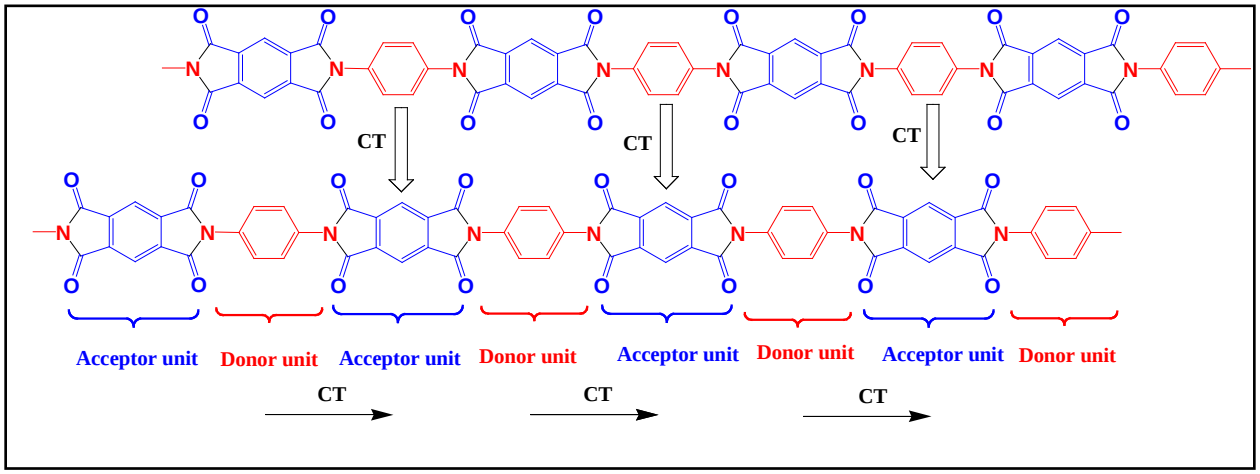

Figure 3: Charge-transfer Interactions in PI

The colorlessness of PI films is commonly evaluated using parameters such as light transmittance at 400 nm (T400), the cutoff wavelength (λ_0, defined as the wavelength at which transmittance becomes typically below 1%, the yellowness index (YI), which indicates the degree of coloration and haze (turbidity). Among

these parameters, T400is arguably the most important factor for obtaining CPI. Although T450 or T500 values (transmittance measured at 450 or 500 nm) are commonly used to evaluate optical transparency, they do not necessarily guarantee the formation of truly colorless polyimides (PIs).In many cases, even when the transmittance at 500 nm (T_{500}) exceeds 80%, the polyimide film may still exhibit noticeable coloration (Itamura *et al.,* 1993).For films with a thickness of approximately 20 μm, T_{400}> 80%, YI < 3 and haze below 1.0% ensures colorless appearance and suitable for image display applications.

The optical transparency of polyimide films is mainly influenced by the monomer structure, synthetic approach (one-step or two-step), imidization method (chemical or thermal), and film processing conditions, including temperature, atmosphere, and solvent type. In wholly aromatic PIs, the main chains are composed of electron-donating diamine units and electron-accepting dianhydride units. Inter- and intrachain donor–acceptor CT interactions can generate an additional absorption band in the visible region, which leads to coloration in aromatic PI films. This behavior follows Mulliken's CT theory: hv_{CT} ($\infty\lambda_{CT}^{-1}$) = IP – EA + C (1), where v_{CT} is the frequency of CT absorption, IP is the ionization potential of the diamine, EA is the electron affinity of the dianhydride, and C is a constant. Since $v_{CT}$is inversely proportional to the wavelength (λ_{max}) of the CT absorption band, reducing the EA of dianhydrides and increasing the IP of diamines raises the CT transition energy. This causes a blue shift (lower λ_{max}), thereby reducing the color intensity of PI films. To increase the ionization potential (IP) of diamines, it is electron-withdrawing groups such as –CF_3 and –SO_2– or halogen atoms (e.g., Cl and F) are introduced into the aromatic diamine structure. Conversely, to decrease the electron affinity (EA) of dianhydrides, electron-donating groups such as –O– can be incorporated. Again, inter-chain CT interactions can also be weakened effectively by introducing bulky groups (e.g., a cardo moiety), and aliphatic/alicyclic segments into backbones. It is now well recognized that introducing alicyclic substituents with low aromatic content—such as cyclobutene, cyclohexane, and cardo groups (e.g., diphenyl cyclohexane and adamantane)—as well as highly electronegative groups like trifluoromethyl (–CF_3) including the incorporation of fluorine atoms and –SO_2, or asymmetric and twisted rigid moieties, polymer chain packing can be disrupted considerably. These modifications effectively suppress CTC formation, leading to improved solubility, enhanced melt processability, and greater optical transparency in polyimides (PIs).

However, such improvements are often accompanied by a trade-off, as the thermo-mechanical stability of the materials tends to decrease. In contrast, the incorporation of highly conjugated and rigid aromatic structures, along with strongly polar, planar, or cross-linkable functional groups such as –CN, –OH, –CF_3, and acetylene, can markedly enhance thermal stability. This enhancement, however, is usually associated with increased coloration in the resulting polyimides. Consequently, achieving an optimal balance between solubility and optical transparency on one hand, and high thermo-mechanical stability on the other, remains a significant challenge.

To achieve highly transparent polyimides without sacrificing their outstanding thermal and mechanical characteristics, extensive molecular engineering approaches have been explored. Representative strategies involve the incorporation of bulky substituents, asymmetric moieties, and rigid yet non-coplanar structural units, along with the introduction of fluorinated groups and the utilization of alicyclic dianhydrides or diamines. Such molecular design strategies effectively weaken interchain interactions, inhibit dense chain packing, and disrupt extended π-conjugation, thereby suppressing the formation CTCs, which are chiefly responsible for the coloration observed in conventional polyimides. As a result, such design approaches enable the development of colorless and transparent polyimides (CPIs) with significantly improved optical properties.

Classification of Colorless Polyimides

Based on the monomers used in their main chains, polyimides are broadly classified into aromatic and non-aromatic PIs. Non-aromatic PIs are further divided into semi-aromatic and fully aliphatic types (Figure 4 and

5). Aromatic PIs are made from both aromatic diamine and dianhydride monomers. Semi-aromatic PIs contain only one aromatic component, where either the diamine or the dianhydride is aromatic but the rest is aliphatic. Fully aliphatic PIs are composed of aliphatic or alicyclic diamine and dianhydride monomers.

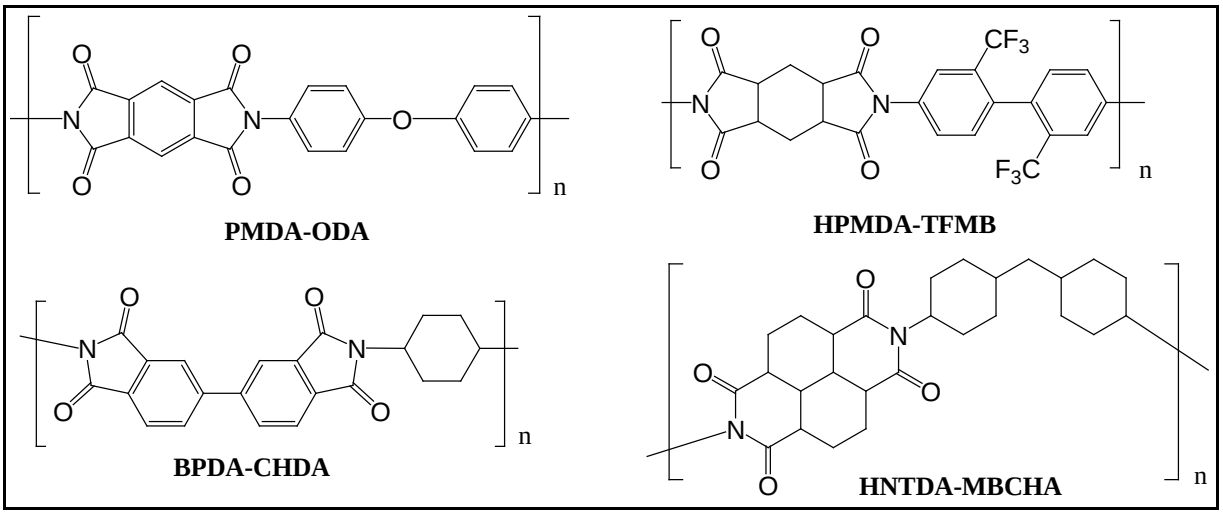

Figure 4: Different Kinds of PIs: Aromatic PI (PMDA-ODA), Semi Aromatic PIs (HPMDA-TFMB and BPDA-CHDA and Fully Aliphatic PI (HNTDA-MBCHA)

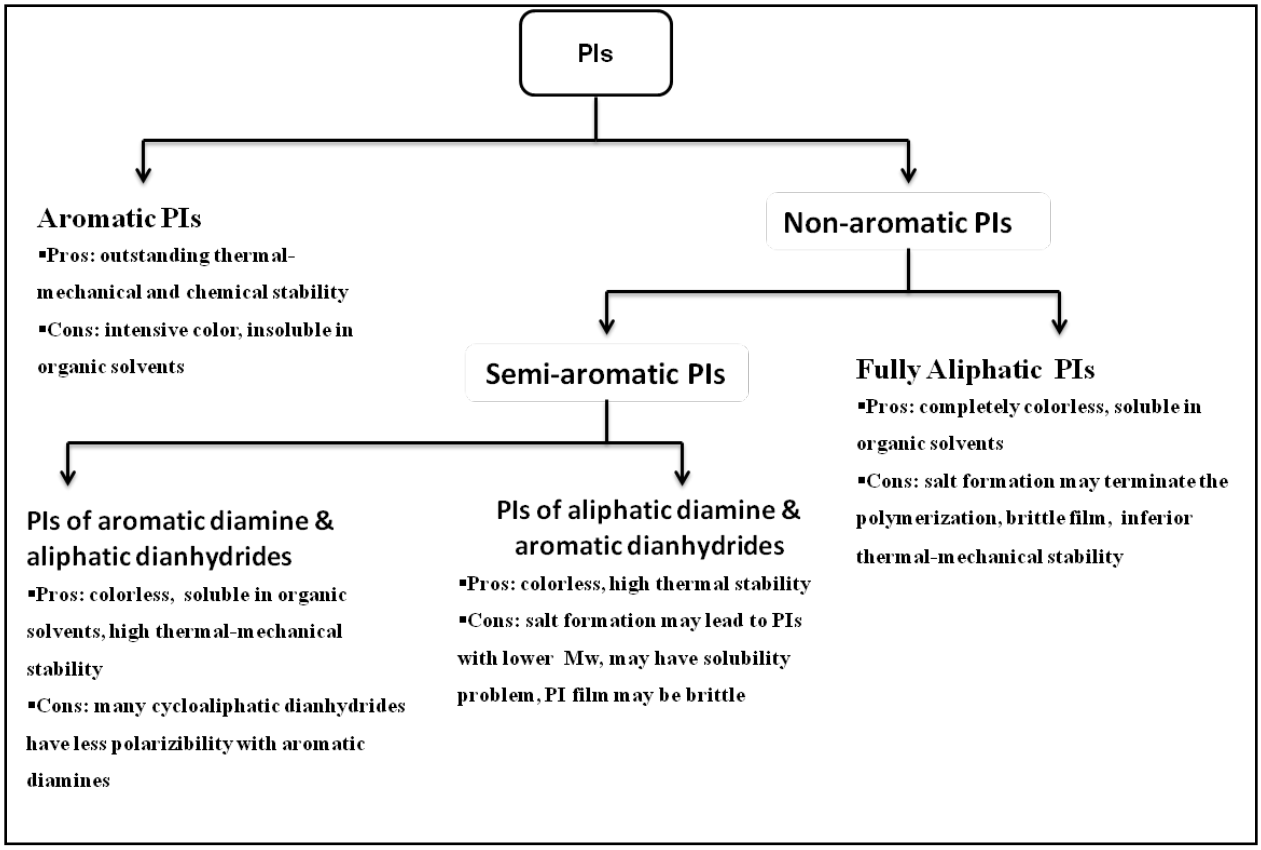

Figure 5: Different Kinds of PIs and Their Properties

Aromatic Colorless PIs

Aromatic polyimides represent one of the most extensively studied and commercially important classes of high-performance polymers. The typical examples of commercially successful aromatic PIs include Ultem® from G.E., DuPont's Kapton®, and Ube Industries Upilex®.Owing to their outstanding thermal stability, excellent mechanical strength, and superior electrical performance, these materials have been widely utilized as substitutes for metals and glass in advanced applications across the electronics, automotive, and aerospace sectors. The origin of many of these advanced thermo-mechanical and electronic properties of aromatic PIs is essentially due the formation of strong CTC between dianhydride and diamine moieties. However, the presence of these CTC interactions also leads to significant coloration in PI films, thereby limiting their applicability in optoelectronic fields where high optical transparency and colorlessness are essential. In addition, aromatic PIs generally exhibit poor processability because of their limited solubility in common organic solvents. Furthermore, most conventional aromatic PIs possess relatively high dielectric constants, which restrict their application in low-κ dielectric materials. Consequently, despite their excellent overall performance, the practical application of aromatic PIs in advanced optoelectronic devices and high-speed multilayer printed circuit boards remain constrained by their poor solubility, high dielectric constant, and inherent yellow to dark-yellow coloration. To overcome these drawbacks, researchers have extensively modified the polymer backbone through various structural design strategies. These include incorporating flexible or asymmetric linkages, introducing non-linear features such as kinks, spiro or bulky groups, as well as cardo or pendant substituents, and utilizing fluorinated aromatic monomers. Such modifications help in developing polyimides that are colorless, more processable, and capable of retaining high thermal stability.

Most of the early-developed colorless polyimides were primarily derived from fluorinated monomers (Figure 6). Rogers at DuPont in 1964 synthesized a CPI from 2,2-bis (3,4-dicarboxyphenyl)-hexafluoro propane dianhydride (6FDA) and 4,4′-(hexafluoroisopropylidene) dianiline (6FpDA). Later, Stclair (1985) and co-workers developed a series of CPIs based on 6FDA and diamines such as4,4'-oxydianiline (ODA). Reuter *et al.*(1988), reported additional CPIs based on 6FDA combined with diamines such as ODA, 3,3′-6F, and 4,4′-6F for optical waveguide applications. Among the various fluorinated CPIs, the 6FDA/TFDB polyimide, synthesized from 2,2-bis (3,4-dicarboxyphenyl) hexafluoro propane dianhydride (6FDA) and 2,2-bis (trifluoromethyl)-4,4′-diaminobiphenyl (TFDB), is considered one of the most successful systems. This polyimide exhibits excellent optical transparency in the visible region, near-colorless characteristics, low dielectric constant, good solubility in polar organic solvents, and outstanding thermal stability, with a glass transition temperature (T_g) exceeding 300 °C (Matsuura *et al.,* 1991). Ando *et al.* (1992) developed perfluorinated polyimides that contain no hydrogen atoms, although these films were not completely colorless. Choi *et al.* (2009) synthesized highly colorless tetra-chlorinated polyimides from 2,2′,5,5′-tetrachlorobenzidine (TCDB). Notably, the fully aromatic BPDA/TCDB polyimide demonstrated exceptional optical performance, with a T_{400}≈ 82%. Xi *et al.* (2024) also synthesized four aromatic colorless polyimides (4,7-9) for optoelectronic applications.

Despite their outstanding optical and thermal properties, these aromatic CPIs face several limitations. Their synthesis is often complex and costly, making them less practical as substrate materials compared to other polymers. Additionally, their CTE values are relatively high, whereas electronic device applications typically require CTE values below 20 ppm/°C.

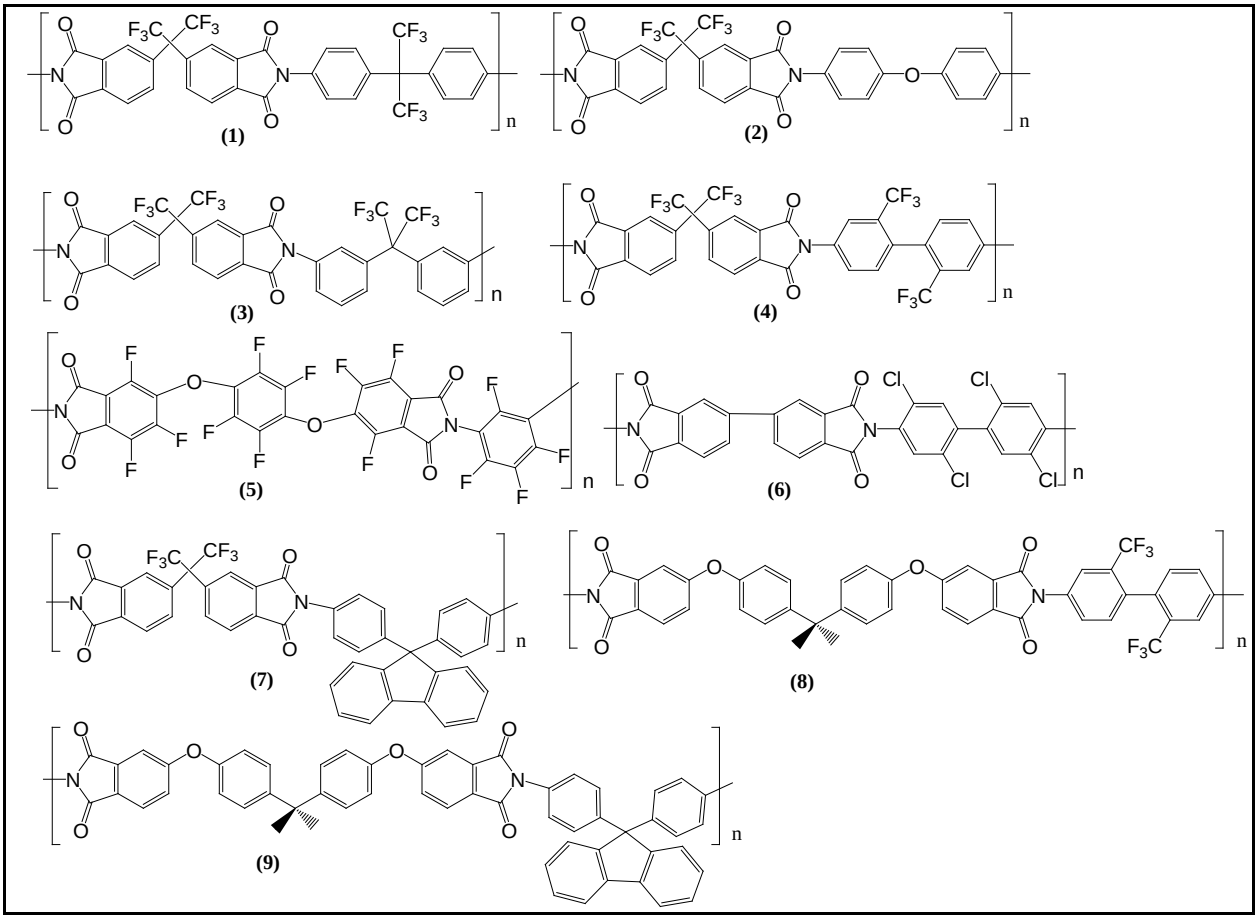

Figure 6: Aromatic Colorless PIs

A highly effective strategy for the synthesis of CPIs involves the incorporation of cycloaliphatic (non-aromatic) diamine and/or dianhydride monomers into the polymer backbone. Alicyclic polyimides have attracted considerable attention for optoelectronic and interlayer dielectric applications owing to their superior optical transparency and lower dielectric constants compared with fully aromatic polyimides. These favorable properties are primarily attributed to their lower molecular packing density, reduced chain polarity, and suppressed intra- and intermolecular charge-transfer (CT) interactions. However, significant challenges remain. The use of aliphatic diamines-in particular alicyclic diamines such as *trans*-1,4-cyclohexanediamine (t-CHDA) often results insoluble salts during the poly(amic acid) (PAA) formation step. This leads to premature chain termination or very low degrees of polymerization, ultimately yielding polymers with low molecular weight, which hinders their practical and industrial application.

In contrast, combining cycloaliphatic dianhydrides with aromatic diamine generally avoids salt formation and can produce colorless PIs. Nevertheless, many cycloaliphatic dianhydrides such as bicyclo [2.2.2] oct-7-ene-2,3,5,6-tetracarboxylic dianhydride (BTA) exhibit poor reactivity toward aromatic diamines. This leads to low-molecular-weight PAAs and results in brittle PI films. In contrast, 1,2,3,4-cyclobutanetetracarboxylic dianhydride (CBDA) stands out due to its unusually high reactivity, attributed to the ring strain in its anhydride structure. CBDA based PIs are usually colorless with high-molecular-weight, excellent thermal and mechanical properties. However, the inherently poor processability of these PIs significantly restricts their practical applications.

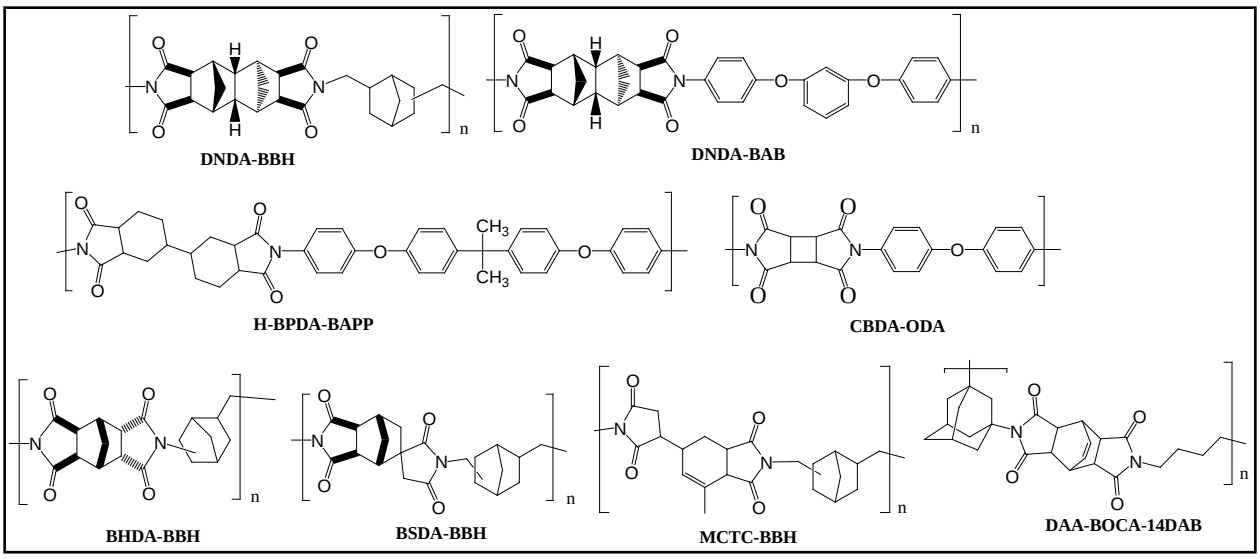

Figure 7: Non-aromatic Colorless PIs

Various alicyclic PIs have been developed to address these challenges. For instance, Matsumoto reported fully alicyclic PIs (DNDA-BBH, Figure 7) derived from polyalicyclic dianhydrides and bicyclic diamines, which exhibited exceptional glass transition temperatures (T_g) up to 400 °C while maintaining excellent colorlessness (Matsumoto, 1999). Similarly, systems based on dicyclohexyl tetracarboxylic dianhydrides combined with aromatic diamines (H-BPDA-BAPP) produced thermally stable (T_g between 210–270 °C) and transparent PI films (Shiotani *et al.,* 2001). Another cycloaliphatic dianhydride, CBDA is among the most effective monomers for producing colorless polyimides. Polyimides formed by combining CBDA with various aromatic diamines (e.g., 4,4'-oxydianiline and related structures) exhibit high transparency, good thermo-mechanical strength and low CTE, although their solubility remains limited when rigid diamines are used (Hasegawa *et al.,* 2007). Other cycloaliphatic dianhydrides, such as CPDA (Matsumoto, 2000) and hydrogenated pyromellitic dianhydrides (HPMDAs), have also been investigated. These exist in multiple isomeric forms with varying polymerizability and properties; for example, H′PMDA-based PIs tend to exhibit lower CTE due to greater chain linearity and rigidity (Hasegawa *et al.,* 2014). In addition, a wide variety of semi-aromatic and fully aliphatic PIs have been synthesized from different polyalicyclic dianhydrides and diamines [bis(2-hydroxyethyl) dodecylamine (BHDA), bis(sulfonamide)diamine (BSDA), Mast Cell Tryptase and Chymase (MCTC), Berberine Hydrochloride (BBH) in Figure 7 and 8]. These systems generally yield colorless, flexible, and free-standing films with good solution processability and high T_g values (typically 280–402 °C). Their optical properties include short cut-off wavelengths (below 235 nm for non-aromatic PIs and ~290–330 nm for semi-aromatic PIs), indicating excellent transparency.

A particularly effective structural motif is the incorporation of adamantane units—rigid, cage-like alicyclic structures—which enhance thermal stability without compromising transparency, solubility, dielectric properties, or CTE (Mathews *et al.,* 2006). Consequently, adamantane-containing semi-aromatic PIs have emerged as promising materials, combining high thermal resistance with desirable optical and processing characteristics.

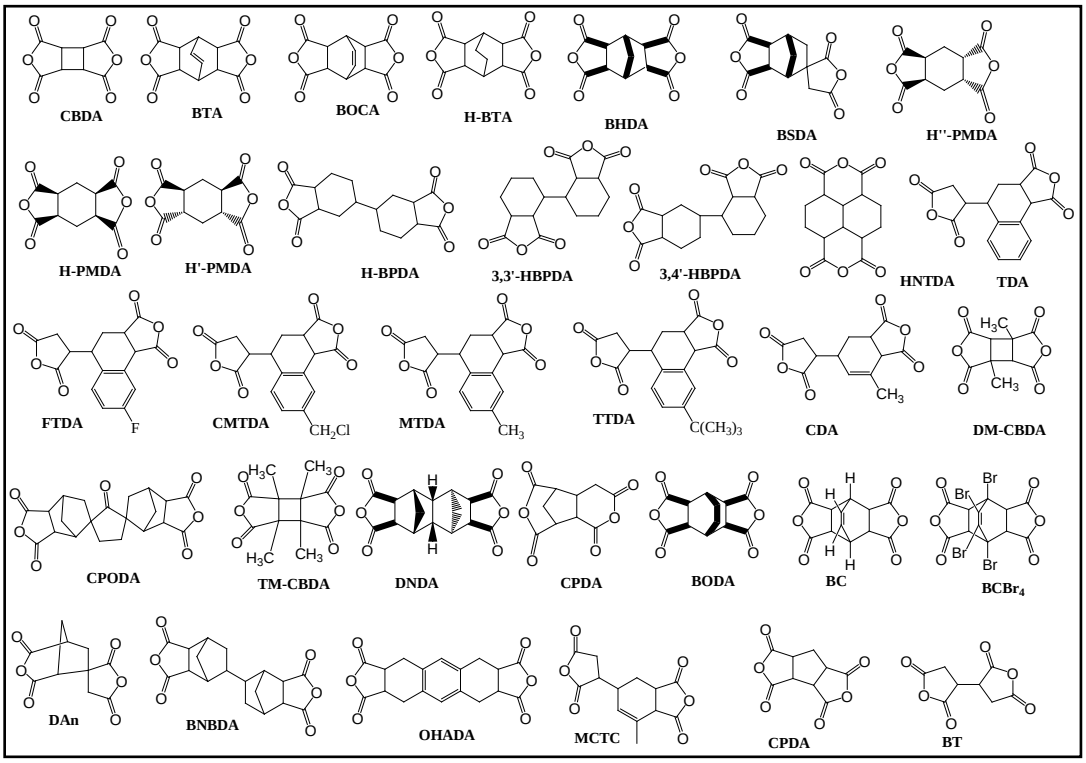

Figure 8: Cyclo-alicyclic Dianhydride Monomers

Non-aromatic (alicyclic) PIs generally exhibit excellent optical transparency along with satisfying solution processability and reasonable thermal stabilities. However, aliphatic polyimides are generally suitable only for applications requiring relatively low thermal stability. This is because the presence of aliphatic moieties increases chain flexibility and reduces backbone rigidity, leading to lower bond strength. Consequently, aliphatic polyimides generally exhibit lower thermal and dimensional stability than their fully aromatic counterparts.

Polymerization

Polyimides are typically synthesized via condensation polymerization of tetracarboxylic dianhydrides and diamines in dry, high-boiling polar solvents, such as Dimethyl Sulfoxide (DMSO), N,N-Dimethylformamide (DMF), N,N-Dimethylacetamide (DMAc), N-Methyl-2-pyrrolidone (NMP), gamma-butyrolactone (GBL), and *m*-cresol, to produce homogeneous poly(amic acid) (PAA) solutions. NMP is widely used for its strong solvency and relatively lower toxicity, but it can cause film coloration, often more than DMAc. GBL is a better alternative due to its balanced solubility, easier removal, lower hygroscopicity, and good oxidative stability. Molecular weight can be controlled by stoichiometric imbalance or monofunctional additives, while high monomer purity and contamination-free conditions are essential for achieving high optical transparency.

General two step synthesis

Polyimides (PIs) are mainly synthesized via a two-step polycondensation process (Figure 9). First, dianhydride and diamine react in polar aprotic solvents such as DMAc and NMP at low temperatures to form PAA. The PAA solution is then cast and imidized—either thermally (up to ~300°C) or chemically (e.g., using acetic anhydride/pyridine). Thermal imidization yields insoluble PIs with higher T_g and thermal stability due to greater molecular ordering, while chemical imidization produces more soluble and transparent PIs.

In chemical imidization, excess acetic anhydride (Ac_2O) and pyridine are added to the PAA solution, followed by stirring at room temperature for 12–24 h. This approach generally requires highly soluble polymer systems to prevent gelation or precipitation during the imidization process. The polymer is then precipitated, washed, and dried to obtain PI powder, with thorough removal of residual reagents to prevent side reactions and coloration. Chemically imidized PIs show better solubility, high optical transparency, and can be processed at lower temperatures (≤250°C), mainly due to end-capping of reactive amino groups.

Highly basic diamines—especially aliphatic or alicyclic ones like trans-1,4-cyclohexanediamine (*t*-CHDA)—can form insoluble salts with dianhydrides during PAA formation, leading to poor polymerization and very low molecular weight (η_{inh} ~0.07–0.08 dLg^{-1}). In contrast, cycloaliphatic dianhydrides with aromatic diamines avoid this issue and yield high-quality, colorless PIs. For polyalicyclic diamines, slow addition of diamine to the dianhydride solution is crucial to obtain a homogeneous PAA, while reversing the order often causes precipitation—an effect not seen with aromatic diamines.

One Step Synthesis

The one-pot thermal imidization procedure is well-suited for less reactive aromatic, fluorinated, and aliphatic/alicyclic monomers that often form insoluble salts during PAA formation. By conducting polycondensation at elevated temperatures without isolating PAA, this approach enables the synthesis of high-molecular-weight, soluble PIs. It is particularly effective for aliphatic polyimides, as imidization regenerates amines from salts, allowing polymerization to proceed. Typically carried out in solvents like *m*-cresol or DMAc with catalysts (e.g., isoquinoline), the process occurs at moderate temperatures (160–200 °C), minimizing side reactions. Overall, this method offers an efficient route to high-quality PIs when conventional two-step synthesis is limited by salt formation or low monomer reactivity.

Preparation of Polyimide Film in the Laboratory

The colorization of polyimide (PI) films is strongly affected by the preparation method. In the conventional PAA route, monomers are polymerized in solvents (e.g., DMAc, NMP), cast as films, and thermally imidized at high temperatures (300–350°C).

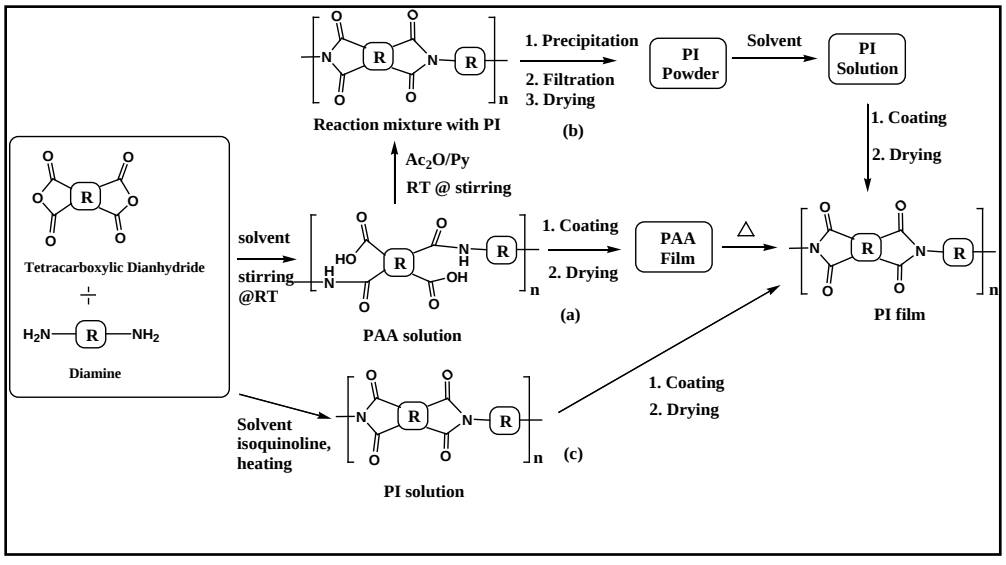

Figure 9: Synthesis and Film Fabrication of Polyimides Through Different Processing Routes: (a) Two-Step Thermal Imidization, (b) Chemical Imidization, and (c) One-Pot Method (Tapaswi & Ha, 2019)

However, instability of Peracetic acid (PAA) and high-temperature curing—especially in air—often lead to significant coloration, making this method less suitable for highly transparent films. In contrast, organo-

soluble PI solutions can be directly cast and dried at relatively lower temperatures (≤ 250°C), avoiding high-temperature imidization and thus minimizing discoloration (Figure 9). Overall, reducing thermal exposure and preventing oxidative conditions are key to achieving colorless PI films.

Recent Molecular Design Strategies for the Development of Colorless Polyimides

A sufficiently high optical transmittance (T_{400}> 80%) is essential for the application of PI films as substrates in display devices. To date, various molecular design strategies have been developed for the synthesis of CPIs. These include incorporating alicyclic structures, introducing bulky pendant groups (e.g., biphenyl, anthrone, fluorene and xanthenes), strong electron-withdrawing groups (–CF_3, –SO_2–), and using non-coplanar 2,2′-disubstituted biphenyl units, ortho-substituted diamines etc. These modifications help suppress charge-transfer interactions and improve optical transparency while preserving thermal performance. In this section, the most recent developments in the synthesis of colorless aromatic and non-aromatic PIs have been discussed in detail.

Introduction of Alicyclic Structures

Semi-alicyclic CPIs with improved dimensional stability were developed by Jiang and co-workers through the polymerization of amide-containing aromatic diamines, including 2,4-Diaminobutyric acid (Me DABA) and Chlorine-substituted diaminobenzanilide (ClDABA) (Figure 10), with alicyclic dianhydrides such as HPMDA and HBPDA (Figure 8) (Jiang *et al.,* 2020). The incorporation of rigid amide-linked diamine units effectively enhanced chain rigidity and suppressed thermal expansion behavior in the resulting PI films. Among the synthesized systems, the HPMDA–Me DABA-based CPI demonstrated the most favorable combination of thermo-mechanical and optical properties, exhibiting a low coefficient of thermal expansion (33.4 ppm/K, 50–250°C), a high glass transition temperature (349°C), and excellent thermal stability with a T5% value of 438.1°C. In addition, the film maintained high optical clarity, showing a transmittance of 82.3% at 400 nm for a thickness of 25 µm, together with low yellowness and haze values of 2.18 and 2.15%, respectively. These findings demonstrate that the introduction of rigid-rod amide functionalities into semi-alicyclic PI backbones is an effective molecular design strategy for achieving low-CTE CPI films with balanced thermal and optical performance suitable for optoelectronic substrate applications.

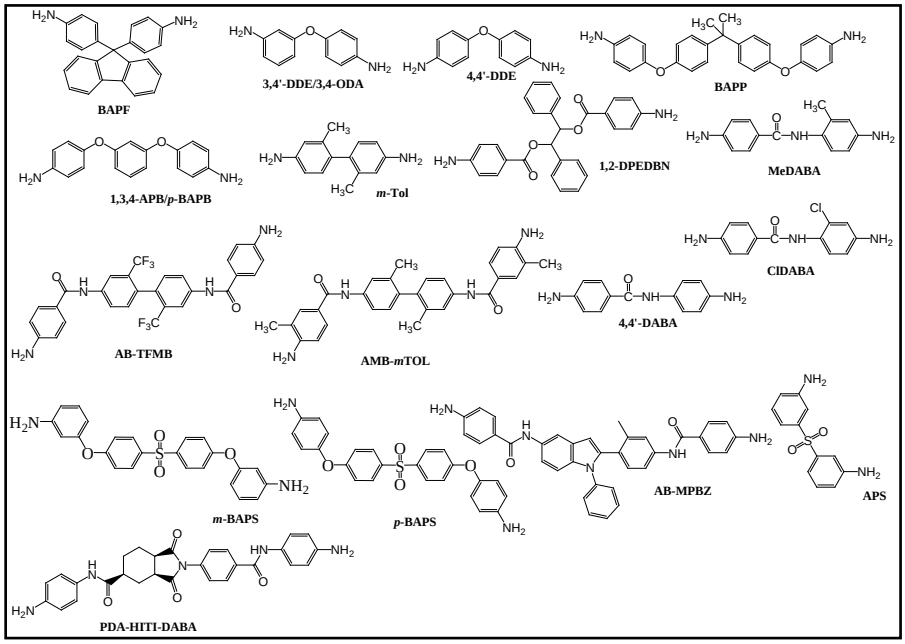

Figure 10: Aromatic Diamines Used for Semi-Aromatic CPIs Synthesis

Miao *et al.* (2020) successfully synthesized three novel adamantane-containing diamines-ADMDA, DMADMDA, and FADMDA (Figure 11) via Friedel–Crafts alkylation. Using these diamines along with four dianhydrides (6FDA, HPMDA, BPDA, and BTA), three series of polyimides (PIs) were prepared through a one-step thermal imidization process. The results demonstrated that the incorporation of highly rigid, bulky, and non-coplanar adamantane moieties into the polymer backbone significantly improved the thermal, mechanical, and optical properties of the resulting polyimides, while simultaneously maintaining good solubility, unlike conventional aromatic polyimides. The T_g and 5% weight-loss temperature (T_5%) values ranged from 285–440°C and 444–540°C, respectively, matching or surpassing those of traditional aromatic systems. In particular, CPIs derived from DMADMDA and alicyclic dianhydrides exhibited outstanding optical properties, including $\lambda_0$below 300 nm, transmittance (T_{400}) above 80%, and low color intensity. The presence of two *ortho*-methyl substituents in DMADMDA increased interchain spacing (d-spacing), leading to higher T_g, lower CTE, and improved optical transparency. However, this modification resulted in somewhat reduced mechanical properties compared to ADMDA- and FADMDA-based counterparts.

Another cycloaliphatic dianhydride, CpODA (Figure 9), was polymerized with various aromatic diamines—1,3-BAB, 4,4′-DDE, 3,4′-DDE, 4,4′-DABA, and *m*-TOL—through both chemical and thermal imidization methods to produce semi-alicyclic polyimides (PIs) (Prof. Toshihiko Matsumoto group) (Ozawa *et al.,* 2021). Most of the PI films exhibited excellent thermal stability, with T_5% above 450°C, decomposition temperatures between 475 to 501°Cand T_g exceeding 330°C. The films also demonstrated CTE in the range of 17–57 ppm/K. All prepared PI films were completely colorless, with cutoff wavelengths below 337 nm, indicating high optical transparency. Notably, the films synthesized via the chemical method displayed superior optical performance, which was attributed to an “end-capping effect.”

Hasegawa *et al.* (2022), synthesized amide/imide-containing aromatic diamines, including AMB-*m*TOL, AB-ATAB, AB-APAB, AB-TFMB, AB-*m*TOL, and PDA-HTI-DABA (Figure 10). The diamine was polymerized with H-PMDA in γ-butyrolactone (GBL). The polyimide films of H-PMDA/AB-TFMB and H-PMDA/AMB-mTOL exhibited a well-balanced set of properties, including low CTE in the range of 24–30 ppm/K, high optical transparency (T_{400}> 80%), elevated glass transition temperatures (T_g > 360°C), and adequate ductility.

Ingo Pinnau and co-workers reported the synthesis of two new organo-soluble and colorless polyimides via the polycondensation of two bicyclic alicyclic dianhydrides, BC and $BCBr_4$, with the spirobisindane-based diamine SBIDA (Figure 11) (Abdulhamid *et al.,* 2019) The resulting CPIs exhibited good thermal stability, with decomposition temperatures of approximately 420°C and 352°C and also showed intrinsic microporosity. These polyimides were readily solution-processable and demonstrated strong mechanical performance, with tensile moduli in the range of 1.15–1.4 GPa, tensile strengths of 27–28 MPa, and elongation at break between 2% and 4%. Notably, the $BCBr_4$–SBIDA system displayed very high oxygen (O_2) permeability while maintaining comparable O_2/N_2 selectivity. These CPIs are considered promising candidates for membrane-based air separation applications owing to their favorable combination of optical transparency, solubility, and thermal stability.

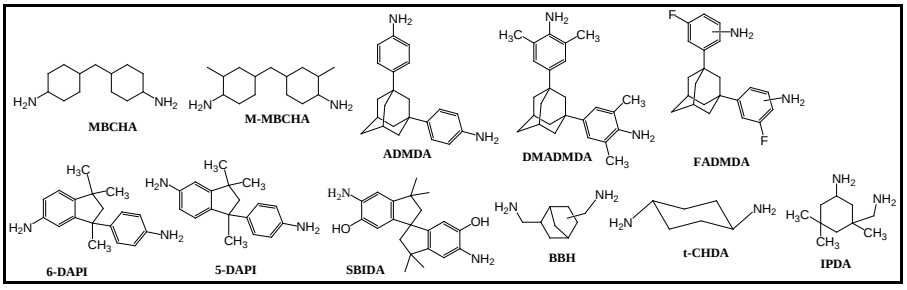

Figure 11: Cycloaliphatic Diamine Monomers Discussed in This Chapter

Hasegawa and co-workers carried out extensive investigations on the development of highly ductile colorless cycloaliphatic polyimide (PI) films, aiming to overcome the intrinsic brittleness commonly associated with such materials (Hasegawa, 2017). Their work systematically clarified the influence of molecular structure on the mechanical flexibility of cycloaliphatic PIs. In thermally imidized systems derived from 4,4′-ODA and various tetracarboxylic dianhydrides, the film ductility was found to decrease in the order of HQDA > PMDA > s-BPDA > TA-HQ > CBDA, indicating that CBDA-based systems are less favorable for achieving mechanically robust and flexible PI films.

The study further demonstrated that the incorporation of ether-linked dianhydrides, including BPADA, ODPA, and HQDA, effectively enhanced the ductility of polyimides prepared from the rigid cycloaliphatic diamine t-CHDA, with BPADA (Figure 12) exhibiting the most significant toughening effect. In the case of the more flexible MBCHA-based system, copolymerization of PMDA/MBCHA with a small amount of IPDA (5–30 mol%) unexpectedly produced substantial improvements in film toughness, despite the inability of the corresponding PMDA/IPDA homopolyimide to form flexible films. In particular, the copolyimide containing 20 mol% IPDA displayed a remarkable elongation at break of 57%, together with high optical transparency (T400 = 83.7%) and a high glass transition temperature (T_g = 317°C). The enhanced ductility was attributed to increased chain mobility and facilitated intermolecular chain slippage within the polymer network.

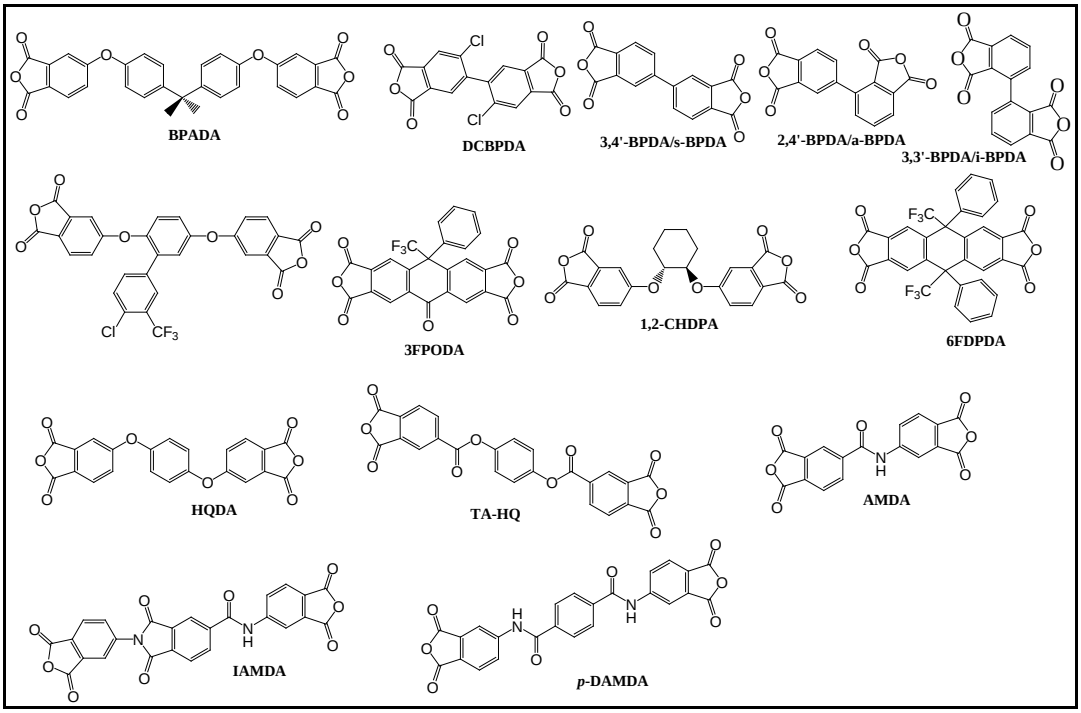

Figure 12: Dianhydride Monomers Discussed in This Section

A novel alicyclic dianhydride, OHADA, was synthesized and polycondensed with 4,4′-ODA to afford a colorless PI film exhibiting high thermal stability with T_g > 300°C. This elevated Tg was attributed to the rigid OHADA structure lacking rotatable single bonds (Hasegawa *et al.,* 2023). Further polymerization with TFMB enhanced the thermal performance, yielding a PI with T_g ≈ 340°C and improved decomposition resistance (higher T_d^5 under N_2) compared to other TFMB-based semi-alicyclic systems, although the CTE remained relatively high. The OHADA/TFMB system also exhibited pronounced thermoplastic behavior, likely due to its ladder-like, sterically distorted structure. Subsequent incorporation of AB-TFMB further

increased T_g to 355°C and reduced the CTE to 41.5 ppm/K, while preserving high optical transparency and good solubility.

Introduction of strong electronegative groups such as trifluoromethyl (−CF3) or fluorine atoms in polyimide main chains

Fluorinated polyimides (PIs), particularly those incorporating trifluoromethyl (–CF_3) groups into their main chains, have been widely studied as an effective strategy to suppress charge-transfer complex (CTC) formation and thereby enhance optical transparency and solution processabilty without deteriorating their excellent properties. In general, increasing the fluorine content in PIs leads to improved transparency and reduced coloration. For example, PI films containing approximately 28% fluorine exhibit significantly enhanced optical properties, with $\lambda_0$around 310 nm and transmittance at 500 nm (T_{500}) of about 94%. However, despite these advantages, highly fluorinated PI films face serious challenges when used as transparent substrates in device fabrication processes such as cleaning, peeling and etching. These films often show poor solvent resistance, leading to swelling or even structural damage upon exposure to solvents, which can compromise device performance. One practical approach to address this issue is to reduce the fluorine content in the PI structure. However, this typically results in a noticeable deterioration of optical properties. Furthermore, the high cost of fluorinated diamine and dianhydrides presents an additional limitation, restricting the widespread application of highly fluorinated PI films.

Min *et al.* (2020) reported solution-processable fluorinated CPIs synthesized via one-step polycondensation of 6FDA with either 6FDAM (Figure 13) or TFMB, yielding 6FDA-6FDAM-PI and 6FDA-TFMB-PI. The resulting films exhibited smooth morphology and suitable surface energy, enabling their use as gate insulators in organic transistors, where enhanced device performance was attributed to improved semiconductor ordering and fluorine-rich interfacial effects (Min *et al.*, 2020).

Liu *et al.* (2016) developed fluorinated poly (ether imide)s from a novel bis (ether dianhydride) TFCPDA (Figure 13) and various aromatic diamines (PDA, ODA, APB, 6FAPB, and 9F-Cl-APB (Figure 13)).The resulting poly (ether imide) films were nearly colorless exhibiting high transparency (%T_{450}≈76–88%), low cutoff wavelengths (<370 nm), excellent solubility, and balanced thermal–mechanical properties. Furthermore, their refractive indices could be precisely tuned through copolymerization, ranging from 1.6217 to 1.5523. The optical performance was attributed to reduced intermolecular interactions induced by –CF_3 and -Cl substituents.

Another type of TFMB-based fluorinated CPI was reported by Jikang Liu and co-workers. In this study, two series of copolyimide films, namely 3F6FP/C-PI-x and 3F6FP/H-PI-x, were synthesized using different molar ratios of 6FDA and 3FPODA dianhydrides (Figure 13) via chemical and thermal imidization processes, respectively (Liu *et al.,* 2026). The resulting colorless copolyimide films exhibited significantly enhanced the thermo-mechanical properties. CPI films resulted from chemical imidization exhibited better optical, thermal, and mechanical performance compared to those obtained via thermal imidization, indicating that the former imidization process is more suitable for fabricating high-performance CPIs. Among the samples, the 3F6FP/C-PI-4 film—prepared by chemical imidization with a 3FPODA to 6FDA molar ratio of 4:6—showed the best overall performance. Its optical and other key properties met the requirements for applications in transparent FPCBs.

A novel semi-alicyclic dianhydride, 6FDPDA (Figure 13) was recently developed by Wang *et al.*(2023). Colorless polyimide films were synthesized by copolymerizing 6FDPDA with two other commercially available aromatic dianhydrides (BPDA and 6FDA) and one fluorinated diamine, TFDB following two-step chemical imidization procedure (Wang *et al.,* 2023). Owing to its ladder-like semi-alicyclic framework, along with bulky –CF_3 and phenyl substituents, 6FDPDA offers two key advantages: effective disruption of conjugation along the polymer backbone and suppression of intermolecular chain stacking. These structural features significantly improve the thermal stability and optical transparency of the resulting CPI films. In particular, when 6FDA was employed as the comonomer, the resulting CPI films exhibited outstanding

performance, including high optical transmittance (%T_{550}≈ 90%), a low YI of 2.45, a CTE of 16.5 ppm/K, and a T_g exceeding 450 °C. All these findings demonstrate that 6FDPDA is a highly promising monomer for the development of high-performance CPI materials, especially for optoelectronic applications such as flexible AMOLED display substrates.

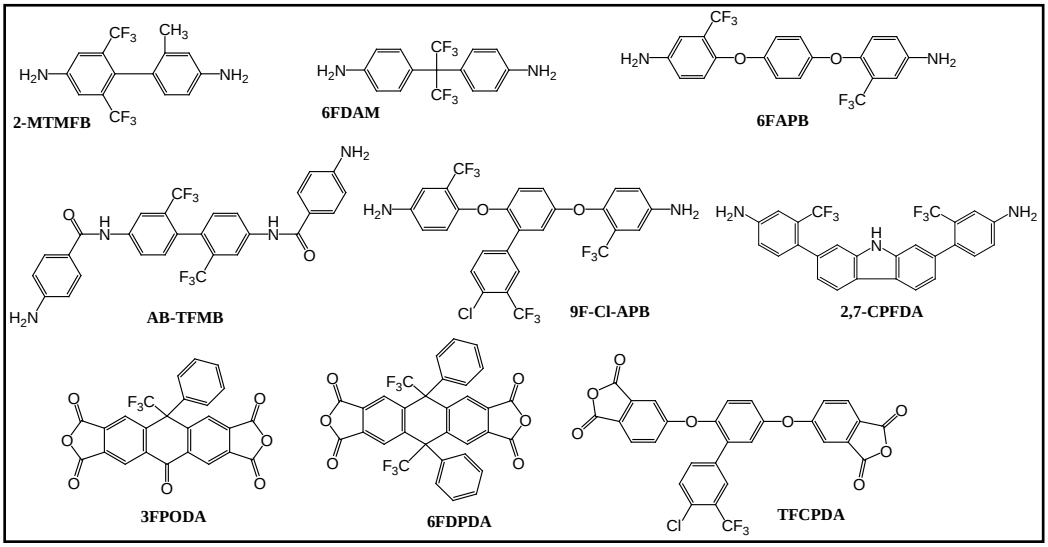

Figure 13: Trifluoromethyl (-CF3) Substituted Monomers

Introduction of Bulky Pendant Substituents

The incorporation of bulky pendant groups such as biphenyl, anthrone, fluorene, and xanthenes into the polyimide network is widely regarded as an effective strategy to enhance solubility while retaining high thermal stability. These bulky substituents reduce chain conjugation and suppress intermolecular charge-transfer interactions, thereby minimizing coloration and improving optical transparency.

Wu *et al.* (2019b) synthesized a new diamine, Benzoporphyrin Derivative Monoacid ring A (BPDMA) (Figure 14), featuring bulky biphenyl pendant groups and *ortho*-dimethyl substitution, through a one-pot condensation reaction of 4-biphenyl carboxaldehyde and 2,6-dimethylaniline. Subsequently, BPDMA was polymerized with various dianhydrides through a one-step polycondensation process at elevated temperature. The resulting PI films were colorless to light yellow, with λ_0 ≈ 286–358 nm and %T exceeding 80% in the 400–780 nm range. In addition, these PIs exhibited excellent solubility in common organic solvents, high T_g values (343–456°C), and good mechanical flexibility (Wu *et al.,* 2019 a).

A new diamine (BAPPA, Figure 14), incorporating anthrone units as pendant substituents was synthesized by Zhang *et al.* (2020). This monomer was polymerized with six different dianhydrides, including ODPA, to prepare polyesterimides with the aim of achieving a balanced combination of optical transparency and thermal stability. The incorporation of anthrone and pyridine moieties into the polymer backbone effectively restricted chain mobility, resulting in significantly enhanced thermal properties. The resulting polyesterimides exhibited high thermal stability with T_g values of 290–388°C. In addition, the cutoff wavelengths (λ_0) were between 374 nm to 427 nm, while the transmittance at 500 nm (T_{500}) was above 83% for films with a thickness of 40 µm. Notably, even the relatively flexible PIODPA-BAPPA system maintained a high T_g of up to 306°C, along with excellent optical transparency (T_{500} = 89%) (Zhang *et al.,* 2020).

Hasegawa *et al.* (2019) synthesized symmetric and asymmetric spiro-type dianhydrides (TA-*s*-Spiro and TA-*a*-Spiro) and diamines (AB-*s*-Spiro and AB-*a*-Spiro) (Figure 14) containing ester linkages and fluorenyl pendant groups to prepare chemically imidized polyesterimides. The resulting polymers exhibited excellent solubility, high thermal stability, and good optical transparency due to the combined effect of ester linkages

and bulky fluorenyl moieties. Among them, the CBDA/AB-a-Spiro/TFMB-based polyesterimides showed an excellent balance of properties, including low CTE (10.5 ppm/K), high transparency (T_{400} = 80.8%), and a high T_g of 351°C. The bulky, linear, and locally planar structure of AB-*a*-Spiro is believed to enhance solubility while simultaneously contributing to the reduced CTE in the resulting polyesterimides.

A new diamine, 9,9-Bis(4-aminophenyl)xanthene (BAPX) in (Figure 14), featuring a pendant xanthene unit, was synthesized and subsequently polymerized with various dianhydrides, including 6FDA. The incorporation of the xanthene unit was found to reduce the crystallinity of the resulting polymers, while significantly enhancing their optical transparency, solubility, and thermal performance. The obtained polyimide films exhibited λ_0 in the range of 367–415 nm, transmittance at 500 nm (T_{500}) between 73.2% and 84.1%, glass transition temperatures (T_g) of 308–348°C. Among them, polyimide derived from BAPX and 6FDA demonstrated the most balanced overall properties, with a λ_0 of 367 nm, T_{500} of 84.1% and T_g of 321°C (Zhang *et al.,* 2019).

Two aromatic diamines (24DABSBF and35DABSBF) bearing spirobifluorene (SBF) units were synthesized via a four-step route involving bromination, borylation, Suzuki coupling, and subsequent reduction of dinitro intermediates. The resulting diamines were polymerized with PMDA, CBDA, and 6FDA through thermal or chemical imidization to yield six polyimides (PIs).The PI films, particularly PI-35CB, PI-356F, PI-24CB, and PI-246F, were nearly colorless and exhibited high optical transparency, with PI-35CB showing up to 95% transmittance at 400 nm. This excellent transparency was due to the amorphous nature induced by the bulky and rigid SBF units, which suppress intermolecular interactions and reduce chain packing. PIs derived from 35DABSBF showed slightly better transparency than those from 24DABSBF, likely due to the lower inherent coloration of the former monomer (Wen *et al.,* 2017).

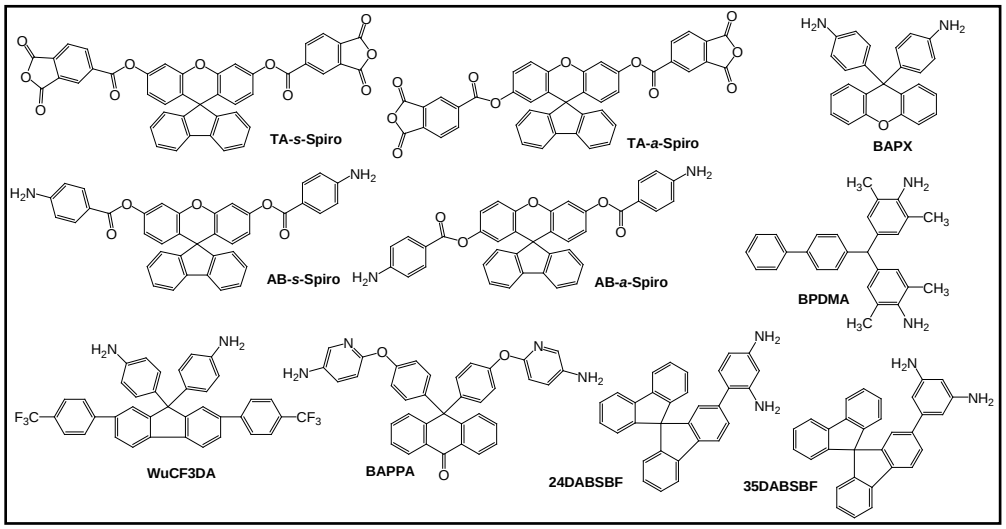

Figure 14: Diamines or Dianhydride Monomers with Bulky Pendant Substituents

Liu *et al.* (2017) synthesized a series of polyimides (PIs) incorporating bis(phenyl)fluorene units substituted with *p*-trifluoromethylphenyl groups. The diamine monomer ($WuCF_3DA$, Figure 14) features a non-planar structure, in which a conjugated fluorene core is connected to phenylamine units through a tetrahedral carbon, with $–CF_3$ groups at the terminal benzene rings. $WuCF_3DA$ was prepared via bromination, Suzuki coupling, and subsequent reduction, with a high yield of 94%. $WuCF_3DA$-based PIs prepared from 6FDA, BPDA, BTDA, and PMDA exhibited excellent thermal stability (T_g up to 494 °C), good solubility, and flexible amorphous films with nearly colorless appearance. The films showed cutoff wavelengths of 374–425 nm and high optical transparency, with $WuCF_3$-6FDA exhibiting 83.7% transmittance at 450 nm and over 90% in the visible region. The enhanced transparency was attributed to the disruption of conjugation by sp^3-

hybridized fluorene carbons and the reduced intermolecular interactions caused by bulky aromatic side groups (Liu *et al.,* 2017).

Introduction of Substituents on The Ortho Position of Diamine

Substitution of methyl, isopropyl, or tert-butyl groups at the ortho position of aromatic diamines introduces steric hindrance around the imide C–N bond, thereby loosening chain packing and weakening intermolecular interactions. This effectively suppresses intermolecular charge-transfer complex formation, leading to enhanced optical transparency of PI films. Simultaneously, the restricted rotational mobility around the imide linkage increases chain rigidity and improves thermal stability, while the enlarged interchain spacing enhances polymer solubility.

Considerable attention has been devoted to the incorporation of methyl (Hasegawa *et al.,* 2022; Nam *et al.,* 2017; Bong *et al.,* 2016), isopropyl (Liu *et al.*, 2015) and tert-butyl (Yi *et al.,* 2015; Huang *et al.,* 2015) substituents at the ortho position of diamines to improve the performance of CPIs. Representative diamine containing these substituents are summarized in Figure 15. Liu *et al.* (2019) synthesized a series of semi-aromatic PIs using alicyclic dianhydrides (CHDA and BCDA) and methyl-substituted aromatic diamines containing bulky phenyl and fluorinated pendant groups, namely BAPM, BAFM, and BATFM (Figure 15). The resulting PI films exhibited excellent optical transparency with cutoff wavelengths of 282–286 nm and transmittance above 89% at 500 nm, along with high T_g values of 364–387 °C. In addition, the polymers showed low dielectric constants (2.72–2.80). Among them, the BATFM/CHDA-based PI demonstrated particularly outstanding transparency and minimal coloration despite its relatively low fluorine content (<10 wt%).

Wu *et al.* (2019b) reported several 6FDA based CPIs with aromatic diamines bearing methyl substituent (2255TMB, 33DMB and 22DMB, Figure 15) with varying number and positions via a one-step polymerization reaction. The resulting PIs showed good solubility, high thermal stability, low dielectric constants and appreciable optical transparency. Among them, 2255TMB-PI, containing four methyl substituents at the 2,2′,5,5′-positions, showed the best overall performance, including high transparency (T_{400}> 82%), high T_g (~407°C), excellent thermal stability (Td_5> 500°C), low CTE (~34.3 ppm/K), and a low dielectric constant (~2.84). The enhanced properties were mainly attributed to the strong steric hindrance effect of the ortho-methyl groups.

Li and co-workers (2017) synthesized several soluble, optically transparent PIs with excellent thermal stability by using alkyl substituted diamine containing naphthalene units. Three naphthalene-based diamines bearing –H (BAN-1), $–CH_3$ (BAN-2), and $–CH(CH_3)_2$ (BAN-3) at the ortho-positions were synthesized and polymerized with ODPA, BPDA, and 6FDA via a one-step microwave-assisted method. All resulting PIs exhibited high optical transparency, with BAN-2 and BAN-3 based PIs showing cutoff wavelengths below 400 nm and transmittance exceeding 84% at 450 nm. Transparency increased with steric hindrance in the order: BAN-3 > BAN-2 > BAN-1, confirming the effectiveness of ortho-substitution in suppressing charge-transfer interactions. Thermally, BAN-2 based PIs showed the highest T_g (>340 °C), while BAN-3 based PIs exhibited relatively lower T_g values. These results demonstrate that increasing steric hindrance improves optical transparency but may slightly reduce chain rigidity and thermal performance.

Wu and co-workers (2020) synthesized a new semi-aliphatic diamine, CHMBTBA (Figure 15), containing bulky cyclohexyl and *ortho-tert*-butyl groups, and polymerized it with various aromatic dianhydrides to prepare semi-aliphatic PIs. The resulting films exhibited excellent solubility, high optical transparency (>86% in the visible region), low coloration, and high T_g values (>310°C). In addition, the polymers showed low water absorption and good mechanical properties. The study demonstrated that the incorporation of *tert*-butyl and cyclohexyl groups is an effective strategy for improving the transparency of PIs while maintaining excellent thermal performance.

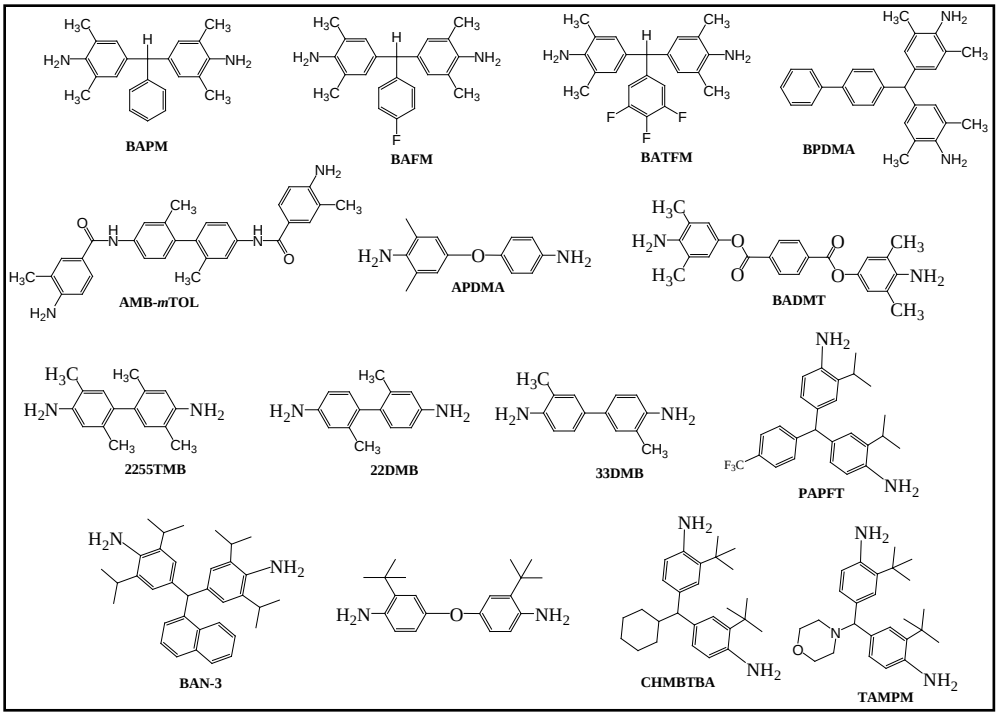

Figure 15: Ortho-Substituted Aromatic Diamines

Conclusion

Colorless and transparent polymeric materials possessing high glass transition temperatures (T_g), low coefficients of thermal expansion (CTE), and excellent thermo-mechanical performance are highly desirable for advanced optoelectronic applications. Among high-performance polymers, polyimides (PIs) are regarded as one of the few materials capable of maintaining T_g values above 300°C. Nevertheless, conventional fully aromatic PIs generally exhibit intense coloration, which restricts their application in optical and electronic devices requiring high transparency. This coloration primarily originates from intra- and intermolecular charge-transfer (CT) interactions between electron-donating diamine moieties and electron-accepting dianhydride units.

Considerable efforts have therefore been devoted to suppressing CT interactions through molecular design strategies, including the incorporation of bulky substituents, asymmetric or non-coplanar structures, fluorinated groups, and alicyclic segments. These modifications effectively enhance optical transparency and solubility while often preserving the excellent thermal properties of PIs. However, the practical development of colorless polyimides (CPIs) is still constrained by the high cost of fluorinated monomers and the relatively low reactivity and thermal stability associated with alicyclic monomers. Despite these challenges, CPIs are considered promising candidates for next-generation flexible and transparent electronic devices. Further research is needed to achieve a balanced combination of processability, optical transparency, thermal resistance, dimensional stability, and low CTE. In this regard, the development of novel monomer architectures through advanced synthetic methodologies, such as cross-coupling and multicomponent reactions, is expected to play a key role in improving performance while reducing production costs, thereby broadening the application potential of CPI materials.

Acknowledgement

The author would like to sincerely acknowledge the Department of Chemistry, Narasinha Dutt College, India, for its continuous support and encouragement throughout the preparation of this article.

References

Abdulhamid, M. A., Ma, X., Ghanem, B. S., & Pinnau, I. (2019). Synthesis and Characterization of Organo-Soluble Polyimides Derived from Alicyclic Dianhydrides and a Dihydroxyl-Functionalized Spirobisindane Diamine. *ACS Applied Polymer Materials, 1*(1), 63–69. https://doi.org/10.1021/acsapm.8b00036

Ando, S., Matsuura, T., & Sasaki, S. (1992). Perfluorinated polyimide synthesis. *Macromolecules, 25*(21), 5858–5860. https://doi.org/10.1021/ma00047a045

Bong, S., Yeo, H., Goh, M., Ku, B. C., Kim, Y. Y., Bong, P.-H., Park, B., & You, N. H. (2016). Synthesis and characterization of colorless polyimides derived from 4-(4-aminophenoxy)-2,6-dimethylaniline. *Macromolecular Research, 24*(12), 1091–1097. https://doi.org/10.1007/s13233-016-4153-y

Choi, M. C., Hwang, J. C., Kim, C., Ando, S., & Ha, C. S. (2010). New colorless substrates based on polynorbornene-chlorinated polyimide copolymers and their application for flexible displays. *Journal of Polymer Science Part A: Polymer Chemistry, 48*(8), 1806–1814. https://doi.org/10.1002/pola.23949

Choi, M.-C., Wakita, J., Ha, C.-S., & Ando, S. (2009). Highly Transparent and Refractive Polyimides with Controlled Molecular Structure by Chlorine Side Groups. *Macromolecules, 42*(14), 5112–5120. https://doi.org/10.1021/ma900104z

Crawford, G. P. (Ed.). (2005). *Flexible flat panel displays*. John Wiley & Sons.

Guan, Y., Wang, D., Song, G., Dang, G., Chen, C., Zhou, H., & Zhao, X. (2014). Novel soluble polyimides derived from 2,2′-bis [4-(5-amino-2-pyridinoxy)phenyl] hexafluoropropane: Preparation, characterization, and optical, dielectric properties. *Polymer, 55*(14), 3634–3641. https://doi.org/10.1016/j.polymer.2014.06.078

Hasegawa, M. (2017). Development of solution-processable, optically transparent polyimides with ultra-low linear coefficients of thermal expansion. *Polymers, 9*(10), 520. https://doi.org/10.3390/polym9100520

Hasegawa, M., Fujii, M., Ishii, J., Yamaguchi, S., Takezawa, E., Kagayama, T., & Ishikawa, A. (2014). Colorless polyimides derived from 1S,2S,4R,5R-cyclohexanetetracarboxylic dianhydride, self-orientation behavior during solution casting, and their optoelectronic applications. *Polymer, 55*(18), 4693–4708. https://doi.org/10.1016/j.polymer.2014.07.032

Hasegawa, M., Horiuchi, M., & Wada, Y. (2007). Polyimides Containing Trans-1,4-cyclohexane Unit (II). Low-K and Low-CTE Semi- and Wholly Cycloaliphatic Polyimides. *High Performance Polymers, 19*(2), 175–193. https://doi.org/10.1177/0954008306073178

Hasegawa, M., Ichikawa, K., Takahashi, S., & Ishii, J. (2022). Solution-Processable Colorless Polyimides Derived from Hydrogenated Pyromellitic Dianhydride: Strategies to Reduce the Coefficients of Thermal Expansion by Maximizing the Spontaneous Chain Orientation Behavior during Solution Casting. *Polymers,14*(6), 1131. https://doi.org/10.3390/polym14061131

Hasegawa, M., Sato, H., Hoshino, K., Arao, Y., & Ishii, J. (2023). Colorless Polyimides Derived from Octahydro-2,3,6,7-anthracenetetracarboxylic Dianhydride. *Macromol, 3*(2), 175–199. https://doi.org/10.3390/macromol3020011

Hasegawa, M., Takahashi, S., Tsukuda, S., Hirai, T., Ishii, J., Yamashina, Y., & Kawamura, Y. (2019). Symmetric and asymmetric spiro-type colorless poly(ester imide)s with low coefficients of thermal expansion, high glass transition temperatures, and excellent solution-processability. *Polymer, 169*, 167–184. https://doi.org/10.1016/j.polymer.2019.02.020

Huang, X., Mei, M., Liu, C., Pei, X., & Wei, C. (2015). Synthesis and characterization of novel highly soluble and optical transparent polyimides containing tert-butyl and morpholinyl moieties. *Journal of Polymer Research, 22*, 169. https://doi.org/10.1007/s10965-015-0820-5

Itamura, S., Yamada, M., Tamura, S., Matsumoto, T., & Kurosaki, T. (1993). Soluble polyimides with polyalicyclic structure. I. Polyimides from bicyclo[2.2.2]oct-7-ene-2-exo,3-exo,5-exo,6-exo-tetracarboxylic 2,3:5,6-dianhydrides. *Macromolecules, 26*(14), 3490–3493. https://doi.org/10.1021/ma00066a005

Jiang, G. L., Wang, D. Y., Du, H. P., Wu, X., Zhang, Y., Tan, Y. Y., Wu, L., Liu, J. G., & Zhang, X. M. (2020). Reduced Coefficients of Linear Thermal Expansion of Colorless and Transparent Semi-Alicyclic Polyimide Films via Incorporation of Rigid-Rod Amide Moiety: Preparation and Properties. *Polymers, 12*(2), 413. https://doi.org/10.3390/polym12020413

Lee, L. T. C., Pearce, E. M., & Hirsch, S. S. (1971). Novel aliphatic polymers containing imide ring. I. Polyspiroimide based on methane tetra acetic acid. .*Journal of Polymer Science Part A-1: Polymer Chemistry, 9*(11), 3169–3174. https://doi.org/10.1002/pol.1971.150091107

Li, T. Y., Huang, H. H., Wang, L., & Chen, Y. M. (2017). High performance polyimides with good solubility and optical transparency formed by the introduction of alkyl and naphthalene groups into diamine monomers. *RSC Advances, 7(65)*, 40996–41003. https://doi.org/10.1039/C7RA07142F

Liu, C., Pei, X., Mei, M., Chou, G., Huang, X., & Wei, C. (2016). Synthesis and characterization of organosoluble, transparent, and hydrophobic fluorinated polyimides derived from 3,3′-diisopropyl-4,4′-diaminodiphenyl-4-trifluoromethyltoluene*High Performance Polymers, 28*(10), 1114–1123.https://doi.org/10.1177/0954008315617230

Liu, H., Zhai, L., Bai, L., He, M., Wang, C., Mo, S., & Fan, L. (2019). Synthesis and characterization of optically transparent semi-aromatic polyimide films with low fluorine content. *Polymer, 163(1)*, 106–114. https://doi.org/10.1016/j.polymer.2018.12.045

Liu, J., Wang, Y., & Tu, G. (2026). Research on the Synthesis and Characterization of Colorless Polyimide Based on a Novel Asymmetric Dianhydride Monomer. *ACS Omega, 11(10)*, 16895–16912.https://doi.org/10.1021/acsomega.6c00472

Liu, J.-G., Ni, H.-J., Wang, Z.-H., Yang, S.-Y., & Zhou, W.-F. (2015). Colorless and transparent high-temperature-resistant polymer optical films: Current status and potential applications in optoelectronic fabrications. In *Optoelectronics—Materials and Devices*. https://dx.doi.org/10.5772/60432

Liu, Y., Gao, C., Xiao, L., Xie, Y., Wang, Y., & Li, W. (2016). Novel soluble poly(ether imide)s with trifluoromethyl and chloride pendant groups for optical materials. *RSC Advances*, 6(20), 16404–16412.https://doi.org/10.1039/C5RA19770H

Liu, Y., Zhou, Z., Qu, L., Zou, B., Chen, Z., Zhang, Y., Liu, S., Chi, Z., Chen, X., & Xu, J. (2017). Exceptionally thermostable and soluble aromatic polyimides with special characteristics: intrinsic ultralow dielectric constant, static random access memory behaviors, transparency and fluorescence. *Materials Chemistry Frontiers, 1*(2), 326–333. https://doi.org/10.1039/C6QM00027D

Mathews, A. S., Kim, I., & Ha, C. S. (2006). Fully aliphatic polyimides from adamantane-based diamines for enhanced thermal stability, solubility, transparency, and low dielectric constant. *Journal of Applied Polymer Science, 102*(4), 3316–3324. https://doi.org/10.1002/app.24800

Matsumoto, T. (1999). Nonaromatic Polyimides Derived from Cycloaliphatic Monomers. *Macromolecules, 32*(15), 4933–4939. https://doi.org/10.1021/ma9903862

Matsumoto, T. (2000). Alicyclic polyimides: An approach from monomer synthesis. *Yuki Gosei Kagaku Kyokaishi (Journal of Synthetic Organic Chemistry, Japan)*, 58(8), 776–786. https://doi.org/10.5059/yukigoseikyokaishi.58.776

Matsuura, T., Hasuda, Y., Nishi, S., & Yamada, N. (1991). Polyimide derived from 2,2′-bis(trifluoromethyl)-4,4′-diaminobiphenyl. 1. Synthesis and characterization of polyimides prepared with 2,2′-bis(3,4-dicarboxyphenyl)hexafluoropropane dianhydride or pyromellitic dianhydride.*Macromolecules, 24*(18), 5001–5005. https://doi.org/10.1021/ma00018a004

Miao, J., Hu, X., Wang, X., Meng, X., Wang, Z., & Yan, J. (2020). Colorless polyimides derived from adamantane-containing diamines. Polymer Chemistry. *Polymer Chemistry, 11(37)*, 6009–6016. https://doi.org/10.1039/D0PY01016B

Min, H., Kang, B., Shin, Y. S., Kim, B., Lee, S. W., & Cho, J. H. (2020). Transparent and Colorless Polyimides Containing Multiple Trifluoromethyl Groups as Gate Insulators for Flexible Organic Transistors with Superior Electrical Stability. *ACS Applied Materials & Interfaces, 12*(16), 18739–18747. https://doi.org/10.1021/acsami.9b23318

Mittal, K. L. (2007). *Polyimides and other high temperature polymers: Synthesis, characterization and applications* (Vol. 4). CRC Press. https://doi.org/10.1201/b12204

Nam, K. H., Kim, H., Choi, H. K., Yeo, H., Goh, M., Yu, J., Hahn, J. R., Han, H., Ku, B. C., & You, N. H. (2017). Thermomechanical and optical properties of molecularly controlled polyimides derived from ester derivatives. *Polymer, 108*, 502–512. https://doi.org/10.1016/j.polymer.2016.11.062

Ozawa, H., Ishiguro, E., Kyoya, Y., Kikuchi, Y., & Matsumoto, T. (2021). Colorless polyimides derived from an alicyclic tetracarboxylic dianhydride, CpODA. *Polymers, 13*(16), 2824. https://doi.org/10.3390/polym13162824

Reuter, R., Franke, H., & Feger, C. (1988). Evaluating polyimides as lightguide materials. *Applied Optics, 27*(21), 4565–4571. https://doi.org/10.1364/AO.27.004565

Shiotani, A., Shimazaki, H., & Matsuo, M. (2001). Preparation of transparent polyimides derived from cis- and trans-dicyclohexyl-3,3′,4,4′-tetracarboxylic dianhydrides. *Macromolecular Materials and Engineering, 286*(7), 434–441. https://doi.org/10.1002/1439-2054(20010701)286:7%3C434::AID-MAME434%3E3.0.CO;2-F

Stclair, A. K., Stclair, T. L., Slemp, W. S., & Ezzel, K. S. (1985). Optically transparent/colorless polyimides. In *Proceedings of the 2nd International Conference on Polyimides* Ellenville, NY, United States. https://ntrs.nasa.gov/citations/19860006910

Tan, Y. Y., Zhang, Y., Jiang, G. L., Zhi, X. X., Xiao, X., Wu, L., Jia, Y. J., Liu, J. G., & Zhang, X. M. (2020). Preparation and Properties of Inherently Black Polyimide Films with Extremely Low Coefficients of Thermal Expansion and Potential Applications for Black Flexible Copper Clad Laminates. .*Polymers, 12*(3), 576. https://doi.org/10.3390/polym12030576

Tapaswi, P. K., & Ha, C.-S. (2019). Recent trends on transparent colorless polyimides with balanced thermal and optical properties: Design and synthesis. *Macromolecular Chemistry and Physics, 220*(3), 1800313. https://doi.org/10.1002/macp.201800313

Wang, Y., Li, Y., Li, F., Shen, J., Zhao, J., & Tu, G. (2023). Novel rigid semi-alicyclic dianhydride with large side groups for high performance colorless polyimides (CPIs). *Polymer Testing, 129*, 108269. https://doi.org/10.1016/j.polymertesting.2023.108269

Wen, P. S., He, R., Li, X. D., & Lee, M. H. (2017 Syntheses and characterizations of high refractive index and low birefringence polyimides containing spirobifluorene in the side chain. *Polymer, 117*, 76–83. https://doi.org/10.1016/j.polymer.2017.04.020

Wu, Q., Ma, X. R., Zheng, F., Lu, X. M., & Lu, Q. H. (2019 a). High performance transparent polyimides by controlling steric hindrance of methyl side groups. *European Polymer Journal, 120*, 109235. https://doi.org/10.1016/j.eurpolymj.2019.109235

Wu, Q., Ma, X., Zheng, F., Lu, X., & Lu, Q. (2019 b). Synthesis of highly transparent and heat-resistant polyimides containing bulky pendant moieties. *Polymer International, 68*(6), 1186–1193. https://doi.org/10.1002/pi.5811

Wu, X. M., Shu, C., He, X. Q., Wang, S. B., Fan, X., Yu, Z. H., Yan, D. Y., & Huang, W. (2020). Optically Transparent and Thermal-Stable Polyimide Films Derived from a Semi-Aliphatic Diamine: Synthesis and Properties. *Macromolecular Chemistry and Physics, 221*(5), 1900506. https://doi.org/10.1002/macp.201900506

Xi, L., Lv, Y., Feng, J., Huang, Y., Huang, Y., Yang, Q., Li, G., & Kong, M. (2024). Synthesis of UV-resistant and colorless polyimide films for optoelectrical applications. *npj Materials Degradation 8, 6.* https://doi.org/10.1038/s41529-023-00422-w

Yang, S.-Y., & Yuan, L.-L. (2018). Chapter 1 - *Advanced polyimide films. In Advanced polymeric materials for optoelectronic applications* (pp. 1–66). Elsevier. https://doi.org/10.1016/B978-0-12-812640-0.00001-9

Yi, C., Li, W., Shi, S., He, K., Ma, P., Chen, M., & Yang, C. (2020). High-temperature-resistant and colorless polyimide: Preparations, properties, and applications. *Solar Energy, 195*, 340–354. https://doi.org/10.1016/j.solener.2019.11.048

Yi, L., Li, C., Huang, W., & Yan, D. (2015). Soluble polyimides from 4,4′-diaminodiphenyl ether with one or two tert-butyl pedant groups. *Polymer, 80*, 67–75. https://doi.org/10.1016/j.polymer.2015.10.045

Zhang, X. L., Song, C., Wei, M. H., Huang, Z. Z., & Sheng, S. R. (2019). Organosoluble and transparent cardo polyimides with high Tg derived from 9,9-bis(4-aminophenyl)xanthenes. *High Performance Polymers, 31*(8), 909–918. https://doi.org/10.1177/0954008318814157

Zhang, Z. Y., Huang, Z. Z., Pan, Y., & Song, C. (2020). New transparent and thermally stable cardo poly(ether imide)s derived from 10,10-bis[4-(4-amino-2-pyridinoxy)phenyl]-9(10H)-anthrone. *High Performance Polymers, 32*(5), 483–492. https://doi.org/10.1177/0954008319883005

Zhuang, Y., Seong, J. G., & Lee, Y. M. (2019). Polyimides containing aliphatic/alicyclic segments in the main chains. *Progress in Polymer Science, 92*, 35–88. https://doi.org/10.1016/j.progpolymsci.2019.01.004

doi: 10.31674/book.2026cdcbs.010

Importance of Zinc in Human Health: A Comprehensive Review

Debarati Dey

Department of Chemistry, Vidyasagar College, Kolkata- 700006, India

Corresponding Author's Email: debaratidey07@gmail.com

Abstract

Zinc is an indispensable trace mineral that plays a fundamental role in human physiology. It modulates numerous biological processes in the human body. It is found to be involved in cellular metabolism, maintaining immunity, linear growth, development of reproductive organs, repair mechanisms, structural integrity in proteins and cell membranes and many more. Zinc is present as a catalytic, structural, and regulatory component in more than 300 enzymes and numerous transcription factors for DNA synthesis, protein synthesis, wound healing, and immune defense mechanisms. Generally, malnutrition and a cereal-based plant diet result in zinc deficiency in humans due to lower bioavailability. Zinc deficiency affects nearly two billion people worldwide. Deficiency of zinc has been associated with growth retardation, impaired immune response, cognitive dysfunction, reproductive disorders, and increased susceptibility to infections. This review discusses the biological importance of zinc, its physiological roles, dietary sources, consequences of deficiency and measures to prevent zinc related disorders that might be a useful guide.

Keywords: *Trace Element; Zinc Containing Enzymes; Zinc Fingers; Zinc Sources; Zinc*

Introduction

Zinc is an essential trace element required for the proper functioning of numerous biological processes in the human body. In earth's crust it is the 24th most abundant element and in the human body it is second most abundant element after iron. Zinc has filled 3d electronic configuration with two electrons in the outer 4s shell. The Zn^{2+} state is highly stable with respect to redox reactions and so does not participate in physiological redox reactions. Due to the d^{10} electronic configuration, Zn^{2+} does not have any crystal field stabilization energy and thus has no preference towards octahedral or tetrahedral sites. Thus, Zn^{2+} is found in both tetra-coordinated and hexa-coordinated forms in biological medium and also can toggle easily between different geometrical forms during its course of action. It is present on the borderline of hard and soft acids and acts as a Lewis acid, lowering the pKa of the medium while avoiding the chance of electron transfer.

French physiologist Raulin first considered zinc to be an essential nutrient in the mid-nineteenth century while observing the growth of a fungus. In early twentieth century in Boston, a series of patients with liver cirrhosis were found to have a very low level of zinc. Nearly simultaneously, a distinct form of dwarfism was identified in Egypt and Iran, along with hypogonadism and delayed sexual development. A zinc supplement and balanced diet containing adequate animal protein initiated their rapid recovery. In 1973, the WHO published an estimated dietary requirement for different nutrients, which included zinc as an essential micronutrient. Many recent reviews (Consales *et al.*, 2024; Pratama *et al.*, 2026; Pavić Vulinović *et al.*, 2026) highlight the indispensable role of zinc for infants and also to prevent different diseases in adults.

Zinc has an exceptional ability to form strong bonds with ligands and can exchange ligands easily. The metal's flexibility towards coordination geometry makes it useful in biosystems. Zn^{2+} is ubiquitous within cells. Zinc is present in all tissues and body fluids and is required for the activity of many enzymes and transcription factors involved in cellular metabolism, immune regulation, and genetic expression.

However, it is not stored within cells, unlike other minerals, viz., iron, copper, etc., to reach a level of toxicity, so regular intake through a balanced diet is necessary. Approximately 10% of the human proteome is associated with expression of ~3000 zinc-containing proteins, including transcription factors. A healthy human body contains ~2-3 g of zinc mainly in the skeletal muscles and bones. Zinc helps to maintain cellular integrity, stability of cell membranes, defense mechanisms for immunity, metabolism of carbohydrates, proteins, lipids, and nucleic acids and involvement in cellular signaling pathways. The role of the mineral can be classified in three major categories: catalytic, structural and regulatory (Roohani *et al.*, 2013).

Biological Functions of Zinc

Zinc plays an indispensable role in a wide range of biological processes essential for human health. These functions can generally be classified into catalytic, structural, and regulatory roles (Lippard & Berg, 1997).

Catalytic Functions of Zinc

Zinc appears in the active site of many hydrolytic enzymes like carboxy peptidase A (for digestion of proteins by cleaving it from C-terminal side), carbonic anhydrase (a lyase hydrating CO_2), thermolysin (hydrolyzes peptide bonds specifically having hydrophobic amino acid side chain and endopeptidase), alcohol dehydrogenase (an oxidoreductase where Zn activates the substrate for redox reactions involving the cofactor NAD^+), alkaline phosphatase, adenosine deaminase, etc.

Through its catalytic role, the positively charged Zn^{2+} lowers the pKa of coordinated water and provides a local high concentration of OH^-, which is unavailable at physiological pH. In a similar manner, the positively charged metal center serves as a general Lewis acid for activation of substrate molecules, mostly by changing coordination. E.g., in carboxypeptidase, Zn^{2+} is coordinated to two imidazole side chains of two histidine residues and bidentate carboxylate residues of glutamic acid. The fifth coordination is to a water molecule, which is activated by Zn^{2+} and is the key feature of the enzyme mechanism. Protein side chains greatly assist the assembly of activated complexes interacting with metal centers. The rate of catalytic reaction is accelerated by internal attack within the coordination sphere of the metal ion or by rearranging the substrate ligand at the active site. The Zn^{2+} ion is uniquely suitable among biological transition metal ions to serve as a Lewis acid without participating in electron transfer reactions.

Zinc in Lyase Enzyme

The specific function of zinc in biological pathways was first recognized in 1939 while studying the catalytic reaction of carbonic anhydrase. At physiological pH the rate of reaction (Equation 1) is slow (~10-2 s^{-1}) in the absence of a catalyst, while the rate is as high as ~106 s^{-1} in the presence of the enzyme. The Zn(II) is coordinated to three histidine imidazole side chains. The fourth coordinating site is occupied by a water or hydroxide to complete a distorted tetrahedral coordination sphere. Once the metal hydroxide unit is formed, binding of CO_2 can occur, followed by nucleophilic attack of hydroxide to produce a metal-bound bicarbonate. Then the product is displaced by water molecules.

$$CO_2 + H_2O \leftrightarrow HCO_3^- + H^+ \qquad \text{(Equation 1)}$$

Zinc in Hydrolytic Enzyme

In 1955 another zinc-containing protein was discovered carboxy peptidase A and then B, synthesized in pancreas. The zinc atom is situated well inside the surface of protein coordinated by two imidazole side chains of histidine residues and a bidentate carboxylate group of glutamic acid. In the fifth coordination site of Zn(II), a water molecule is attached, which is activated by the metal, giving a penta coordinated metal center. This step is the key feature of the enzyme mechanism. In the presence of a substrate, the carboxylate group of glutamic acid becomes nearly unidentate and rearranges to keep the coordination

number constant. This kind of mechanism is common to zinc as it does not have any structural preference.

Other well-known zinc-containing hydrolase enzymes are alkaline phosphatase that promote the reaction (Equation 2).

$R\text{-}O\text{-}PO_3^{2-} + H_2O \leftrightarrow R\text{-}OH + HPO_4^{2-}$ (Equation 2)

Here also a pair of Zn(II) ions serve as a general Lewis acid, polarizing the substrate and rendering it a better electrophile.

In addition to carboxypeptidases, zinc-dependent aminopeptidases that cleave N-terminal residues are also important in peptide hormone regulation and peptide homeostasis (Bhat, 2026).

Zinc in Oxidoreductase Enzyme

Generally, zinc is present in enzymes that do not undergo any redox reaction. However, there are few enzymes, like alcohol dehydrogenase, super dismutase, etc., where zinc is present as an activator but not participating in redox reactions. Lever alcohol dehydrogenase converts primary alcohols to aldehydes.

$RCH_2OH + NAD^+ \leftrightarrow RCHO + NADH + H^+$

Alcohol is oxidized to aldehyde by essential coenzyme NAD^+. . Two zinc ions are found in different environments in the enzyme. One Zn(II) in the active site is coordinated to two cysteinate sulpher atoms, one histidine nitrogen atom and a water molecule. The other Zn(II) is bonded to four cysteine thiolate ligands and is inaccessible to solvent and plays a structural role. The zinc in the active site binds directly with alcohol substrate by loss of bound water and deprotonation of ligand to form RO^-. However, binding of coenzyme NAD^+ does not need the presence of Zn(II); rather, a change in conformation of the protein occurs from open to close form. This conformational change helps to position the substrate-binding pocket at an appropriate distance and orientation with respect to the coenzyme. This facilitates the crucial step in the enzyme mechanism, namely, the transfer of a hydride ion from α–carbon of the alcohol to the nicotinamide ring of NAD^+ to form NADH. Following hydride transfer, NADH dissociates from the enzyme. The role of zinc is twofold: firstly, deprotonation of alcohol substrate rendering it better hydride ion donor and secondly, positioning the substrate in the active site in a suitable way leading to direct hydride transfer to the coenzyme.

Superoxide dismutase is another oxidoreductase that contains Zn^{2+} along with copper. The copper toggles between +1 and +2 states to catalyze the disproportionation of superoxide, while Zn^{2+} is also essential for its activity. Coordination of a histidine ring nitrogen atom to Zn^{2+} lowers the pKa of other ring nitrogen atom and it prefers to bind to a proton rather than Cu^{2+}, which was initially bonded. Cu^+ reduces superoxide and itself turns to Cu^{2+}. Zn^{2+} helps to create the electric field gradient that attracts superoxide. Another possible role of Zn^{2+} is to confer thermal stability to superoxide dismutase. This suggests that zinc also has some anti-inflammatory properties that help to reduce oxidative stress.

Nucleotide Activation

Several zinc enzymes are involved in nucleic acid metabolism, especially phosphodiesters and nucleases. Zn^{2+} is present in DNA and RNA polymerases, which catalyze the polymerization of mononucleotide triphosphate building blocks to form polymers. The exact mechanism is yet to be established. Additionally, zinc plays an important role in the synthesis and degradation of nucleic acids, which are essential for cellular replication and gene expression.

Structural Functions of Zinc

Zinc is found to be contained in transcription factor IIIA (TFIIIA) and plays a vital structural role, the central core of small nucleic acid binding domains, referred to as ‘zinc fingers'. In TFIIIA the metal binding domain directly interacts with DNA. Many other classes of zinc-containing proteins are found to be involved in gene regulation. Most DNA and RNA polymerases contain Zn^{2+} ions.

TFIIIA is a site-specific DNA-binding protein that plays a central role in controlling the transcription of 5S ribosomal RNA genes in African claued toad Xenopus. The role of Zn is twofold. The protein isolated from Xenopus oocytes contains two to three equivalents of zinc, which are much more tightly bound to the protein and are resistant to removal by dialysis of TFIIIA-5SRNA complex against chelating agent EDTA solution. However, when RNA is destroyed using a nuclease, then only Zn^{2+} can be replaced. Moreover, the protein binds DNA to a specific sequence of ~45 base pairs, which upon binding remain resistant to nuclease activity.

Analysis of amino acid sequence of TFIIIA led to an exciting hypothesis that amino acid sequence remains nearly constant, having two cysteine and two histidine residues, which are considered to be potential zinc-binding sites. These domains are called zinc fingers. The EXAF study reveals that two S atoms are 2.30 Å apart and two N atoms are at 2.00 Å apart, consistent with the tetrahedral structure of Zn^{2+}.

Regulatory Functions of Zinc

In addition to its catalytic and structural roles, zinc serves as an important regulator of cellular signaling pathways. Zn^{2+} ions are detected in synaptic vesicles that release upon stimulation outside the cell (Costa *et al.*, 2023). This suggests that perhaps Zn^{2+} acts as a carrier of information between the cells. Cells allow Zn^{2+} ions via transmitter-gated ion channels and regulate intracellular targets. Extracellular Zn^{2+} activates growth factor receptors that decide cell proliferation, differentiation, growth and apoptosis. These processes are essential for tissue development, immune responses, and the maintenance of overall physiological balance. Intracellular Zn^{2+} also participates in various signaling pathways. Intracellular zinc ions remain mostly bound to metallothionein and glutathione. It influences hormone release, nerve signal transmission, and immune system responses.

Versatile Role of Zinc and Its Source

One of the remarkable functions of zinc is that it has antiviral property and it plays an important role in maintaining a healthy immune system. Zinc influences both innate and adaptive immune responses and plays a crucial role in protecting the body against infections. Zinc is required for the normal development and function of immune cells such as neutrophils, macrophages, natural killer cells, and lymphocytes. Zinc acts as a key regulator in various organelles in the cell as its concentration in different cellular organelles varies in normal as well as stressed condition and the micronutrient helps in inter-organelle communications (Brito *et al.*, 2026). These cells form the primary defense mechanisms against invading pathogens. Zinc deficiency causes inefficient immune function and reduces the activity of immune cells that alter cytokine production, which leads to increased susceptibility to infections, e.g., respiratory illnesses like pneumonia, gastrointestinal infections like diarrhea, and viral diseases and also reduces neuropsychological performance. Recently a zinc supplement was found to result in a better healing response for COVID-19-affected patients (Pal *et al.*, 2020; Jin *et al.*, 2024).

Zinc regulates many important cellular events. It is used as a potential therapeutic agent against several diseases. It plays a crucial role in both intra and extracellular signaling pathways. Intracellular zinc is found mostly bound to sulfur-containing amino acids like methionine and glutathione and the concentration of free zinc varies from picomolar to nanomolar range. Intracellular zinc signaling can be classified into three kinds depending on their duration. The first one is an immediate or rapid response

where zinc is released from cells on stimulation and does not last long. The second kind of signal gets increased for nearly an hour after stimulation and the third type of signal is where zinc levels are altered several hours after the external stimulation. This last kind of signal is a late, non-immediate signal, dependent on the transcriptional regulation of zinc transporters, where intracellular concentration of zinc varies through one or more days. Zinc ions are detected in the presynaptic vesicles of neurons and released upon exocytic stimulation. The Zn^{2+} released is taken up by postsynaptic cells. Zn^{2+} can also enter the cell via transmitter-gated ion channels. Different secretary cells like endocrine and exocrine pancreas, mammary glands, prostate glands, intestine and platelet cells contain Zn ions in their vesicles.

Zinc has an important role in bone growth, too. Besides the main constituents of bone like calcium, magnesium and phosphorous, zinc is essential and its deficiency leads to linear growth retardation. Zn has a stimulatory effect on osteoblastic bone formation. Increased activity of a zinc-containing enzyme, alkaline phosphatase, is shown to increase calcium deposition. Zn^{2+} regulates both intracellular and extracellular Ca^{2+} ion concentration. Increase in Zn^{2+} ion concentration in cytoplasm controls Ca^{2+} concentration. The interaction between Zn^{2+} and Ca^{2+} seems to be bidirectional—the Zn^{2+} ion can alter Ca^{2+} and vice versa. Zinc also has a role to control diabetes. Insulin synthesis, storage and structural stability are controlled by zinc.

Human reproductive systems, both male and female, are highly controlled by zinc. It helps in development of male reproductive organs, testosterone hormone regulation, sperm cell production and hence fertility (Solomons, 2013). High zinc ion concentration is found in prostate gland and seminal fluid. In females zinc regulates ovarian function, menstrual cycle, different hormone secretion, egg development and fertilization. Zinc is proven to be very important during pregnancy for fetal growth and immune system development. Zinc oxide nanomaterials can be synthesized through various methods, viz., physical, chemical, biological or eco-friendly green methods and have been found to show antimicrobial, anti-inflammatory and anticancer activity (Maurya *et al.*, 2026). Even zinc-based bimetallic nanoparticles (with copper, silver, gold, and manganese) are found to show multiple biomedical activities (Fayed & Reda, 2026).

The main source of zinc is food found from animal proteins like red meat, chicken, eggs, fish, seafood and dairy products. The plant source includes legumes, whole grains, seeds, nuts, mushroom and leafy vegetables. However, presence of phytates in plant sources reduces zinc absorption in the intestine (Prasad, 1991). Fermentation, soaking, sprouting decrease phytates and improve zinc absorption. A recent review by Tokarczyk and Koch (2025) focuses on the bioavailability and corresponding bioaccessibility of zinc in various food materials. High temperature stress on rice can cause less bioavailability of zinc, which can be improved by using zinc oxide nanoparticles synthesized via a green method (Yadav *et al.*, 2026). Zinc ions and zinc-embedded carbon quantum dots are used recently to inhibit fumarase activity (Navaser & Kalhor, 2026).

Deficiency of Zinc and Supplementation

As zinc is an essential trace element, it is required throughout life, though in varied amounts, viz., the daily requirement for infants (2-3 mg), childhood (3-8 mg), adolescence (5-6 mg), pregnancy (11-12 mg), etc. Inadequate intake of food requires supplementation. Severity of common cold, respiratory infections, child diarrhea can be reduced using zinc supplementation (Alam *et al.*, 2023). Zinc supplements are widely used to improve health of pregnant women and infants (Diao *et al.*, 2025). Common symptoms of zinc deficiency are low birth weight, growth retardation, weak immunity, hair loss, skin problems, sexual impairment, etc (Hambidge, 2000). Moreover, zinc deficiency increases the possibility of heavy metal toxicity like cadmium, arsenic and lead (Wong *et al.*, 2025). Zinc oxide nanoparticles synthesized via an environmentally friendly green method are found to have prominent antimicrobial properties (Habtemariam *et al.*, 2026). Recent research on zinc supplementation in animals reveals that nano-ZnO

is much effective supplement than inorganic zinc oxide and Zn-lysine complex due to greater solubility in water and less precipitation in the gastrointestinal tract (Alipour *et al.*, 2026). Zinc dynamics across the trophic system have been investigated by a group of scientists to know the connection of its bioavailability in soil to plants and ultimately to human systems that might improve agriculture and hence health and nutrition (Mandal *et al.*, 2026).

Conclusion

The importance of zinc in human physiology is unquestionable. It is required for normal growth and development throughout the human life cycle. Starting from DNA synthesis, growth of new cells, survival, repair, proliferation, and even apoptosis—the participation of zinc is well established. The effect of zinc varies depending on cell type, its concentration, health condition and even under normal and pathological conditions. The demand of the body also varies depending on age, gender and physiological condition. Several disorders in humans appear due to deficiency of the mineral resulting from malnutrition that may induce other diseases. Zinc supplementation for much illness is observed to be lifesaving. The versatile role of zinc in preventing infection, diabetes, aging, neuropsychological impairment is well documented. Further research in this field will be helpful in exploring the therapeutic potential of the mineral for prevention and management of various diseases.

Acknowledgement

The author duly acknowledges Department of Chemistry, Vidyasagar College, Kolkata, India for support.

References

Alam, J., Nuzhat, S., Billal, S. M., Ahmed, T., Khan, A. I., & Hossain, M. I. (2023). Nutritional profiles and zinc supplementation among children with diarrhea in Bangladesh. *The American Journal of Tropical Medicine and Hygiene*, *108*(4), 837. https://doi.org/10.4269/ajtmh.22-0532

Alipour, A., Ganjkhanlou, M., Zali, A., Hashemi, S., Mortazavi, M. H., Palangi, V., ... & Hosseini-Ghaffari, M. (2026). Effects of zinc supplementation forms (ZnO, Zn-Lysine, Nano-ZnO) on growth performance and metabolic health in pre-weaned Holstein calves. *Scientific Reports*. https://doi.org/10.1038/ s41598-026-51255-x

Bhat, S. (2026). Zinc-dependent aminopeptidases: new perspectives on structure, function, and biomedical applications. *Frontiers in Chemical Biology*, *5*, 1752191. https://doi: 10.3389/fchbi.2026.1752191

Brito, S., Kim, J., & Bin, B. H. (2026). Zinc as a master regulator of intracellular organelle homeostasis. *Experimental & Molecular Medicine, 58*, 1341–1357. https://doi.org/10.1038/s12276-026-01706-2

Consales, A., Agostoni, C., Cazzola, R., Ottria, R., & Giannì, M. L. (2024). Tracing zinc's role in preterm infants' health: a narrative review. *Advances in Nutrition*, *15*(12), 100295. https://doi.org/10.1016/j.advnut.2024.100295

Costa, M. I., Sarmento-Ribeiro, A. B., & Gonçalves, A. C. (2023). Zinc: from biological functions to therapeutic potential. *International Journal of Molecular Sciences*, *24*(5), 4822. https://doi.10.3390/ijms24054822

Diao, S., Feng, Y., Peng, X., Liu, D., Huang, L., Zeng, L., & Zhang, L. (2025). The Efficacy of Zinc Supplementation Alone or in Combination for Improving Pregnancy and Infant Outcomes: A Systematic Review and Meta-Analysis. *Journal of Evidence‐Based Medicine*, *18*(3), e70061. https://doi.org/10.1111/jebm.70061

Fayed, B., & Reda, A. E. (2026). Zinc meets metal: are Zn-based bimetallic nanoparticles the future of biological nanomedicine?. *Discover Applied Sciences*, *8*, 436. https://doi.org/10.1007/s42452-026-08236-6

Habtemariam, T. H., Anjullo, S. H., & Abebe, G. M. (2026). Green synthesis and antibacterial activity of zinc oxide nanoparticles using Croton macrostachyus Hochst. ex Delile extracts. *RSC advances*, *16*(16), 14492-14508. https://doi: 10.1039/d6ra00724d

Hambidge, M. (2000). Human zinc deficiency. *The Journal of Nutrition*, *130*(5), 1344S-1349S. https://doi.org/10.1093/jn/130.5.1344S

Jin, D., Wei, X., He, Y., Zhong, L., Lu, H., Lan, J., ... & Liu, H. (2024). The nutritional roles of zinc for immune system and COVID-19 patients. *Frontiers in nutrition*, *11*, 1385591. https://doi.org/10.3389/fnut.2024.1385591

Lippard, S. J., & Berg, J. M. (1997). *Principals of Bioinorganic Chemistry*. University Science Books, US. Mandal, A. K., Kumar, J., Dey, J. K., Chhetri, A., Das, S., Kumar, V., ... & Hossain, A. (2026). Zinc in Soil–Plant–Human Systems: A Synthesis of Its Fate, Essential Roles, and Health Implications. *Scientifica*, *2026*(1), 2944933. https://doi.org/10.1155/sci5/2944933

Maurya, S., Anupam, Tripathi, S., Chaubey, S., & Soni, A. (2026). Recent advances in the synthesis and applications of zinc oxide nanomaterials for healthcare energy and environmental systems. *Discover Chemistry*, *3*(1), 98. https://doi.org/10.1007/s44371-026-00570-3

Navaser, A., & Kalhor, H. R. (2026). Zinc ions and zinc-embedded carbon quantum dots as competitive inhibitors of fumarase: preferential inhibition of the reverse reaction. *Journal of Materials Chemistry B., 14*, 2359-2372. https://doi: 10.1039/D5TB02141C

Pal, A., Squitti, R., Picozza, M., Pawar, A., Rongioletti, M., Dutta, A. K., ... & Prasad, R. (2020). Zinc and COVID-19: basis of current clinical trials. *Biological trace element research*, *199*(8), 2882. https://doi.org/10.1007/s12011-020-02437-9

Pavić Vulinović, M., Micek, V., Breljak, D., Vrhovac Madunić, I., Madunić, J., & Ljubojević, M. (2026). Overview of the zinc functional interactome through health hallmarks and medical conditions. *Nutrients*, *18*(2), 336. https://doi.org/10.3390/nu18020336

Prasad, A. S. (1991). Discovery of human zinc deficiency and studies in an experimental human model. *The American Journal of Clinical Nutrition*, *53*(2), 403-412. https://doi.org/10.1093/ajcn/53.2.403

Pratama, B. P., Khairullah, A. R., Kurniasih, D. A. A., Mustofa, I., Wardhani, B. W. K., Sukmanadi, M., ... & Wibowo, S. (2026). Zinc in Human Health: A Comprehensive Review of its Biological Roles and Clinical Implications. *Trends in Sciences*, *23*(1), 11556-11556. https://doi.org/10.48048/tis.2025.11556

Roohani, N., Hurrell, R., Kelishadi, R., & Schulin, R. (2013). Zinc and its importance for human health: An integrative review. *Journal of Research in Medical Sciences: The Official Journal of Isfahan University of Medical Sciences, 18*(2), 144. https://pubmed.ncbi.nlm.nih.gov/23914218/

Solomons, N. W. (2013). Update on zinc biology. *Annals of Nutrition and Metabolism*, *62*(Suppl. 1), 8-17. https://doi.10.1159/000348547

Tokarczyk, J., & Koch, W. (2025). Dietary Zn—Recent advances in studies on its bioaccessibility and bioavailability. *Molecules*, *30*(13), 2742. https://doi.org/10.3390/molecules30132742

Wong, C. P., Beaver, L. M., & Ho, E. (2025). Protective role of dietary zinc on DNA damage, oxidative stress, and metal toxicity. *Frontiers in Molecular Biosciences*, *12*, 1618318. https://doi: 10.3389/fmolb.2025.1618318

Yadav, A., Bhatia, A., Bana, R. S., Ranjan, R., Dhakar, R., Shivay, Y. S., ... & Kumar, A. (2026). Green zinc oxide nanoparticles improve zinc bioavailability and mitigate high temperature stress in rice. *Scientific Reports,16*, 6573. https://doi.org/10.1038/s41598-026-36046-8

doi: 10.31674/book.2026cdcbs.011

Experimental Support for the Charecterization of Carbon Allotrpoes and Nanocomposite Materials for Easy Analysis

Prasenjit Mandal[1]*, Sk Imran Ali[2]

[1]Department of Chemistry, Santipur College, Santipur, Nadia- 741404, West Bengal, India

[2]Department of Chemistry, University of Kalyani, Kalyani, Nadia- 741235, West Bengal, India

**Corresponding Author's Email: mandalprasenjit21@gmail.com*

Abstract

The rapid advancement of nanotechnology necessitates precise and comprehensive characterization of synthesized nanomaterials to correlate their physicochemical properties with functional performance. In the present study, several nanomaterials were synthesized via chemical routes and systematically characterized using a suite of complementary analytical techniques. The structural properties, crystallinity, phase purity, and crystallite size were investigated by Powder X-ray Diffraction (PXRD). The morphological features, particle size, shape, and surface topography were examined by Scanning Electron Microscopy (SEM) with Energy Dispersive X-ray Spectroscopy (EDX) and Transmission Electron Microscopy (TEM) / High-Resolution TEM (HRTEM). To determine the 3D surface topography, surface roughness, and precise height profile of the nanomaterials at the nanoscale using Atomic Force Microscopy (AFM). The elemental composition and distribution were confirmed by EDX. Functional groups, chemical bonding, and surface chemistry were analyzed by Fourier Transform Infrared Spectroscopy (FTIR) and Raman Spectroscopy. Optical properties, including band gap energy, with characteristic D and G bands confirming phase purity and defect density, and the percentage of S and P character of materials, absorption behavior, and surface plasmon resonance were evaluated using UV-Visible Spectroscopy (UV-Vis). Colloidal stability, hydrodynamic size, and surface charge were determined by Dynamic Light Scattering (DLS) measurements. Thermal stability and composition were further assessed by Thermogravimetric Analysis (TGA/DTA). The combined results confirm the successful synthesis of nanoscale materials with controlled size, uniform morphology, and desirable structural and optical characteristics, validating their potential for applications in catalysis, sensing, biomedical, and energy storage devices.

Keywords: *Carbon Allotrpoes; DLS; FTIR; Nanomaterials; SEM; TEM; UV-Vis; XRD*

Introduction

The application of a suitable analytical technique to inquire into the internal properties, like structure and elemental composition, of a prepared sample is essential in the field of nanomaterials. Characterization technique is imperative for understanding and investigating features, structure, mechanism, composition etc. of the prepared samples (Hannay, 1967). In the present work, several extensive analytical techniques were used and are discussed here. The structure of the prepared materials was determined by techniques such as powder X-ray diffraction (PXRD), Raman spectroscopy, Nuclear Magnetic Resonance (NMR) spectrometry, Fourier Transform Infrared (FT-IR) spectroscopy, Energy-dispersive X-ray analysis (EDX) and Thermogravimetric analysis (TGA). The dimension and morphology of the prepared samples were analyzed by Scanning Electron microscopy (SEM), Transmission Electron microscopy (TEM), Atomic Force microscopy (AFM) and Field Emission Scanning Electron microscopy (FESEM). Photophysical features of the prepared samples were analyzed by Ultraviolet-visible (UV-Vis) spectroscopy. Gas chromatography (GC) and High Resolution Mass spectrometry (HRMS) were used for the determination of the yield and nature of products of chemical reactions. Composition of materials was also studied by Atomic Absorption spectrometry (AAS). This is the fundamental working principle of several characterization techniques used

for analysis of carbon allotrope and nanomaterials-based nanocomposites that come under the scope of the various research works. Protocols of the various reactions and studies undertaken have also been described and also depicted in Figure 1.

Figure 1: Different Charecterization Techniques for Carbon Allotrpoes and Nanocomposite Materials

Characterization techniques

The following characterization techniques are discussed here in details.

1. Powder X-ray Diffraction (PXRD)
2. Raman Spectroscopy
3. Thermo Gravimetric Analysis (TGA)
4. Fourier Transform Infrared Spectroscopy (FT-IR)
5. Scanning Electron Microscopy (SEM), Field Emission SEM (FESEM)
6. Energy- Dispersive X-ray Analysis (EDX)
7. High Resolution Transmission Electron Microscopy (HRTEM)
8. Ultraviolet-Visible Spectroscopy (UV-Vis)
9. Atomic-force Microscopy (AFM)
10. Nuclear Magnetic Resonance Spectrometry (NMR)
11. Atomic Absorption Spectrometry (AAS)
12. High Resolution Mass Spectrometry (HRMS)
13. Gas Chromatography (GC)

Powder X-ray Diffraction (PXRD)

Powder X-ray Diffraction is a non-destructive analytical technique to examine crystal phase composition and crystallographic structures of prepared materials (Moore & Reynolds, 1997). The basic use of XRD in the present work was to examine the actual phases and crystallographic structures of prepared

compositions, comparing the resulting PXRD pattern with the standard diffraction data in the database of the Joint Committee on Powder Diffraction Standards (JCPDS). In order to do this, solid powder samples were analyzed by monochromatic X-ray from Cu Kα radiation and short wavelength, λ = 1.5418 Å. The scanning rate and 2ɵ range of the operating system were typically 0.02º per second and 10º to 80º. Sharp peaks indicated that the prepared materials were pure crystallites, while broad peaks implied that the prepared materials had an amorphous structure. JCPDS is a non-profit scientific organization that collects, edit, publish, and distribute powder X-ray diffraction data of several materials with known crystallographic structures. In the present work, powder X-ray diffraction technique was carried out using a Rigaku MiniFlex 600 instrument in most of the cases. This is shown in Figure 2.

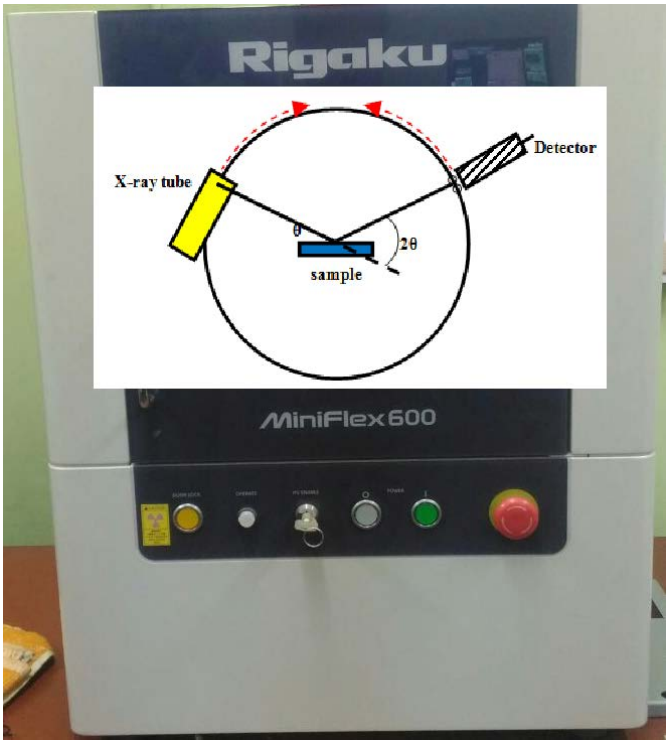

Figure 2: Instrumental Setup of Powder XRD Analysis, Rigaku MiniFlex 600.

Raman Spectroscopy

Raman spectroscopy is a contactless and non-destructive analytical technique to ascertain molecules under investigation (Raman & Krishnan, 1928). It is a very powerful method and is also broadly used to analyze purity and the crystalline nature of carbon-based nanomaterials. Thus, Raman spectroscopy is a very important tool to analyze graphene or graphene oxide, for example, to find out the number of layers of such materials. This procedure yields information about rotational, vibrational and other such transitions in molecules. Raman spectroscopy involves interaction of photon and matter in which the photon is inelastically scattered and excited to higher rotational or vibrational energy levels, the process being known as Raman effect. In 1928, the Raman effect was discovered by C. V. Raman (Ferraro *et al*., 2003; Smith & Dent, 2019). The main components of commercially available Raman spectrometers are: sample holder, illumination setup, monochromator, scattered light collection system and detection system. In the present work, Raman spectroscopic analysis was carried out using a WITEC CRM200 Raman system with a 532 nm laser (2.33 eV) source and 100x objective lens as shown in Figure 3

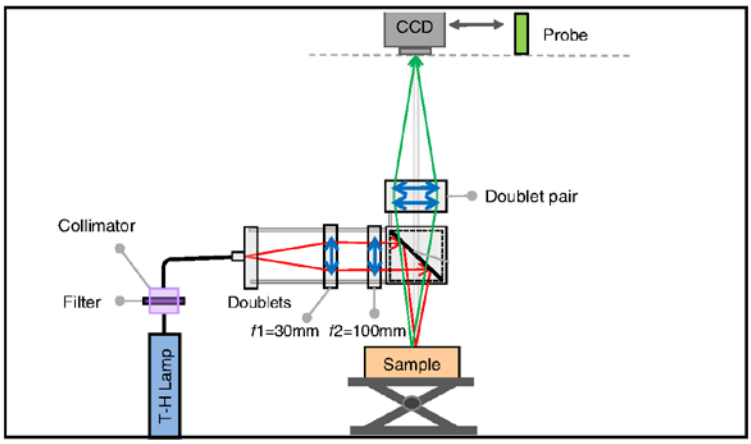

https://www.witec.de

Figure 3: Instrumental Setup of Raman Spectroscopy, WITEC CRM200 Confocal Raman System

Thermogravimetric Analyses (TGA)

Thermogravimetric analysis was first explored more than 50 years ago. Nowadays, it is a widely used method for studying the nature of materials and their thermal stability. Generally, it is used to find out particulate characteristics of prepared materials that exhibit certain rate of change in the amount of mass loss and/or gain with temperature. This information also reveals any dehydration or oxidation occurring in thermal treatment of the sample under a controlled atmosphere (Li & Rees, 1986). Thermogravimetric analysis is also used to investigate the chemical stability of the prepared materials (Valodkar *et al.,* 2003; Mercuri *et al.,* 2006). In the case of graphene-based nanocomposite materials, TGA is regularly conducted in air as a quantitative method to find out the composition of graphene or graphene oxide and other implanted nanoparticles. In the present work, thermogravimetric analysis was carried out mostly using a NETZSCH TG-209-F3 instrument, as shown in Figure 4.

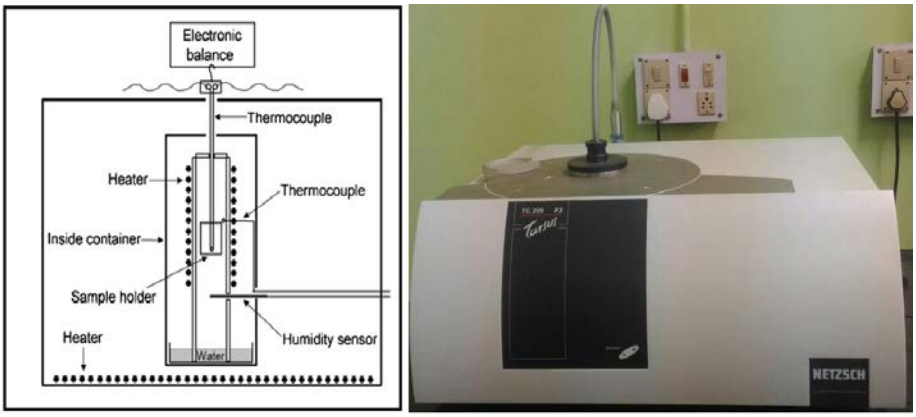

Figure 4: Instrumental Setup of Thermogravimetric Analysis (TGA) NETZSCH TG-209-F3

Fourier Transform Infrared Spectroscopy (FT-IR)

With fast Fourier transform in operation, Cooley and Tukey introduced Fourier Transfoem Infrared (FT-IR) spectroscopy in 1965. Infrared spectrum of a sample gives information about various vibrations that may occur in the sample. Identifying each vibrational band with standard functional groups provides an idea of the chemical compound or compounds that may exist in the sample. An FTIR spectrometer concurrently collects high-resolution spectral data over a range of wavelengths, typically 400 to 4000 cm^{-1}. This analysis is extensively used in polymer science, organic synthesis, petrochemical engineering, food and

pharmaceutical industries (Sing, 1985). The different phases of the synthesized sample may be completely characterized by this instrument (Skoog *et al.,* 2007; Islam *et al.,* 2011). In the present work, FT-IR spectroscopy was performed with an EPA Method 320 - Vapor phase organic and inorganic emissions by extractive FTIR, as shown in Figure 5.

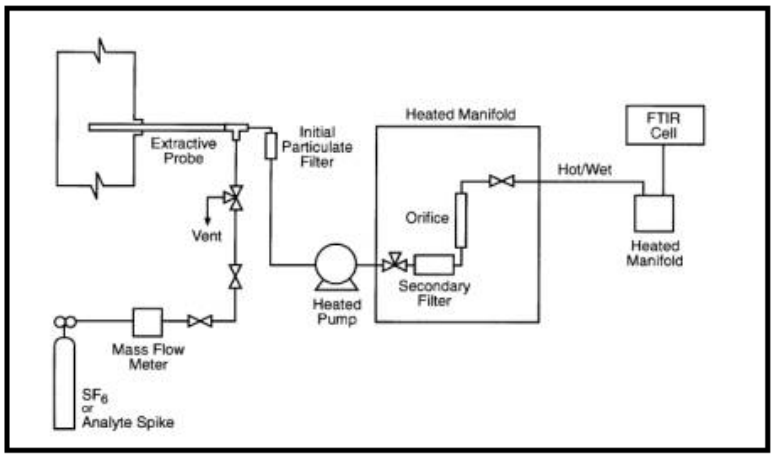

https://www.epa.gov , https://www.epa.gov

Figure 5: Instrumental Setup of Fourier Transform Infrared Spectroscopy (FT-IR)

Electron Microscopy (FESEM)

Scanning electron microscope (SEM) usually performed by electron diffraction method to study the morphology of a sample. The sample shape or size of particles and the properties of surface were studied by a high resolution of FE-SEM (field emission scanning electron microscope). It generated high-resolution images of high magnification due to the use of electrons instead of light in electron microscopy (Che *et al.,* 2003). All the tested samples are used in powder from this characterization technique. The beam of electrons is normally scanned in raster scan pattern, electrons beam is focused on the sample by scanning to detect the signal to generate an image of the sample (Miyata & Kuroda, 1999). In my research work, the images were taken using FEI Quanta 400F FESEM, as shown in Figure 6.

Figure 6: Instrumental Setup of Electron Microscopy (FESEM), FEI Quanta 400F FESEM

Energy- Dispersive X-ray Spectroscopy (EDX)

EDX is a nondestructive analytical tool used for the analysis of chemical and elemental composition of a sample. The EDX instrument is comprised of three parts, namely the processing electronics, the detector, and display and MCA. After the beam of electrons hits the sample, the X-rays are collected by the detector.

Therefore, usually standard electron microscopic instruments (e.g. SEM, TEM) can also perform EDX analysis. Small areas in the sample are scanned by the beam of electrons. In the present work, EDX analysis was carried out using FEI Quanta-400F FESEM instrument as shown in Figure 7

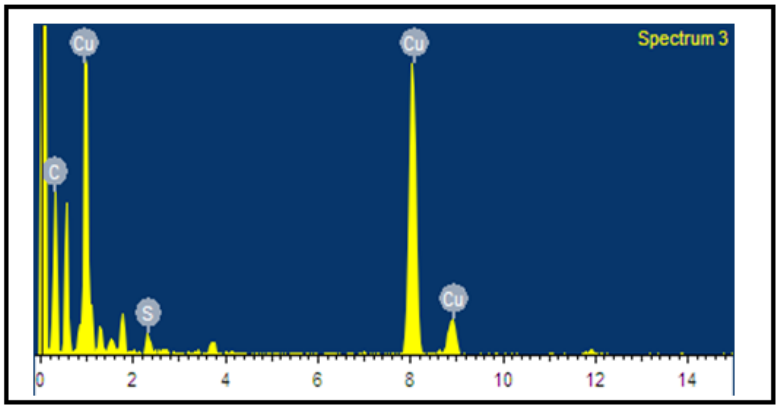

Figure 7: Experimental Data of a Reference Sample in Energy- Dispersive X-ray Spectroscopy (EDX), FEI Quanta-400F FESEM

Transmission Electron Microscopy (TEM)

For material science, Transmission Electron microscopy (TEM) is a very useful technique. The fundamental principles of optical microscopy and TEM are the same. A very high-energy electron beam is used in TEM to generate the specific morphology, crystal structure, shape, size and composition of the prepared sample (Tüysüz *et al.,* 2008). Size distribution of nanoparticles in a sample can be easily carried out using TEM. Selected area electron diffraction (SAED), part of TEM analysis, gives useful information about crystalline or polycrystalline nature of the sample. Very fine crystalline nanostructure and its lattice parameters can also be profoundly determined by high-resolution TEM (HRTEM) analysis (Williams & Carter, 2009; Ernst & Ruhle, 2003). At first, a small amount of the sample is dissolved in ethanol (or any volatile solvent). To homogenizehe solution, ultrasonication may be used. After that, a small drop of the solution is placed on a carbon coated copper grid, the solvent evaporated, and the grid mounted in the electron microscopy chamber. In the present work, the nanomaterials were characterized using a JEOL JEM-2010 instrument as shown in Figure 8.

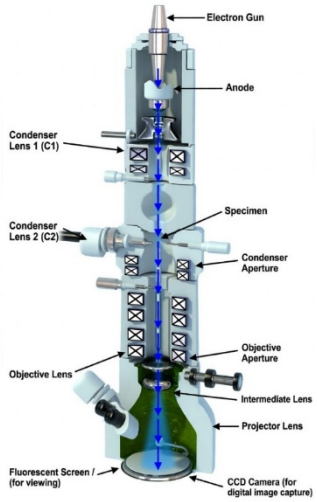

https://www.jeol.com

Figure 8: Instrumental Setup of High-Resolution Transmission Electron Microscopy (HRTEM)

Ultraviolet-Visible Spectroscopy (UV-Vis)

Ultraviolet and visible spectrophotometry is the technique related to absorption or reflectance seen in the visible or ultraviolet part of spectral region (200 to 800 nm) at room temperature. Molecules that contain π electrons or non-bonding electrons can absorb ultraviolet or visible electromagnetic radiation. Fundamentally, electrons need to move from a lower energy to a higher energy orbital. Ultraviolet-visible (UV-Vis) spectroscopy is regularly used in the area of analytical chemistry for determining quantity of several analytes. These can be highly conjugated organic compounds, transition metal ions, and biological macromolecules. It can also be used to analyze materials, using reflectivity measurements by the same instrument (Hawkes & Kasper, 1989). The same method of analysis can also be used in gases. The samples are dispersed ultrasonically in deionized water (or some other solvent) and then poured into quartz cuvettes for the measurement (Forker *et al.,* 2012). In the present work, the prepared samples were characterized using a Specord-200 (Analytik Jena, Germany) spectrophotometer as shown in Figure 9.

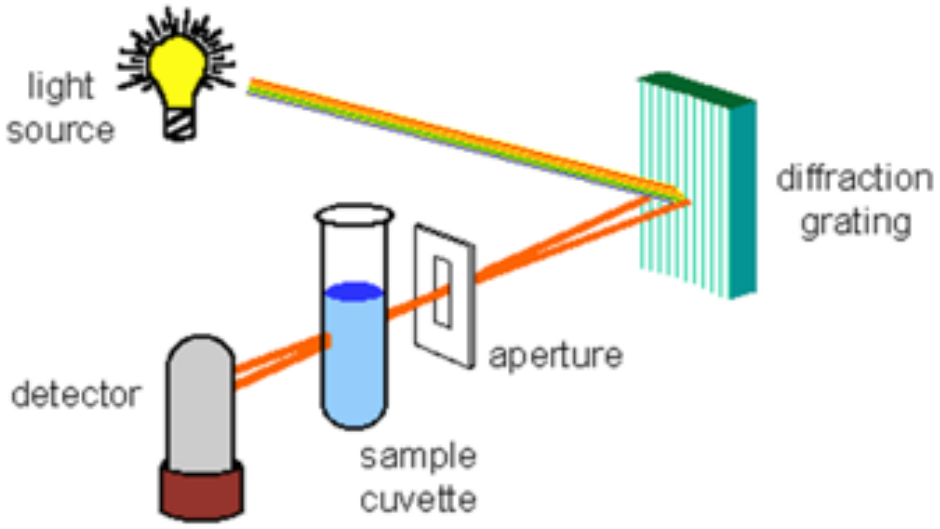

https://www.analytik-jena.com

Figure 9: The Schematic Representation of the Instrumental Setup of UV-Vis Spectroscopy

Atomic-Force Microscopy (AFM)

Atomic Force microscopy (AFM) is a type of scanning probe microscopy (SPM). It can resolve structures of the order of nanometers. This is a thousand times better than the optical diffraction limit. The microscopy related to this method involves quantum mechanical tunneling. Any type of sample, e.g., composite, ceramic, polymer, biological samples or nanoscaled material, can be examined by atomic force microscopy. This technique can operate both in tapping and non-contact modes. Electric potentials are used for detecting surface features by conducting cantilevers that are equipped with silicon tips of high resolution that engage with the surface of the sample that moves along it in different options (modes) and electric potentials make for returning signals. While the force between the cantilever and the sample, AFM can measure the force as a function of the distance between the cantilever and the sample, the force can be measured by AFM as a function of distance between the two. This can be used to provide force spectroscopy. With the help of relevant height differences upon scanning, the thickness and sizes of the particle can be observed and evaluated. In the present work, AFM was used in tapping mode to analyze the structure of graphene, graphene oxide and graphene-based nanocomposites. In this work, the prepared samples were examined using a 2010 NT-MDT NOVA-1.0.26 AFM instrument, as shown in Figure 10.

Figure 10: Instrumental Setup of Atomic Force microscopy (AFM), 2010 NT-MDT NOVA-1.0.26

Nuclear Magnetic Resonance (NMR)

In the 1940s, Felix Bloch and co-workers, and Edward Purcell and coworkers, developed NMR spectroscopy in condensed media and were awarded the Nobel Prize in Physics in 1952 for their work. NMR spectroscopy is mainly used to determine the chemical structure of an organic molecule. It can also make available detailed information about the molecular reaction state of a particular chemical reaction, the nature of reaction dynamics, phase change, conformational change, diffusion and the nature of the chemical environment of molecules in a solvent. NMR spectra are distinctive, can be well-resolved, are analytically easy to handle, and are often highly predictable for small molecules. NMR technique is often enough to confirm the identity of an organic compound. Apparently indistinguishable functional groups present in a molecule can be separated and distinctly identified by NMR. In the present work, prepared samples or reaction products were identified using a BRUKER Ultrashield 400 MHZ NMR instrument, shown in Figure 11.

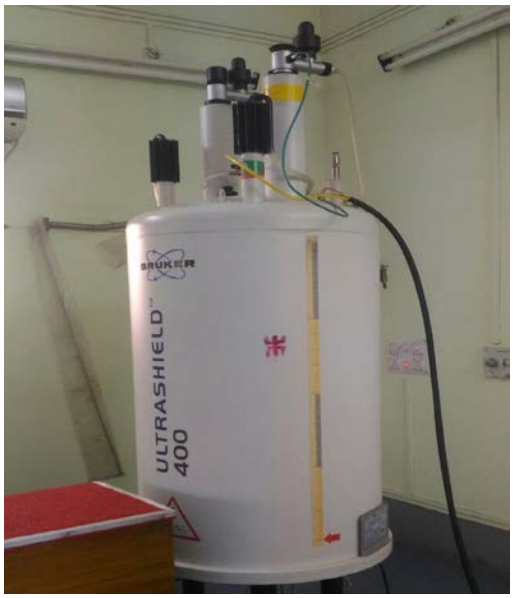

Figure 11: Instrumental Setup of Nuclear Magnetic Resonance (NMR) - Bruker Ultrashield 400 MHz Spectrometer Used in the Present Work.

Atomic Absorption Spectroscopy (AAS)

Atomic Absorption spectroscopy (AAS) is a procedure used in analytical spectrometry for determining quantitative information of chemical elements present in a sample. It is based on the phenomenon of absorption of electromagnetic radiation of a particular wavelength by atoms excited at high temperature in a flame or in graphite furnace. For atomization, flame and electrotherapy vaporizers are the most common techniques. But several other methods are also available for specific tasks. It is useful in analyzing trace metals in water from lakes, rivers, and oceans; in pharmaceuticals; in drinking water; in foodstuffs and beverages; in geological and mineralogical samples; in biological fluids; in petroleum products; in forensic analysis; etc. Spectrometry related to atomic absorption was used as the first analytical method and the fundamental principles were worked out in the second half of the nineteenth century by people like Bunsen and Kirchhoff. The method relies on the relationship between spectrophotometric absorption at a specific wavelength and the concentration of an analyte within a sample. The relation is known as the Beer-Lambert law.

In brief, atomic electrons can move to a higher energy orbital by absorbing light of definite wavelength. This wavelength is specific for a definite transition of an electron in a particular atom. The radiation flux in the atomizer is measured with and without a sample using a detector (Walsh, 1955). It shows the ratio between the two absorbance values, from which the concentration of analyte can be obtained from the Beer-Lambert law. In the present work, the prepared samples were analyzed using an AA-240 Agilent Atomic Absorption spectrometer, as shown in Figure 12.

Figure 12: Instrumental setup of Atomic Absorption Spectroscopy (AAS)

High Resolution Mass Spectroscopy (HRMS)

High-resolution mass spectrometry is the basic technique for identifying or confirming the molecular formula of a new compound through accurate measurement of the mass of the molecular ion and various charged fragments obtained by interaction of the molecule with a beam (Biemann, 1990). Mass spectrometers have evolved over the years through many stages. The birth of high-resolution mass spectrometers having double focus was possible due to modified and improved electronics and proper understanding of ion optics during the 1960s. The structural application was thought of mainly for organic compounds, but later it was applied to other fields of chemistry like characterization of organometallic and inorganic compounds.

Nowadays, it is also used to study much larger compounds such as biopolymers (Burlingame *et al.,* 1996; Bowers *et al.,* 1996). In the present work, the prepared compounds were analyzed using a Waters XEVOG2-S-QTOf mass spectrometer as shown in Figure 13.

Figure 13: Instrumental Setup of High-Resolution Mass Spectrometry (HRMS) - Waters XEVO G2-S QTof System

Gas Chromatography (GC)

Gas chromatography (GC) is a very common analytical tool, used in analyzing and sorting out various volatile compounds in a reaction mixture. The compounds also have to be thermally stable over the operating temperature range of GC. GC is a specific gas-liquid chromatographic technique, which involves getting a sample vaporized and injected onto the head of a chromatographic column without decomposition. The gaseous mobile phase of GC is usually an inert gas that can transport the sample through the column by its flow. The column is present in the liquid stationary phase of GC, which is an inert solid that adsorbs the gases. GC can be used for testing the purity of a particular substance or to analyze and sort out several compounds in a mixture. It also determines the relative amounts of such components in the mixture.

In gas chromatography, normally an inert (e.g., helium) or unreactive (e.g., nitrogen) gas acts as the mobile or carrier phase. The stationary phase comprises a microscopic layer of liquid or polymer that is on a solid (inert) support present inside a block of glass tube known as a column. The injected mixture of compounds vaporizes and then comes in contact with various stationary phases present in column walls. The scope of interaction between the column and injected compounds is not the same for each compound. Hence, every single compound elutes at different times, known to be the retention time of the compound. Comparison of these retention times gives an important analytical value to identify volatile compounds. The essential parts of GC include the mobile phase of a carrier gas that must be inert like nitrogen, an inlet to deliver the sample to a column, the column where separations occur, an oven as a thermostat for the column, a detector to register the presence of a chemical in the column effluent, and a data system to record and display the chromatogram. In the present work, the reaction products were determined or quantified (GC data) using a Varian 430 gas chromatograph equipped with a 30 m CP-SIL8CB capillary column and a flame ionization detector as shown in Figure 14.

Figure 14: Instrumental Setup of Gas Chromatography (GC)- Varian 430, 30m CP-SIL8CB Capillary Column System

Conclusion

The present work provides comprehensive experimental support for the efficient characterization of carbon allotropes and their nanocomposite materials. The integrated application of techniques such as XRD, Raman, FTIR, SEM, TEM, AFM, UV-Vis, and TGA enables a clear, reliable, and easy analysis of structural, morphological, optical, and thermal properties. This multi-technique approach not only confirms the successful synthesis and quality of the materials but also establishes a simplified analytical framework to develop new kinds of carbon allotropes and nanocomposite materials. This work will be highly beneficial for future research and application-oriented development of the advanced research field of graphene-based nanomaterials.

Acknowledgement

The author would like to express his sincere gratitude to all those who supported the successful completion of this work. The author also would like to thank the principal of Santipur College and the head of the Department of Chemistry at Santipur College, India, for providing the infrastructure, invaluable guidance, constant encouragement, and insightful suggestions throughout the course of this work.

References

Biemann, K. (1990). [13] Utility of exact mass measurements. In *Methods in enzymology* (Vol. 193, pp. 295-305). Academic Press. https://doi.org/10.1016/0076-6879(90)93421-G

Bowers, M. T., Marshall, A. G., & McLafferty, F. W. (1996). Mass spectrometry: recent advances and future directions. *The Journal of Physical Chemistry*, *100*(31), 12897-12910. https://doi.org/10.1021/jp960154u

Burlingame, A. L., Boyd, R. K., & Gaskell, S. J. (1996). Mass spectrometry. *Analytical Chemistry, 68*(12), 599–652. https://doi.org/10.1021/ac960021u

Che, S., Lund, K., Tatsumi, T., Iijima, S., Joo, S. H., Ryoo, R., & Terasaki, O. (2003). Direct observation of 3D mesoporous structure by scanning electron microscopy (SEM): SBA-15 silica and CMK-5 carbon. *Angewandte Chemie-International Edition*, *42*(19), 2182-2185. https://doi.org/10.1002/anie.200250726

Ernst, F., & Rühle, M. (Eds.). (2013). *High-resolution imaging and spectrometry of materials*. Springer Science & Business Media.

Ferraro, J. R., Nakamoto, K., Brown, C. W., Ferraro, J., & Nakamoto, K. (2003). *Introductory raman spectroscopy* (Vol. 434). San Diego: Academic press.

Forker, R., Gruenewald, M., & Fritz, T. (2012). Optical differential reflectance spectroscopy on thin molecular films. *Annual Reports Section" C"(Physical Chemistry)*, *108*(1), 34-68. https://doi.org/10.1039/c2pc90002e

Hannay, N. B. (1967). Trace Characterization, ed. by WW Meinke and BF Scribner, NBS Monograph 100, U-S. *Government Printing Office, Washington, DC*.

Hawkes, P., & Kasper, E. (1989). Principles of electron optics, Acad. *Press, London*.

Islam, M., Mondal, S., Mondal, P., Roy, A. S., Hossain, D., & Mobarak, M. (2011). Open air O-arylation reaction of phenols with aryl halides catalyzed by polymer-anchored copper (II) complexes. *Transition Metal Chemistry*, *36*(1), 1-11. https://doi.org/10.1007/s11243-010-9426-2

Li, C. Y., & Rees, L. V. (1986). Thermogravimetric studies of faujasites with different SiAl ratios. *Zeolites*, *6*(3), 217-220. https://doi.org/10.1016/0144-2449(86)90052-7

Mercuri, L. P., Matos, J. R., Li, Z., & Jaroniec, M. (2006). Comparative thermogravimetric and adsorption study of highly ordered mesoporous materials. *Journal of colloid and interface science*, *296*(1), 377-380. https://doi.org/10.1016/j.jcis.2005.08.043

Miyata, H., & Kuroda, K. (1999). Direct observation of mesoporous silica by high resolution scanning electron microscopy. *Advanced Materials*, *11*(10), 857-860. https://doi.org/10.1002/(SICI)1521-4095(199907)11:10%3C857::AID-ADMA857%3E3.0.CO;2-7

Moore, D. M., & Reynolds, R. J. (1997). *X-ray Diffraction and the Identification and Analysis of Clay Minerals* (2nd Ed). Oxford University Press, New York. pp. 332. https://doi.org/10.1017/S0016756898501501

Raman, C. V., & Krishnan, K. S. (1928). A new type of secondary radiation. *Nature*, *121*(3048), 501-502. https://doi.org/10.1038/121501c0

Sing, K. S. (1985). Reporting physisorption data for gas/solid systems with special reference to the determination of surface area and porosity (Recommendations 1984). *Pure and applied chemistry*, *57*(4), 603-619. http://dx.doi.org/10.1351/pac198557040603

Skoog, D. A., Holler, F. J., & Crouch, S. R. (2007). *Principles of instrumental analysis* (6th ed.). Thomson Brooks/Cole. pp. 169-173. https://books.google.co.in/books?id=GrOsQgAACAAJ&redir_esc=y

Smith, E., & Dent, G. (2019). *Modern Raman spectroscopy: A practical approach* (2nd ed.). Wiley.

Tüysüz, H., Lehmann, C. W., Bongard, H., Tesche, B., Schmidt, R., & Schüth, F. (2008). Direct imaging of surface topology and pore system of ordered mesoporous silica (MCM-41, SBA-15, and KIT-6) and nanocast metal oxides by high resolution scanning electron microscopy. *Journal of the American Chemical Society*, *130*(34), 11510-11517. https://doi.org/10.1021/ja803362s

Valodkar, V. B., Tembe, G. L., Ravindranathan, M., Ram, R. N., & Rama, H. S. (2003). A study of synthesis, characterization and catalytic hydrogenation by polymer anchored Pd (II)-amino acid complexes. *Journal of Molecular Catalysis A: Chemical*, *202*(1-2), 47-64. https://doi.org/10.1016/S1381-1169(03)00249-8

Walsh, A. (1955). The application of atomic absorption spectra to chemical analysis. *Spectrochimica Acta*, *7*, 108-117. https://doi.org/10.1016/0371-1951(55)80013-6

Williams, D. B., & Carter, C. B. (2009). The transmission electron microscope. In *Transmission electron microscopy: a textbook for materials science* (pp. 3-22). Boston, MA: Springer Us. https://doi.org/10.1007/978-0-387-76501-3_1

Subject Index

Published by :

LINCOLN UNIVERSITY COLLEGE
DKU016 (B)

2022 SETARA COMPETITIVE UNIVERSITY COLLEGE

ISO 9001:2015 Certified

ISBN 978-967-2819-54-7

eISBN 978-967-2819-55-4

www.lucp.net